Multi-Scale Modelling of Damage Initiation and Progression in Textile Composite

by

Philipp Römelt

Department of Aeronautical and Automotive Engineering

Loughborough University

Doctoral Thesis

Submitted in partial fulfilment of the requirements for the award of Doctor of Philosophy (Ph.D.) of Loughborough University

July 2012

Abstract

Composite materials play an ever increasing role in the design of modern day aeronautical and automotive structures due to their weight saving potential. Generally progress in constituent material production and composite manufacturing have resulted in lower costs for composite structures, which has made them more attractive for a number of industries, including the aeronautical and automotive industries.

However, while sufficiently accurate numerical models exist to model damage initiation and progression in metal structures similar models are not yet available for composite structures. Yet the ability to model damage accurately is an integral part of the design process in both the aeronautical as well as the automotive industry.

Due to the more complex microstructure of textile composites compared to metals a numerical model to predict the behaviour of a macrostructure needs to take microstructural effects into account. Multi-scale modelling approaches are uniquely suited to efficiently incorporate not only micro-scale affects but also higher scale affects like tow buckling.

Therefore a multi-scale approach to model damage initiation and progression in textile composites based on the finite element method is presented in this thesis. A number of mechanical tests of a benchmark composite are conducted to measure input parameters for the multi-scale approach as well as mechanical behaviour for comparison with model predictions.

The multi-scale approach is used to predict the mechanical behaviour of the benchmark composite for two different load cases, pure tension and pure shear. Results for the pure shear load case show significant deviations between predicted and experimentally measured stress-strain curve. For the pure tension load case transverse strain predictions also deviate significantly from the experimental data, stress-strain data in the loading direction however show good agreement between predicted values and experimentally measured data.

Whilst further improvements are still required, the approach presented in this thesis provides a solid foundation for designers to predict damage initiation behaviour and progression in textile composites.

Acknowledgements

I would like to thank Dr. Paul Cunningham of Loughborough University for supervising the work presented in this thesis and for letting me run free most of the time but reeling me back in when I needed it. Without his constructive criticism this work would be so much poorer. Thanks also to Prof. Joe Loughlan and other members of Loughborough University staff, who provided support, either physically or morally, in many different ways.

My fellow Ph.D. students also provided me with great support throughout my thesis, sometimes in form of advice, sometimes just with a cup of tea and a chat. Those requiring a special mentioning are Liz Bowyer, Chris Harvey and Shou Dai.

Finally, I would like to say a special thank you to my wonderful wife Anne for providing support throughout the time at Loughborough and during what proved to be a difficult writing up period after our return home.

Nomenclature

A:	cross –sectional area	[mm^2]
A':	calibration coefficient for thermoelastic signal	[MPa/DL]
a,b:	major and minor elliptical axis parameters	[mm]
d:	crack length	[mm]
C:	tow path amplitude	[mm]
D,E:	tow path sinusoidal function parameters	[mm]
E:	Young's Modulus	[kN/mm^2]
G:	shear modulus	[kN/mm^2]
K:	stiffness	[kN/mm]
K:	bulk modulus	[kN/mm^2]
L:	tow path wavelength	[mm]
L:	unit cell length	[mm]
P:	concentrated load	[kN]
S:	thermoelastic signal	[DL]
t:	thickness	[mm]
V:	volume fraction	[-]
W:	weight fraction	[-]
x,y,z:	coordinates	
α:	thermal expansion coefficient	[1/°C]
δ:	crack tip opening displacement	[mm]
ρ:	density	[kg/mm^3]
ε:	strain	[-]
ν:	Poisson's ratio	[-]
σ:	standard deviation	[mm]

σ:	stress	[GPa]
φ:	tow path shift angle	[°]
θ:	tow cross section tilt angle	[°]

Subscript:

f:	fibre
r:	resin
x,y,z:	global coordinate directions
1,2,3,4,5,6:	principal material directions

Acronyms

UD: unidirectional

CFD: computational fluid dynamics

FEM: finite element method

TSA: thermoelastic stress analysis

RFI: resin film infusion

RTM: resin transfer moulding

VARTM: vacuum assisted resin transfer moulding

RIFT: resin infusion under flexible tooling

DCB: double cantilever beam

RVE: representative volume element

B-spline: Belizier spline

Micro-CT: micro computed tomography

NUC: non uniformity correction

pdf: probability density function

cdf: cumulative distribution function

FFT: fast fourier transform

Table of Contents

List of Figures

List of Tables

1 Introduction

1.1 Textile Preforms

Textile preforms come in a wide range of shapes and architectures, which can roughly be grouped into woven, braided, stitched and knitted. Kamiya et [1] al give a detailed overview over the different techniques of preform manufacture.

Weaves are made of interlacing yarns with a number of different weave patterns available, allowing for the production of large areas of woven cloths at low costs. Due to its traditional use in the clothing industry, weaving is widely used to manufacture preforms. Hybrid weaves are also easily generated by interweaving different types of tows. One such type of hybrid are Uniweaves, in which strong, stiff yarns, so called primary yarns, are interwoven with fine yarns, called secondary yarns, which hold the primary yarns together during handling. As a general rule, yarns running along the length of the fabric are called warp yarns and yarns perpendicular to warp yarns across the width of the fabric are called weft yarns. In the weaving process warp tows are kept straight and parallel in a loom whilst the weft tows are inserted transverse to the warp direction using different techniques ranging from free flowing tows to carrier vehicles such as a rapier.

Different types of 2D weaves, plain, satin are distinguished by the number of warp tows that a weft yarn moves over before changing its plane of movement. Of all weave styles available a plain weave is the simplest with yarns interlaced in an alternating over and under pattern (Figure 1). This simple pattern results in high fabric stability and firmness with a minimum of yarn slippage during handling. If the same yarn types are used both in weft and warp direction, the fabric displays uniform in-plane strength and stiffness. On the downside, the fabric is only moderately permeable, which can result in problems during fibre impregnation. Also due to the high number of exchanges the fibres are highly crimped, which reduces in-plane stiffness and strength [2].
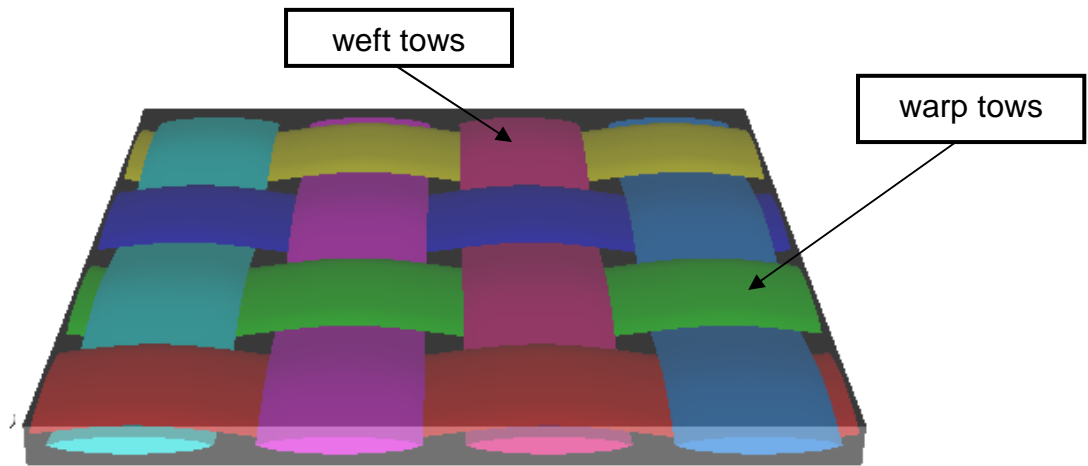
Figure 1: Plain 2D Weave

A number of 3D woven preforms, called Interlocks are also available, which consist of multiple layers of straight yarns (both warp and weft yarns) that are connected through the thickness by warp weavers. Interlocks can be categorized by the number of layers that warp weavers penetrate and the angle of its path through the composite. In an orthogonal through-thickness interlock for instance the warp weavers orthogonally pass through the thickness of the entire composite (Figure 2), for an angle interlock the warp weavers pass through the thickness at an angle smaller than 90 deg (Figure 3), whilst for a two layer-by-layer angle interlock weave the warp weavers only binds two layers together (Figure 4). The advantage of 3D weaves is an improvement in through thickness properties even for shaped composite parts. According to Bogdanovich [3] 3D weaves have a number of benefits over traditional laminates. Not only is delamination suppressed, fracture toughness, damage tolerance and impact and ballistic resistance are improved. Furthermore, due to a reduction in notch sensitivity, fatigue life is extended. Finally, since no lay-up is required both time and money are saved during the manufacturing process.
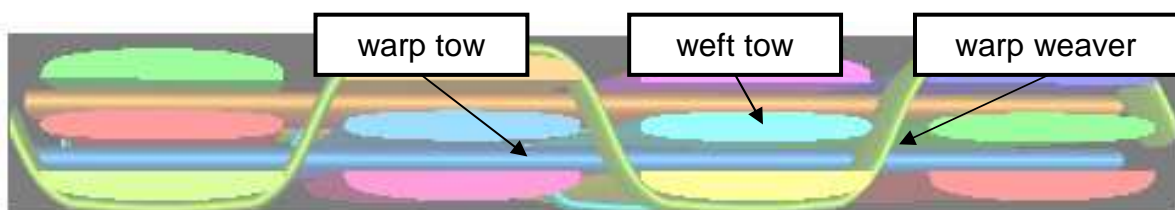
Figure 2: Orthogonal Interlock 3D Weave
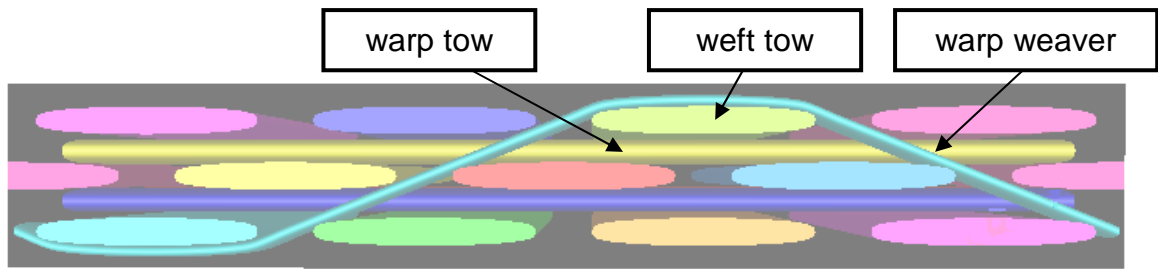
Figure 3: Angle Interlock 3D Weave
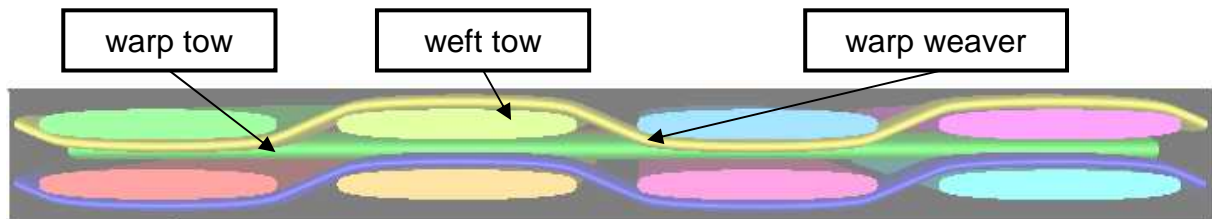
Figure 4: Layer-By-Layer Interlock 3D Weave

Two different kinds of knitted fabrics are distinguished, warp-knitted and weft-knitted fabrics. In warp-knitted fabrics (Figure 5 a) loops run lengthwise in the fabric, these are called wales [4]. These fabrics are more formable and can be produced at a high rate but are also more expensive. In weft-knitted fabrics loops are made horizontally across fabric, these are called courses (Figure 5 b). These are less stable than warp-knitted and slow to produce but also cheap. Therefore they are usually used in prototype production, whereas warp-knitted fabrics are used in mass production [1],[5]. The mechanical properties of knitted fabrics are only slightly better than those of composites with short fibre reinforcements. This is due to low yarn count, the complex yarn paths, which are highly looped, and damage of the yarns during the knitting process. Impact resistance however is quite high. The major advantage of knitted fabrics is that they display a low resistance to deformation and it becomes possible to manufacture complex shapes to near net shape, which reduces material wastage and production time. Therefore the process is suitable for rapid production of complex shapes at low cost [1],[5].

(a)   (b)
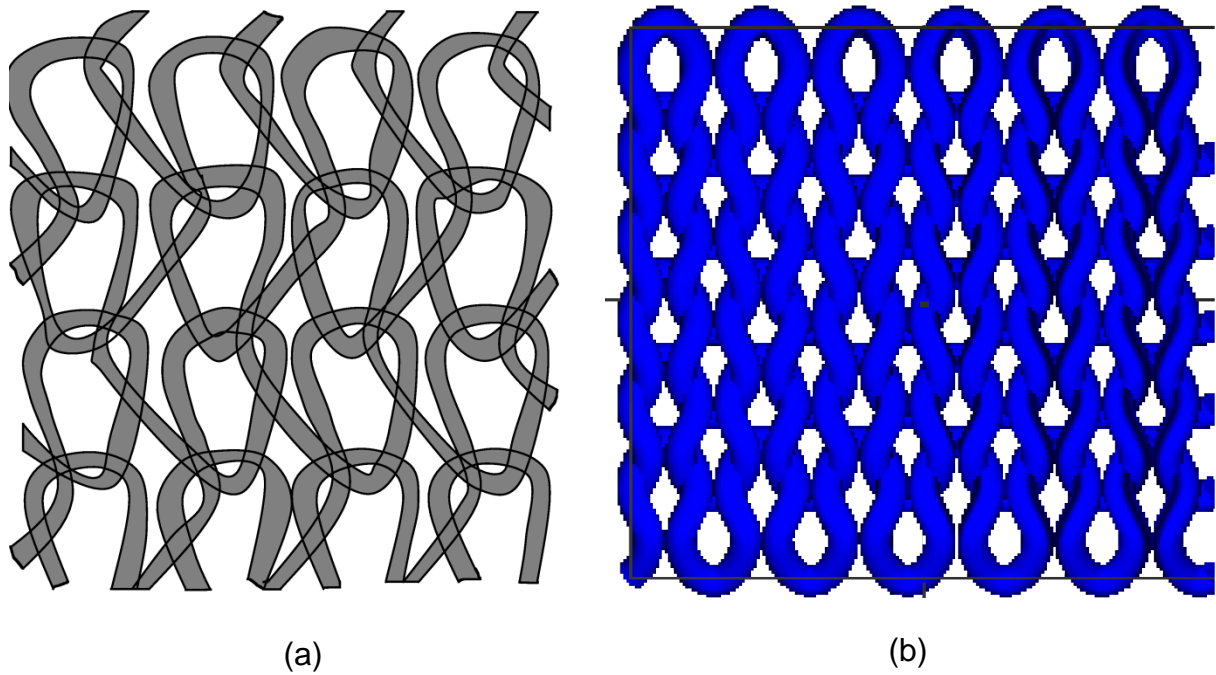
Figure 5: 2D Knitted Fabric (a) Warp – Knitted (b) Weft - Knitted

Stitching of fabrics significantly increases damage tolerance of the part by providing a mechanical link between preforms. During manufacture it also makes handling of the dry prefoms easier and also compacts them, which decreases mechanical compression required of the tool. However, stitching can cause significant damage to the preform fibres, which degrades in-plane properties. Two different forms of stitches exist, the modified lock and the chain stitch. The chain stitch requires only one thread, whereas more are required for the modified lock stitch, which are tension adjusted to form knots on the outside of the laminate, which minimizes distortion within the fabric [1].

Braids (Figure 6) are the strongest of all types of reinforcement patterns available, inherently suited for beamlike structures. It improves the torsional load capability, impact resistance and damage tolerance. They are produced by a series of yarn carriers that follow intersecting circular paths to form a tubular fabric. It is distinguished between two-step, four-step and multi-step braids, depending on how many times the yarn carriers intersect. The final fabric configuration is controlled by the use of a mandrel. In a tri-axial braid fixed axial yarns are included. These yarns remain straight and therefore retain their axial properties. The overall properties of the braid can be influenced by the size of the axial yarn and the angle of the biased yarns. Flat sheets are produced by cutting the tube along its axis. Braids can be used

to produce thick, near-net section preforms. In 3D braids, yarns interlock through the thickness so no individual layers can be distinguished [2].
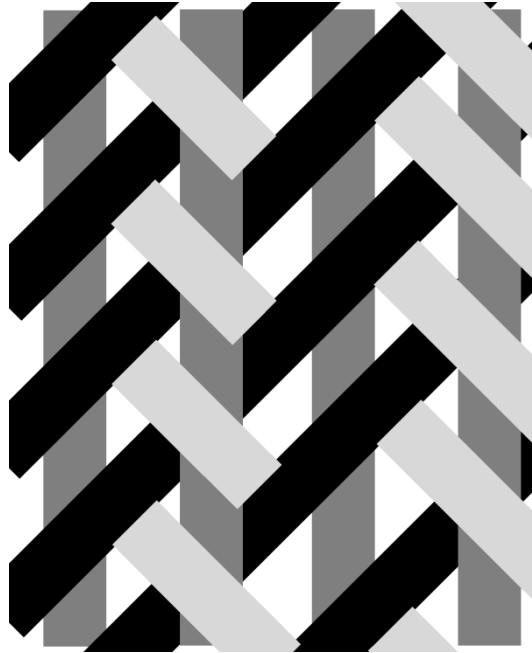
Figure 6: 2D Braid

When trying to reinforce uncured prepregs using stitching, severe fibre damage is caused. Drilling and inserting metal fasteners on the other hand is very tedious. Z-pins offer a much more efficient way, locking the layers together by both friction and adhesion. These types of reinforcements increase the resistance to delamination and impact damage progression although they are not very efficient at reducing delamination and crack initiation. The improvements in resistance to delamination and impact damage progression come from the efficient containment of crack propagation [6].

Z-pins can be made from titanium alloy, steel or carbon composites, typically with diameters ranging from 0.2 to 1.0 mm with pin contents from 0.5 to 4.0 vol%, which means 8 to 70 pins per cm^2. To ensure even spacing, a carrier foam is used, which contains the pins and is discarded after the pins have been inserted using ultrasonic guns (Figure 7). This is the most commonly used method of inserting z-pins for high production rates. The gun generates high frequency compressive waves, which drive the pins into the prepreg, and moderate heating, which softens the prepreg, helping pin incorporation. After pins have been inserted then conventional processes, e.g. vacuum bagging and autoclave, can be used to cure the stack. Z-pinning, therefore,

is just an additional step in traditional laminate manufacturing processes, hence the overall manufacturing process is not significantly affected [6]. One disadvantage with z-pinning is the degradation of in-plane properties. First of all fibre breakages can be caused by inserting the pins. Fibres are forced aside during manufacture, which not only increases fibre crimp and waviness at the pin location, but also creates voids, which become resin channels. Therefore resin rich areas develop at the pin location. In case of closely spaced pins these resin rich areas coalesce. Furthermore swelling increases the overall volume of the stack, reducing fibre volume fraction. Swelling is caused by two effects. Firstly the laminate has to expand to accommodate the z-pins, secondly the pins increase resistance against compaction during curing. Careful control of the z-pinning and cure process is therefore required. Finally, different thermal expansion between pins and prepreg results in pre-stresses due to autoclave curing. Overall in-plane properties seem to reduce linearly with z-pin volume content. Also fatigue life of the prepreg material is decreased with increasing pin content and diameter. Therefore low numbers of small diameter pins are the most beneficial [6].
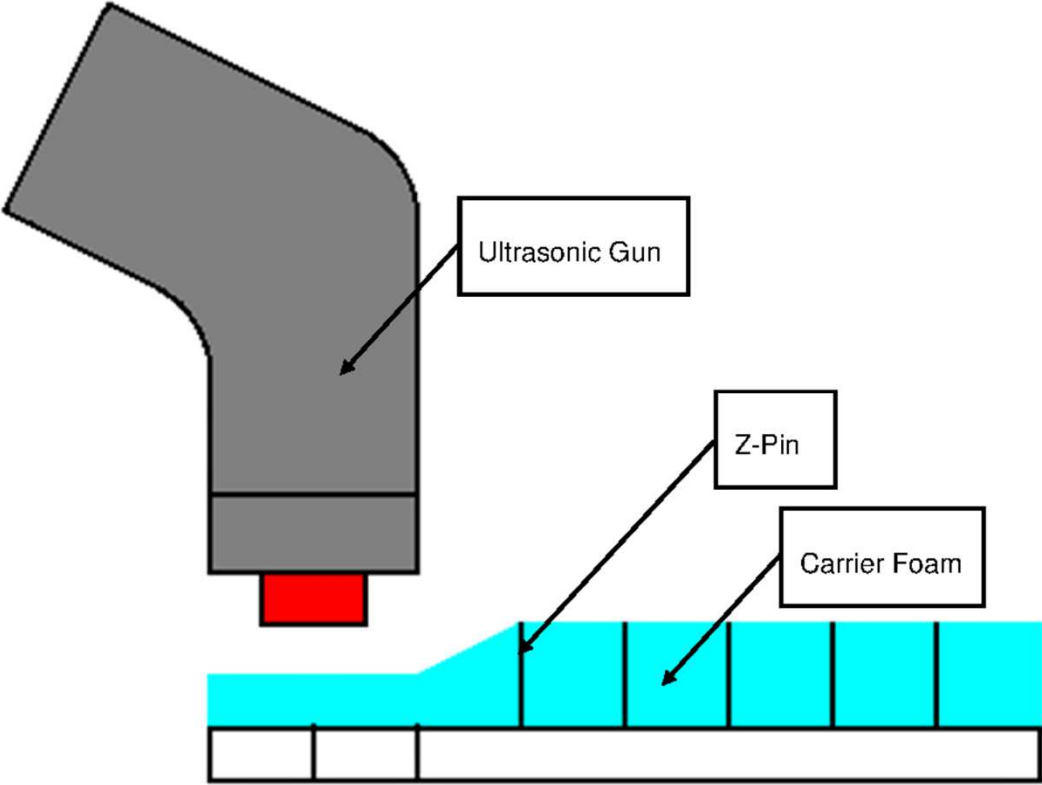
Figure 7: Z-pinning using Ultrasonic Gun

1.2 Applications of Textile Composites

Greenhalgh and Hiley [7] cite the superior resistance to delamination as the main reason for using textile composites as this property makes them perfectly suitable for impact damage tolerant designs like stiffened wing panels. This is despite the significant reduction of in-plane properties compared to traditional unidirectional (UD) laminates and difficulties in the manufacture of large composite parts due to excessive voids forming during manufacture.

Similar points are made by Rueckert and Kolax [8], who do not see textile composite in a favourable light because of their strong dependence on resin infusion manufacturing techniques and difficulties in producing parts of consistent quality. They also claim that weight optimised designs are not possible when applying textile composites. Despite this they cite textile composites as possible materials for aircraft frames, fittings and reinforcements for window cutouts.

As a contrast to Rueckert and Kolay [8], Kobayashi and Ito [9] have demonstrated that weight reductions of 30% and more can be achieved for fighter plane parts that fulfill all necessary requirements concerning strength and fatigue. In the same year at the same conference Bogdanovich [10] claimed that recent advances in understanding of the mechanics of textile composites and cost reductions due to improved manufacturing techniques opened the door for composites for a wide range of applications including boat hulls, automotive parts, bridge decks, windmill blades and thermal protection tiles.

Similar opinions had been voiced earlier in a review paper by Leong et al [5], who claim that the ability to manufacture near net shape parts and good formability are major advantages of textile composites over traditional composite materials, despite the degradation of in-plane properties due to fibre crimp.

Mouritz et al [11] also suggested that a wide range of applications could be found for textile composite for economical reasons as well as their mechanical properties at a time when textile composites were used sparingly and only for highly specialized parts like structural joints in aircraft.

Designing textile composites for the applications mentioned above requires detailed knowledge of the mechanical properties and damage behaviour of the materials

used. With the increasing availability of powerful computers in the last 25 years, the use of numerical analyses to solve fluid-mechanical problems has also increased significantly. In order to reduce time and cost during the design process, more and more design steps are done using virtual tests with only final real world tests done for model validation and proof of compliance with existing regulations. Therefore, validated numerical procedures to predict mechanical properties and damage propagation behaviour are required to be used during the virtual steps of the design process. The aim of this thesis is to develop and validate such a numerical procedure using both experimental and computer-based engineering methods.

1.3 A Virtual Design Process for Textile Composites

A fully virtual design process for textile composites, starting with preform manufacture and ending with stiffness and strength analyses, is suggested in the following subsection. This thesis will focus on the final step of the design process with the aim of developing and validating a finite element based process, applicable to different types of textile composites, to estimate mechanical properties as well as predict damage initiation and propagation.

In the first step mechanical models of tows are used to model the preform manufacturing and draping processes using multi body dynamics [12]. This way the final preform shape as well as stresses and strains of tows can be calculated. This allows for an estimation of the amount of damage sustained by tows during manufacturing as well as residual stresses in the preform. It also provides input parameter, namely permeability and material spatial distribution, for the next step of the design process.

The second step is a model of the resin infusion and curing process using a coupled computational fluid dynamics (CFD) and finite element method (FEM) analysis [13]. This allows the modelling of preform compaction and deformation due to hydrostatic pressure during infusion. Also, void content and void positions can be estimated as well as residual stresses and deformation due to thermal effects during cure and post-cure. All these factors have a significant effect on properties of the finished composite structure and must be taken into account in the next step of the design process.

The third step involves the estimation of elastic, plastic and thermal properties as well as strength predictions and fatigue behaviour of the finished composite structure using FEM analysis. This requires a multi-scale modelling approach capable of modelling macro-scale material behaviour from constituent material properties as well as damage initiation and propagation models.

The aim of this thesis is to develop, and validate experimentally, such a multi-scale modelling approach on the basis of FEM, which allows for the prediction of elastic properties and damage progression in textile composites independent of the textile architecture, constituent materials and loading conditions. Whilst a number of approaches exist that use detailed finite element models of unit cells or define equivalent unit cells using analytical approaches, the approach presented here uses a full finite element model to derive properties for an equivalent cell, which is the used to model a larger size structure.

1.3.1 A Multi-Scale Modelling Approach

The multi-scale modelling approach takes a complex, detailed and therefore computationally expensive finite element model of a single representative cell, called a unit cell (Figure 8), as a starting point.
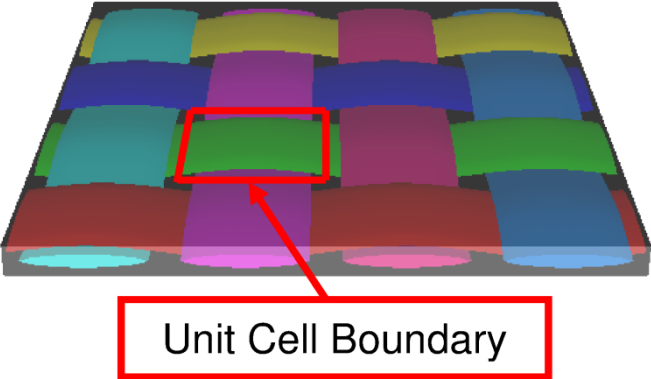
Figure 8: Unit Cell Boundary in a Plain Weave

It is created to model meso-scale damage initiation and progression and will be referred to as the full finite element unit cell model (Figure 9 a) throughout this thesis. However, due to its computational size it is not possible to model a macrostructure using unit cell models with this level of detail. Therefore a simplified and less computationally expensive representative unit cell model, referred to as the equivalent binary unit cell model (Figure 9 b), derived from the full finite element unit

cell model results, is presented. In order to model damage initiation and progression on the macro-scale, the macrostructure composite is assembled using a number of equivalent binary unit cells. This assembly will be referred to as the macrostructure binary model throughout this thesis.
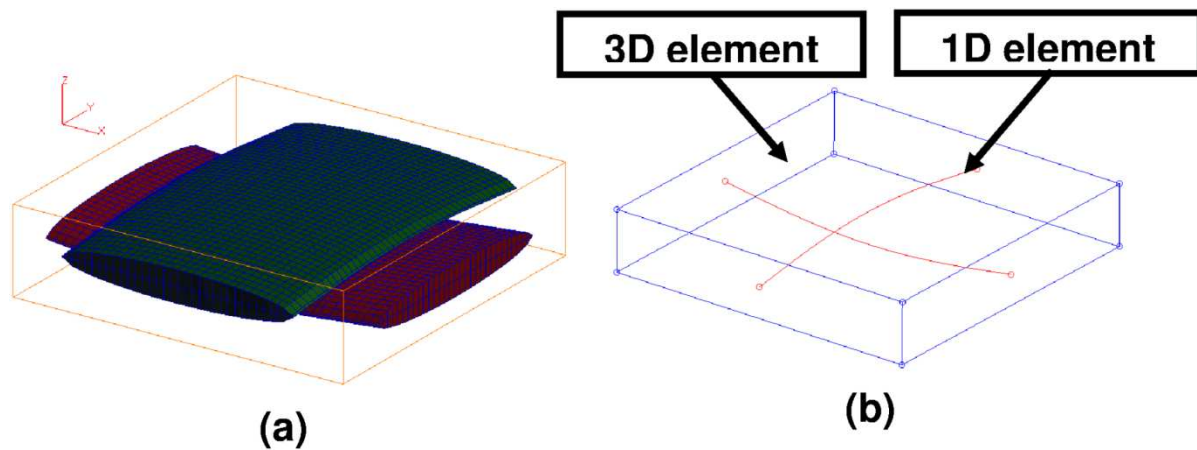
Figure 9: Full Finite Element Model and Equivalent Binary Unit Cell Model

The multi-scale approach described is applicable to any possible architecture of textile composites, woven, braided, stitched etc as well as any type of loading, either mechanical or thermal. In this thesis it is demonstrated and validated for a woven glass fibre laminate with a plain weave architecture and an epoxy resin as matrix material under uniaxial tension and in-plane shear loading.

Since the first two steps, preform manufacture and resin infusion and curing, of the proposed design process were not done virtually, some data had to be measured experimentally on a 2.5 mm thick plain weave glass fibre laminate with the same reinforcement architecture as the virtual material. First geometrical input parameters for the full finite element and equivalent binary unit cell model had to be measured using digital microscopy. Secondly mechanical properties as well as full field stress data also had to be measured experimentally for comparison with properties and stress distributions predicted by the multi-scale modelling approach.

The whole process of implementation and validation of the approach is summarised in Figure 10.
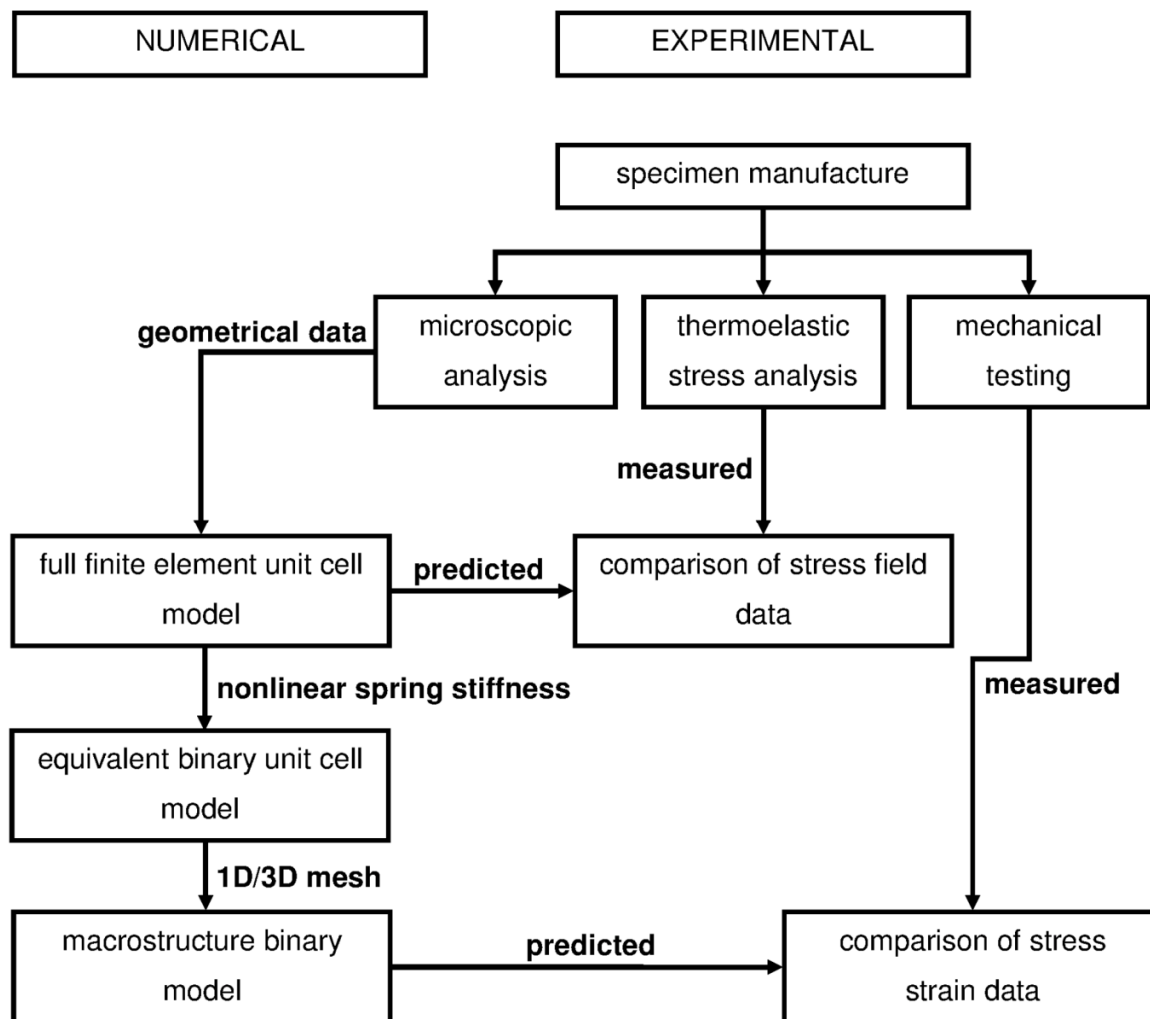
Figure 10: Multi-Scale Modelling Approach for Damage Progression in Textile Composites

1.4 Outline of Chapters

The thesis starts with a literature review to give an overview over present day applications and manufacturing techniques of textile composites as well as the general behaviour under different mechanical loading conditions, including fatigue loading. Current techniques to model geometrical and mechanical properties, including damage behaviour, of textiles are also included as well as techniques for full field stress or strain analysis. The literature review is presented in Chapter 2.

Some terms in this thesis, such as warp and weft, are seldom encountered in the field of composites engineering outside the specialized literature on textile composites. Therefore, all textile specific terms in this thesis will be used in accordance with the definitions laid out by Pastore [14] in NASA Contractor Report

191539 to which the reader is kindly referred for detailed descriptions and definitions of textile terminology.

Chapter 3 gives an overview over the methodology used to obtain experimental data for input parameter calculation and model validation. Three different types of analyses were conducted, namely digital microscopy, tensile and shear tests as well as a thermoelastic stress analysis. These analyses are described in more detail in Chapters 4 to 6.

Chapter 4 presents the digital microscopy analysis conducted to calculate averaged geometrical parameters of tow path and cross-section for both full finite element unit cell and equivalent binary unit cell model.

Chapter 5 gives details on the thermoelastic stress analysis (TSA) conducted to assess the stress field on the surface of a test specimen. This is needed for validation of the full finite element unit cell model results by comparing the surface stress distribution predicted by the model with the stress distribution measured by the TSA.

Chapter 6 provides details on the tensile and shear tests conducted to experimentally measure stress – strain curves for different loading conditions, uniaxial tension and pure in-plane shear. These measured stress – strain curves were compared to stress – strain curves predicted by the macrostructure binary model for validation purposes.

Details on modelling technique, material models employed, boundary conditions etc. for the full finite element models are presented in Chapter 7. Model validation using TSA data and results are also discussed in that chapter.

Chapter 8 presents an analytical approach to derive nonlinear spring stiffness data as input parameter for the equivalent binary unit cell. Model setup for equivalent and macrostructure binary models are also shown and predicted stress – strain data are presented and compared with measured stress – strain data for validation purposes.

The final chapter, Chapter 9, gives a summary and discussion of the results presented in this thesis and suggests a number of points for further research that could lead to improvements in the multi-scale modelling approach.

2 Literature Review

2.1 Manufacturing Techniques for Textile Composites

In his 2002 paper Bader [15] gives an evaluation concerning the costs and realizable production rates of available composite manufacturing techniques. Composites of the highest quality with high fibre volume fractions can be achieved using autoclaving techniques. These processes however are also the most expensive because of high equipment and labour costs due to being very labour intensive, which also leads to slow production rates. These labour costs are somewhat reduced with the use of automated tape lay-up or towpreg placement where layers of fibres preimpregnated with uncured resin are laid out using robots before they are vacuum bagged and cured. However, whilst reducing labour additional costs for the robots they significantly add to the equipment costs. Automated towpreg placement coupled with autoclave curing is another manufacturing process with high equipment costs and slow production rates but with the ability to manufacture high quality composites. It is essentially a derivative of the filament winding process. Preimpregnated tows or tows impregnated with liquid resin are laid up before autoclave curing using an automated machine comparable to a tape-layup machine. Whilst very similar to the automated tape-lay-up machine process the automated towpreg placement process is more flexible concerning the composite part shape and slightly more cost efficient due to lower feedstock costs.

In the same paper Bader [15] also lists a number of processes with higher production rates and/or higher production costs. One of these is the diaphragm process, which is similar to the hot forming process used for metal parts. In the diaphragm process fibres are preimpregnated with a thermoset resin to form a rigid sheet. This sheet is then heated to above the resin's melting point and pressed into a mould to form the part. Whilst being able to achieve high production rates the diaphragm process is rather expensive due to the need for thermoplastic prepregs and complex high cost tooling, which needs to be temperature resistant. Fibres also tend to move in areas of geometric features such as areas of high curvature.

Very limited but also very economical is the use of sheet moulding compound where randomly chopped fibres are mixed with resin and placed in a hot mould. The

material, including the fibres, flows through the mould when heated. This can be assisted by the application of high pressure. The process is very economical due to high production rates and low material costs, however it is limited to about 40% fibre volume fraction and the use of chopped fibre mats, which results in comparatively low stiffness and strength of the finished component.

A fully automated process for manufacturing base shapes such as beamlike or sheet structures is the pultrusion process where dry fibres are drawn into a part shaped die and resin is injected at the mouth of the die. This process can be fully automated, reducing labour costs, at very high production rates. Equipment costs however tend to be quite high.

Resin Film Infusion (RFI) and Resin Transfer Moulding (RTM) are both low cost alternatives to the use of prepregs due to lower feedstock costs. In the Resin Film Infusion process resin is laid up in a mould with the dry fibre in form of a film. After vacuum bagging the film is melted and the resin flows through the preform due to atmospheric pressure being applied by a vacuum. Therefore, no autoclave is required, which means a significant reduction in costs compared to prepregs. Han et al [16] agree that Resin Film Infusion allows for the fast and cheap production of complex composite parts. In the RTM process a liquid resin is drawn through a preform laid up in a mould. The process of resin flowing through the mould is sometimes assisted by a vacuum in a process called vacuum assisted resin transfer moulding (VARTM). Both processes are limited in the type of resin systems that can be used, which have to be supplied in the form of film in case of Resin Film Infusion or need to be within a certain viscosity limit for RTM, but have much higher production rates since they allow multiple parts to be formed using one set of tools.

In [18] Summerscales and Searle focus on four different types of resin infusion under flexible tooling (RIFT) processes and their applications ranging from marine type applications (e.g. minehunter superstructures, yacht hulls, sonar domes etc.) to wind turbine blades, military applications (e.g. advanced composite armoured vehicles) and land transport applications. In general RIFT processes can be used to manufacture parts close to the original preform shape, care must be taken however to avoid flows that result in areas being starved of resin.

The first RIFT process discussed in the paper by Summerscales and Searle [18] is similar to Resin Transfer Moulding (RTM) with the second tooling side replaced by a flexible skin with the resin being drawn through the preform in the in-plane direction. This not only reduces material and tooling costs but also allows for the manufacture of large structures at a higher quality than hand lay-up with the additional advantage of achieving higher fibre volume fractions due to preform compaction prior to infusion. This was observed experimentally by Somashekar, Bickerton and Bhattacharyya [17] using x-ray tomography to measure preform compaction during composite manufacture. Their investigation showed three separate mechanisms of preform compaction, one elastic, which is released after the pressure on the composite is released, the other viscoelastic with compaction reducing slowly over time and one permanent leading to a clear reduction in tow cross-sectional area after composite manufacture compared to preform tow cross-sections.

As with RTM the resin systems that can be used with the process described first by Summerscales and Searle [18] are limited due to the requirement of low viscosity for effective resin flow through the preform as uneven flow can result in unimpregnated areas. Overall the process is relatively complex with significant pre-moulding preparations required as the quality of the final part is sensitive to the integrity of the vacuum bag. The second process is a variation of the first with a distribution medium placed either on top or within the dry fibre preform, which allows resin to flow through the preform thickness rather than in the in-plane direction, allowing for improved composite quality. The third process described in the paper is the resin film infusion, which has already been mentioned in this review. An additional advantage of resin film infusion identified by Summerscales and Searle [18] is that unlike for RTM and its variants resin systems with low viscosity can be used due to short resin flow distances, ie a maximum distance of the component thickness. The last process described uses partially preimpregnated materials, which is being heated resulting in the resin melting and flowing through the preform under a vacuum. These materials are called semi-prepregs.

Controlling the pressure distribution during the infusion process is a major factor influencing the quality of the finished composite part since uneven resin flow can lead to void formation [18] and high rates of resin flow lead to high hydrostatic pressures, which damage the preform and also lead to increased void formation [19]. Hou and

Jensen [20] showed that using double vacuum bagging allows for good control of the pressure distribution and consolidation pressure on the preform resulting in the ability to manufacture high quality composites.

2.2 Mechanical Behaviour of Textile Composite

One of the major distinguishing features of textile composites from a mechanistic point of view is the non-uniform distribution of stress and strain within the composite. This may cause significant problems when trying to measure average strain across a length of a test specimen using strain gauges, as strain results are incomplete if the gauge length is smaller than a unit cell [21]. This has been identified as a major source of error for strain measurements [3]. Therefore Lang and Chou [21] published a number of guidelines for strain gauge selection when investigating textile composites. Using gauges of appropriate sizes essentially eliminates variations due to the underlying microstructure of the composite.

Critical parameters that influence the mechanical behaviour of textile composites are geometrical flaws and deviations in the preform due to manufacturing processes. For woven composites for instance warp tows are held in tension during the weaving process, resulting in significantly lower tow waviness, or crimp, than in the weft tows, which again results in a better performance of a woven composite in warp tow direction even if the same tows are used in the warp and weft direction [22]. Compaction pressure during composite manufacture also affect the mechanical properties since higher compaction pressures lead to a higher number of geometrical flaws [22].

Nonlinear behaviour of textile composites is not down to damage initiation alone. Plastic straightening of tows in tension [23] have been observed as well as viscoelastic behaviour and plastic flow of matrix material for shear loaded textile composites [24].

In a 2008 paper Lomov et al [25] demonstrated a comprehensive method to experimentally study damage initiation and progression of textile composites under pure tensile loading conditions using a wide range of experimental techniques including acoustic emissions, full-field strain mapping and c-scanning and x-ray tomography. An initial geometric characterization of the textile composite structure is

done, including damage due to thermal and mechanical loading during composite manufacture. Next a tensile test is conducted with stress, strain and acoustic emission data recorded. Ultrasonic c-scan and x-ray tomography inspections are conducted after significant acoustic events to assess the position and size of damage sites.

Daggumati et al [26] investigated the damage initiation and progression in a 5-harness satin weave under static tension following the roadmap laid out by Lomov et al [25]. The acoustic emission data suggested that there was a large variation in damage initiation stress due local variations in the geometry of the composite. It was also found that earliest initiation of damage occurred near the edges of the weft tows in the inner plies of the composite (Figure 11) and grew from there through the weft tows and matrix both in through-thickness direction and transverse to the loading axis. Catastrophic failure occurred due to sudden rupture of the warp tows. The preferred damage initiation in the inner plies is due to higher stresses because of the supporting effect of neighbouring plies.
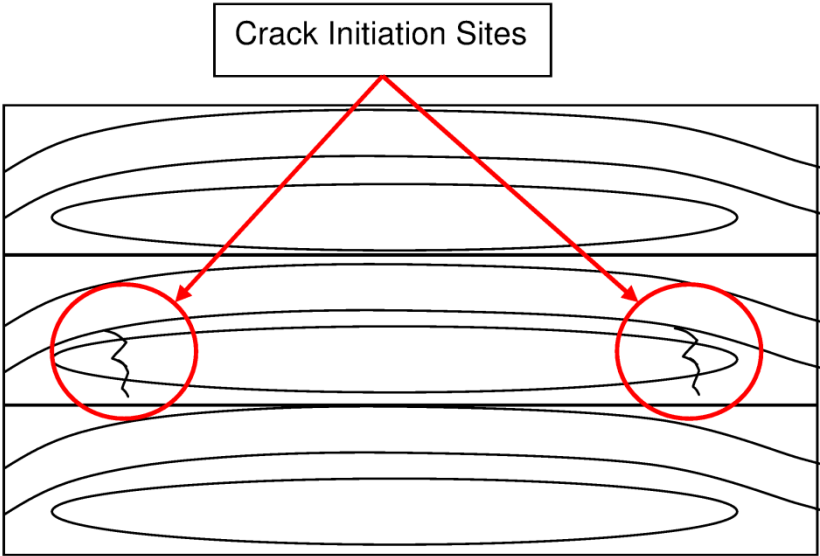
Figure 11: Crack Initiation at Weft Tow Edges in Inner Ply

Similar observations were made by Gao et al [27] who investigated damage accumulation in a carbon epoxy eight harness satin weave laminate under pure tensile loading using light microscopy. Cracks initiated in the centre and outside edges of the weft tows and grew perpendicular to the loading direction. Tow matrix

interface failure was also observed near the region of highest crimp in the tow with catastrophic failure occurring due to warp tow failure.

Similar observations have been made Ivanov et al [28] for triaxial braided composites using the roadmap approach laid out in [25]. Instead of failure initiating in the centre of the composite, cracks initiated at the surface near regions of high fibre crimp, transverse to the loading direction and continued to grow from there in the transverse and through thickness direction.

Quinn, McIlhagger and McIlhagger [29] also observed damage initiation at the composite surface when investigating SAT 4 fabrics under pure tension using electronic speckle pattern interferometry for full field strain measurements. They concluded that binder tows cause additional crimp in fibres at the surface as well as resin rich pockets in the same area resulting in higher stresses at these sites. The increase in tow crimp also explains the degraded in-plane performance of 3D woven composites compared to 2D woven composites.

Stig and Hallström [30] did a comparison of the mechanical behaviour of 3D woven composites compared to a 2x2 twill and a non-crimp fabric composite under different loading conditions. Generally 3D woven composites performed better in out-of-plane tests, such as the out-of-plane strength test, a test where coin sized test specimens are pulled apart, bending test and short beam shear test. This better performance is due to an improved interlaminar shear strength because of the through thickness reinforcements. However, the decrease in in-plane performance is due to fibre crimp which is increased by the presence of the through-thickness reinforcements.

Pochiraju [31] conducted a complete investigation of the behaviour of 3D woven and braided composites under different loading conditions. Nine different types of specimens were used for the investigation, two different types of interlock weaves and a four step circular braid, two different architectures and two overall composite thicknesses were investigated for each type respectively.

In tension all composites showed similar behaviour with damage initiating at the tow matrix interface and growing perpendicular to the loading direction. Final failure occurred when the tows in loading direction failed, at this stage the interface of tow and matrix had failed completely perpendicular to the loading direction. The fracture surface after catastrophic failure showed characteristics of a brittle material. In

compression the shape of the fracture surface was much more varied, usually with an angle of about 45° suggesting a shear mode failure. Specimens were crushed by the fixture during shear tests therefore no evaluation of the shear failure modes could be done. However, at even low strains matrix yielding could be observed. Nonlinear material behaviour was also observed during the bending test, with the slope of the measured stress-strain curve starting to decrease at about 80% failure load and significant load drops occurring at 95% failure load due to failure in the specimen.

Detailed examinations of the failure mechanisms of 3D woven composites were conducted by Callus et al [33] for different types of architectures, all with very similar in-plane properties due to similar amounts of tow crimp. Major crack initiation sites were found between the through-thickness reinforcements and the matrix as well as between in –plane tows and the matrix. Additional nonlinear behaviour was seen due to plastic straightening of in-plane tows. Catastrophic failure occurred when the axial tows ruptured. Unlike Cox et al [23] no lock-up phenomenon was observed. For some kinds textile composites catastrophic failure does not occur with axial tow failure. Load levels near peak load can be retained even after most axial tows have failed. This phenomenon is called lock-up, after axial tow failure additional load is carried by the through-thickness reinforcement leading to a compression of the composites. This compression leads to an increase in friction between the failed axial tows and the matrix, effectively clamping the axial tows and preventing pull-out of failed axial tows.

Cox et al conducted detailed investigations on the damage evolution of layer to layer and through-the-thickness angle interlocks in uniaxial tension [23], compression [32] and bending [34]. In general it can be said that tows fail as discreet units both in tension and compression at sites of geometric flaws in the preform [34] such as tow crimp and tow damage due to preform and composite manufacture. Because of the spatial distribution of these flaws and the tows' tendency to debond from the surrounding matrix when they fail, neighbouring tows are protected and therefore usually stay intact even after load redistribution Also, some failure mechanisms are affected by other modes of failure, an example for this could be the initiation of tow microbuckling at tow matrix interface failure sites. Therefore the interaction of different failure mechanisms also needs to be investigated.

Under pure tension, cracks start initiating at strains of about 0.01 with the damage behaviour dominated by the transverse tows as was reported by Cox, Dadkhah and Morris [23] and by Daggumati et al [26], Gao et al [27] and Pochiarju [31] for other types of textile composites under pure tension. This suggests that damage behaviour under pure tension is always dominated by the transverse tows for all types of textile composites, though no detailed comparison of damage behaviour of different types of textile composites can be found in the literature. Even before damage initiation, at about 0.006 strain, nonlinearity is observed in the stress – strain curves due to plastic straightening of the axial tows. Failure in compression is dominated by kink band formation, localized tow buckling at tow matrix interface sites (Figure 12). This kink band formation is facilitated by local geometrical flaws [32]. Failure mechanisms under bending load are virtually similar to tensile and compressive failure mechanisms, though the compressive strain required to initiate kink band formation is slightly higher as reported by Cox et al [34].
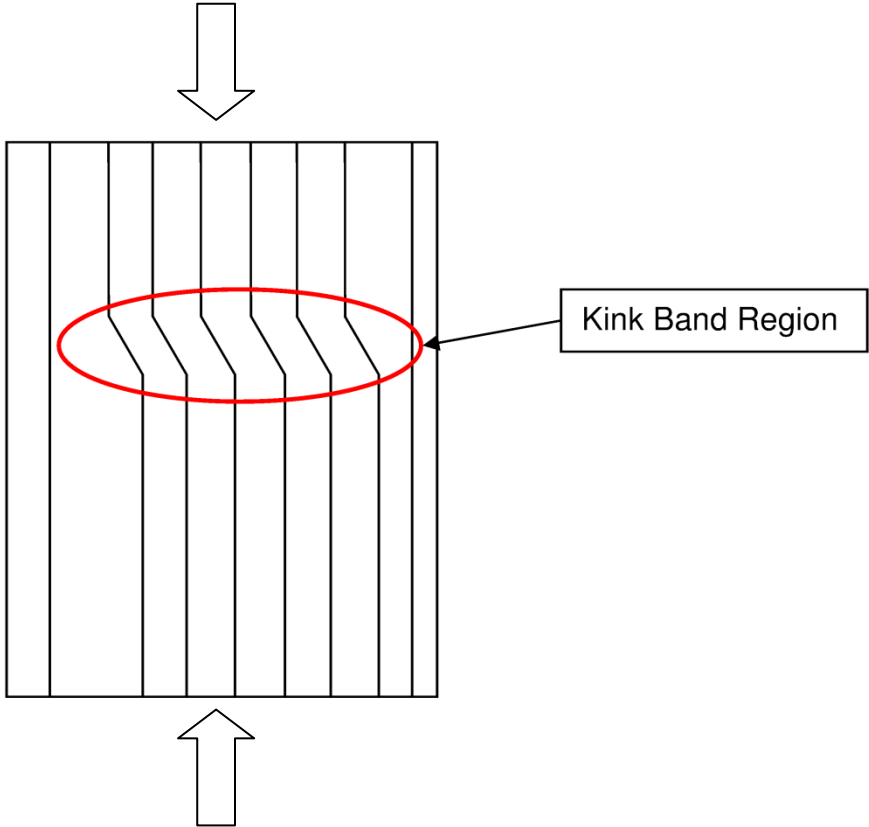
Figure 12: Kink Band Formation under Compressive Loading

Leong et al [35] investigated the effect of through-thickness reinforcements, also called binders, and their path on damage initiation in 3D woven composites. For this

they looked at two different angle interlock weaves with the same overall binder lenght, one with a sinusoidal binder path and the other with a 90° orthogonal binder path. Since the sinusoidal binder path was longer than the orthogonal binder path but the same overall binder length was used for both, the composite containing the sinusoidal binder path got squashed resulting in higher stress concentrations and larger resin rich areas and therefore earlier damage initiation.

According to Kuo, Ko and Lo [36] 3D composites tend to be thicker than classical laminates meaning the out-of-plane shear behaviour, also called transverse shear behaviour, needs to be investigated. Kuo, Ko and Lo [36] and later Kuo, Fang and Lin [37] looked at the failure behaviour of 3D orthogonal woven carbon-carbon composites in compression and under transverse shear loading. Similar to Cox et al's [32] observations the composite failed due to kink band formation at sites of tow flaws under compressive loading. The first failure modes observed for the test specimens loaded in transverse shear were matrix cracking and tow matrix interface failure, resulting in significant nonlinearities after damage initiation and during damage progression [37]. Catastrophic failure is due to instantaneous failure of axial tows with the fracture surface running along the path of the through thickness reinforcement.

2.3 Delamination Behaviour of Textile

One major advantage of 3D textile composites is the increased resistance to delamination. Mouritz, Baini and Herzberg [38] investigated the mode I interlaminar fracture toughness, the strength against delamination under out-of-plane loading, of different kinds of textile composites, including braided, knitted, stitched and 3D woven, all of which showed improved mode I performance. Tests were conducted using standard double cantilever beam (DCB) tests according to ASTM D5528 (Figure 13). The main toughening mechanism identified for braided composites was the branching of delaminations around the braided tows, leading to a spiralling unstable crack growth around the tows. However, this means that the fracture toughness of braided composites is sensitive to the braid angle. For knitted composites the delamination is following tortuous paths due to extreme local variations on tow path. This continuous change in delamination path direction leads to a very good performance of knitted composites in DCB tests. The toughening

mechanism for both stitched and through-thickness woven composites is the bridging of cracks by the stitches and through-thickness reinforcements respectively. This leads to a reduction in the crack opening displacement which in turn reduces the stress concentration near the crack tip. An additional toughening mechanism is observed for 3D woven composites, namely crack branching near the bridging site.
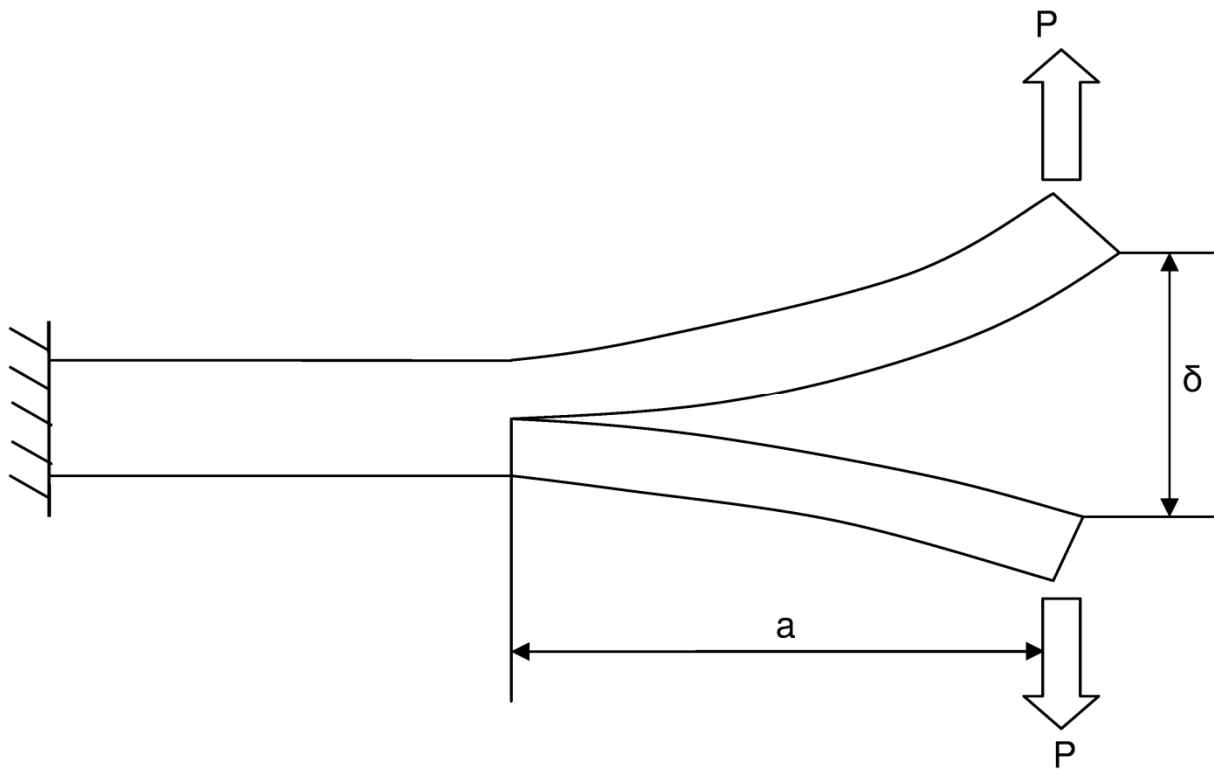
Figure 13: Double Cantilever Beam (DCB) Test

The effect of through-thickness reinforcements on the mode I fatigue properties, meaning the growth of cracks under cyclic out-of-plane loading, of 3D woven composites were investigated by Rudov-Clark and Mouritz [39] using a double cantilever beam (DCB) test. Major improvements in mode I fatigue properties compared to traditional UD laminates could be seen for increasing through-thickness reinforcement content due to crack bridging and lock-up. However, whilst major improvements could be seen compared to traditional laminates, excessive through reinforcement content can lead to a decrease of fatigue life for in-plane tension due to an increase in defects and geometrical flaws in the composite. In addition to that shear stresses between through-thickness reinforcements and the matrix can lead to plastic flow on the matrix resulting in increased crack growth. Similar behaviour is observed for other textile composites. Mouritz [40] investigated the effect of different

types of through-thickness reinforcements, namely 3D woven, z-pinned and stitched, on in-plane tensile fatigue properties. All three types of reinforcements lead to a significant reduction in in-plane tensile fatigue life due to an increase of local flaws.

An increased resistance to delamination also has a positive effect on fatigue properties in in-plane compression. Dadkhah, Cox and Morris [41] looked at the performance of various 3D woven composite architectures under compression-compression fatigue loading. They observed that the principal failure mechanisms under these loading conditions was kink band formation rather than delamination, in fact no delamination cracks were observed during the composites fatigue life with almost no cracking observed in the vicinity of kink bands. As was noted earlier, kink bands form at sites of geometrical flaws. Due to the stochastic nature of the distribution of these flaws, kink band formation is not limited to a small area but rather spatially distributed across the entire composite.

2.4 Modelling of the Mechanical Behaviour of Textile Composites

2.4.1 Geometrical Modelling of Textiles

In a 2007 paper Lomov et al [42] listed a number of requirements a modelling procedure for textile composites needs to fulfil. They identified three different scales which the procedure had to include, the microscale, on which the arrangement of fibres in a representative volume element (RVE) of the composite architecture are modelled, the mesoscale, which defines the internal structure of the RVE and the macroscale showing the distribution of RVEs in the complete composite structure. Therefore an automated, integrated FE-modeller should have the capability to correctly model the geometry from a few standard geometrical input parameters on all three scales with the ability to perform automatic simplifications and corrections in case of overlaps and interpenetrations: These corrections might also be required for boundary condition assignment and meshing. A meshing engine with the capability to assign material properties based on local constituents and geometry is also required. Homogenization schemes also need to be included to calculate averaged RVE properties for further use in higher scale models. Finally, appropriate damage criteria and property degradation schemes need to be included to model damage initiation and progression.

Crookston, Long and Jones [43] listed a number of mathematical models and software codes available for geometrical modelling of RVEs. McBride and Chen [44] suggested a simple model based on four sinusoidal curves to represent tow paths, an approach that worked well for balanced dry plain weaves. A more general model based on the minimization of tow bending energy was developed by Verpoest and Lomov [45] and implemented in the WiseTex software package. Pastore [43] suggested the use of a computer code to automatically sweep a tow cross-section along a Belizier spline, also called B-spline, representing the tow path. Deformation behaviour of tows was included by the use of a virtual work approach. Robitaille [46] suggested using vectors to define tow path centres. Cross-sections were defined around these vectors to generate volume representations of tow volumes. This approach, in addition to model random variations in tow paths and material parameters using Monte-Carlo Methods, was implemented in the TexGen software package. A common characteristic of all approaches discussed above is the need for experimentally determined data on tow cross-sections and paths. Indeed according to Ansar, Wang and Chouwei [47] accurate information on geometric parameters are required for correct unit cell representation. As was already discussed, tow paths can best be represented using either a sinusoidal path or Bezier splines [43]. Tow path cross-section can also be represented by using standard mathematical functions such as elliptic, lenticular, circular or rectangular [47] or even power elliptical [48].

When Blacklock et al [49] and Rinaldi et al [50] used x-ray tomography to measure yarn cross-section shapes and paths they found large deviations from the mean average for both cross-section shape and tow path. These large deviations need to be incorporated into a geometric modeller since geometrical flaws in tows severely affect the composites mechanical properties. Therefore random variations were included in a geometry generator using Monte-Carlo type simulations.

Daggumati et al [51] used a micro computed tomography (micro-CT) analysis to measure geometrical values for a 5-harness satin weave. Deviations were not included in their subsequent analysis, averaged values were used instead.

2.4.2 Analytical Models

Over the years a number of analytical models have been developed, many based on the Mosaic model originally developed by Ishikawa and Chou [43]. For the Mosaic

Model the RVE, also called unit cell, is broken down into a number of subcells with the fibre crimp represented as step changes between individual subcells (Figure 14). Rule-of-mixture is then used to calculate the properties of each individual subcell, which are assembled using isostrain and isostress assumptions, meaning a volumetric averaging of stresses and strains across the unit cell [52]. Property knockdown factors (factor values were dependent on the mode and severity of the damage) were used in combination with a maximum strain failure criterion to model progressive failure. The Mosaic Model was later modified by Ishikawa and Chou [43] for satin weaves, where regions without tow crimp were treated as UD laminates and regions with tow crimp were treated using the Mosaic Model, this new variation was called the bridging model.
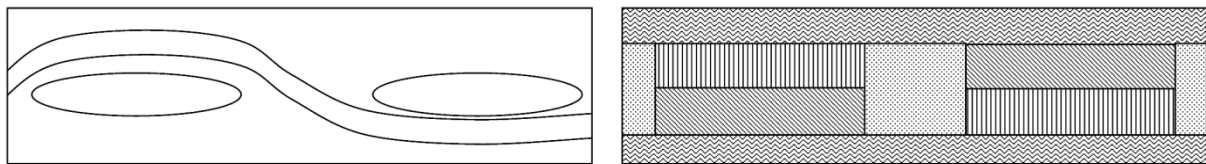
Figure 14: Mosaic Model

Similar approaches were taken by Dimitrienko and Turner [43], who assumed that tows in different directions behaved like separate plies, thereby ignoring tow interactions, and Vandeurzen [43], who generated a database of 108 different subcell blocks, which could be assembled to form any possible RVE. Naik and Ganesh [53] also idealized a woven laminate into a three layer laminate, on being a layer of pure matrix. Each layer was treated separately using classical laminate theory before being combined under isostrain conditions. Tan, Tong and Steven [54] used numerical methods to solve a micromechanics model where tows were modelled as beams following a sinusoidal path. Nodes of the beam models were connected to a fixed constraint using nonlinear springs to simulate an elastic foundation provided by the matrix.

2.4.3 FE-Based Modelling

Later more advanced models were developed using the Finite Element Method. A major assumption for the meso-scale modelling of unit cells is the treatment of tows. Glaessgen et al [55] suggested modelling tows as a continuum rather than on a basis of individual fibres, which reduced meshing effort and computational time and

therefore allowed for a more effective analysis of textile composite unit cells using finite element models. However, Lin et al [56] showed that for loadcases where tow behaviour is dominated by transverse tow stiffness and transverse-longitudinal shear internal tow behaviour is not captured when modelled as a solid. To mitigate this Lin et al [56] suggested embedding truss elements in the solid elements of the tows, similar to the binary model, which is discussed later in this review. Correctly modelling tow and constituent material behaviour is an important factor in correctly modelling the effects of damage progression in textile composites as was shown by Blassiau , Thionnet and Bunsell [57] who used a micro-scale finite element model to predict the load transfer between damaged tows, incorporating stress concentrations at intact tows due to viscoelastic effects after individual tow failures and fibre matrix debonding.

Mayes and Hansen [58] defined some basic assumptions, namely linear elastic behaviour of the tows and nonlinear elastic behaviour of the matrix material as well as a perfect bond between fibre and matrix, whilst Dasgupta, Agarwal and Bhandarkar [59] assumed nonlinear material properties for both matrix and tows.

Whitcomb and Srirengan [60] attempted a detailed investigation of the effect of approximations on the solution of FE based unit cell models including damage progression models. First a convergence study was conducted for a plain weave unit cell model under pure tension with meshes using up to 192 20-node hexa elements, which showed a strong influence of mesh sizes on model results. Owen, Whitcomb and Varghese [61] did a limited convergence study on plain weave unit cell models, achieving convergence using between 13,824 and 27,648 20-node quadratic solid elements. For convergence of a plain weave unit cell model Dasgupta, Agarwal and Bhandarkar [59] required only 2208 eight node solid elements.

In order to reduce computational time, symmetries within the unit cell were exploited to reduce model size, resulting in a model of 1/32 of a unit cell. A generalized procedure for the estimation of internal boundary conditions in a unit cell for symmetry exploitation was later developed by Whitcomb, Chapman and Tang [62]. This procedure allowed for the definition of local coordinate systems and planes of symmetry for further reduction of the unit cell geometry. Two major assumptions were made for the derivation of this procedure. Local displacements within a unit cell

were assumed to be the same for the same local point in all unit cells and that stresses and strains are identical in all unit cells. Guagliano and Riva [63] employed a submodelling technique to reduce model sizes for damage progression analyses in a plain weave laminate. A coarse laminate mesh was used to derive boundary conditions for a more detailed model of 1/32 of a unit cell.

However, Ivanov et al [64] demonstrated that damage is likely to develop near the surface of test specimens first. This was confirmed by Owens, Whitcomb and Varghese [61], who investigated the effect of boundary conditions on finite element based unit cell models. Results for periodic, finite thickness and finite thickness and finite width boundary conditions were compared for different types of composite architectures, namely a plain weave laminate, a UD tape laminate and a mix of the two. These showed a clear dependency of results on the distance from the free edge and the local geometry around the unit cell. Rupnowski and Kumosa [65] also noted a dependency on through thickness stresses for different stacking sequences in the numerical simulation of an 8-harness satin weave under biaxial loading. They also noted that shear stresses caused significantly more stress at the fibre matrix interface boundary than pure tension and a significant effect of residual thermal stresses from the cure and post-curing process.

Ivanov et al [64] suggested a numerical technique to derive boundary conditions for unit cells depending on the distance from the composites surface. Periodic boundary conditions are assumed for unit cell situated in the centre of the laminate. The resulting displacements on the unit cell boundary for periodic boundary conditions are then scaled for unit cells closer to the laminates surface. Scaling factors are calculated iteratively using a macro-scale composite structure model with effective lamina properties, the deformations at the boundary of the detailed unit cell model are scaled until the resulting deformation energy matches the deformation energy of the macro-scale model at the position of the detailed unit cell model.

Another parameter affecting the material properties of textile laminates is the phenomenon of nesting. For some manufacturing processes layers of dry fibre preform are stacked and then compressed. This leads to tows of one layer sliding into the spaces between tows of the layer below. It is due to this feature, a purely geometrical effect, which increases with the number of layers in a laminate, that

experimental results show a wide scatter in measured values [66]. This was confirmed numerically by Daggumati et al [51], who used a multi-scale approach to model damage progression of a 5-harness satin weave. 3D periodic boundary conditions were used for unit cells situated in the centre of the laminate and in-plane periodic boundary conditions for unit cells at the surface. Additional subsurface unit cells, with different degrees of nesting, were modelled to include the supporting effect of other layers in the laminate. Results from these analyses showed that the effect of nesting have a significant influence on predicted damage initiation and progression.

Le Page et al [67] suggested modelling a textile laminate using 2D elements by taking a cross-section through the laminate and assigning appropriate boundary conditions. In a first analysis a cut was made normal to the loading direction for a plain weave laminate under uniaxial tension loading assuming isostrain conditions at the cut surface. The model's complexity was further reduced by modelling tow crimp as step change in tow path similar to the Mosaic Model [43], which resulted in an unrealistic loss of in-plane stiffness. Therefore, more realistic tow paths were used in a second model [68] taking a cross-section cut in the loading direction for the same laminate used in the first model. Starter cracks were introduced into both models by hand and energy release rates calculated for cracks propagating in the through thickness and perpendicular to the loading direction. Model results showed a strong dependency of the energy release rate due to matrix cracking on the local geometry, i.e. the amount of nesting.

2.4.4 Property Degradation due to Damage

One of the first property knockdown schemes was introduced by Blackketter, Walrath and Hansen [69], who modelled a unit cell of a plain weave using 256 20-node solid hexa elements. A maximum stress failure criterion, based on material orientation within the unit cell, with a knockdown scheme for individual elastic constants depending on the mode and severity of failure to model damage was incorporated in the model. Different degradation schemes have been proposed in combination with a number of damage criteria. Guagliano and Riva [63] suggested using a linear degradation scheme with a maximum stress criterion to investigate the effect of fibre crimp on the damage behaviour of a plain weave composite. Daggumati et al [51] employed a Hoffmann failure criterion, a criterion based on the interaction of four

different failure modes. Similar failure criteria, distinguishing between different modes of failure, were used by Heß and Himmel [70] who used Puck's delamination criterion and a max stress criterion for all other modes of failure in combination with a selective property reduction scheme when comparing, using numerical models, damage behaviour of stitched and un-stitched non-crimp fabrics under different loading conditions.

Dasgupta, Agarwal and Bhandarkar [59] predicted progressive failure in transverse tows of a woven fabric composite with Tsai-Hill's criterion. A comparative study of three different failure criterions, namely maximum stress, Hoffmann, whose criterion takes the interactions of different failure modes into account, and Hashin, who presented a set of criteria, each valid for a certain failure mode, was conducted by Tserpes and Labeas [71] for modelling damage progression in non-crimp fabric composites.

Ivanov et al [72] employed a damage model based on energy release rate with a property degradation scheme based on a single damage parameter, which was normalized by the energy release rate at damage initiation to account for differences in energy release rates of different failure modes during damage progression. Energy based damage mechanics were also used by Iannucci and Willow [73] to model impact damage in a woven composite material. Interface elements were placed where damage was expected, requiring prior knowledge of the damage path. Five different failure modes were considered, namely warp and weft tensile fracture and compressive failure as well as tow matrix debonding. A single damage parameter incorporating the effects of all five damage modes as a function of stress rate propagation was used for property degradation [74]. Three different property reduction schemes were investigated by Whitcomb and Srirengan [60], the first involving an instant reduction of all material parameter after a maximum stress was reached, the second involving an instant knockdown of selected material parameters and the third involving a coupled selective reduction of material parameters.

2.4.5 Equivalent Modelling Techniques

A modelling technique not based on a full finite element model of a unit cell was presented by Key, Six and Hansen [75]. The technique was based on micromechanics and started by breaking down the unit cell into three constituents,

namely warp tows, weft tows and matrix. Volume averaging was then used to first combine properties of two of the three constituencies, with the resulting material properties again volume averaged with the remaining constituent. Damage criteria, based on Hashin's criteria, for each individual constituent in combination with a selective property degradation scheme were later added by Mayes and Hansen [58]. This was later modified by Key, Schumacher and Hansen [76] to include quadratic stress interaction failure criteria with instantaneous degradation for the tow constituents and a continuous damage evolution law, including visco-elastic and plastic effects, for the matrix.

A model embedding detailed unit cell models in a coarsely meshed macro-scale structure was suggested by Šmilauer et al [77] for a notched beam under a three point bending load. The notched area was modelled in more detail with repetitive full finite element model unit cells incorporating a linear softening law coupled with a maximum stress criterion. However, like the technique suggested by Venkat Rao , Mahajan and Mittal [78], who used cohesive elements along the crack path to model tow matrix interface damage for carbon-carbon composites, the crack path needs to be known apriori.

A much simplified and therefore less computationally expensive and robust method of modelling textile composites is the so called voxel technique [79] [80]. For this technique grid points are defined on the surface of a RVE of a textile composite. Similar to the mosaic model [43], the properties of the through-thickness structure of the textile composite underneath the grid points are then averaged using an isostrain assumption. Constituent properties had to be estimated first. In the case of the matrix a uniform isotropic material behaviour was assumed. For the tows Chamis micromechanics model was used to estimate orthotropic tow properties. The resulting representative volumes, also called voxels, were then combined to form the full RVE. To model progressive failure a property degradation scheme was used similar to that of Blackketter, Walrath and Hansen [81] in combination with a maximum stress criterion for voxels dominated by tows and Bauwen's criterion, a pressure dependent yield criterion for polymers [82], for voxels dominated by the matrix material. In-plane edges of the resulting RVE were kept straight whilst top and bottom edges were allowed to move freely. After damage initiated in a voxel, the

mesh around the damage site was refined and later coarsened depending on the local stress gradient.

Prodromou, Lomov and Verpoest [42] suggested a method of homogenising properties, including failure, in a five step procedure, each step representing a more general subcell with the homogenised unit cell the result of the final step. Tserpes, Labeas and Pantelakis [83] used a similar technique of cellular solids in combination with a multi-scale damage model. Six different Hashin type failure modes were considered with a stiffness degradation depending on the mode of failure to model progressive damage.

Another simplified technique of modelling textile composite is the binary model, which was developed by Cox, Carter and Fleck [84] (Figure 15). In the binary model axial tow stiffness is modelled using 1D spring elements, whilst the remaining tow and surrounding matrix properties are included in a single 3D solid element, called a representative medium element. Nodes of 1D and 3D elements are coupled numerically. This coupling constraint is rigid in the undamaged state but allows for relative displacements to model the effect of friction between tow and matrix after the tow matrix interface has failed. Properties for the effective medium elements were derived using the rule-of-mixture equations for transverse properties since volume averaged methods could not be used because of a non-uniform strain distribution in the unit cell [85]. The stiffness of the 1D tow elements was derived from Hashin's model for UD laminates using an equivalent spring model and a similar approach was used for the coupling stiffness between 1D and 3D element nodes. Element deletion of 1D elements after violation of a maximum strain criterion was used for modelling tow failure [86].
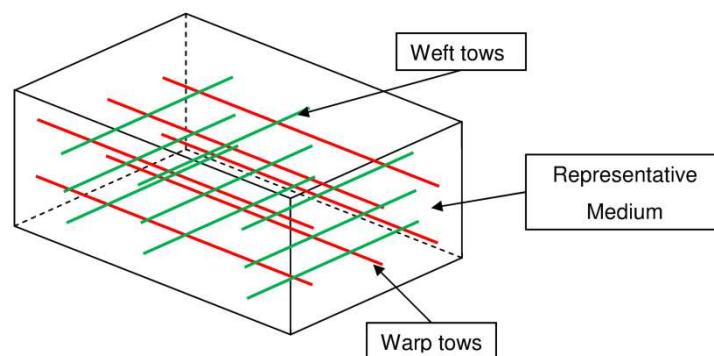
Figure 15: Binary Model

Strain prediction of the binary model are highly mesh dependent due to the use of the 1D elements with the mismatch on properties between the 1D and 3D elements leading to stress singularities [87]. In order to overcome this problem, gauge averaging was introduced by Cox and Yang [88]. Systematic studies showed that if the gauge was larger than a tow width the stress fields would become non-singular and mesh-independent whilst giving reasonably reliable results on the local strain distribution within the cell. This allowed for the introduction of a maximum tensile strain criterion for tow rupture and a maximum shear stress criterion for matrix failure. Nonlinear micro-cracking in the matrix was modelled using a nonlinear material model for the matrix [89]. As was already discussed earlier, spatial distributions of geometrical flaws have a significant effect on damage initiation and propagation in textile composites. Therefore a Monte Carlo type simulation was introduced to include geometrical and material flaws in the binary model. Also a dilation strain was introduced, depending on the relative displacement of 1D to 3D element nodes due to tow sliding, to account for the pressure applied on the matrix by a sliding tow during pull-out.

2.5 Experimental Methods for Finite Element Model Validation

Several experimental techniques are available to validate numerical model predictions, including full stress or strain field measurements, measurement of damage size and areas using microscopy and noise emission techniques. Validation of models is required due to a number of simplifications made during the modelling process, a list of possible sources of errors has been compiled by Ivanov et al [90]. This list includes deviations of tow cross-sections from statistical averages as well as nesting. It also lists numerical errors due to bad FE mesh shapes and approximations used in damage criteria and degradation models.

2.5.1 Full Strain Field Techniques

In a 2008 paper Lomov at al. [91] presented a digital image correlation technique, which can be used to validate full finite element model predictions of strain distribution in the top and bottom layers of textile composites, which is described further in [90]. The technique uses optical measurements of the position of a fine reflective grating, 1200 lines per mm, under laser light. Damage initiation sites and

crack propagation can be identified by correlating strain measurements on specimen surfaces under different load levels. Areas showing a deviation from linear strain increases are classified as damage sites. However, in order to differentiate the periodicity of the strain field and noise generated by local variations a numerical Fourier analysis of the strain field harmonics has to be conducted. Due to the effects of the noise and the additional numerical analysis required to separate noise from the measured data only the periodicity of the strain field can be validated, a quantitative measurement of the strain distribution is not possible.

2.5.2 Thermoelastic Stress Analysis

The stress distribution on the top and bottom of a textile composite can be measured using a thermoelastic stress analysis (TSA), making use of the thermoelastic effect first discovered by Lord Kelvin [92]. Local changes in volume of a material lead to small changes in the material's local temperature, which, in the field of thermodynamics, are described mathematically using so called equations of state. In case of mechanical loading local changes in volume due to elastic strain cause changes in temperature in the order of 0.001 °C. Therefore, applying a cyclic load to a test specimen leads to cyclic variations in temperature of the specimen's surface, which can be measured using an infrared camera (Figure 16). Surface temperature and infrared signal are related by Planck's law, which is both nonlinear and material dependent, meaning careful calibration of test equipment is required before TSA is conducted [93]. If adiabatic conditions are assumed, the small changes in surface temperature of a specimen can be related mathematically to the first invariant of the local stress tensor using thermodynamic principals.
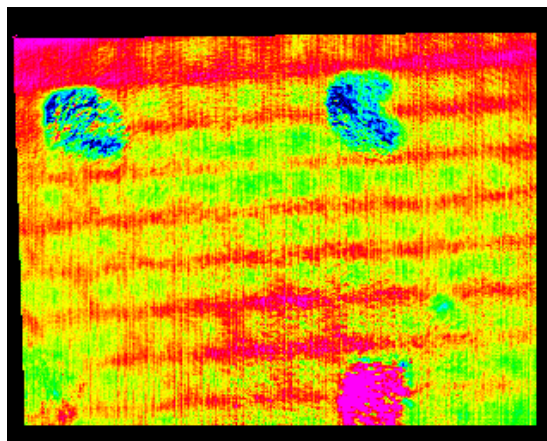
Figure 16: TSA Image of a Plain Weave Textile Composite

Wong, Sparrow and Dunn [94] describe a mathematical relationship of the measured infrared signal to the ratio of local temperature change for isotropic materials depending on a material's thermal properties. This relationship, defined by a so called thermoelastic constant, can be strongly dependent on the applied mean stress and stress amplitude due to a temperature since material properties tend to be temperature dependent, prompting Wong, Sparrow and Dunn [95] to revise TSA theory to include mean stress effects. The effects of thermal dependency on the infrared signal in TSA have also been documented by Pitaressi and Patterson [92]. They also noted that residual stresses in the material also affect the TSA signal, a fact that allowed Wong, Sparrow and Dunn [95] to calculate residual stress values using their revised TSA theory.

A factor affecting temperature measurements taken using infrared cameras is the effect of specimen motion due to deformation under cyclic loading [96]. Not only does it lead to a change in local emissivity at specimen edges but also to signal changes due to pixels changing position. For loading frequencies different to the camera's picture frame rate hot spots in the material move relative to the fixed camera position due to specimen deformation. This can lead to spurious results, which is why a motion compensation of infrared images is required before the actual TSA is conducted.

Stanley and Chan [97] successfully applied TSA to composite materials by taking infrared measurements of chopped-strand-mat discs and thin-walled Kevlar/Resin cylinders cyclically loaded in compression. Therefore they proved that the equation relating stresses to temperature change was valid for orthotropic materials and merely needed rewriting to reflect anisotropy of material properties.

Initial TSA theory assumed adiabatic conditions to relate stresses to changes in temperature. Wong [98] however theorized that true adiabatic conditions cannot be achieved for composite materials due to differences in layer properties in a laminate leading to differences in temperature changes and therefore heat conduction between layers. This can be somewhat mitigated but not completely eliminated by using high frequencies to apply loads, which leaves the heat no time to dissipate.

TSA was used by Emery, Dulieu-Barton and Cunningham [93] to detect fatigue damage in composite structures. Friction effects at damage sites lead to significant

changes in local temperatures, which can be easily detected using infrared cameras. Information about damage severity can be derived from the comparison of damaged and undamaged TSA signals. However, high changes in local temperature due to friction can lead to an increase in average specimen temperature, which can affect the TSA signal. Therefore a decoupling strategy for damage and stress heating is required. Such a decoupling strategy, based on experimental calibration of test equipment, is presented by Dulieu-Barton et al in [99]. A power law relationship is assumed between the number of photons emitted by a body and its temperature. The factors of that power law are calculated using a cylinder of the specimen material filled with water. The water and therefore the material is heated or allowed to cool whilst the cylinder is loaded cyclically in the elastic region of the material property and the thermoelastic response is measured. The change in TSA signal, ie the number of photons emitted from the cylinder is then plotted against the cylinder temperature so that the two constants governing the power law relationship of number of photons emitted to material temperature can be calculated. This power law is used in subsequent TSA of a structure of the same materials as the calibration cylinder to correct for the change of average specimen temperature due to high local changes in temperature.

Frühmann, Dulieu-Barton and Quinn [100] applied TSA to textile composites. In order to reduce reflections of the test specimen's surface, the specimen's surface was slightly abraded using fine sanding paper. To filter out any remaining reflections, a non-uniformity correction was performed, calibrating the camera to measure an even temperature distribution on the unloaded specimen surface. In order to reduce noise the infrared images taken were compensated for motion using a vector tracking algorithm, which works by tracking the distance between clearly distinguishable features on the specimen surface throughout the infrared images

Thermal and mechanical properties, needed to quantitatively calculate stresses on the surface of a flat plain weave test specimen using TSA theory, were estimated using standard equations for UD laminates, namely rule-of-mixture and Schapery's equation [100]. Schapery's equation [101] derives from the complementary and minimum potential energy principal, upper and lower bounds of thermal properties are calculated using virtual tractions and displacements, which are applied to the composite surfaces. The difference between the complementary and potential energy

is minimized by variation of the applied tractions and displacements. Although the derivation of the equation shown by Scharpery [101] does include the temperature dependency of constituent properties, the approach assumes linear behaviour of the entire composite and linear interactions of the constituent materials. This approach was later modified by Khan and Muliana [102] to include viscoelastic effects, by combining a micromechanical model to predict viscoelastic behaviour of a composite with Scharpey's equation, resulting in a micromechanical model to predict thermal expansion coefficients based on representative volume elements.

Scharpey's equation was used by Frühmann, Dulieu-Barton and Quinn [100] to calculate coefficients of thermal expansion of a plain weave and a 2x2 twill woven textile composite. Elastic properties were predicted using rule-of-mixture. However, due to the highly crimped nature of the fibres in textile composites, simplified predictions based on fibre volume fractions can be a significant source of error for the predicted parameters [100]. Indeed it was concluded that standard theories were not sufficiently accurate to estimate thermal and mechanical properties for a quantitative calculation of stresses and must therefore be measured experimentally [103].

An additional problem for measuring the TSA response of textile composites is the separation of noise from the actual TSA signal. As was mentioned before by Ivanov et al [90] the interlacing pattern of textile composites leads to a non-uniform distribution of strain, which makes it difficult to separate noise and therefore leads to difficulties when interpreting TSA measurements. In order to investigate this Frühmann, Dulieu-Barton and Quinn [104] looked at the TSA response of a 2x2 twill woven composite under low loads, which were chosen to avoid the initiation of fatigue type damage during the analysis.

Due to the difficulties in calculating stress data from TSA signals, which were discussed above, all results were presented as temperature data normalized by the averaged temperature across the specimen. A local change in the standard deviation from the average temperature was taken as a sign of either damage initiation or a redistribution of loading due to damage initiation at another site. However, it was found that a local decrease in the surface temperature at one site due to damage initiation does not necessarily lead to an increase in surface temperature at another site, which poses a problem for interpretation of damage propagation since the local

decrease in temperature does affect the averaged temperature over the entire surface which is used for normalization of temperature data [104], [105]. In the experimental work presented by Frühmann, Dulieu-Barton and Quinn [104], conducted on 2x2 twill woven composites, a sharp decrease in the TSA response of transverse tows was observed after about 200 cycles for a single ply loaded up to a maximum of 20% failure stress. This was due to cracks through the centre and at the edge of the transverse tows, which leads to a reduction of the load carried by the tow. Similar results were observed for 2x2 twill composites under fatigue loading, using the same experimental technique as described above [105] with TSA measurements being taken at certain intervals between fatigue load cycles. Again a sharp decrease of TSA response was observed for the transverse tows only, where damage is increasing with an increasing number of cycles, with the strongest TSA response overall being measured for the boundary between axial and transverse tows.

One of the practical drawbacks of TSA is the requirement for a regular cyclic load being applied to the structure under investigation due to the use of a lock-in amplifier using a reference signal, usually from the load cell, to filter the measured TSA signal. Regular cyclic loads however are difficult to achieve for structures outside laboratory conditions [106]. Therefore Frühmann, Dulieu-Barton and Quinn [106] suggested measuring the response of a transient load applied to the structure. Two methods of applying this transient load were suggested, one a step input from a testing machine, the other an impact loading using a pendulum. Both types of loads were applied to a flat UD laminate plate, whose thermal properties had been measure experimentally to calculate the temperature change due to the applied load using TSA theory for validation purposes. An artificial stress concentration point in the form of a hole was also included to see if the stress concentration could be measured. Good agreement between experimentally measured data and analytical calculated temperature changes were observed for the step load applied by a testing machine. In a second step an artificial delamination was introduced in the UD laminate to check if this type of damage would also be picked up using the proposed experimental technique. This delamination was not easily detected by the step load applied but could be picked up using the pendulum test. This is due to the fact that delaminations do not significantly affect in-plane tensile properties but have a significant influence on the bending

stiffness and localized buckling effects, the primary loading for the impact tests. The suggested use of transient loading can therefore be applied to detect damage in composite structures.

2.5.3 X-Ray Tomography and Acoustic Emission

Another way of detecting damage in composites is the use of x-ray tomography or acoustic emissions. Kinney et al [107] used x-ray tomography to study the damage distribution in an Al/SiC composite getting similar results compared with light microscopic analyses conducted on the same type of composite. Unlike for the light microscopic analysis the composite can be investigated as it is, meaning no cutting and polishing of test specimens is required. Therefore the same test specimen can be checked for crack positions and lengths at different load levels rather than having to load different specimens to different load levels and the cut up for microscopic analysis. Badel et al [108] employed x-ray tomography to measure the deformation of tows during loading. Tow cross-sectional shapes were approximated from the tomography results at different load levels. The results from the unloaded state were used to build a full finite element model a unit cell. Results for different levels of load were compared to full finite element model predictions for model validation purposes.

Elastic energy is released from composites at damage initiation and progression sites in form of acoustic waves [109]. These can be detected in-situ during load application by acoustic sensors bonded to the test specimen. Damage locations can be located by using the time difference of the sound waves arrival at different sensor sites. For this the materials speed of sound needs to be known, which can be done by introducing a test signal into the structure prior to loading. Correlation of the acoustic emission data with data from strain gauges or load cells allows for an effective calculation of load levels at damage initiation and damage positions within the test specimens.

2.6 Summary

Defining a unit cell geometry is not straightforward since geometrical variations, due to variations of constituent components and the manufacturing process, can have a significant effect on local properties in the composite [22], especially on non-linear

behaviour. However, according to Rinaldi et al [50] it is valid to use averaged geometric parameters when defining a unit cell.

Non-linear behaviour of textile composites can be due to reasons other than damage progression such as plastic tow straightening [23], tow viscoelastic behaviour [24] and plastic matrix flow [127]. Therefore, in order to model damage initiation and progression correctly, these non-linear effects have to be included in the model.

Three FE-based techniques are available to model textile composites. The full finite element model technique [55]-[74] uses a detailed unit cell model with a large number of degrees-of-freedom (dof) to calculate a detailed map of the stress-strain distribution within the unit cell. With the voxel [75]-[83] and binary model techniques [84]-[89] equivalent cells are defined, which reproduce the unit cell stress-strain behaviour in an averaged sense using a much lower number of dof. All three techniques use knock down factors to model stiffness degradation due to damage progression. Damage initiation is estimate using a number of different criteria, which are either stress-, strain- or energy based [50], [62], [68], [69].

Experimental data can be used to validate FE-based model predictions. Besides the comparison of predicted averaged stress-strain behaviour with experimentally measured data according to ASTM Standards [110], [111] other techniques are available. When cracks initiate and propagate elastic energy is released in the form of acoustic waves travelling through the composite, which can be measured using both microphones and accelerometers [109]. Other techniques can be used to map the stress or strain distribution on the surface of a test specimen. Full field strain measurements use optical cameras, which record changes in the position of complex patterns on the specimen's surface, to map local strains [90], [91]. The thermoelastic stress analysis (TSA) uses an infrared camera to measure local changes in temperature due to loading [92]-[100],[103]-[106], which can then be related to the local state of stress, resulting in a map of the stress distribution on the specimen's surface.

3 Specimen Manufacture

3.1 Introduction

Geometrical information on the unit cell architecture such as tow path and cross-section are required as input for a detailed unit cell model as well as experimentally measured stress-strain and full-field stress data for model validation purposes. To obtain those experimental data a laminate of 30 plies of plain woven E-glass fabric and an epoxy matrix was manufactured as a benchmark for testing and modelling. Three different tests were conducted on this benchmark laminate. First digital microscopy was used to measure tow path and cross-section parameters. Secondly a thermo-elastic stress analysis was done to gather information on the stress field on the laminates' surface. Finally standard tensile and shear tests, according to ASTM D3039 [110] and ASTM D3518 [111], were conducted to measure the stress-strain behaviour of the laminate.

3.2 Laminate Manufacture

A total of four 30 ply plain weave glass fibre epoxy laminate plates were manufactured, from which all test specimen were cut. For manufacture Gurit's RE86P dry plain glass fibre weave was used [112]. The weave has an area weight of 85 g/m^2, fibre tex is 34 for both the warp and weft fibres, fibre counts are 12 ends/cm in the warp direction and 12.5 ends/cm in the weft direction. To achieve a thickness of 2.5 mm, as required by both ASTM D3039 [110] and ASTM D3518 [111], 30 plies were required as can be seen in the calculation equation 3-1, where t is the laminate thickness, n_{layers} the number of layers in the laminate, ρ_f the density of the fibre material and V_f the fibre volume fraction. The resin used was Gurit's Prime-20LV resin with a slow hardener [113]. After mixing resin and hardener, at a ratio of 100:26 by weight, the mixture was degassed for about 30 minutes before infusion.

For all calculations requiring fibre and matrix densities the material data shown in Table 1 are used.

E-glass density ρ_f	2.55 g/cm^3 [114]
Prime LV20 epoxy resin ρ_r	0.936 g/cm^3 [113]

Table 1: Glass Fibre and Resin Densities

$$t = \frac{n_{layers} \times m_{weave}}{\rho_f \times V_f} = 2.5 \; mm \qquad\qquad (3\text{-}1)$$

The laminate was manufactured using a vacuum assisted resin infusion process with double bagging to ensure constant consolidation pressure and therefore low void content and uniform thickness [20]. Layers of dry plain E-glass fibre weave were cut from a role of fabric and laid up depending on the specimen type. After the layers had been laid up, peel ply and a distribution medium were put on top of the plies. The stack was then double bagged after inlet and outlet coils and tubes were added. During the infusion a vacuum was applied to the outlet tube and the inlet tube was submerged in a bucket of degassed resin. A breach unit was put into the outer vacuum bag to allow the attachment of a vacuum pump. The entire stack is shown in Figure 17. A tap on the outlet side was opened first to clear all remaining air out of the inner vacuum bag. Then a vacuum was applied to the outer vacuum bag via the breach unit to ensure constant consolidation pressure. Finally a tap on the inlet side was opened to allow resin to be infused in the dry preform. Both taps, on the inlet and the outlet side, were closed as soon as resin could be seen in the outlet pipe. A photographic sequence of the stacking procedure before infusion is shown in Figure 18 to Figure 22.
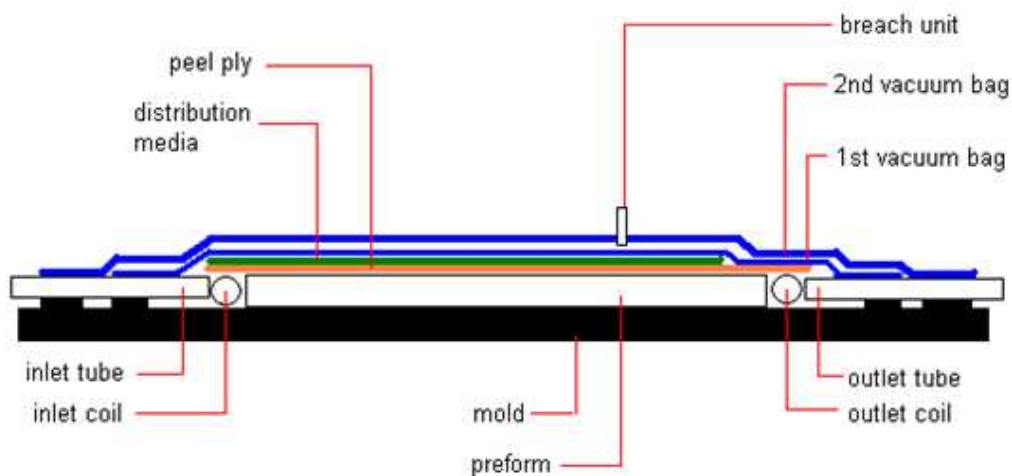
Figure 17: Mold Build-Up

First 30 layers are cut from a role of dry glass fibre plain weave and stacked on a glass plate, which has been cleaned thoroughly and then sprayed with release agent.

Figure 18: Dry Preform on Mould

Peel-ply as well as a distribution medium are added on top of the stack. Inlet and outlet coils are also included at both ends of the stack. The purpose of the distribution medium is to distribute the liquid resin across the dry glass fibre. However, if it would cover the entire stack, resin would flow across the stack too quickly, leading to resin starved areas.
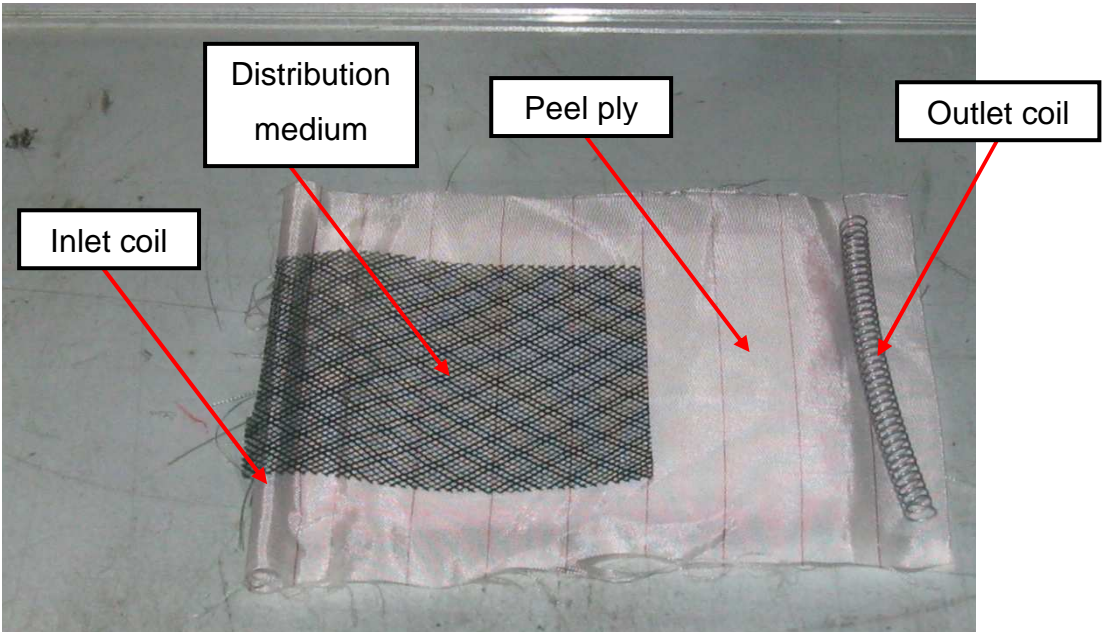
Figure 19: Stack with Peel – Ply and Distribution Medium

Two lines of tacky tape are put down on the glass plate around the stack of dry glass fibre. Inlet and outlet tubes are taped down on the tacky tape at both ends of the stack.
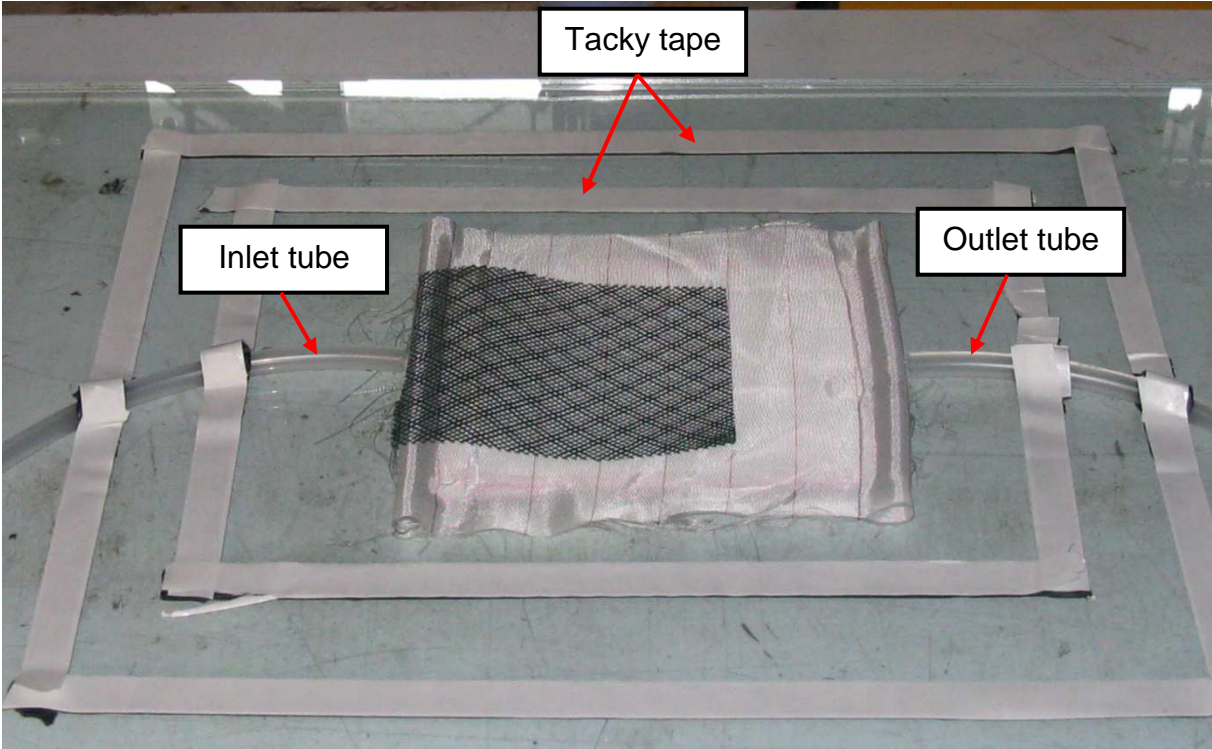
Figure 20: Mould with Tacky Tape and Tubes

After that a first vacuum bag is taped down on the inner tacky tape line.

Figure 21: Mould with Vacuum Bag

Some breather fabric is added and the second vacuum bag is taped down on the outer tacky tape line. The bag is pierced and then resealed using a breach unit. In order not to leave an imprint on the finished composite plate, the breach unit is located at one of the corners of the plate.
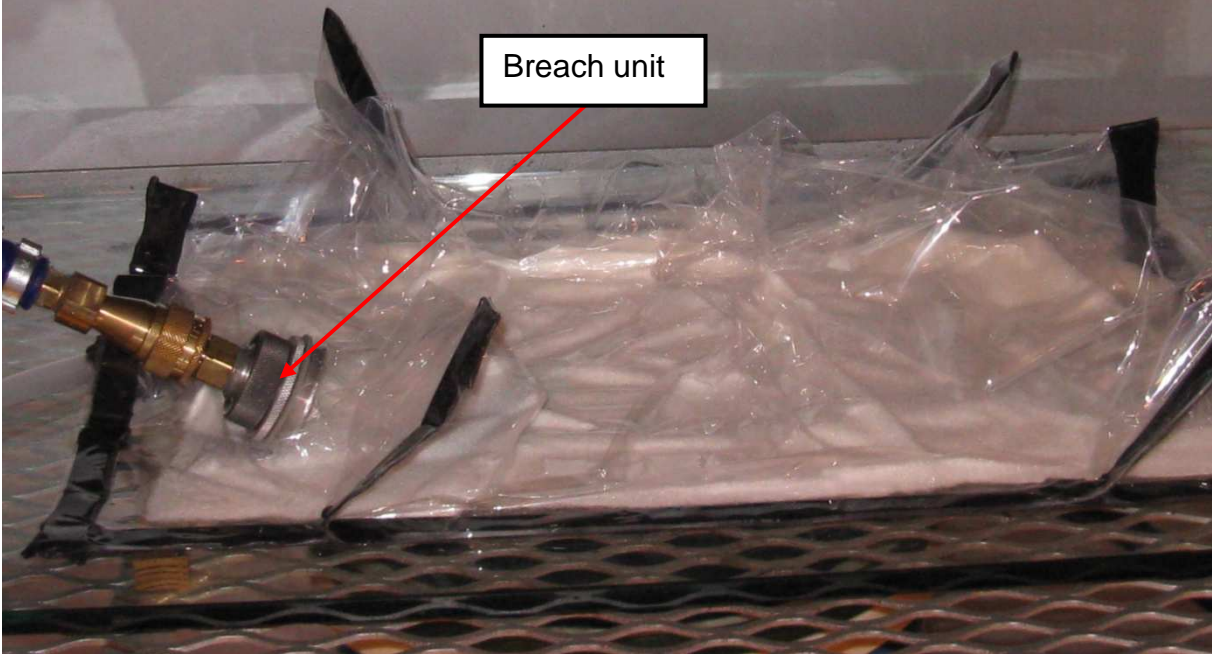
Figure 22: Mould with Vacuum Bag and Breach Unit

The composite was then cured and post-cured. During the curing and post-curing cycle the laminate went through three different temperature stages, at 45°C for one hour, 55°C for another hour and finally 65°C for 16 hours. Changes in temperatures between different stages happened at a constant rate of 2°C/min.

The finished plates were almost square with a width of 220 mm and a length of 230 mm. Fibre volume fraction was measured using the plate area and weight as shown in equation 3-2, where V_f and W_f are the fibre volume and weight fractions respectively and ρ_f and ρ_m the fibre and matrix material densities. The fibre volume fractions for each plate are summarized in Table 1.

$$V_f = \frac{W_f/\rho_f}{W_f/\rho_f + (1 - W_f)/\rho_m} \qquad (3\text{-}2)$$

plate	1	2	3	4
lay-up	$[(0/90)F]_{30}$	$[(0/90)F]_{30}$	$[(0/90)F]_{30}$	$[\pm45F]_{30}$
preform mass [g]	272	272	272	272
panel mass [g]	462	456	456	459
W_f [%]	58.9	59.6	59.6	59.3
V_f [%]	39.1	39.9	39.9	39.0

Table 2: Laminates Fibre Volume Fractions

Depending on the test conducted, specimens were cut in different directions from the plates. For the first two plates warp and weft tows were oriented in the 0°/90° directions. From these plates, microscopy and tensile test specimens were cut.

The first two plates were cut into three equally sized parts and then cut up further into thin strips for microscope analysis and tensile test specimens. The pattern of these strips is shown in Figure 23. Samples 1 and 2 are the tensile specimens, 3 to 41 are used in the digital microscopy. Samples 3, 8 to 12, 17 to 22 and 27 to 35 were cut from the plates through the thickness in the warp direction, meaning these samples showed warp tow cross-sections and weft tow paths while samples 4 to 7, 13 to 16, 23 to 26 and 36 to 41 were cut through the thickness in the weft direction, showing weft cross-sections and warp tow paths. The other plates were cut into strips of the same shape as Samples 1 and 2 of the first two plates and used for the TSA analysis and shear tests.
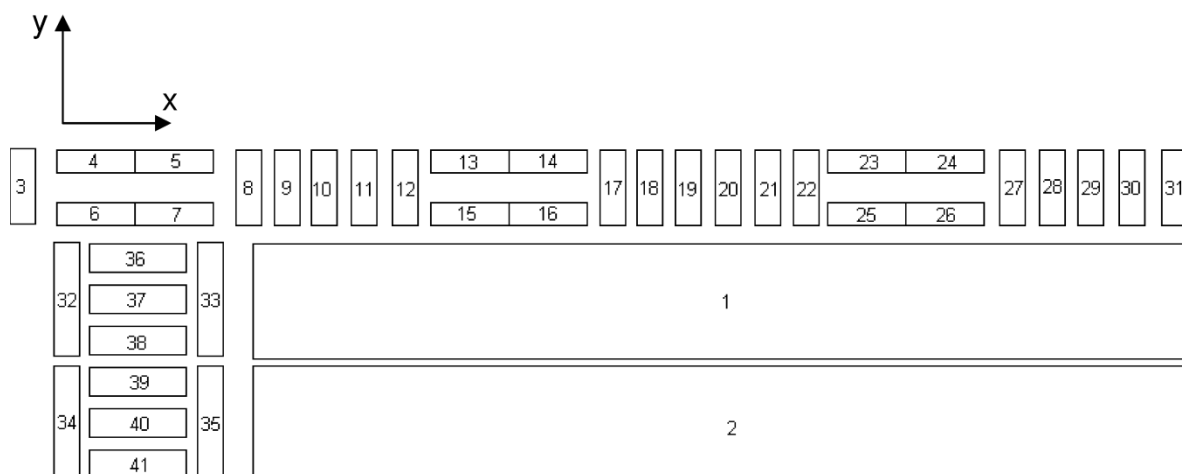
Figure 23: Laminate Cut-Up Pattern

The same ply orientation was used for the TSA analysis, for which specimens were cut from plate number 3. The shear tests specimens were cut from plate number 4 with the warp and weft tows oriented in the ±45° directions.

4 Digital Microscopy

4.1 Specimen Preparation

The thin strips, numbered 3 to 41, cut from the first two plates were used for the microscopic analysis and therefore cast in an epoxy resin and then polished. Three specimens were cast in a single cup of resin to make one microscopic sample in order to reduce polishing time. The epoxy resin was mixed with hardener at a ratio of 25:3 by weight with yellow dye added to provide contrast under the microscope. The mixture was then degassed for 30 minutes.

Polishing consisted of 5 stages using a STRUERS LaboPol-5 polishing machine Figure 24. In the first stage the specimens were ground down by hand using very rough sanding paper. The machine stages were further coarse grinding, fine grinding, rough polishing and fine polishing. Polishing surface types, suspension used, polishing speed, force levels, with which the specimens were pressed into the surface, and polishing time were chosen according to recommendations made by STRUERS. Details of the polishing process are listed in Table 3 and a polished sample is shown in Figure 25.

Figure 24: STRUERS LaboPol-5 polishing machine

Step	polishing surface	suspension	speed [rpm]	force [N]	time [sec]
1	SiC-paper	-	300	30	60
2	MD-Largo	DiaPro Allegro/Lar	150	25	240
3	MD-Mol	DiaPro Mol	150	20	240
4	MD-Chem	OP-S, 0.04µm	150	20	80

Table 3: Microscopic Specimen Polishing Stages

Figure 25: Polished Digital Microscopy Specimen

4.2 Digital Microscopic Methodology

The digital microscopy analysis was done using a Reichert-Jung MEF -3 high performance microscope (Figure 26) with two images, one with 20 times magnification and one with 80 times magnification, taken of each sample. An open source image analysis software, JMicroVision Version 1.2.7, was then used to gather information on tow path and tow cross-section. To achieve this, lines were drawn along the tow path centre line and around the tow cross-section and the coordinates of these start and end points were recorded. These coordinates were utilized to fit standard mathematical functions through the recorded points.

Figure 26: Reichert-Jung MEF-3 Microscope

After the required parameters had been established for each specimen they were processed further using standard statistical techniques to calculate averages and get a sense of the amount of variation of these parameters. Parameters were grouped in selected intervals for visualization purposes and the number of samples within each interval plotted. Mean average values μ and standard deviations σ were calculated using equations 4-3 and 4-4, where x is the sample value investigated and n the number of samples. These were then used to plot the probability density (pdf) and cumulative distribution (cdf) functions using equations 4-5 and 4-6. For ease of comparison, the probability density function was plotted in the same graphs as the number of samples for each interval in Figure 29, Figure 31, Figure 37, Figure 39 and Figure 40.

$$\mu = \frac{1}{n}\sum_{i=1}^{n} x_i \tag{4-3}$$

$$\sigma = \sqrt{\frac{1}{n-1}\sum_{i=1}^{n}(x_i - \mu)^2} \tag{4-4}$$

$$\text{pdf: } f(x) = \frac{1}{\sigma\sqrt{2\pi}} exp\left(-\frac{1}{2}\left(\frac{x-\mu}{\sigma}\right)^2\right) \tag{4-5}$$

$$\text{cdf: } F(x) = \frac{1}{\sigma\sqrt{2\pi}} \int_{-\infty}^{x} exp\left(-\frac{1}{2}\left(\frac{x-\mu}{\sigma}\right)^2\right) dx \tag{4-6}$$

4.3 Tow Path Parameter Determination

The 20 times magnified images were used to determine tow path parameters. Short line segments were placed along the centre axis of a number of tows (Figure 27) and

the coordinates of the beginning and end points of each line segment were recorded. A standard sine function was then fitted through these points (Figure 28) for each tow using the least-square fit algorithm shown in equations 4-15 and 4-16. The wavelength L of the sine function was measured directly from the microscopic image.
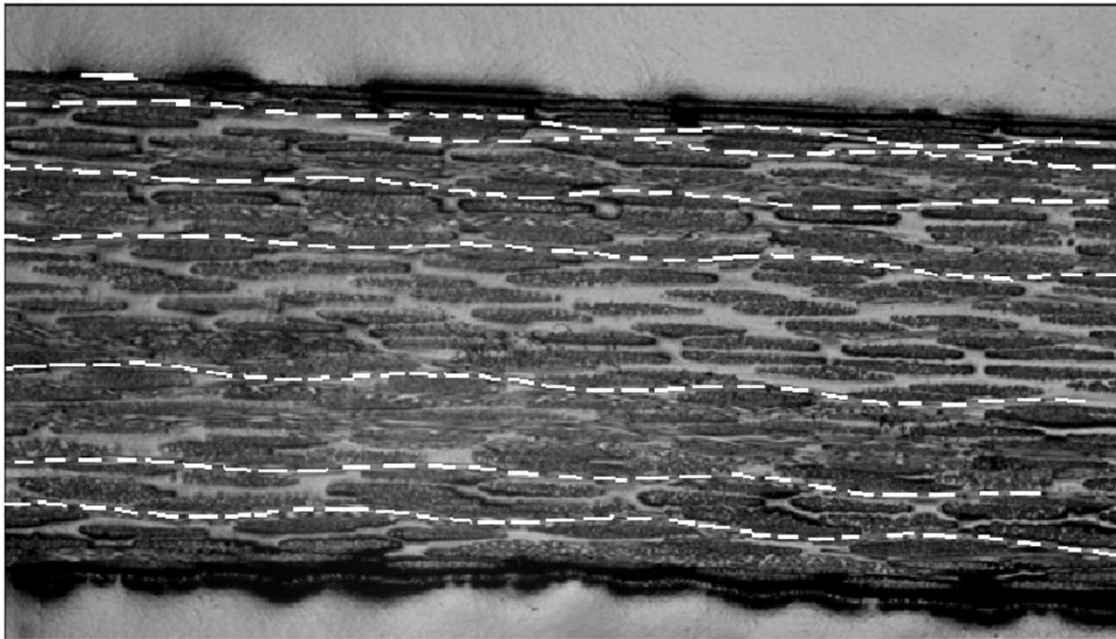
Figure 27: Tow Path Microscopic Image (20 Times Magnification)
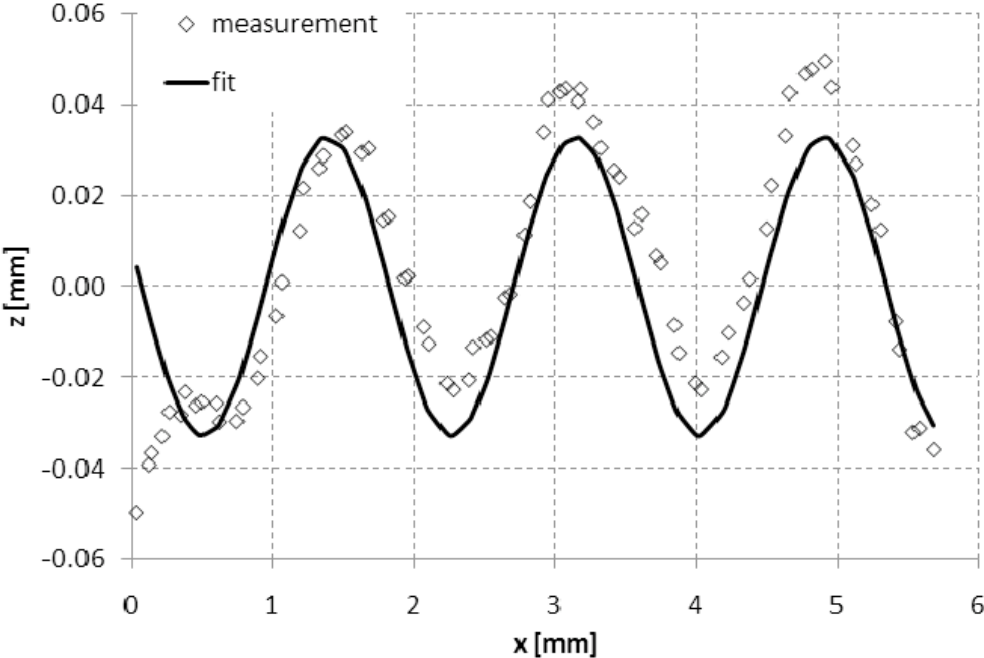
Figure 28: Tow Path Fit Compared with Microscopic Data

Starting with a standard sine-function as defined in equation 4-7, where D and E are parameters of the respective sin and cos components and x the position along the tow path, which has a wavelength L:

$$z(x) = D \sin\left(\frac{2\pi x}{L}\right) + E \cos\left(\frac{2\pi x}{L}\right) \tag{4-7}$$

The recorded coordinates of the beginning and end points of the line segments placed on the microscopic image x_i and z_i were used to set up the least-square fit algorithm as shown in equation 4-8. Variables i was used as a running index and n to denote the total number of samples.

$$f := \sum_{i=1}^{n} \left(z_i - \left[D \sin\left(\frac{2\pi x_i}{L}\right) + E \cos\left(\frac{2\pi x_i}{L}\right)\right]\right)^2 \rightarrow min \tag{4-8}$$

In order to achieve a minimum for the least-square fit function the first derivative by an independent parameter is set equal to zero. The method is demonstrated here for the parameter D. Executing the derivation with respect to parameter D yields the following equation:

$$\frac{df}{dD} = 2 \sum_{i=1}^{n} \left(z_i - D \sin\left(2\frac{\pi x_i}{L}\right) - E \cos\left(2\frac{\pi x_i}{L}\right)\right)\left(-\sin\left(2\frac{\pi x_i}{L}\right)\right) = 0 \tag{4-9}$$

Multiplying out the brackets simplifies the equation to:

$$\sum_{i=1}^{n} \left[-2z_i \sin\left(2\frac{\pi x_i}{L}\right) + 2D \sin^2\left(2\frac{\pi x_i}{L}\right) + 2E \cos\left(2\frac{\pi x_i}{L}\right) \sin\left(2\frac{\pi x_i}{L}\right)\right] = 0 \tag{4-10}$$

This equation can be simplified further using standard trigonometric functions:

$$2 \sin^2 x = 1 - \cos 2x \tag{4-11}$$

$$2 \cos x \sin x = \sin 2x \tag{4-12}$$

Leading to the equation looking as follows:

$$\sum_{i=1}^{n} \left[-2z_i \sin\left(2\frac{\pi x_i}{L}\right) + D\left(1 - \cos\left(4\frac{\pi x_i}{L}\right)\right) + E \sin\left(4\frac{\pi x_i}{L}\right)\right] = 0 \tag{4-13}$$

It is now possible to isolate the parameter D on the left-hand side, yielding:

$$D \sum_{i=1}^{n} 1 - \cos\left(4\frac{\pi x_i}{L}\right) = 2 \sum_{i=1}^{n} z_i \sin\left(2\frac{\pi x_i}{L}\right) - E \sum_{i=1}^{n} \sin\left(4\frac{\pi x_i}{L}\right) \tag{4-14}$$

Rewriting the remaining sum on the left hand side and dividing both sides by that remaining sum yields the final equation for parameter D:

$$D = \frac{2 \sum_{i=1}^{n} z_i \sin\left(\frac{2\pi x_i}{L}\right) - E \sum_{i=1}^{n} \sin\left(\frac{4\pi x_i}{L}\right)}{n - \sum_{i=1}^{n} \cos\left(\frac{4\pi x_i}{L}\right)}$$

(4-15)

The derivation of parameter E is analogous to the derivation for parameter D resulting in the following equation:

$$E = \frac{2 \sum_{i=1}^{n} z_i \cos\left(\frac{2\pi x_i}{L}\right) - D \sum_{i=1}^{n} \sin\left(\frac{4\pi x_i}{L}\right)}{n + \sum_{i=1}^{n} \cos\left(\frac{4\pi x_i}{L}\right)}$$

(4-16)

These equations cannot be solved analytically due to the coupling of parameters D and E. Therefore these equations had to be solved numerically using an iterative process. A Python code, which is shown and tested in Appendix A, was programmed to perform these iterations. Initial values for D and E were assumed to be half the absolute difference between the highest and lowest z value in the experimentally measured data. The initial values for D and E were then used to calculate new values for D and E using equations 4-15 and 4-16 with D being updated first. The iteration ended when the difference for both updated values of D and E were less than 0.0001 compared to the values in the previous iteration step.

From the resulting parameters D and E amplitude C and phase φ were calculated using equations 4-17 and 4-18.

$$C = \sqrt{D^2 + E^2}$$

(4-17)

$$\varphi = \frac{E}{D}$$

(4-18)

4.4 Tow Path Parameter Results

The probability density function (pdf) of the tow path wavelength shows a clear Gauss distribution (Figure 29) and good agreement with a histogram of numbers of samples within certain classes of values. A maximum value of 2.33 is reached for the pdf. The cumulative distribution function (cdf) reaches a value close to 1, 0.998 to be exact, for a value of 2.1 mm. The calculated mean average for this distribution is 1.603 mm with a standard deviation of 0.164 mm.
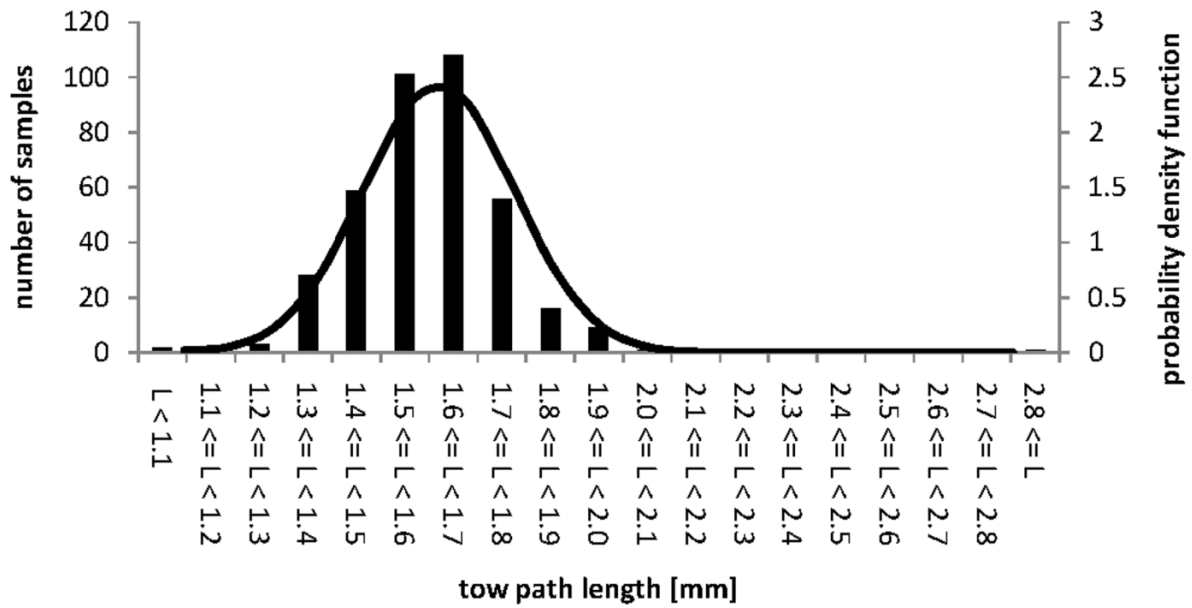
Figure 29: Tow Path Wavelength Distribution
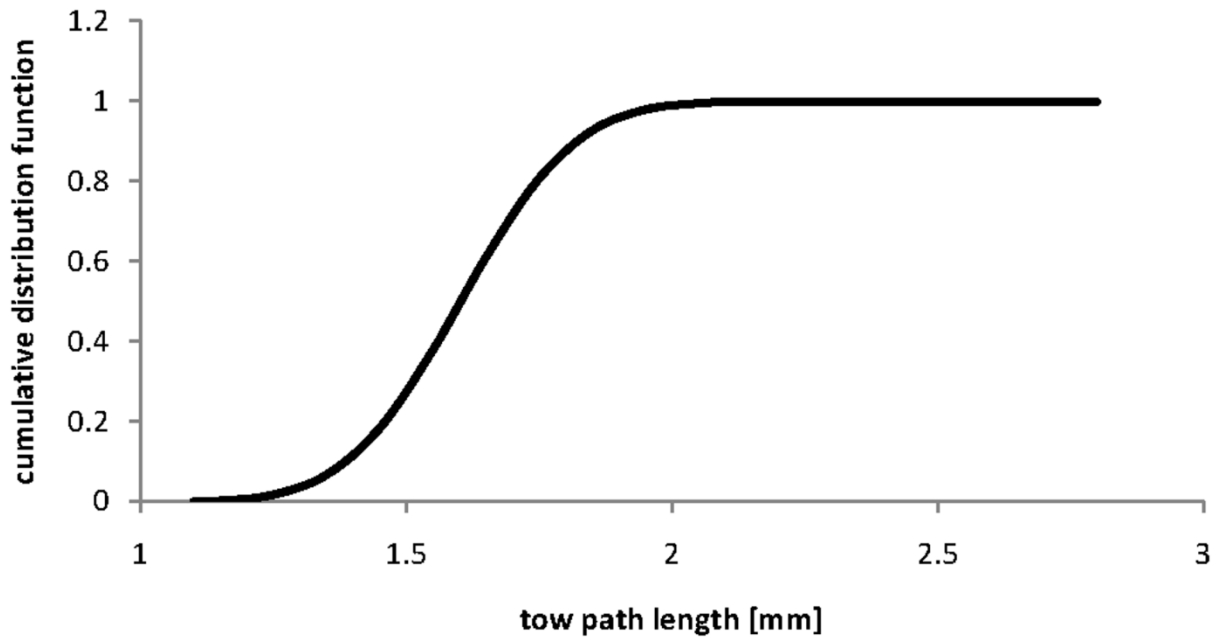
Figure 30: Cumulative Distribution Function of Tow Path Wavelength

Similar to the tow path wavelength distribution, the pdf for the tow path amplitude shows a clear Gauss distribution and good agreement with a histogram of numbers of samples within certain classes of values. A maximum value of 46 is reached for the pdf. The cumulative distribution reaches a value of 0.981 from a value of 0.57 mm. The calculated mean average for this distribution is 0.025 mm with a standard deviation of 0.009 mm (Figure 31).
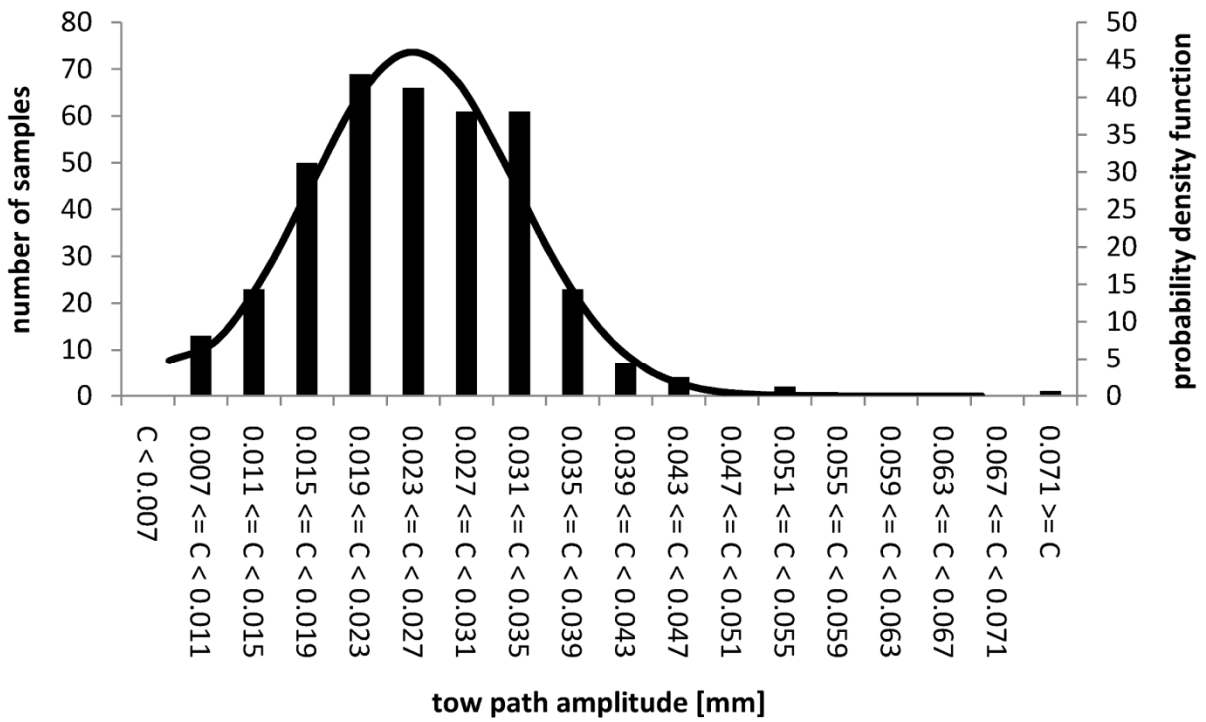
Figure 31: Tow Path Amplitude Distribution
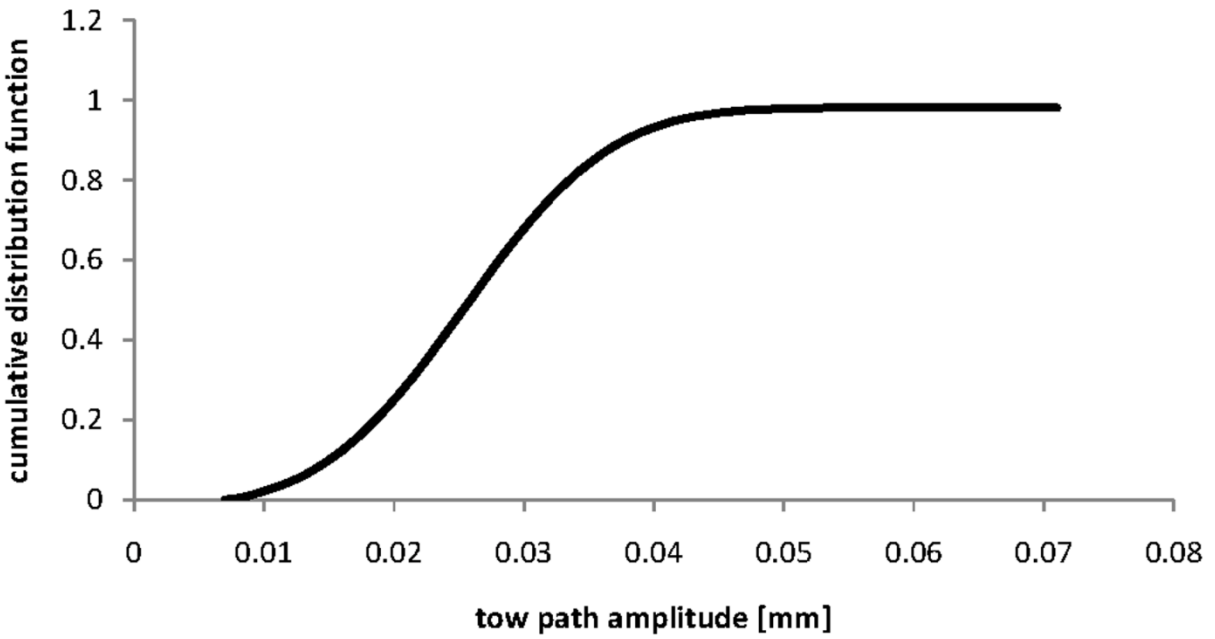
Figure 32: Cumulative Distribution Function of Tow Path Amplitude
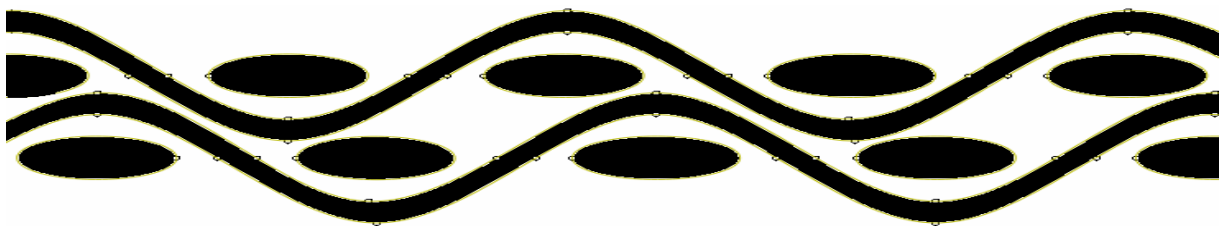
Figure 33: Nesting in a Plain Weave Laminate

Both tow path amplitude C and tow wavelength L plots show a Gauss distribution, which is expected if a sufficient number of samples are used. The tow path phase φ however does not show a Gaussian distribution but an almost constant distribution over the entire range. This is due to nesting where the tows in different layers slide in the space between neighbouring tows when pressure is applied to a stack of layers (Figure 33). An even distribution across the spectrum of tow path phases is therefore expected (Figure 34).
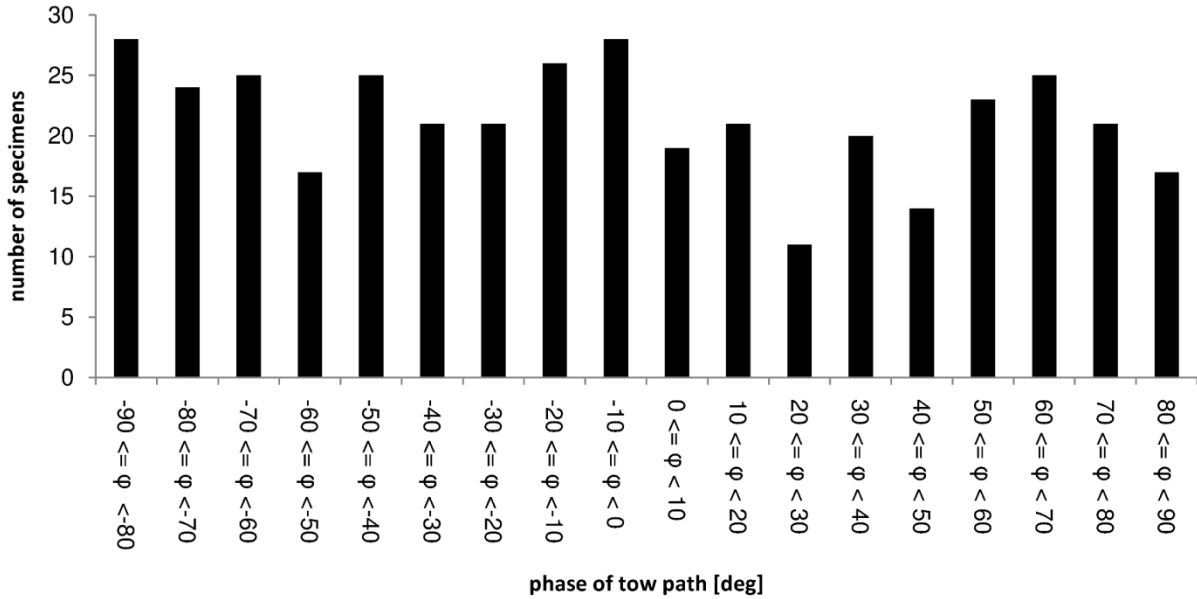
Figure 34: Distribution of Tow Path Phase

4.5 Tow Cross-Section Parameter Determination

The image analysis software used for this thesis was not capable of drawing ellipses, which is why tow cross-section parameters had to be determined similarly to the tow path parameters, using the 80 times magnified images. Line segments were placed along the outer boundary of tow cross sections (Figure 35) and again the spatial coordinates of these beginning and end points of these lines were recorded. A standard ellipse was fitted through these points for each individual cross-section (Figure 36), using the least-square fit algorithm shown in equations 4-25 and 4-26. The standard elliptical equation is not unique in a mathematical sense with two possible results for every value of the independent variable. This causes convergence problems for least-square fit algorithms trying to solve for the major and minor half-axes parameters a and b. One way of achieving stable convergence

towards a unique solution is by calculating the squared values of parameters a and b, rather than the actual values. The resulting derivation of the equations is demonstrated for parameter a.
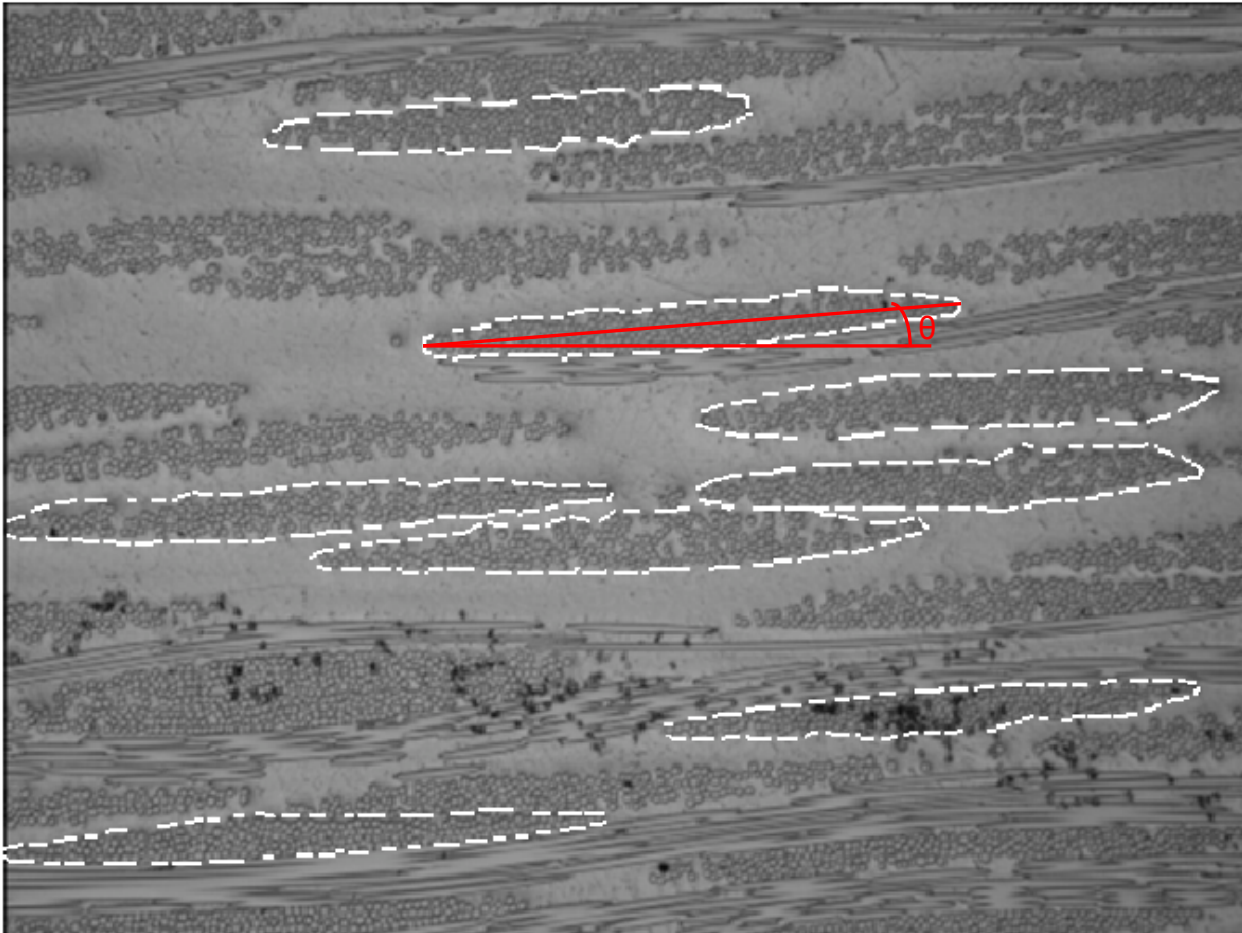
Figure 35: Ellipse Microscopic Image (80 times magnification)
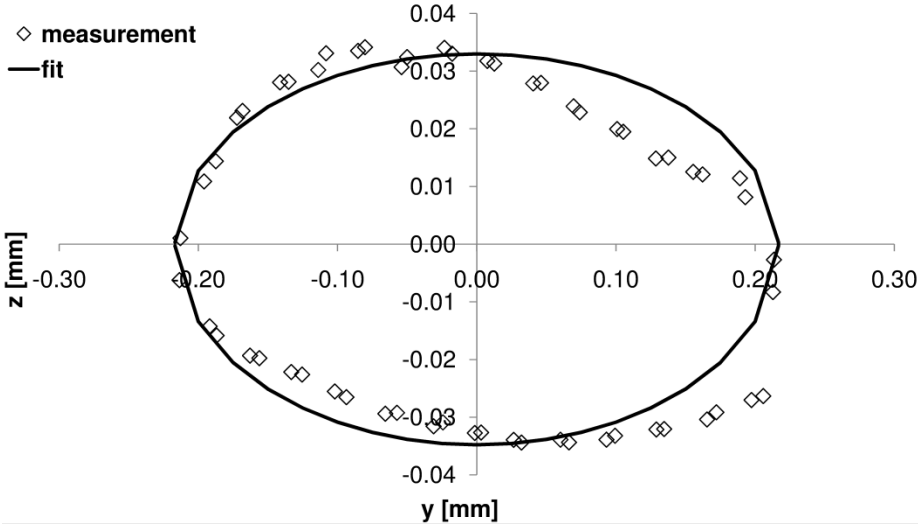
Figure 36: Ellipse Fit Compared with Microscopic Measurement

Starting with a standard ellipse function, where parameters a and b are the major and minor half axis parameters with y and z being the coordinate values of a point along the ellipse:

$$z = \pm b \sqrt{1 - \frac{y^2}{a^2}}$$

(4-19)

For a total number of samples n and running index i, the least-square fit function was set up in the following way:

$$g := \sum_{i=1}^{n} \left(z_i^2 - \left[b^2 \left(1 - \frac{y_i^2}{a^2} \right) \right] \right)^2 \rightarrow min$$

(4-20)

At this stage we substitute u for a^2 and v for b^2, which gives:

$$g := \sum_{i=1}^{n} \left(z_i^2 - \left[v \left(1 - \frac{y^2}{u} \right) \right] \right)^2 \rightarrow min$$

(4-21)

Again the first derivative by the independent parameter is set to zero, resulting in the following:

$$\frac{dg}{du} = 2 \sum_{i=1}^{n} \left[\frac{x_i^2}{u} + \frac{y_i^2}{v} - 1 \right] \left[-2 \frac{x_i^2}{u^2} \right] = 0$$

(4-22)

Multiplying out the right-hand-side yields the following equation:

$$= -4 \sum_{i=1}^{n} \left[\frac{x_i^4}{u^3} + \frac{y_i^2 x_i^2}{u^2 v} - \frac{x_i^2}{u^2} \right] = 0$$

(4-23)

After reversing the substitution the equation looks as follows:

$$-4 \sum_{i=1}^{n} \frac{x_i^4}{a^6} - 4 \sum_{i=1}^{n} \frac{y_i^2 x_i^2}{a^4 b^2} + 4 \sum_{i=1}^{n} \frac{x_i^2}{a^4} = 0$$

(4-24)

Parameter a^2 can now be isolated on the left-hand side, which gives:

$$a^2 = \frac{\sum_{i=1}^{n} y_i^4}{\sum_{i=1}^{n} x_i^2 - \frac{\sum_{i=1}^{n} (y_i^2 z_i^2)}{b^2}}$$

(4-25)

Similarly, parameter b^2 can be derived with the equation looking as follows:

$$b^2 = \frac{\sum_{i=1}^{n} z_i^4}{\sum_{i=1}^{n} z_i^2 - \frac{\sum_{i=1}^{n}(y_i^2 z_i^2)}{a^2}}$$

(4-26)

These equations also could not be solved analytically because of the coupling of major half axis a and minor half axis b. Again a Python code, shown and tested in Appendix A, was programmed to solve the resulting equations iteratively using a procedure similar to the one used to calculate tow path parameters. Initial values for a^2 and b^2 are estimated using the maximum and minimum y and z values from the microscopic data. New values are then calculated for a^2 and b^2, using equations 4-25 and 4-26, with a^2 being updated first and the iteration ending when the difference between updated and previous values for a^2 and b^2 were less than 0.0001 respectively. The actual values of the axes were calculated after the iterative process was completed by taking the square roots of the iteration results. As can be seen in Figure 35, the elliptical cross-section is not necessarily level in the microscopic image but tilted at an angle θ. Therefore, the iteration was repeated with the y and z coordinates modified as shown in equations 4-27 and 4-28, ỹ and ž being the transformed coordinate values, to account for different levels of tilt.

$$\tilde{y} = y\cos(\theta) + z\sin(\theta)$$

(4-27)

$$\tilde{z} = z\cos(\theta) + y\sin(\theta)$$

(4-28)

With the standard solution of the elliptical equation shown in 4-29, a quality check for each level of tilt can be conducted with the best fit being the iterative solution that gives the minimum value of k for equation 4-30.

$$\frac{y^2}{a^2} + \frac{z^2}{b^2} = 1$$

(4-29)

$$k = \sum_{i=1}^{n} 1 - \left(\frac{y_i^2}{a^2} + \frac{z_i^2}{b^2}\right)$$

(4-30)

4.6 Tow Cross-Section Parameter Results

The probability density function shows a clear Gauss distribution (Figure 37) and good agreement with a histogram of numbers of samples. A maximum value of 56.3

is reached for the pdf. The cumulative distribution reaches a value of 0.997 from a value of 0.061 mm. The calculated mean average for this distribution is 0.037 mm with a standard deviation of 0.007 mm.
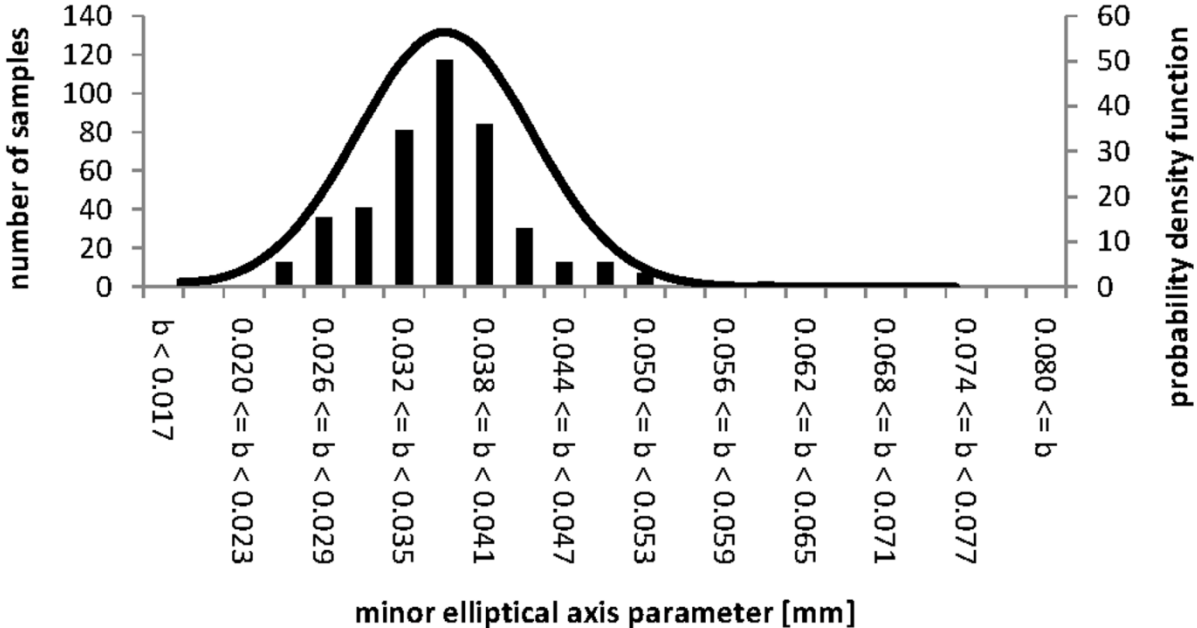

Figure 37: Minor Elliptical Axis Parameter Distribution
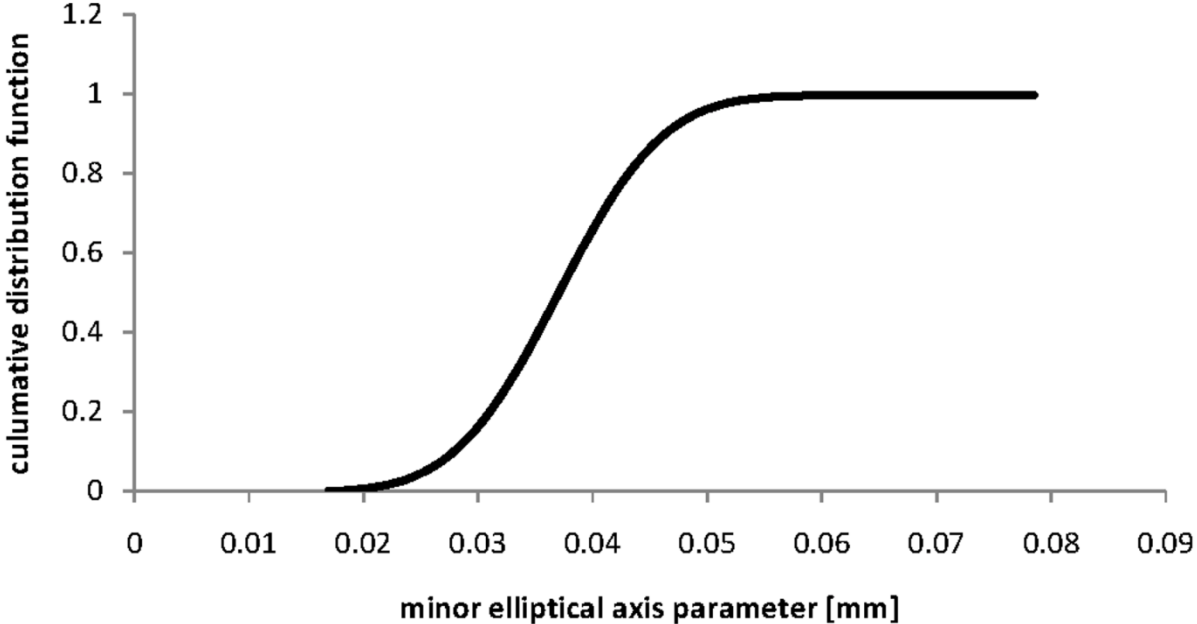
Figure 38: Cumulative Distribution Function of Minor Elliptical Axis Parameter
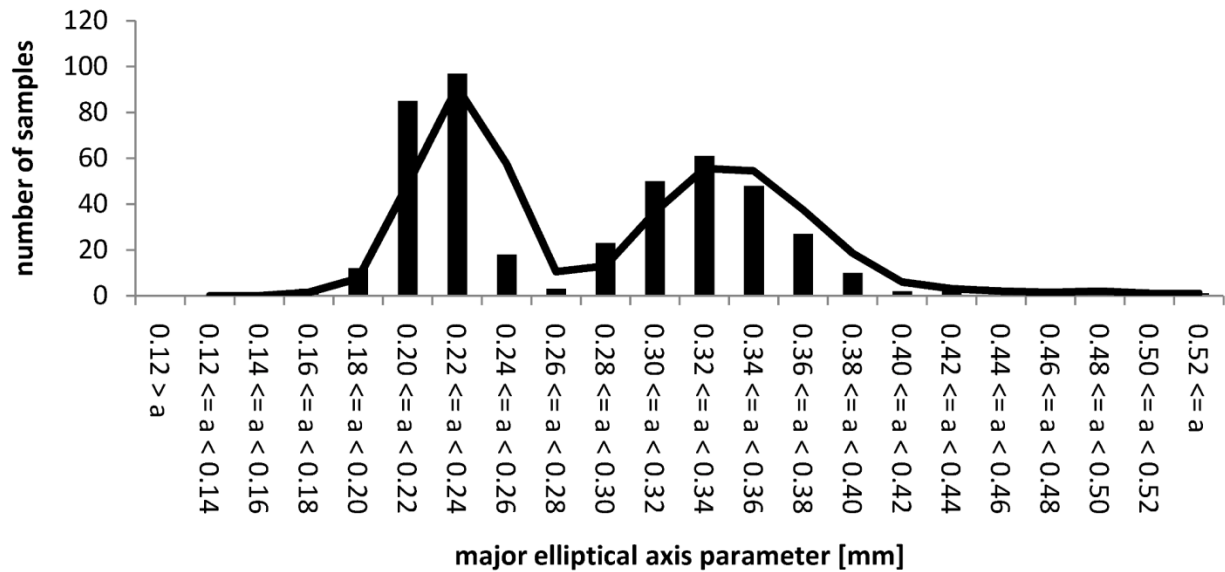
Figure 39: Major Elliptical Axis Parameter Distribution

For the major elliptical axis parameter the probability density function does not show a clear Gauss distribution but a bimodal distribution, two distinct Gauss distributions overlaying each other. These two different distributions are due to a difference in fibre count of about 4% between warp and weft yarns of the plain weave dry preform, meaning the warp tow cross-section is slightly larger than the weft tow. Therefore a mean average cannot be calculated from this distribution with certainty, requiring an additional quality check. The distribution of the tow cross-sectional area is more approximate to a Gauss distribution (Figure 40) as the major elliptical axis parameter distribution. A mean average value of the major axis parameter is therefore calculated from the mean average tow cross-section A using equation 4-31.

$$a = \frac{A}{\pi b}$$
(4-31)

From the probability density function for the cross-sectional area a mean average of 0.033 mm^2 with a standard deviation of 0.011 mm^2 can be calculated. A maximum value of 36.2 is reached for the pdf. The cumulative distribution reaches a value of 0.996 from a value of 0.0675 mm^2 for the tow cross-section. Calculating the mean average major elliptical parameter from the mean average tow cross-section results in a value of 0.284 mm, which is almost identical to the mean average value of 0.282 calculated from the measured major elliptical axis parameter distribution.
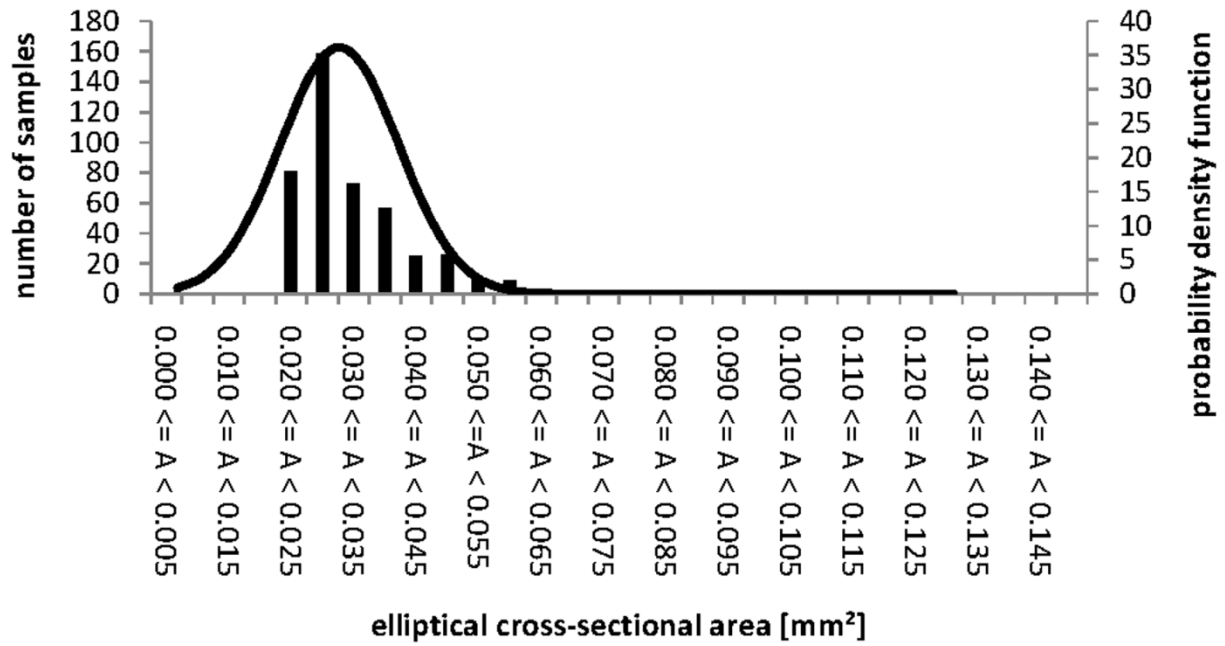
Figure 40: Distribution of Tow Cross-Sectional Area
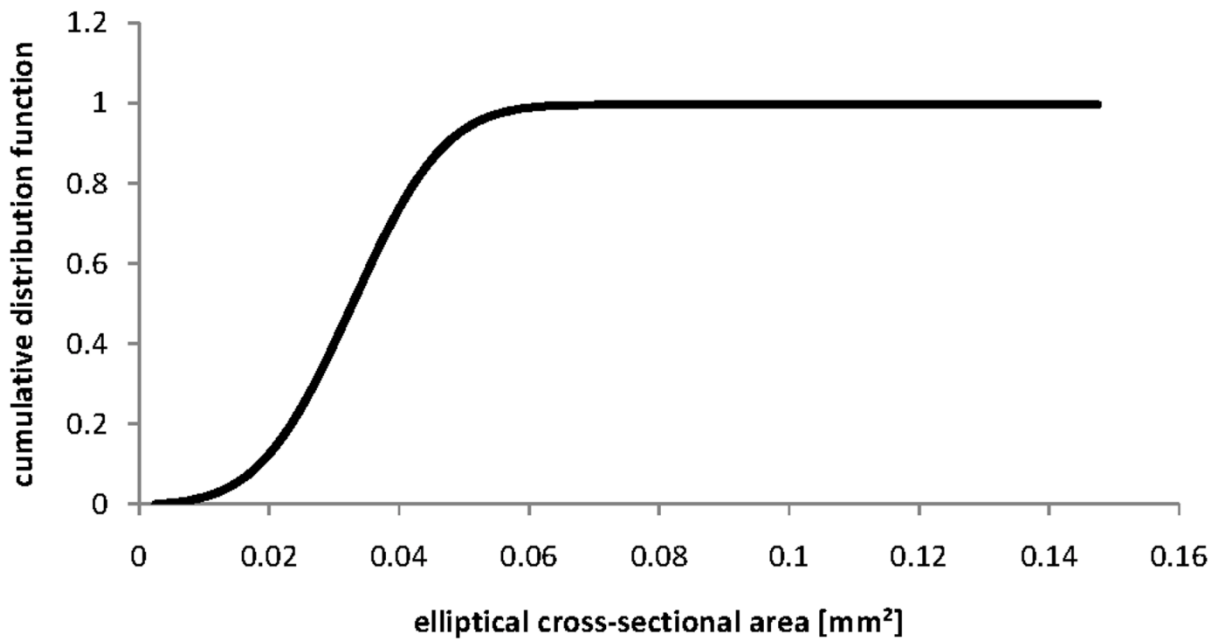
Figure 41: Cumulative Distribution Function of Tow Cross-Sectional Area

4.7 Summary

In general, all probability distribution functions show long tails on both ends, which is due to outliers in the experimental results. Overall, the methods used to estimate tow path and section parameters were somewhat crude and relied heavily on the eye of the experimenter, therefore a number of outliers would be expected. Additionally, due to the small size of the specimens, large variability is expected for all investigated

parameters [49], [115]. However, averages for all parameters can be calculated with statistical significance.

This means a significant amount of variation for all parameters. However, the amount of variation in the microscopic analysis conducted here are consistent with the amount of variation of these parameters found in the literature [49], [115], [116].

According to Ivanov et al [117] and Le Page et al. [118], these variations significantly influence local initiation and progression of damage within a unit cell. However, according to Hivet and Boisse [119] detailed modelling of the woven composite meso-structure is overly complex and simplified models should be used. Therefore mean average values calculated, summarised in Table 4, will be used for the detailed finite element analysis in this thesis.

Parameter [unit]	Mean Average Value ± Standard Deviation
Tow path amplitude [mm]	0.025±0.009
Tow path wavelength [mm]	1.604±0.164
Tow cross section major axis [mm]	0.284
Tow cross section minor section [mm]	0.037±0.007
Tow cross sectional area [mm²]	0.033±0.011

Table 4: Mean Average Values of Tow Geometrical Parameters

Since no afford was made to have tows with the same tex number in the same direction for the benchmark laminates, no distinction between higher and lower tex tows was made when calculating mean averages of geometrical parameters.

5 Thermoelastic Stress Analysis (TSA)

In order to model damage initiation and progression correctly the stress distribution within the unit cell must be predicted accurately. A good way of judging the accuracy of a full finite element unit cell model is to compare the stress distribution predicted by the model to an experimentally obtained stress distribution. Therefore a thermoelastic stress analysis (TSA) is conducted on samples from a laminate with the same lay-up and fibre volume fraction as the tensile test specimen. The results of that analysis are later compared with the stress distribution predicted by a full finite element model of a unit cell with the same architecture as the test specimens.

TSA is based on the thermoelastic effect [92]-[106], meaning that when materials change their volume due to mechanical work they also change their temperature. Wong [98] has shown that this change in temperature ΔT can be related to the principal stresses σ_1 and σ_2 on the surface of the material using the thermal expansion coefficients α_{11} and α_{22} as shown in equation 5-1.

$$\Delta T = -\frac{T}{\rho C_P}(\alpha_{11}\Delta\sigma_1 + \alpha_{22}\Delta\sigma_2) \tag{5-1}$$

The changes in temperature are usually very small, in the order of 1/1000 °C [92], but can be measured using an infrared detector. Equation 5-1 can be modified to relate the signal measured by the detector, called the thermoelastic signal S, to the specimen surface's principal stresses by a calibration coefficient factor A' as it is shown in equation 5-2.

$$A'S = \alpha_{11}\Delta\sigma_{11} + \alpha_{22}\Delta\sigma_{22} \tag{5-2}$$

A generalized procedure to measure the calibration coefficient experimentally has been suggested by Emery et al [120].

A single step change in loading results in a temperature change which quickly dissipates when the load is kept constant. However, if a cyclical load is applied, the temperature changes continuously around a constant mean with the change in load. The resulting cyclical signal measured by the infrared detector can be post processed using a Fourier analysis to calculate the signals magnitude and the phase angle between loading and resulting temperature change.

5.1 Specimen Preparation

The specimens for the thermoelastic stress analysis were cut according to ASTM D3039 [110] (Figure 42) with the same fibre orientation as for the tensile test specimen discussed in chapter 6. Unlike the specimens for the tensile and shear tests the specimens for the TSA analysis were not tested to failure. Therefore the shape of the specimen did not need to be modified to achieve fracture in the centre. This is discussed in detail in Chapter 6. To avoid picking up marks left by the tooling used during manufacture on the bagging side, the surface on the tooling side of the specimen was used in the analysis. Specimens were numbered TSA1, TSA2 and TSA3.
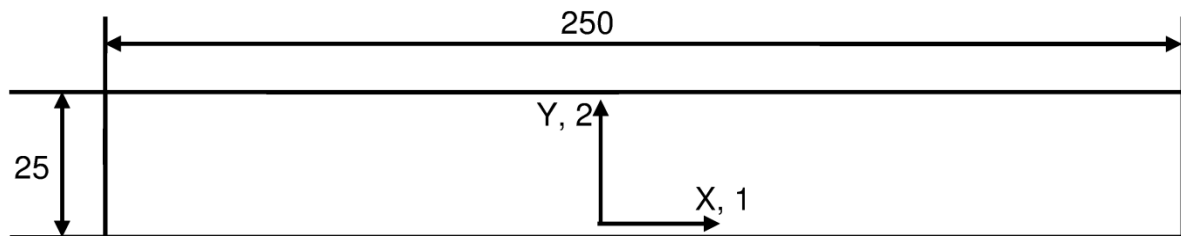
Figure 42: TSA test specimen geometry

The initial analysis showed that the infrared camera picked up its own reflection when using the plain specimen. Therefore a thin coat of matt black paint was sprayed on the specimen to try and reduce those reflections. Also, when a macro-lens was put on the camera its own reflection was visible even when black paint was applied. A non-uniformity correction (NUC), where the camera sensors are adjusted to give an even signal of the entire surface, was therefore done using the Cirrus camera control software.

5.2 TSA Testing Methodology

An INSTRON 8872 fatigue testing machine (Figure 43) was used to apply a cyclic load on the specimen with an amplitude of 3 kN around a mean load of 4 kN, which results in a maximum axial stress of 112 MPa, about a third of the mean average failure stress of 368 MPa determined for the same composite in Chapter 6. Applying the load at a high frequency means thermal conduction away from the high stress areas is minimized, which improves the accuracy of the temperature measurement. The effect of applying the load at different frequencies has been investigated by

Frühmann [103], where it was found that applying the load with a frequency between 20Hz and 30Hz results in temperature readings accurate enough for the identification of stress concentration points. In this thesis a frequency of 20 Hz was used.

Figure 43: INSTRON 8872 Fatigue Testing Machine

A 20 second video of the loaded specimen was shot with a FLIR SILVER 450M infrared camera with a frame rate of 50 frames per second and processed using the ALTAIR thermal imaging software to measure the thermo-elastic response. The camera was fixed in position with the lens being 100 mm from the specimen surface. A black curtain was put around the testing machine to provide an even background and also block exterior lights, to reduce reflections on the specimen. A G27 macro-lens was used to get more detailed information on the stress state within a single unit cell.

Since the motion on the specimen's surface due to deformation is recorded as well as the thermoelastic response, the recorded movie had to be motion compensated, for which a Random Motion Compensation software was provided by FLIR. Markers on the specimen were required for the Motion Compensation to work. Therefore small marks were put on the specimens using a fine pencil (Figure 44). In the motion compensation software a vector is defined between unique features, in this case the

pencil marks, of the sample surface. These marks are then tracked by the software throughout the entire movie and the changes in length and direction of the vector between them are calculated for every frame. These changes in position from one frame to the next is equal to the rigid body motion of the specimen between frames, therefore the change in position of a pixel between frames can be compensated for.
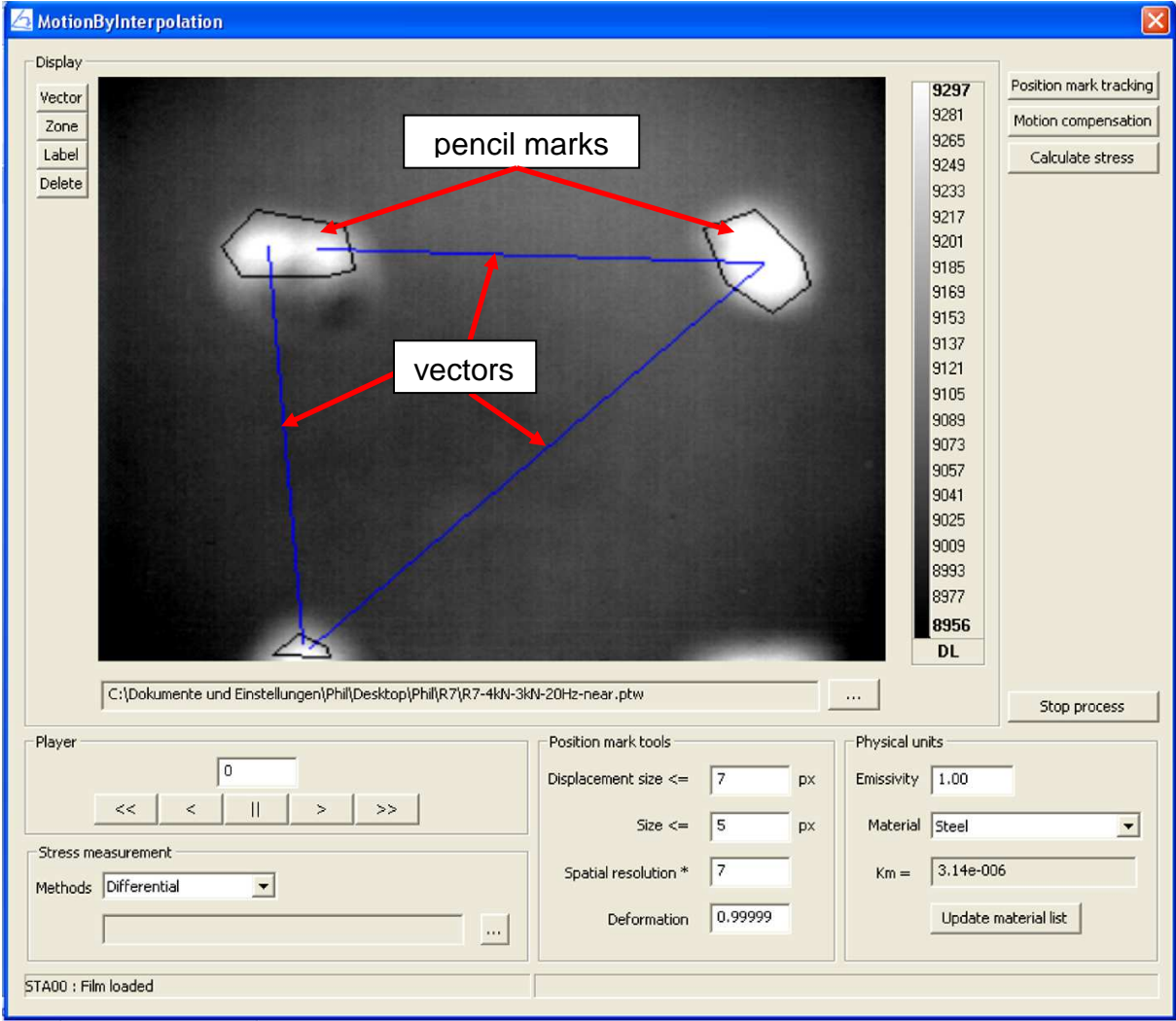
Figure 44: Motion Compensation for TSA Results

After motion compensation the thermoelastic stress analysis was then conducted using the ALTAIR LI software. The software uses a Fast Fourier Transform (FFT) approach to calculate the magnitude and phase as well as the average of the thermoelastic signal of individual pixels and therefore individual points on the specimens.

However, equation 5-2 shows that in order to relate results from the TSA analysis to principal surface stresses of the specimen requires prior knowledge of the thermal

expansion coefficients α_{11} and α_{22}, which cannot be measured without a significant amount of afford. Since the aim of the TSA analysis in this thesis is not to show the actual stress values but to validate the stress distribution predicted by the full finite element model, actual stress values do not need to be calculated. The variation across the specimen's surface of the thermoelastic signal measured by the detector is sufficient to identify stress concentration points.

After a map of the thermoelastic signal has been generated, using the FFT approach, that map is exported as an Altair picture format, which is imported into the next specialized software, Altair LI, for further postprocessing. In this software lines are defined across three discernable unit cells, three in the warp tow or x direction and three in the weft tow or y direction, (Figure 45) for each specimen. Lines are numbered using a two number system and the name of the specimen. The first number after the specimen name is a counter whilst the second number denotes the principal direction that the line runs in, meaning 1 for the x- or warp direction and 2 for the y- or weft direction. Along these lines the thermoelastic signal is determined and the mean average as well as the minimum and maximum level is calculated. These thermoelastic signal values are exported from Altair LI in a plain text format and imported in EXCEL, where the value at each point of every line plot is divided by the mean average value of the line it belongs to in order to calculate its relative value. They are then plotted against the normalised line length, the distance from the starting point of the line to the point the value is determined divided by the length of the line. These line plots of relative values are referred to as normalised thermoelastic signal in Figure 46 to Figure 51.
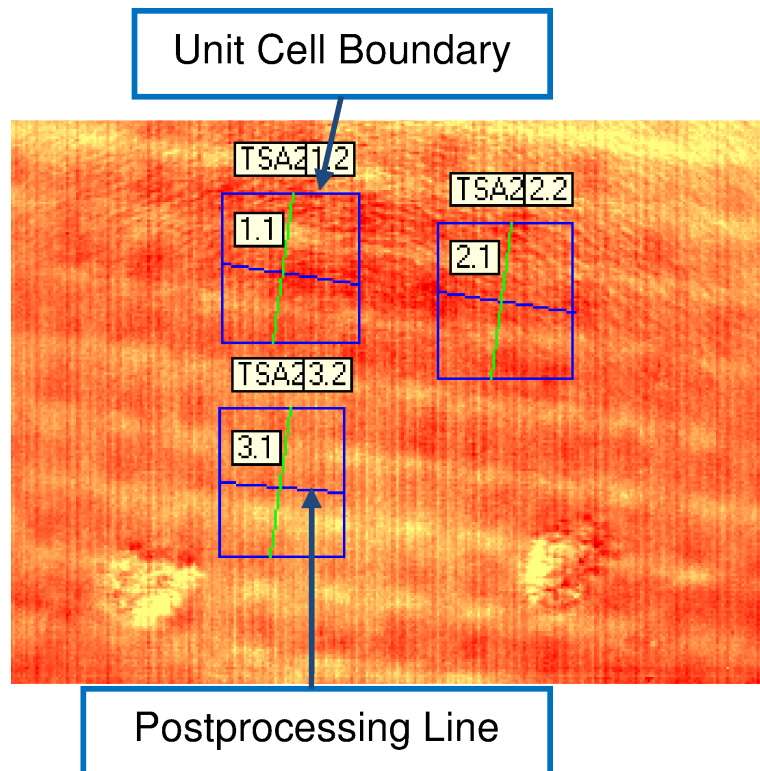
Figure 45: TSA Unit Cell Result Postprocessing Lines

5.3 Results

Figure 46 to Figure 51 show the normalised thermoelastic signal of individual pixels, meaning the value of the thermoelastic signal for a pixel divided by the mean average thermoelastic signal of the line plotted through this pixel. Values vary between about 0.7 and 1.4 for all measured signals independent of whether the signal was determined in the X- or Y-direction. A similar distribution across a woven composite can be found in Frühmann [103]. The standard deviation for each signal is between 0.07 and 0.14, or 7% and 14%, with the mean average being 1.0 for each signal line due to the normalisation of the data. The recorded thermoelastic signals show a high amount of what seems to be regular oscillation with a wavelength of about 0.1 to 0.05, which is shorter than the unit cell length of about 1. This suggests a regular source of noise overlaying the signal.
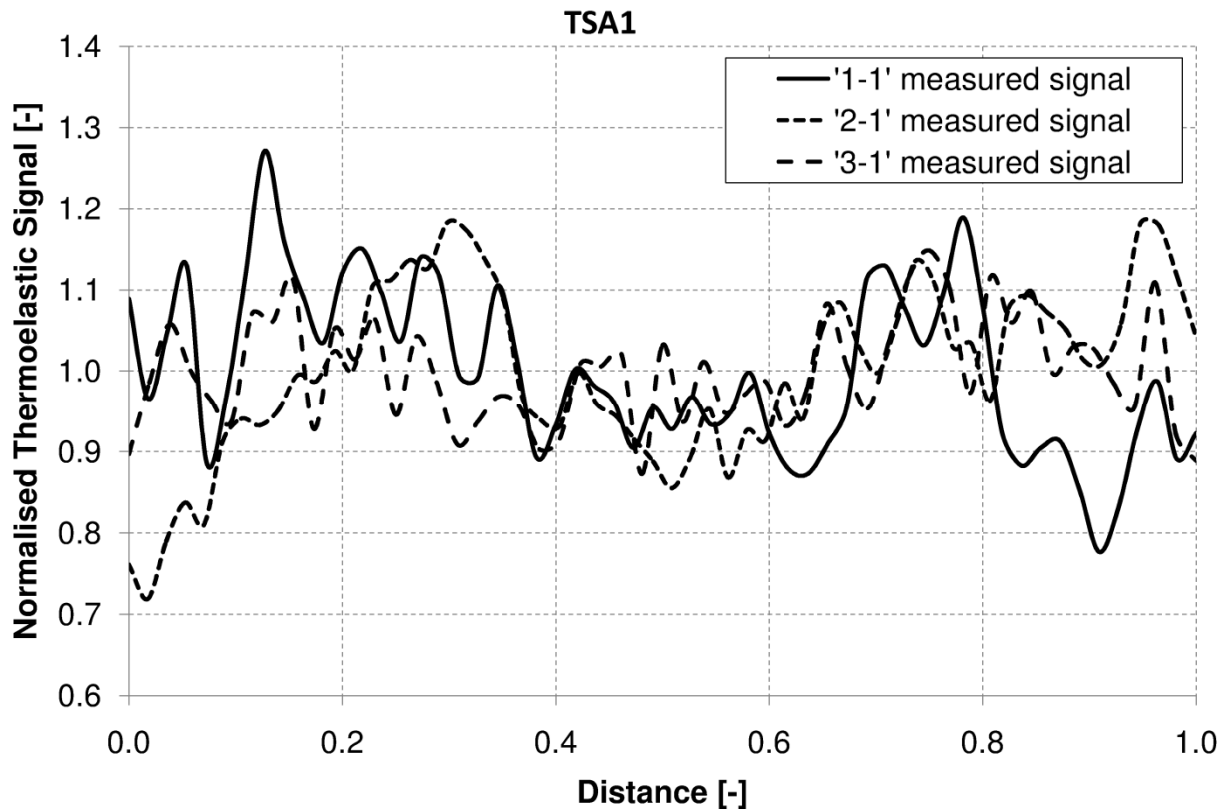
Figure 46: Normalised Thermoelastic Signal of Specimen TSA1 in X-Direction
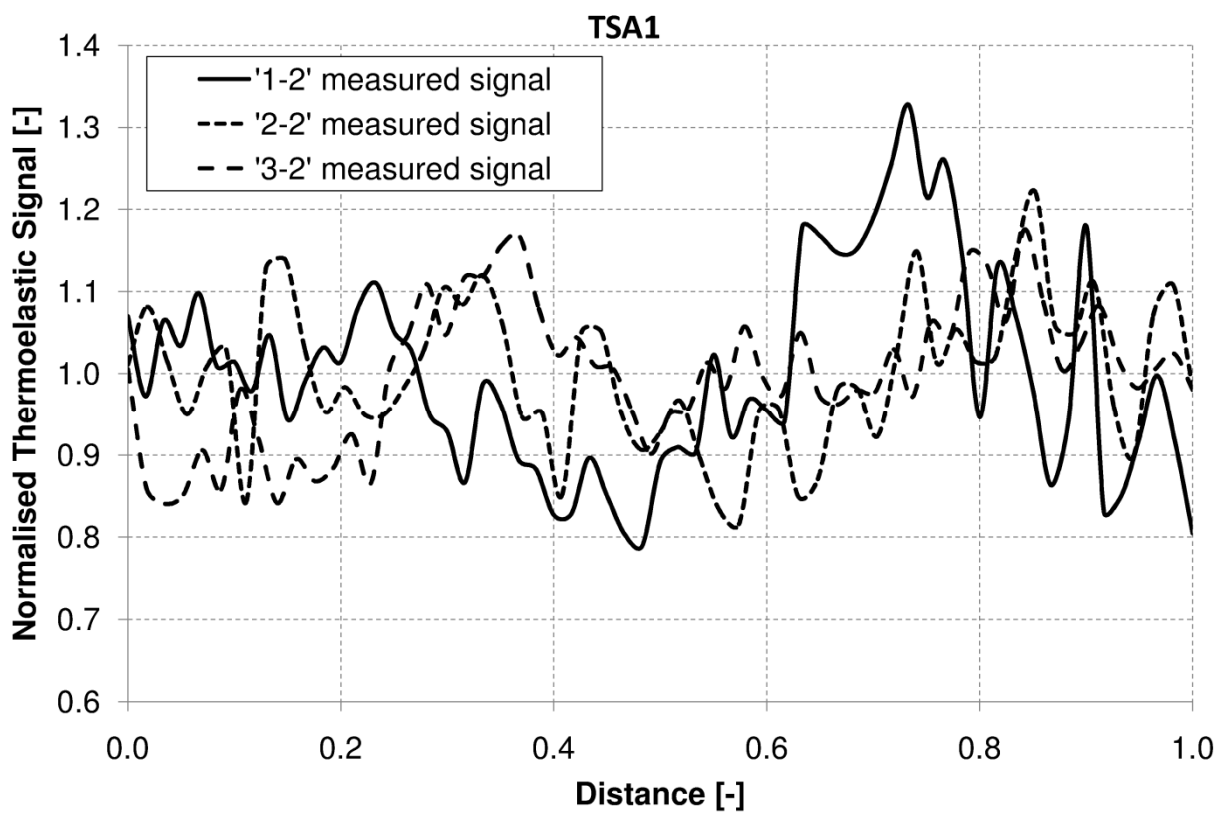
Figure 47: Normalised Thermoelastic Signal of Specimen TSA1 in Y-Direction
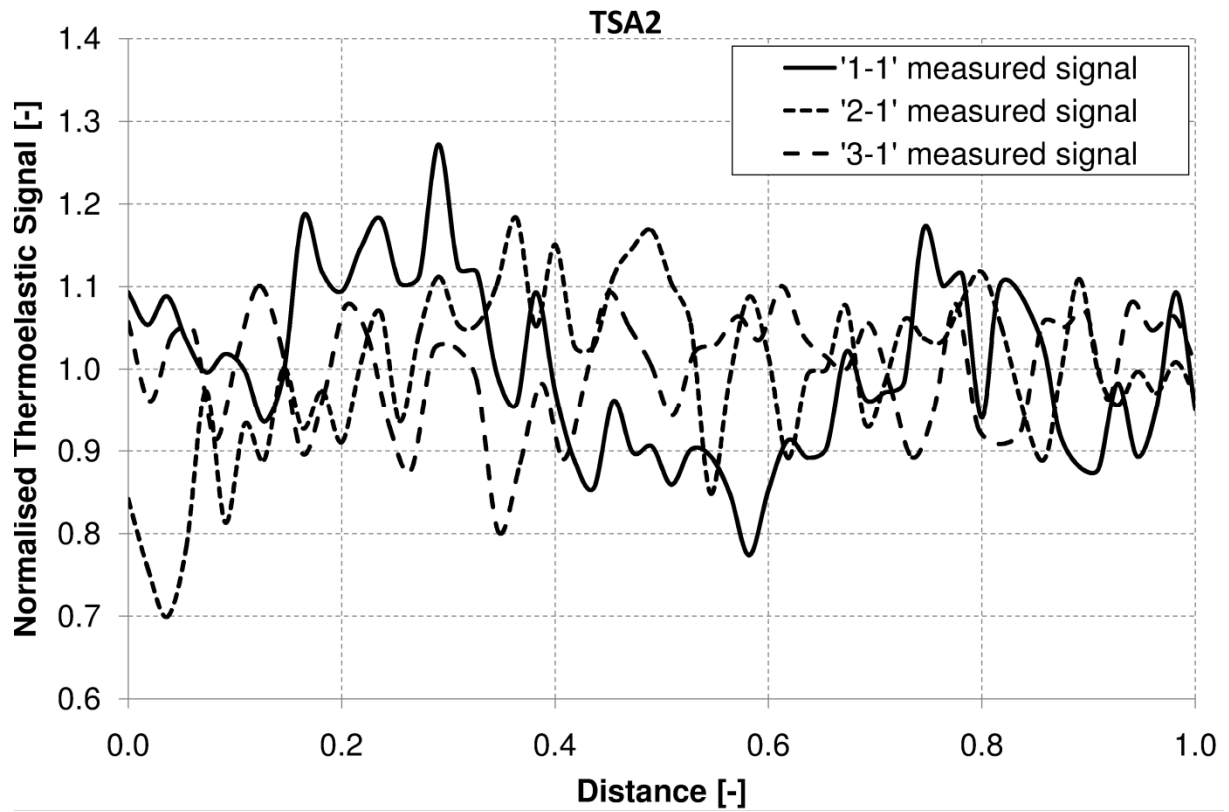
Figure 48: Normalised Thermoelastic Signal of Specimen TSA2 in X-Direction
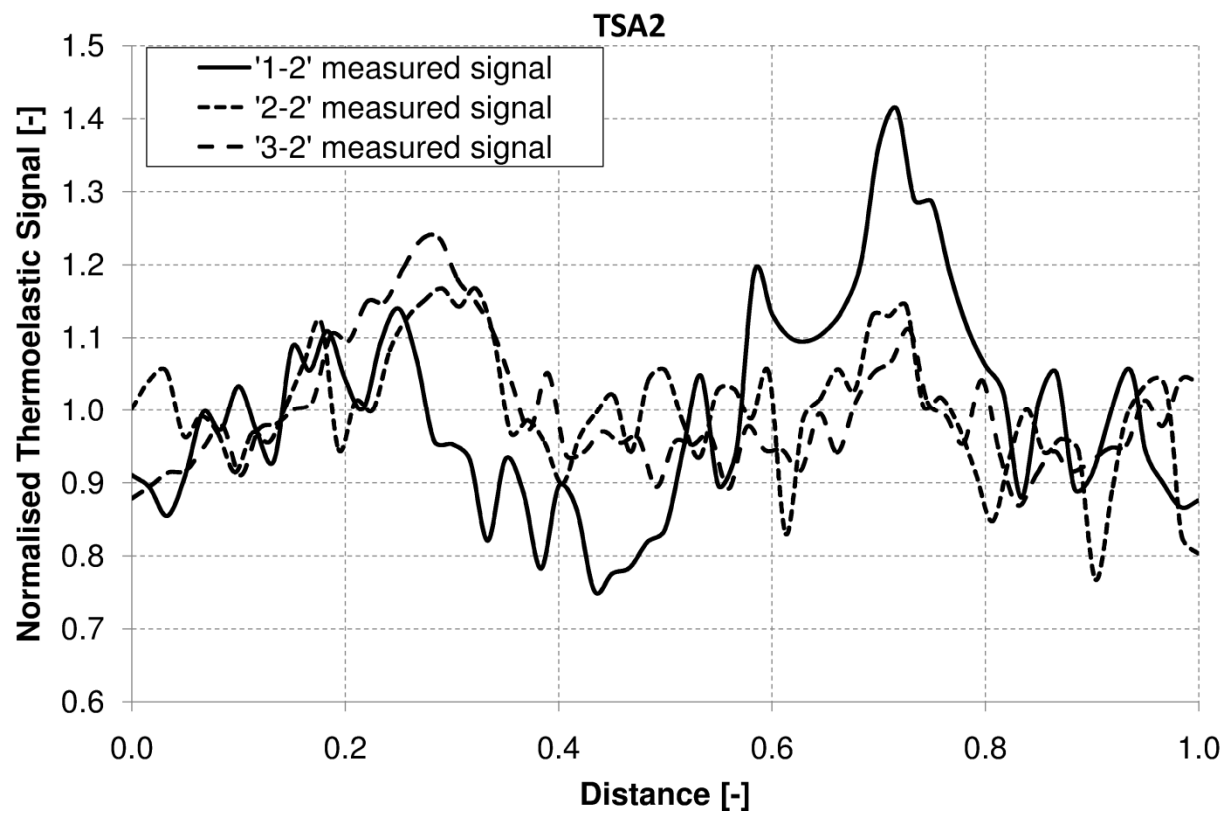
Figure 49: Normalised Thermoelastic Signal of Specimen TSA2 in Y-Direction
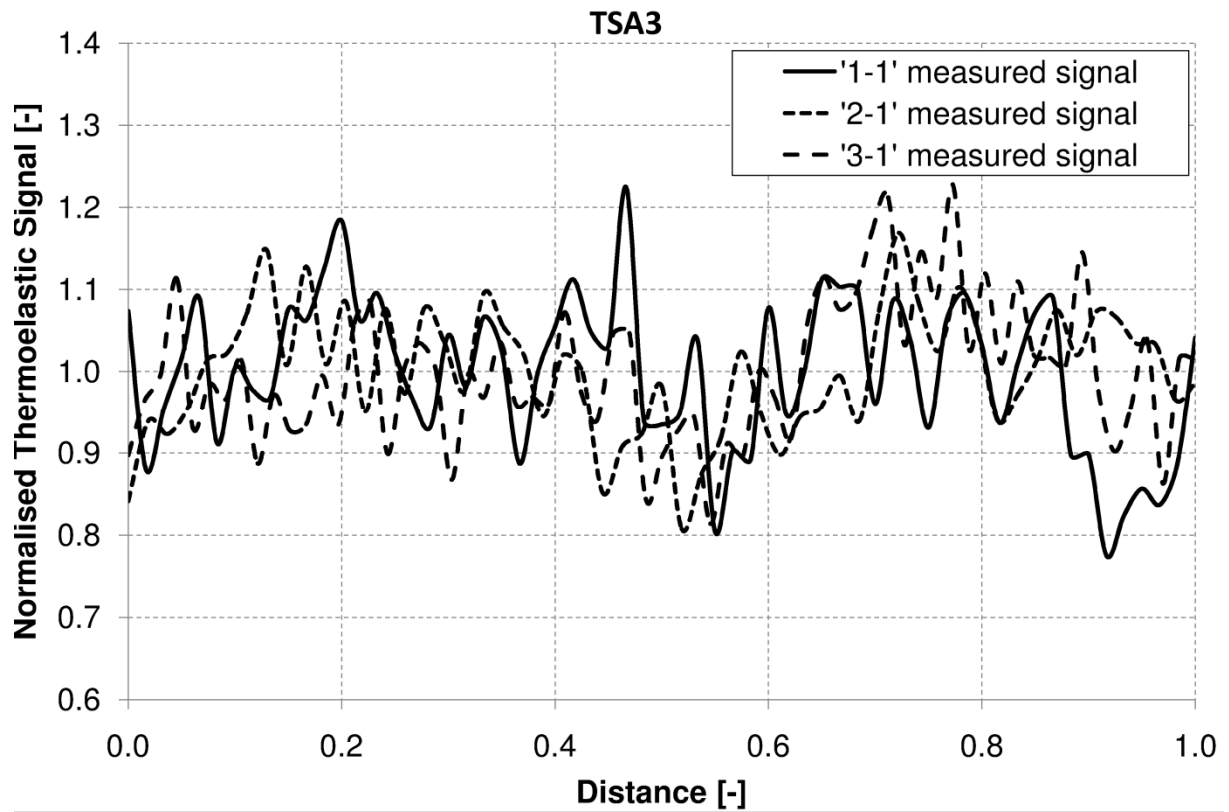
Figure 50: Normalised Thermoelastic Signal of Specimen TSA3 in X-Direction
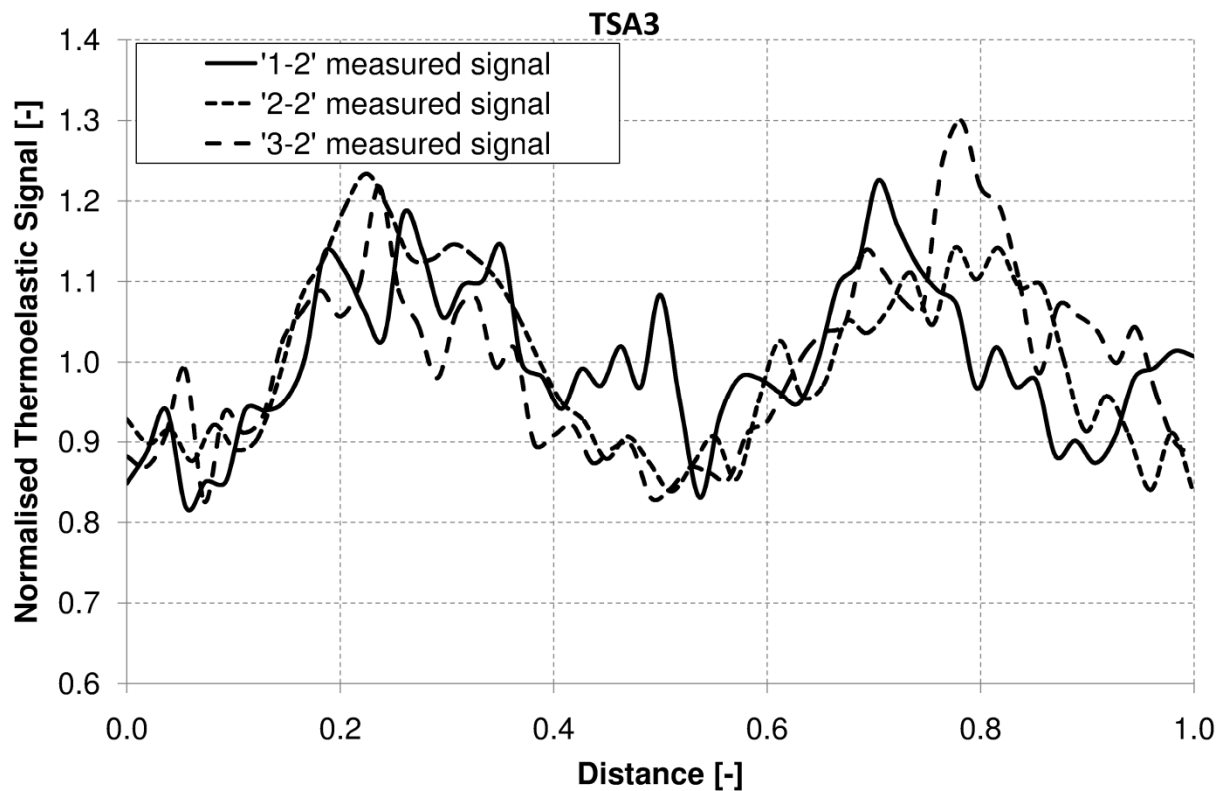
Figure 51: Normalised Thermoelastic Signal of Specimen TSA3 in Y-Direction

In order to identify a trend in the data and to a certain extent filter out the signal noise, a polynomial function, as shown in equation 5-3, is fitted through all data points in a certain direction using a least square algorithm build into EXCEL. To achieve the best fit the highest order polynomial function, which was sixth order, available in EXCEL was used. The resulting polynomial coefficients are listed in Table 5 and the resulting polynomials shown in Figure 52 for the X-direction and Figure 53 for the Y-direction.

$$f(x) = a_6 x^6 + a_5 x^5 + a_4 x^4 + a_3 x^3 + a_2 x^2 + a_1 x + a_0 \qquad (5\text{-}3)$$

	a_6	a_5	a_4	a_3	a_2	a_1	a_0
X - Direction	67.49	-204.04	228.26	-144.03	23.494	-1.119	0.9476
Y - Direction	107.07	-318.56	351.09	-174.78	37.807	-2.652	0.9964

Table 5: Coefficients for Polynomial Fit through Thermoelastic Signal Data Points
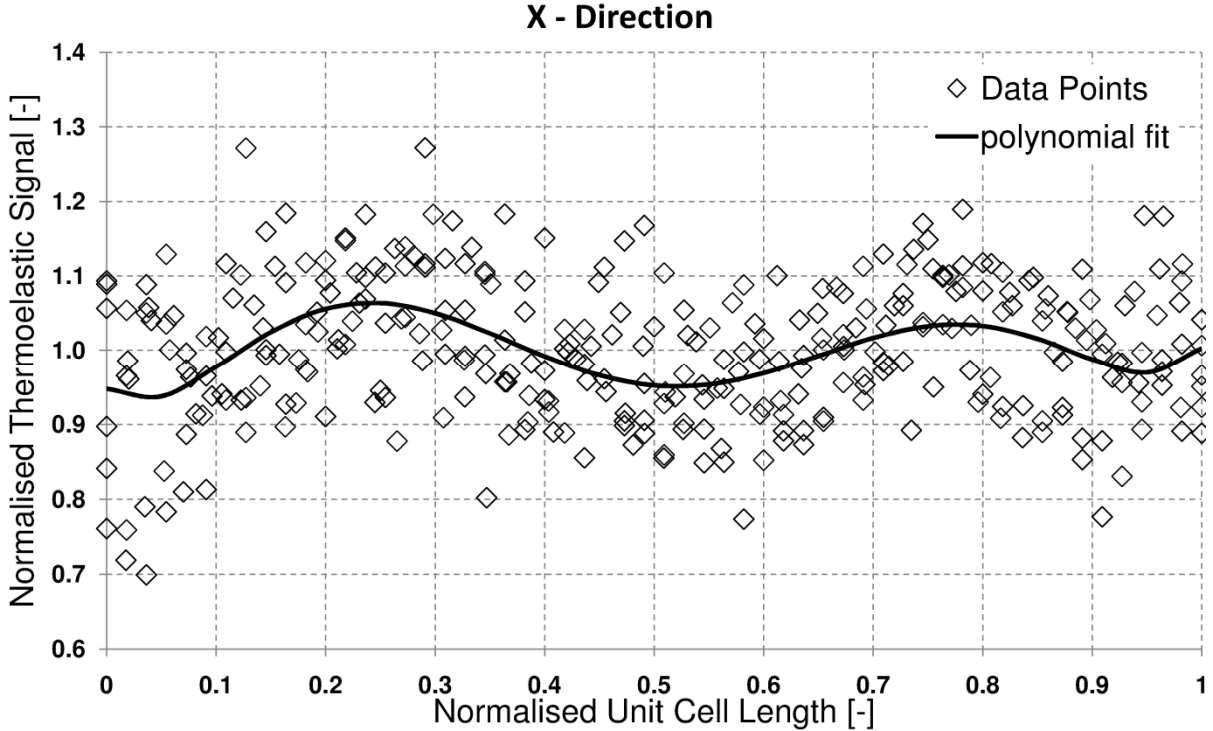
Figure 52: Normalised Thermoelastic Signal Plot with Polynomial Fit in X-Direction
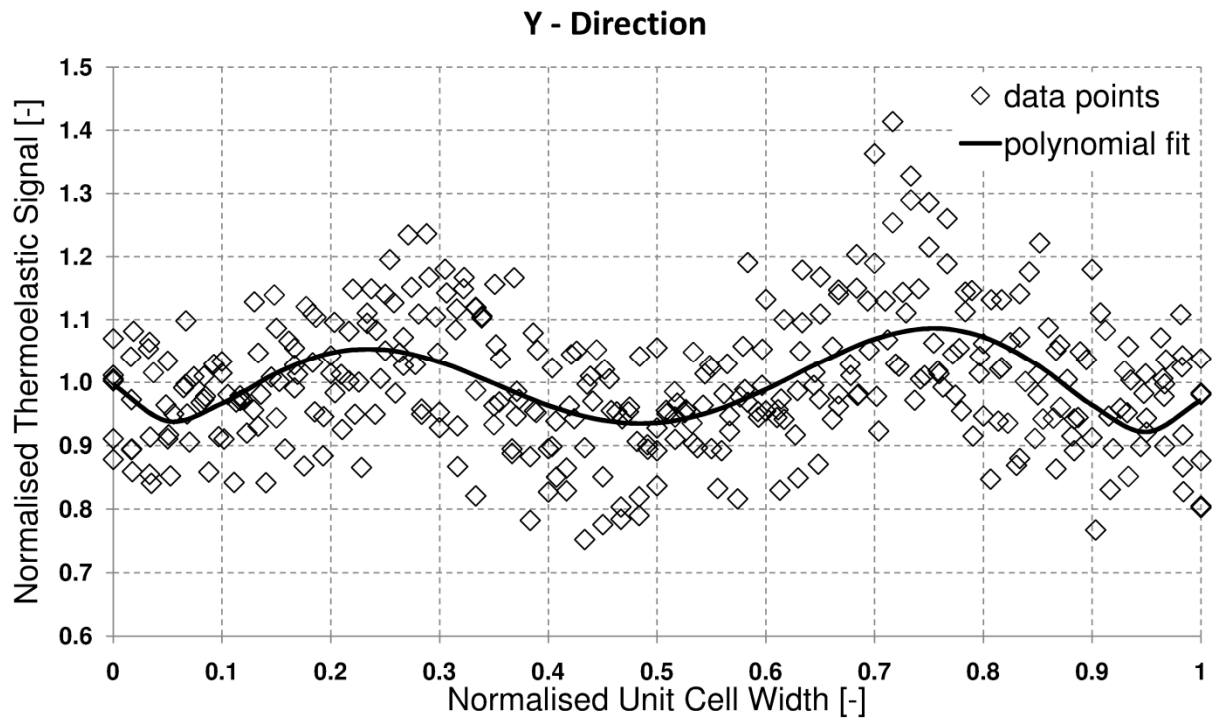
Figure 53: Normalised Thermoelastic Signal Plot with Polynomial Fit in Y-Direction

5.4 Summary

The measured thermoelastic signal distribution is similar to that shown by Frühmann [103] with distinct "hot spots" in both warp and weft direction. These "hot spots" can be identified in the polynomial fit to the thermoelastic response shown in Figure 52 and Figure 53. Since the thermoelastic signal can be directly related to mechanical stress, its distribution is the same as the stress distribution. Therefore, the sixth order polynomials used to identify trends in the thermoelastic signal from the test specimens can be used for comparison with the stress distribution predicted by the numerical models in Chapter 7 to validate the prediction.

6 Tensile and Shear Test

In order to validate the numerical model results, material specimens were tested under tensile and shear loading: The resulting experimentally measured stress – strain data are compared with numerical model predictions in Chapter 7.

6.1 Specimen Preparation

Both tensile and shear test specimens were cut from the laminate, which has been described in detail in Chapter 3, according to ASTM D3039 [111]. Tensile test specimen were cut in the warp direction of the benchmark laminate, shear test specimen at a 45° angle between warp and weft fibre. However, early tests showed premature failure of the specimen due to local stress concentrations at the gripping points (Figure 54). Therefore preliminary tests were conducted with different specimen shapes in order to achieve a fracture in the centre part of the specimen.
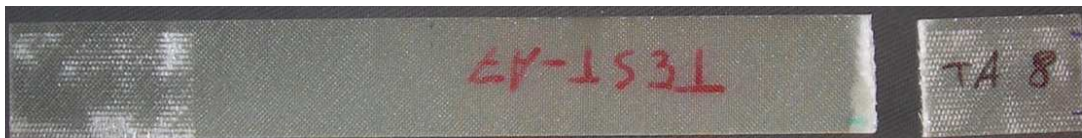
Figure 54: Fractured Test Specimen According to ASTM D3039

In order to reduce local stresses at the gripping point, rectangular aluminium tabs, 50 mm long and 25 mm wide, were bonded to the ends of the specimens using Araldite. When the specimen still failed prematurely near the grips (Figure 55), the geometry was changed to a shape according to BS 2782-10 [121].

Figure 55: Fractured Test Specimen According to ASTM D3039

Further changes were made when the specimen failed again prematurely, this time at the shoulder of the specimen (Figure 56).

Figure 56: Fractured Test Specimen According to BS2782-10 With Tabs

Instead of a low radius shoulder and a constant width section, a so-called dogbone shape specimen was used. The specimens' width decreases with a constant radius towards the middle of the length of the specimen, where the cross-section is the smallest. The geometry of this specimen is shown in Figure 57. Tabs were not required for these specimens, as the desired failure now occurred at the smallest cross section away from any stress concentrations due to clamping pressure by the grips (Figure 57).

Figure 57: Fractured Dogbone Specimen

In the actual tests, strain was measured using strain gauges. Following recommendations made by Lang and Chou [122] strain gauges with gauge lengths larger than a single unit cell were bonded to the specimens.

For the tensile load case a 45° strain gauge rosette was bonded to the point of smallest width of the tensile test specimens (Figure 58) following the guidelines set out in ASTM E1237 – 93 [123].
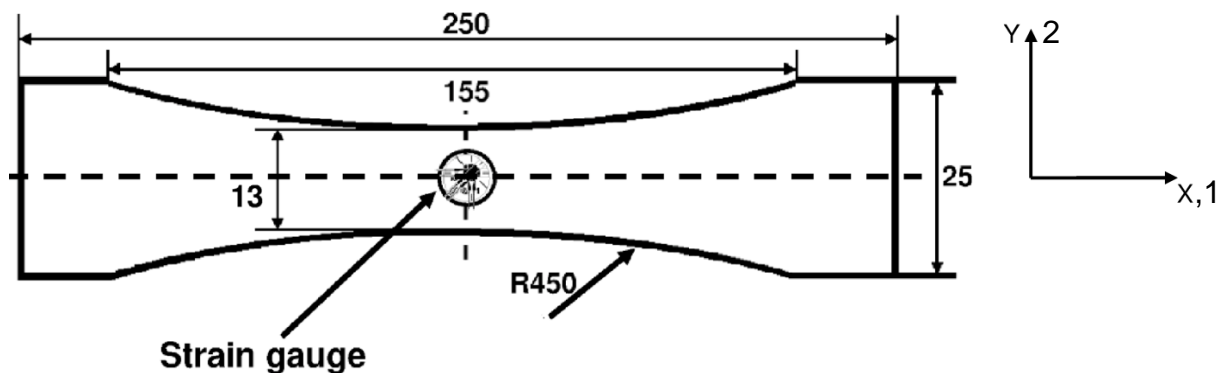
Figure 58: Test Specimen Geometry and Strain Gauge Positions for Tensile Test

The specimen surface was first cleaned and then slightly roughed using fine sanding paper before adhesive was applied. Gauge directions were named with subscript xx in the axial direction meaning the direction that load is applied on the dogbone specimen, subscript yy in the direction transverse and in-plane to the loading and subscript xy for the direction 45° between axial and transverse direction. The strain gauges used were UFRA-5-11-3L with 3m-long integrated lead wires from TML.

For the shear tests two linear strain gauges, FLA-6·350-23 with a gauge length of 6 mm from Tokyo Sokki Kenkyujo CO, LTD, were used in the positions and orientations shown in Figure 59. Bonding the gauges was done using the same procedure already used for the strain gauge rosette. Subscripts for the gauge directions remained xx for the load direction and yy for the transverse direction, even though fibre orientation was rotated 45° compared to the tensile tests.
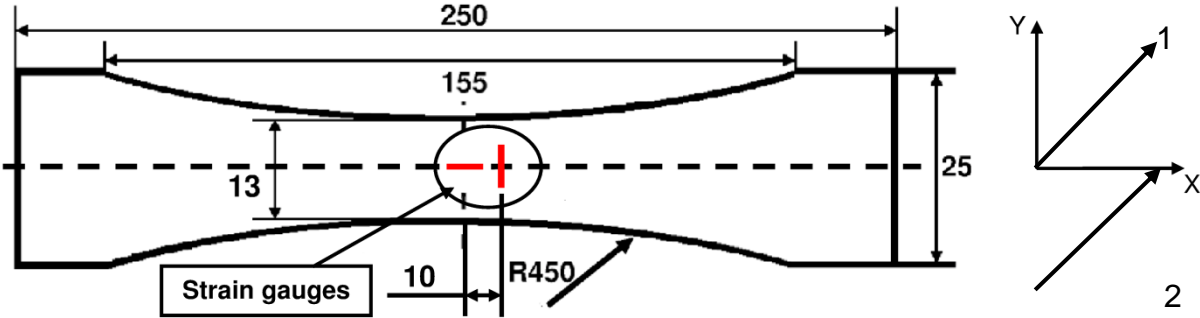
Figure 59: Test Specimen Geometry and Strain Gauge Positions for Shear Test

6.2 Tensile and Shear Test Methodology

Tests were conducted according to ASTM D3039 [110] for the tensile load case and ASTM D3518 [111] for the shear load case. During the tests loads were applied using an INSTRON 5500R-6025 testing machine (Figure 60). The machine's cross head speed was set to 2 mm/min to ensure quasi-static loading.

Strain gauge values, machine crosshead displacement and load cell output were recorded with a National Instruments cDAQ 9172 data acquisition system using the NI 9219 strain measurement and NI 9205 Analog Output Modules, with LabView Express as a signal processing software. The data for each test was written to a separate text file, which was then imported using EXCEL for postprocessing.

Figure 60: INSTRON 5500R-6025 universal testing machine

6.3 Data Postprocessing

Principal normal and shear stresses σ_1, σ_2 and τ_6 in the specimens were calculated by dividing the forces P_{axial} measured from the load cell by the smallest cross sectional area $A_{specimen}$ of the specimen (32.5 mm^2). For the tensile tests equation 6-1 was used, and for the case of shear tests equation 6-2 was used. Principal strains ε_1, ε_2 and γ_6 could be calculated from the measured strain data ε_{xx} and ε_{yy} using equations 6-3 and equation 6-4 for tensile and shear strain respectively. Stress-strain curves were plotted using EXCEL.

$$\sigma_1 = \frac{P_{axial}}{A_{specimen}} \tag{6-1}$$

$$\tau_6 = \frac{P_{axial}}{2A_{specimen}} \tag{6-2}$$

$$\varepsilon_1 = \frac{1}{2}\left(\varepsilon_{xx} + \varepsilon_{yy}\right) + \frac{\sqrt{2}}{2}\sqrt{\left(\varepsilon_{xx} - \varepsilon_{xy}\right)^2\left(\varepsilon_{xy} - \varepsilon_{yy}\right)^2}$$

$$\varepsilon_2 = \frac{1}{2}\left(\varepsilon_{xx} + \varepsilon_{yy}\right) - \frac{\sqrt{2}}{2}\sqrt{\left(\varepsilon_{xx} - \varepsilon_{xy}\right)^2\left(\varepsilon_{xy} - \varepsilon_{yy}\right)^2} \tag{6-3}$$

$$\gamma_6 = \varepsilon_{xx} - \varepsilon_{yy} \tag{6-4}$$

A third-order polynomial was fitted to the stress – strain curves resulting from the tensile tests (Figure 62 to Figure 64). No single function could be fitted to the stress – strain curves resulting from the shear tests. Therefore the curves were split into two parts, with a linear function fitted through the first part, up to 0.01 strain, and a natural log function through the remaining part (Figure 74 and Figure 75). The averaged stress-strain curves were calculated using the averaged polynomial, linear and logarithmic coefficients respectively. Stress values were calculated for an interval of set strain data. The resulting stress values were subtracted from the averaged stress - strain curve and the highest absolute difference values were used to establish the upper and lower bounds of the experimental range.

6.4 Tensile Test Results

6.4.1 Damage and Fracture Characterization

Figure 61 shows the tensile test specimens after fracture. All show the same type of fracture, perpendicular to the loading direction with a small step, meaning small areas of delamination can be observed near the fracture zone. However, during testing no delamination was observed before catastrophic failure of all specimens, suggesting that the delamination observed after failure is due to local shear stress peaks during catastrophic failure.

Figure 61: Fracture of Tensile Test Specimen

Experimental analyses by Daggumati et al [116],Callus et al [124], Gao et al [27], Lomov et al [25] and Pochiraju and Chou [31] showed that woven laminates with similar architectures fracture in the same manner. Damage initiates at the weft tow – matrix interface and propagates perpendicular to the loading direction leading to tow straightening after the entire matrix has failed and eventually total failure when tow

failure strains are reached. Pochiraju and Chou [31] also observed similar types of fracture surfaces for 3D woven composites loaded in tension.

6.4.2 Stress – Strain Results

A summary of the tensile test results, including the averaged stress – strain curves as well as the upper and lower bounds are shown in Figure 68. A similar summary is plotted for transverse strain against axial strain in Figure 69. Averaged curves are calculated by fitting standard polynomials to each individual curve and averaging the resulting polynomial factors.

In order to calculate an averaged stress-strain curve for comparison with numerical results standard mathematical functions were fitted to the experimental curves using EXCEL's automated fitting functionality. In case of the tensile test results third-order polynomials, $f(x) = a_3x^3 + a_2x^2 + a_1x + a_0$, were used. The polynomial parameters resulting from the fits are listed in Table 6. Figure 62, Figure 63 and Figure 64 show the individual measured stress - strain curves and the functions fitted through them. The fits agree very well with the actually measured stress – strain curves with mean average differences lower than 1% for every curve.

Specimen	a_0	a_1	a_2	a_3
tension1	1.83	20,134	-254,082	2×10^6
tension2	2.76	22,232	-373,201	6×10^6
tension3	-14.45	25,508	-503,839	9×10^6
tension4	0.84	22,564	-244,101	2×10^6
tension5	0.18	22,682	-337,341	5×10^6
tension6	1.00	22,216	-313,668	3×10^6
tension7	1.11	21,791	-286,549	3×10^6
tension8	0.82	21,963	-259,396	2×10^6
tension9	1.12	21,042	-253,977	2×10^6
mean average	0.0765	21,999	-274,763	4.25×10^6

Table 6: Polynomial Parameters of 3rd Order Polynomials Fitted to Tensile Stress-Strain Curve

As can be seen in Figure 62, there is an offset of about 0.00057 axial strain of the experimentally measured stress-strain curve for tension specimen 3. This offset results in a value of -14.45 for the a_0 polynomial parameter in the fit for this specimen, which means an offset of -14.45 MPa along the stress axis at zero strain, which is about 5% of a failure stress of 300 MPa. Since the a_0 polynomial parameter dominates the polynomial results for low strain values the fit for specimen 3 is ignored when the mean averages of the fitted polynomial parameters are calculated.
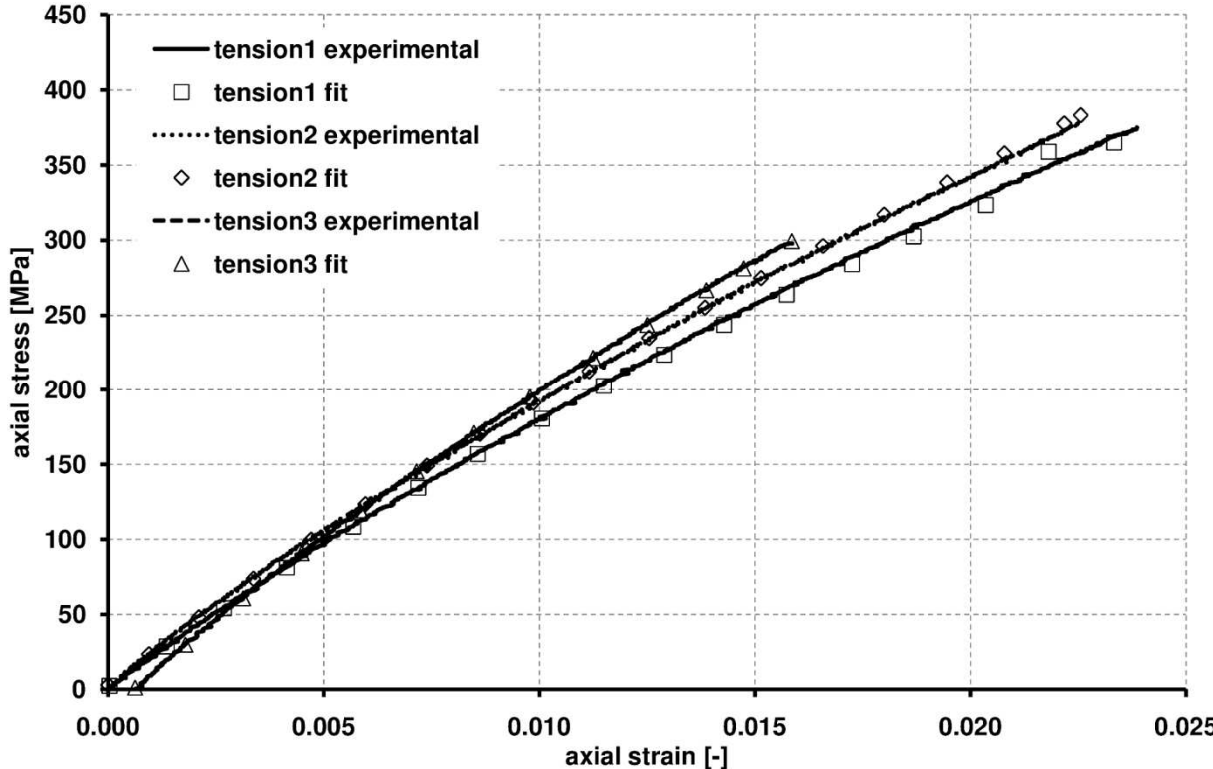
Figure 62: Comparison of Experimental and Fitted Stress-Strain Curve for Specimen tension1 to tension3
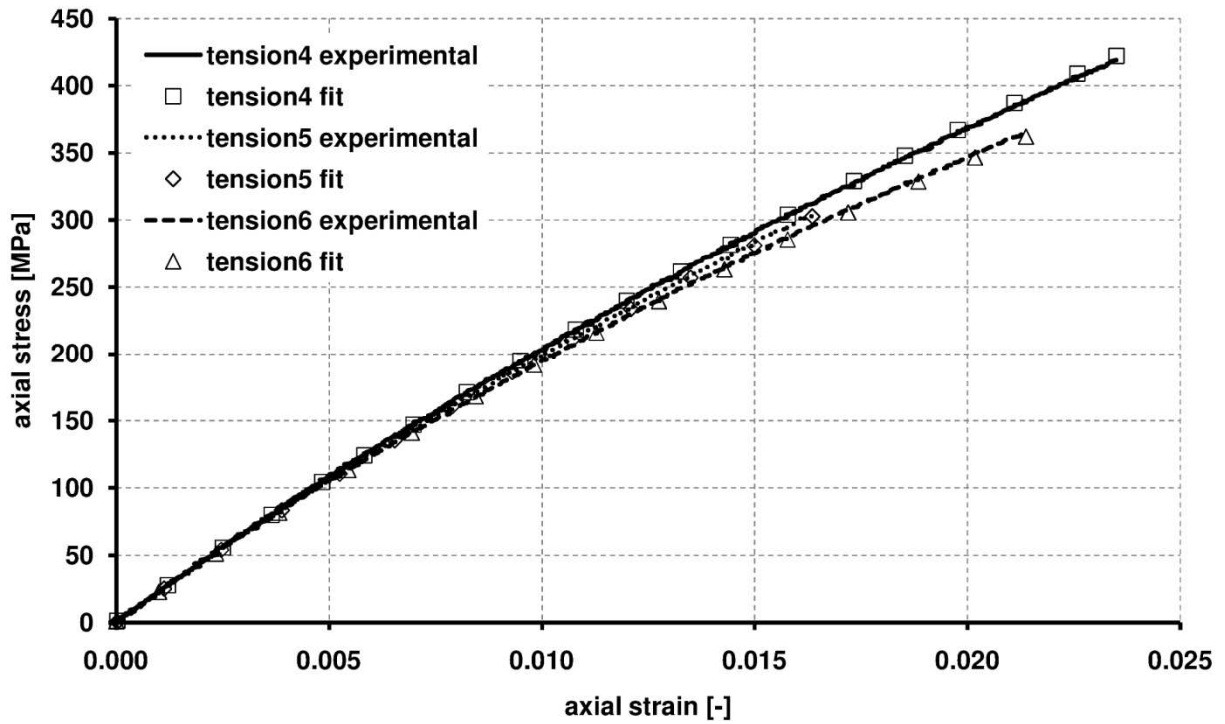
Figure 63: Comparison of Experimental and Fitted Stress-Strain Curve for Specimen tension4 to tension6
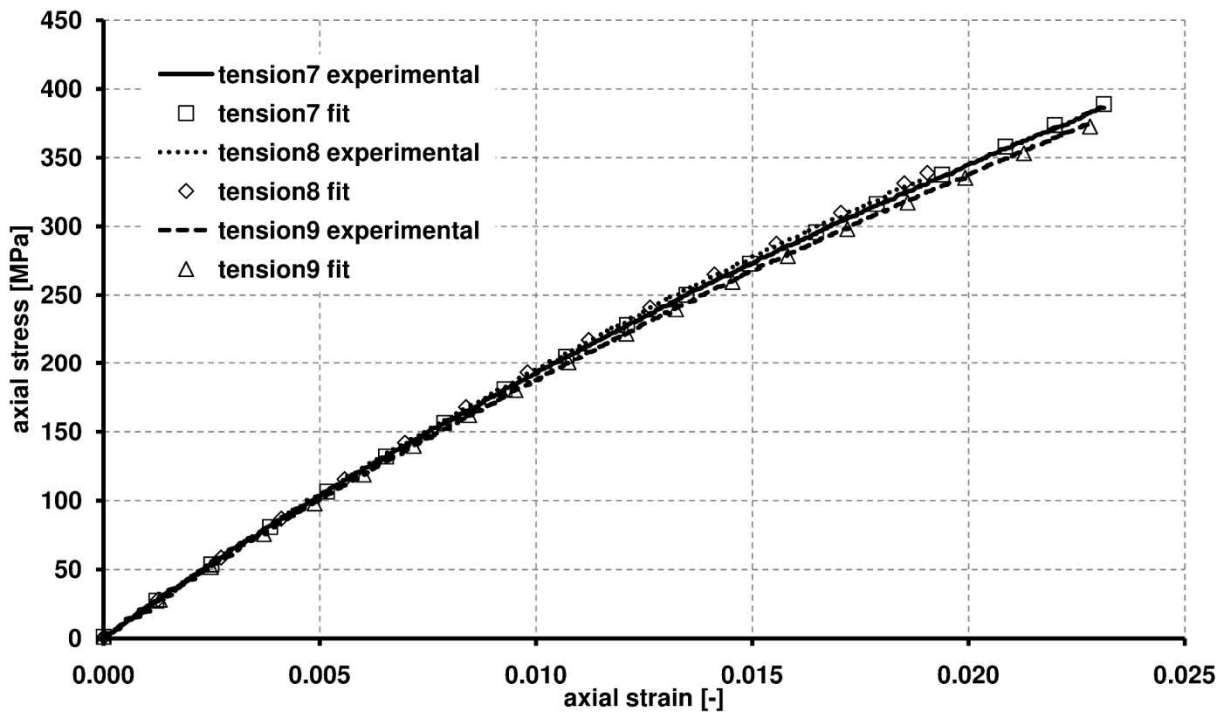
Figure 64: Comparison of Experimental and Fitted Stress-Strain Curve for Specimen tension7 to tension9

The averaged axial strain – transverse strain curve is calculated in a similar manner to the averaged stress – strain curve by fitting standard mathematical functions to the

experimental curves using EXCEL's automated fitting functionality. In the case of the transverse strain results second-order polynomials, $f(x) = a_4x^2+a_5x+a_6$, were sufficiently accurate to represent the experimental data. After the fit was done it was discovered that the offset factor a_6 is always equal to zero, it is therefore not included in the polynomial parameters listed in Table 7. Figure 65, Figure 66 and Figure 67 show the individual stress - strain curves and the fitted functions. Although the axial strain - transverse strain curve is noisier than the stress – strain curve, the fits agree very well with the measured axial strain – transverse strain curves with the mean average differences lower than 1% for every curve.

specimen	a_4	a_5
tension1	3.043	-0.141
tension2	3.018	-0.114
tension3	1.974	-0.145
tension4	3.378	-0.155
tension5	3.410	-0.132
tension6	3.094	-0.130
tension7	2.978	-0.140
tension8	3.113	-0.146
tension9	3.186	-0.142
average	3.022	-0.138

Table 7: Polynomial Parameters of 2nd Order Polynomials Fitted to Shear Stress-Strain Curve
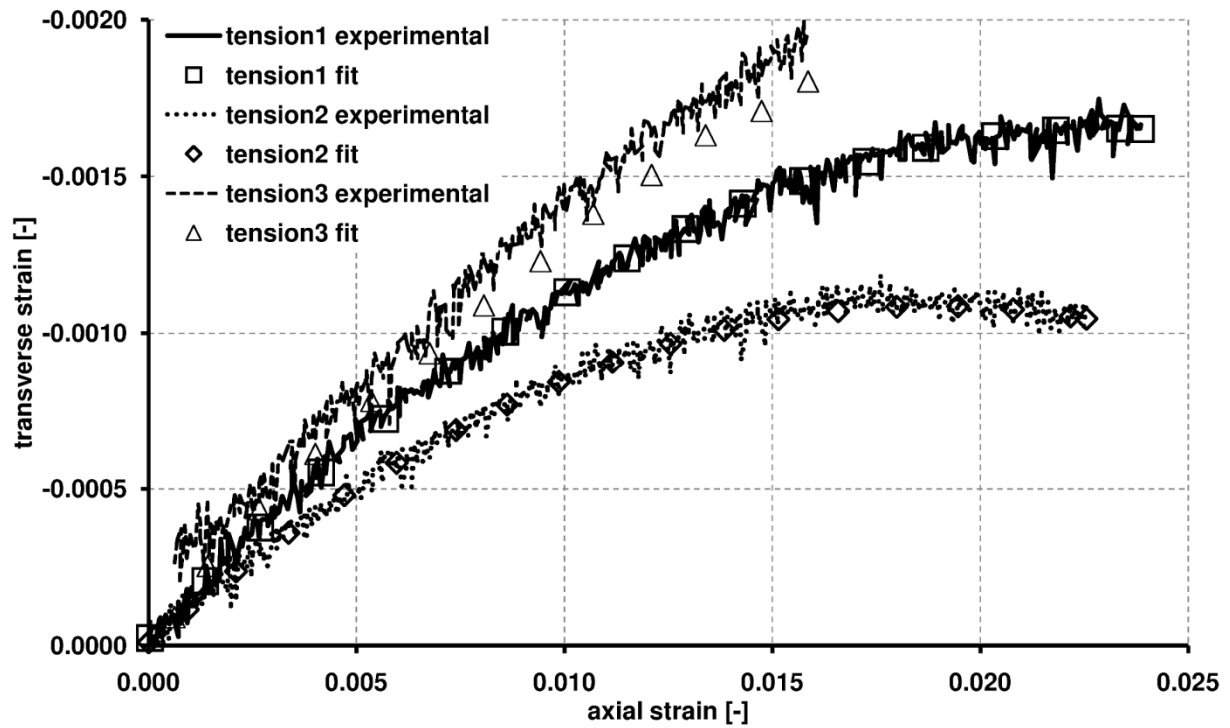
Figure 65: Comparison of Experimental and Fitted Axial Strain- Transverse Strain Curve for Specimen tension1 to tension3
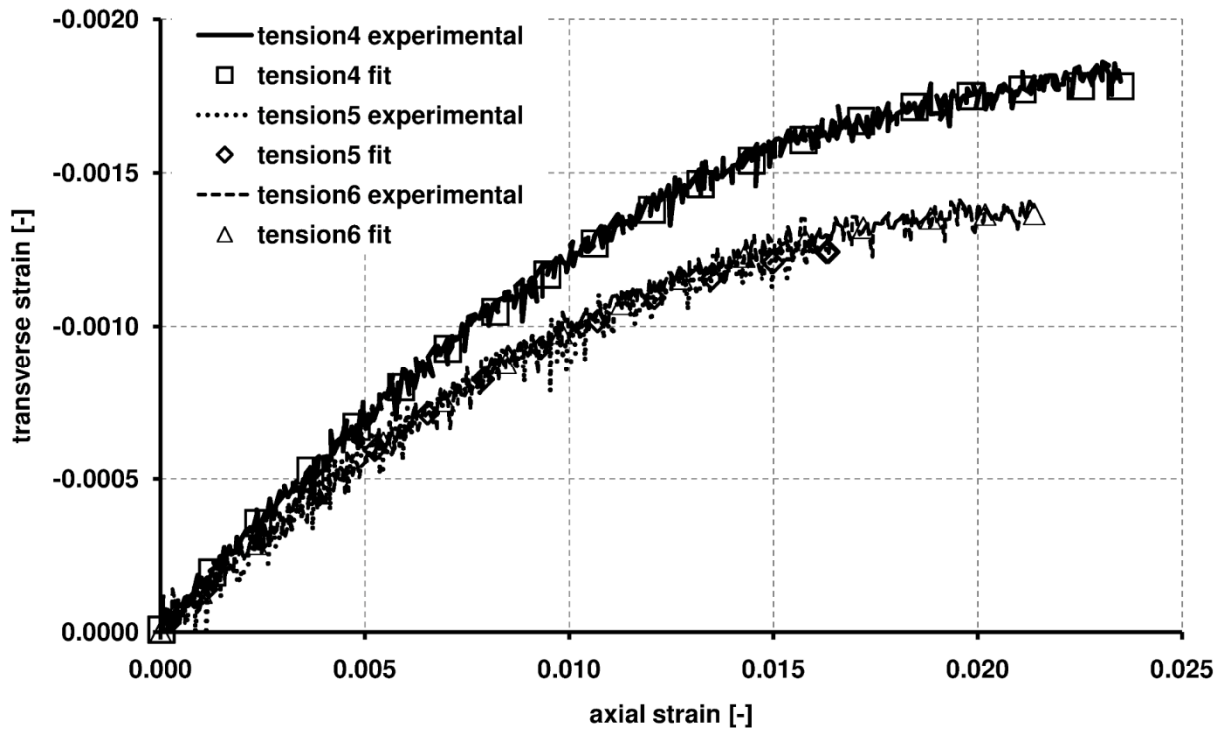
Figure 66: Comparison of Experimental and Fitted Axial Strain- Transverse Strain Curve for Specimen tension4 to tension6
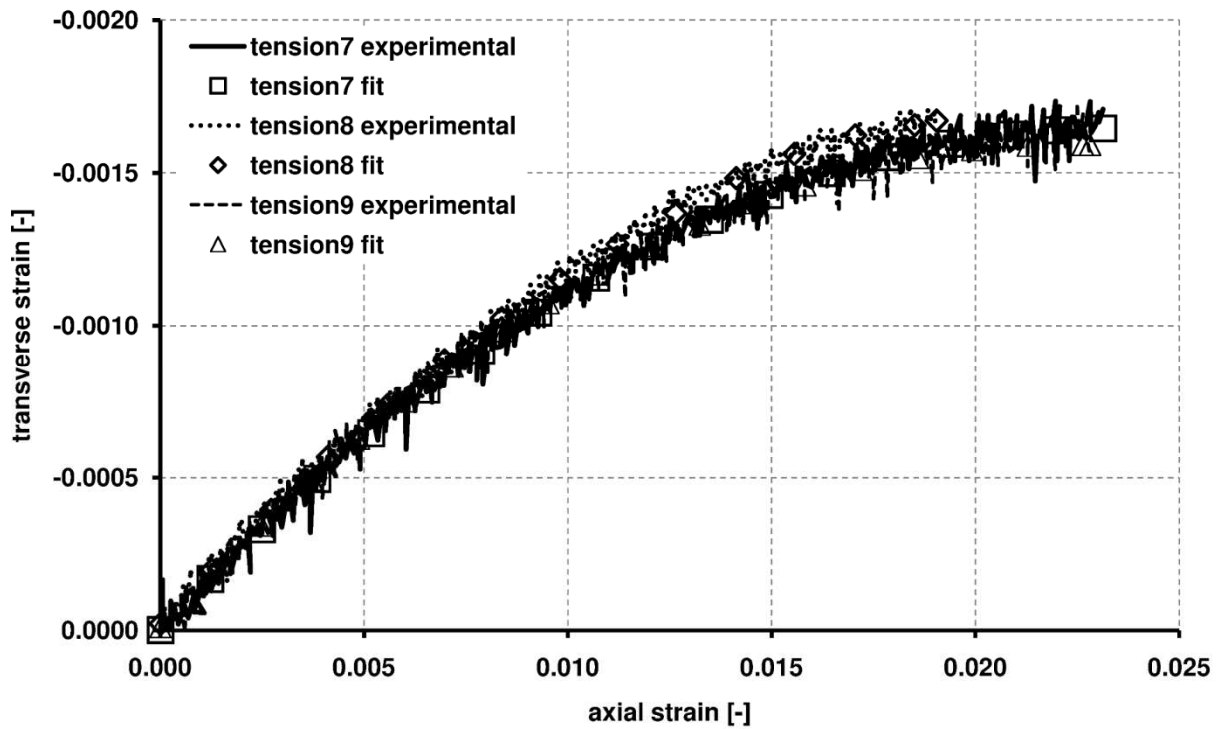
Figure 67: Comparison of Experimental and Fitted Axial Strain- Transverse Strain Curve for Specimen tension7 to tension9
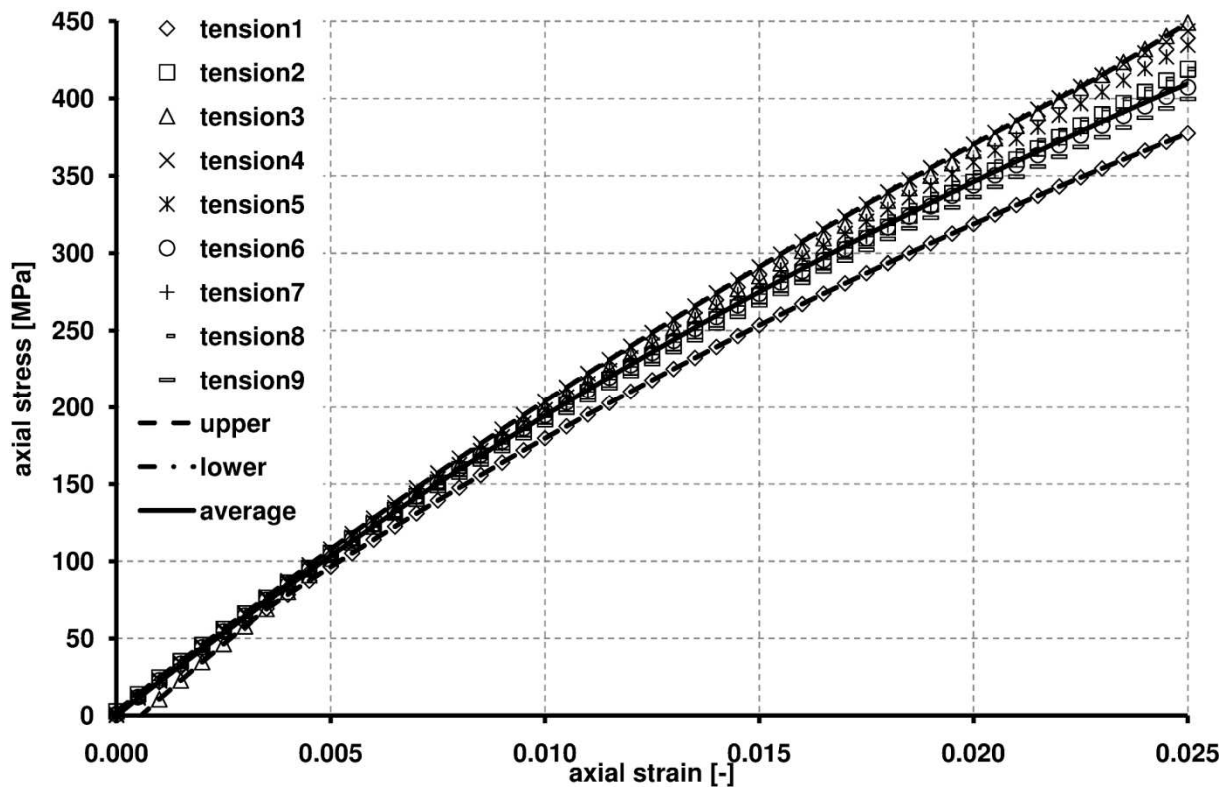
Figure 68: Axial Stress vs Axial Strain
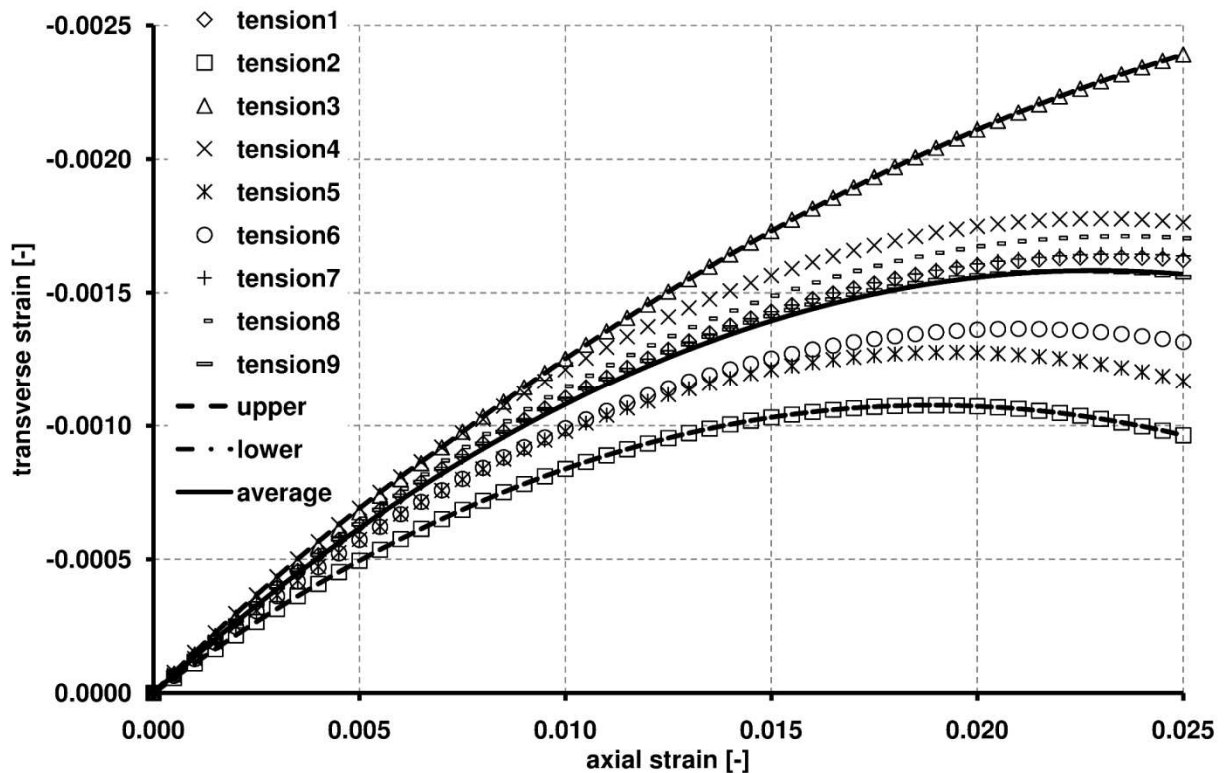
Figure 69: Transverse Strain vs Axial Strain

Generally, the results clearly show nonlinear behaviour, which made it difficult to calculate elastic properties. Young's modulus E is defined as the slope of the stress-strain curve in the linear section, with two data points required to calculate the slope. Poisson's ratio is defined as the negative ratio of change of transverse strain and change of axial strain. However, results can depend on which points are chosen to calculate slope and stress and strain value deltas. Procedures on which data points to choose to calculate these properties are outlined in ASTM D3039 [110], ASTM E111-04 [125] and BS 2782-10 [121]. For this thesis the procedure given in ASTM D3039 [110] is used. It requires the smaller stress and transverse strain values to be taken at 1000 µε axial strain and the second value to be taken at 3000 µε axial strain [110] as is shown in Figure 70.
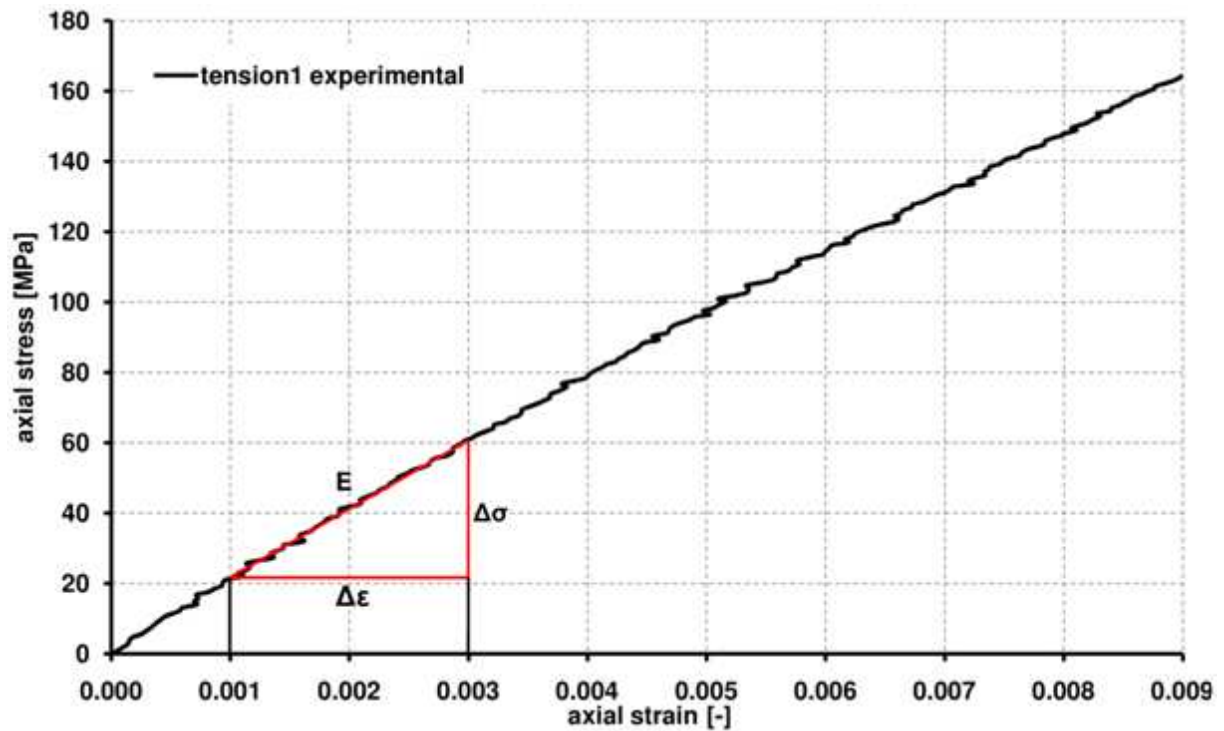
Figure 70: Procedure to Calculate Young's Modulus According to ASTM D3039 [110].

Using the procedure described above results in the mechanical properties shown in Table 8.

Specimen	E_{11} [GPa]	v_{12} [-]	failure strain [-]	failure stress [MPa]
tension1	16.14	0.267	0.0239	375
tension2	16.71	0.213	---	392
tension3	18.39	0.280	0.0212	298
tension4	18.24	0.290	0.0235	419
tension5	17.68	0.247	0.0239	---
tension6	17.00	0.245	0.0214	364
tension7	16.92	0.265	0.0231	386
tension8	17.36	0.277	0.019	335
tension9	16.65	0.268	0.0228	374
mean average	17.23	0.261	0.0224	368

Table 8: Averaged Measured Mechanical Parameters from Tensile Tests

On average, the laminate had a Young's modulus of 17.23 GPa and a Poisson's ratio v_{12} of 0.261. The values for Young's modulus, Poisson's Ratio and ultimate stress as well as strain are within the range expected for a two-dimensionally woven glass fibre epoxy laminate manufactured using vacuum assisted resin infusion, according to

Daniel and Ishai [126]. Values measured in the tensile tests in this thesis are below the values shown in Daniel and Ishai [126], which is due to the lower fibre volume fraction, which was between 39% and 40% compared to fibre volume fractions of 45% to 55% in Daniel and Ishai [126].

The nonlinear behaviour can be explained by the initiation and progression of matrix cracking as well as the behaviour of the constituent materials. In general, matrix material like the one used in the tensile and shear testing behaves visco-elastically [127], which results in nonlinear behaviour of the laminate [128]. Dry glass fibre tows can also show nonlinear stress-strain behaviour as shown by Bazhenov et al [128], which again affects the stress-strain behaviour of the laminate. Additionally, Cox et al [23] have described the straightening of carbon warp tows with increased loading to be plastic and therefore introducing additional nonlinearity in the stress – strain curve for carbon fibre. Though a similar phenomenon has not been described for glass fibre in the literature, the presence of a similar effect cannot be excluded.

The test results also show some variation for all mechanical parameters, generally the measured stress – strain curves vary about 7% about the mean on average, especially towards the end of the test. Measured axial strain – transverse strain curves vary even more, between -38.6% and 52.2% around the mean average at an axial strain of 2.5%. Young's Modulus varies from 16.14 GPa (-6.3%) and 18.39 GPa (6.7%). Failure stresses range from 298 MPa to 419 MPa, a variation of -19.0% to 13.9%. Although high, these variations are consistent with the amount of variation found in the literature [116]. The microscopic analysis (Chapter 4) showed a high amount of variation of tow paths and cross-sections within the laminate itself. Ivanov et al. [117] have demonstrated that the behaviour of individual unit cells, especially when it comes to crack initiation and propagation, is highly dependent on the local weave architecture, such as tow path and cross-sections within the unit cell as well as tow path and cross-section in the neighbouring cells. Some of these variations average out in the entire laminate but small differences between the different laminates manufactured, e.g. in local fibre volume fraction and tow orientation, can lead to substantial variations in resulting stress-strain data.

6.5 Shear Test Results

6.5.1 Damage and Fracture Characterization

Figure 71 shows the fracture of the shear test specimens. Unlike for the tensile test specimen, no microscopic data on damage initiation and progression is available in the literature. Therefore, it cannot be judged whether the type of fracture observed is typical for these kinds of samples. However, during the numerical simulation stress concentration points were found to be similar for both the tensile and shear tests (Chapter 5). This would suggest that damage in the shear tests initiates and propagates in a manner similar to the tensile tests, which was somewhat confirmed by the type of fracture shown by shear test samples Shear1, Shear2 and Shear3 (Figure 71). These specimens failed at an angle of about 45° to the direction of loading, which is the direction of the weft tows in the shear test. For specimen Shear4 however failure occurs at an angle much higher than 45° while Shear5 fails in the direction perpendicular to the loading direction (Figure 71). This somewhat arbitrary behaviour of the specimens would suggest that local variations of tow orientation significantly affect the direction of failure, which would be confirmed by large variations in the measured stress – strain curves. However, that was not the case as can be seen in the following section. Therefore, microscopic analyses of damage initiation and propagation should be conducted to learn more about the effect of local variations on the resulting fracture behaviour.
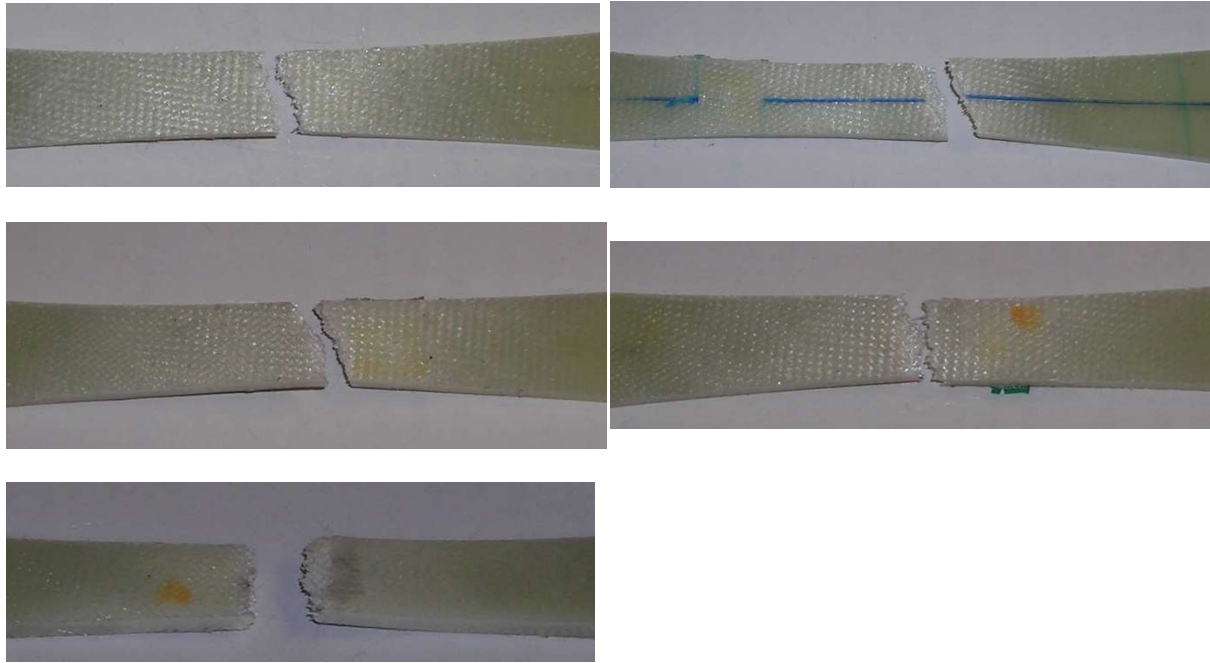
Figure 71: Fracture of Shear Test Specimen

6.5.2 Stress – Strain Results

During the shear testing the bond between strain gauges in the axial direction and the specimen failed, resulting in no reliable data being available for axial strains greater than 0.05, which can be seen in Figure 72. Therefore, all the following graphs only show stresses up to a principal shear strain of 0.1. However, the measured stress – strain curves at that stage already showed significant nonlinear behaviour so that a comparison with a numerical model predicting damage initiation and propagation is still sensible.
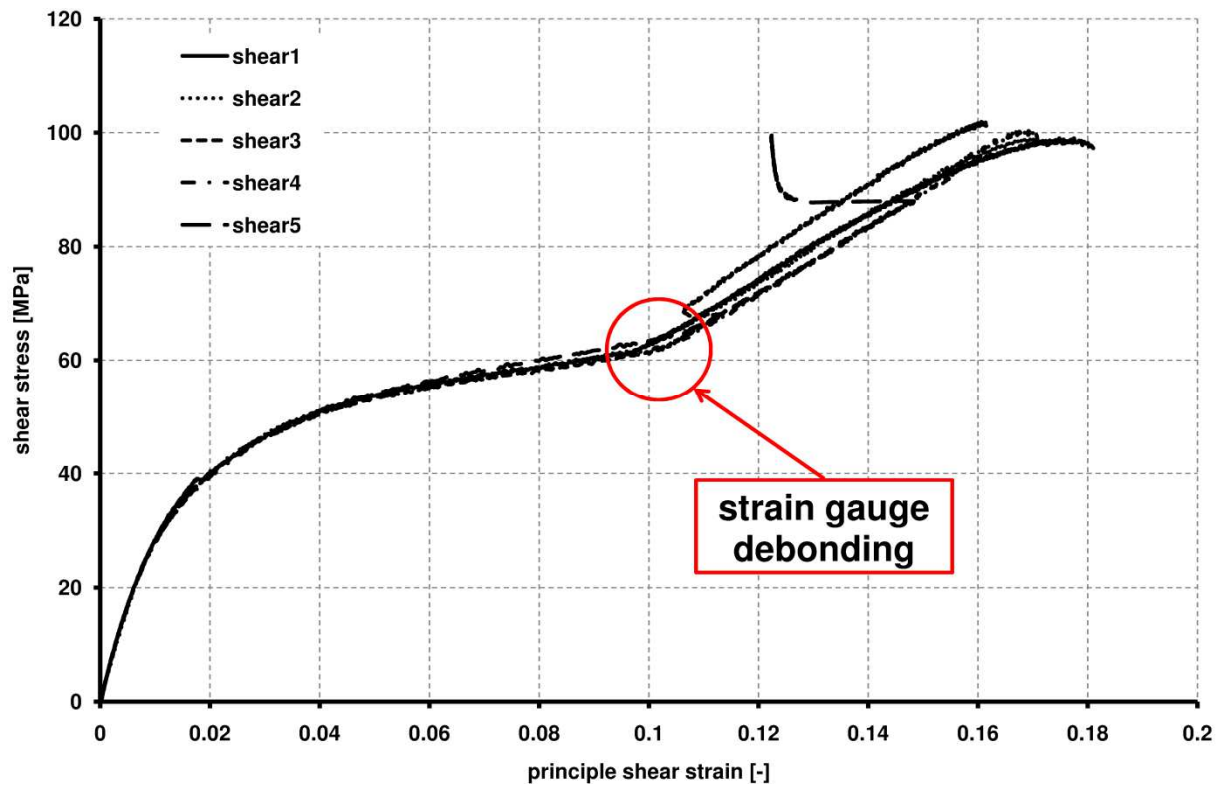
Figure 72: Shear Stress vs Principal Shear Strain Showing Strain Gauge Debonding

Figure 73 shows a summary of all shear tests, including averaged stress – strain curves as well as upper and lower bounds. The specimens behaved linearly for principal shear strains up to 0.005, after which the laminate starts behaving nonlinearly. Again this is most likely due to crack growth in the matrix and nonlinear constituent behaviour. A procedure to calculate elastic properties, similar to ASTM D3039 [110], is outlined in ASTM D3518 [111]. Shear modulus is defined as the slope of the shear stress - strain curve, which can be calculated using two data points. However, data points need to be chosen consistently since the choice of data points can affect results. Therefore, the standard requires the lower stress value to be taken at a strain value between 1500 µε and 2000 µε and the higher stress value at a strain value about 4000 µε higher than the lower strain value [111]. This procedure was used to calculate the shear modulus shown in Table 10, resulting in an averaged shear modulus of 3.14 GPa.
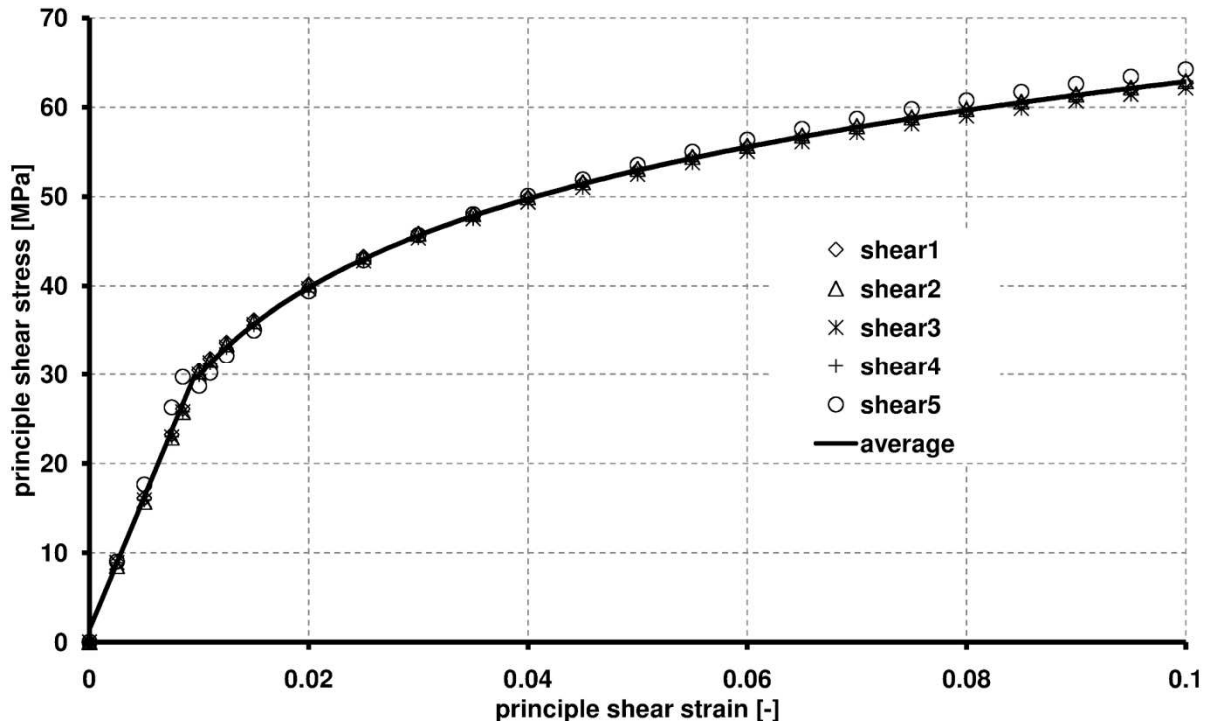
Figure 73: Shear Test Summary

Again in order to calculate an averaged stress - strain curve for comparison with numerical results functions were fitted to the experimental curves. For the initial part of the stress - strain curve, for principal shear strains of up to 0.005, a linear function was used, $f(x) = a_1x+a_0$. For strains greater than 0.005 a natural log function, $f(x) = b_1ln(x)+b_0$, was fitted to the stress - strain curve. The functions' parameters are listed in Table 9. Figure 74 and Figure 75 show the individual stress - strain curves and the fitted functions. The fits agree well with the measured stress – strain curves with mean average differences being about 11% in the worst and just under 3% in the best case. The higher difference compared to the tensile stress-strain curve fits is due to a lower quality fit at the point of change between the linear and log functions.

	a_0	a_1	b_0	b_1
shear1	1.816	2,860	94.91	13.99
shear2	1.332	2,877	95.54	14.17
shear3	1.837	2,821	94.26	13.95
shear4	1.721	2,832	94.75	14.08
shear5	0.418	3, 449	99.74	15.42
mean average	1.425	2,968	95.84	14.32

Table 9: Function Parameters for Linear and Natural Log Functions
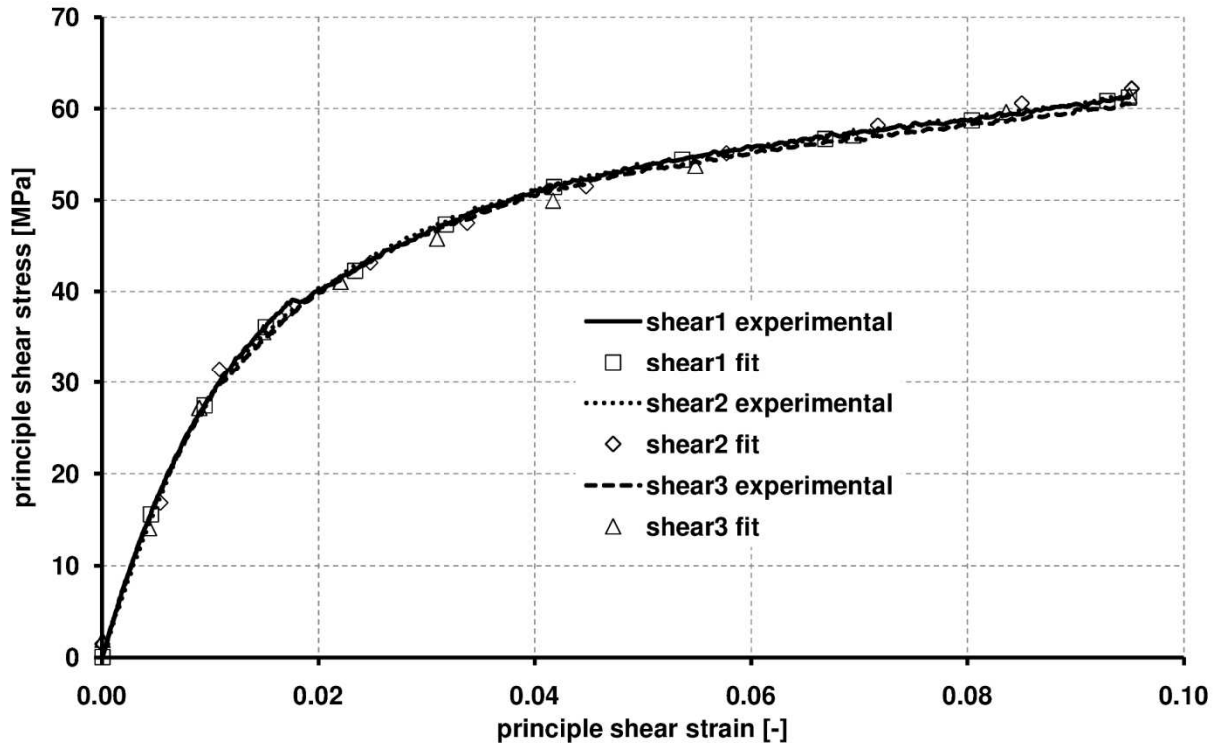
Figure 74: Comparison of Experimental and Fitted Stress-Strain Curve for Specimen Shear1
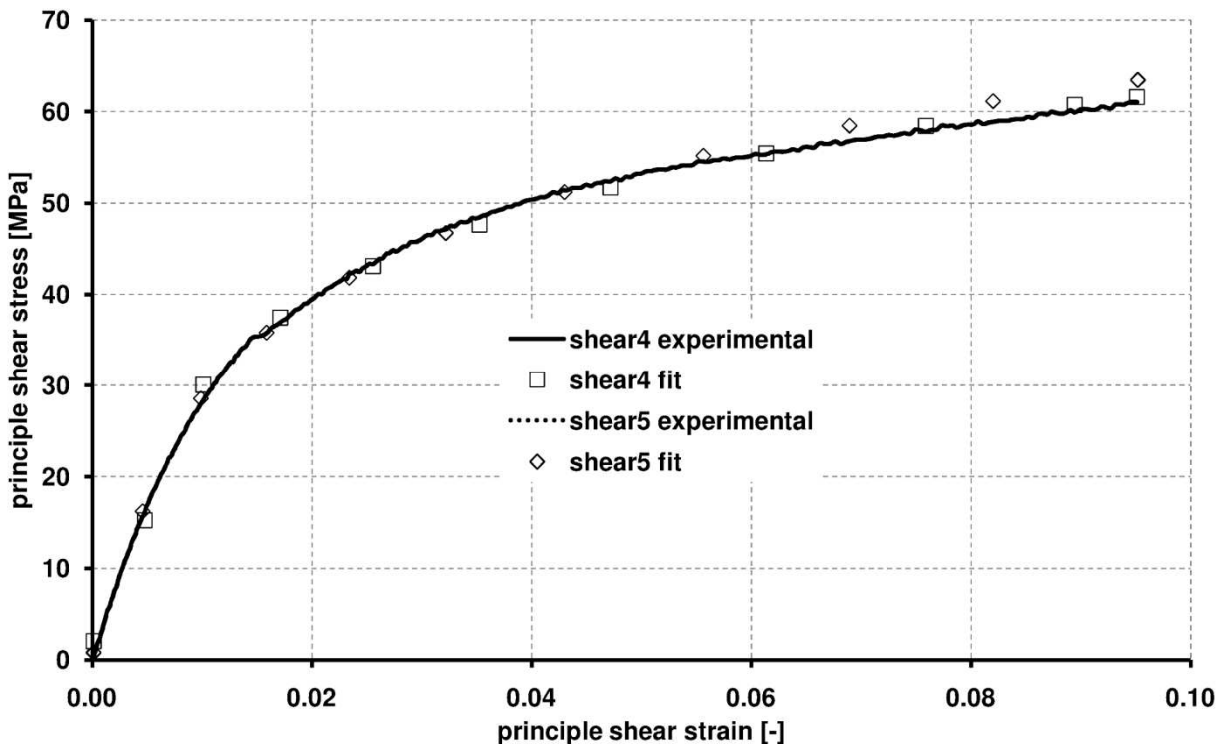
Figure 75: Comparison of Experimental and Fitted Stress-Strain Curve for Specimen Shear4 and Shear5

Specimen	G_{12} [GPa]
shear1	3.12
shear2	3.16
shear3	3.12
shear4	3.11
shear5	3.21
mean average	3.14

Table 10: Elastic Shear Properties

The level of variation in the shear stress-strain curves is lower than the variation shown in the tensile stress-strain curves, about 2% compared to 7% in the tensile stress-strain data, since in the lower shear strain range shear behaviour of the laminate is dominated by the matrix rather than the glass fibre weave.

6.6 Summary

Averaged stress – strain curves have been calculated in this chapter, giving a good summary of the measured stress – strain data. Overall the agreement between measured and fitted curves is very close with deviations between the two less than 5%. Therefore the averaged curves can be used for comparison with numerical model predictions for model validation in Chapter 7.

7 Numerical Analysis of Textile Composites

7.1 Full Finite Element Unit Cell Model

7.1.1 Modelling Procedure - Overview

A multi-scale approach has been used in this thesis to numerically model progressive damage. As was shown in the literature review (chapter 2) a number of ways are available to model a single unit cell on the meso-scale, namely the full finite element approach [55], [60], [62], [63] the voxel technique [79], [80] and the binary model [84]-[89]. Two of these approaches are used in this thesis. The single unit cell was modelled using the full finite element approach and the geometric parameters needed to generate the model were measured using a light microscope (chapter 4). An equivalent binary unit cell model was then defined, which replicated the stress - strain behaviour of the full finite element model. These equivalent binary model unit cells could then be used to model a macro-structure. In this thesis the macro-structure was the critical cross-section of a test specimen used in chapter 6 so that the stress-strain behaviour predicted by the model could be compared to the stress-strain behaviour measured for the benchmark laminate.

The geometry and subsequent mesh were generated using PATRAN, which was then used to create an ABAQUS/Standard input file. This input file was amended with a text editor to include material and section properties, boundary conditions and to define solver parameters as well as request output data. ABAQUS/Viewer and MetaPost were used for postprocessing, namely for visual results presentation and generating force and displacement data generation for further processing using EXCEL.

7.1.2 Unit Cell Geometry Definition

The first challenge when modelling a unit cell using a full finite element approach is to decide on the exact geometry of the unit cell. In the literature [14], [60], [62] the term unit cell is defined as the smallest part of a structure whose behaviour is representative of the behaviour of the macro-structure. This leaves a lot of freedom when choosing unit cell geometry.

A single cross-over of warp and weft tow was chosen as unit cell for ease of mesh generation and because of the relatively low computational resources required for modelling. Values for the major elliptical axis parameter and minor elliptical axis parameter as well as the sinusoidal tow path parameters, amplitude and wavelength, were measured in the microscopic analysis (chapter 4) and are summarised in Table 4. However, due to the statistical nature of the geometrical parameters, the resulting unit cell geometry cannot be simply mirror or rotated to form a structure of multiple unit cells. Since only one cell was modelled in detail and the output generated used to define a simplified cell it was more important for the cell to have the correct fibre volume fraction and tow curvature.

Another problem is the complex architecture of the unit cell. Especially the elliptical cross-section of the tows and the high thickness gradients of the matrix materials, which lead to difficulties during meshing resulting in high skew angles, high aspect ratios and sharp internal angles (Figure 76). The mesh quality can be somewhat improved by moving individual nodes, however due to the nature of the geometry an improvement in quality at one position can lead to a lower mesh quality in neighbouring regions.

The problem of high skew angles, high aspect ratios and sharp internal angles could also theoretically be resolved by either increasing the order of elements used to mesh the geometry or by refining the mesh locally. However, both these solutions come with high computational costs because mesh sizes quickly increase to over a million degrees of freedom for even simple problems [63]. Therefore, the presence of a number of elements with high skew angles, high aspect ratios or sharp internal angles are tolerated and models only refined to the point of convergence [55]. Again due to the complex geometry this can already result in large models with a high demand for computational resources. Whitcomb et al [62], Guagliano and Riva [63] and Tang and Whitcomb [129] have suggested exploiting symmetries within a unit cell to reduce the model size and therefore computational costs. However, this requires additional effort when applying boundary conditions, which can be complex for more complex states of loading of the macro-composite. Breaking down the unit cell into different parts for meshing can lead to misaligned meshes on the individual parts, which means artificial gaps can result when these meshes are combined,

which in turn leads to reduced global unit cell stiffness. Therefore, a detailed check of the final mesh should be conducted.

bad aspect ratio and sharp internal angles

bad aspect ratio
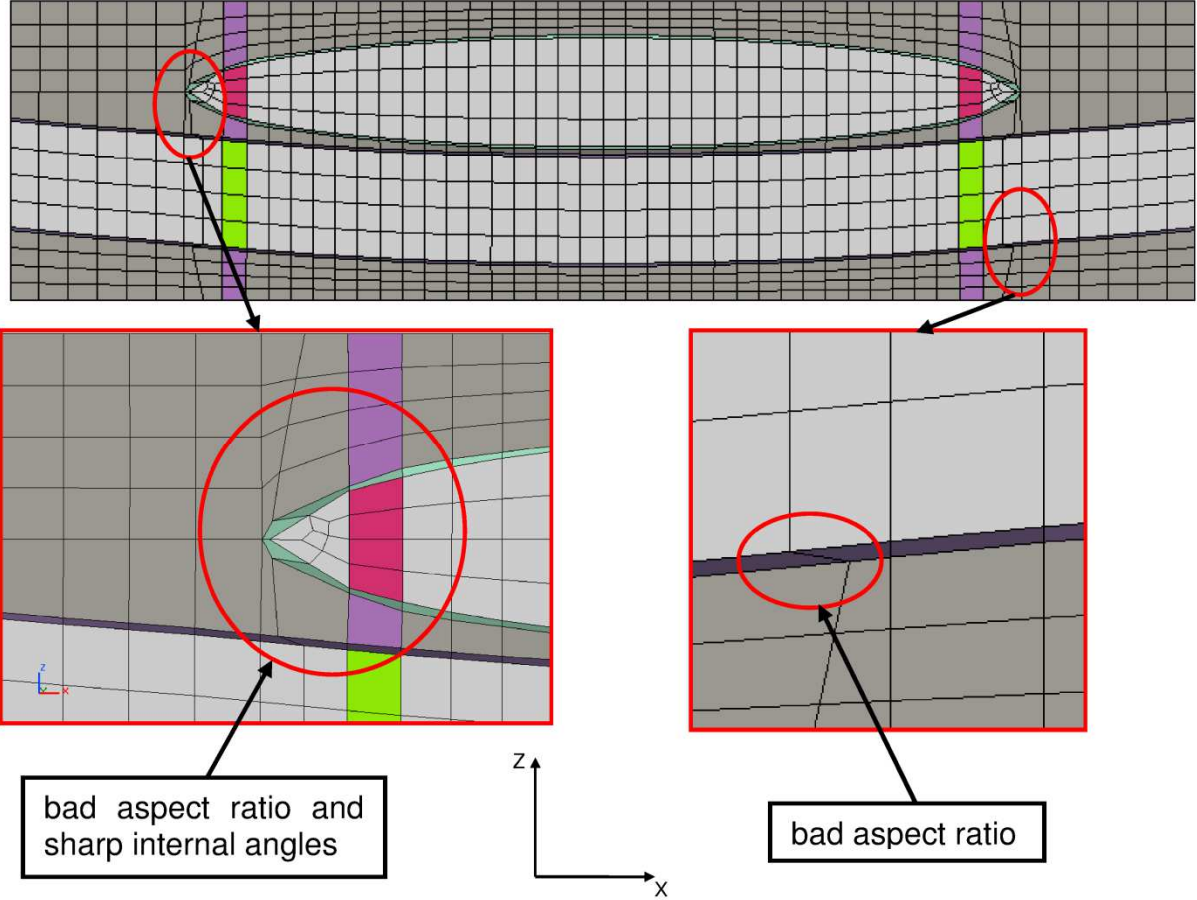
Figure 76: Bad Element Shapes in Full Finite Element Unit Cell Model

In the following analysis the full finite element unit cell model used a total of 39,032 three dimensional 8-node solid elements (117,096 dof) of which 1040, about 3%, were flagged as distorted with an internal angle greater 135° or smaller 35°. Recommendations for mesh sizes have been published by various sources in the literature, e.g. [55], [61], [60]. Whitcomb et al [60] achieved convergence for 1/32 of a plain weave unit cell with as little as 6294 degree of freedom. Glaessgen et al's [55] model of a plain weave unit cell used 50,000 degree of freedom, whereas Owens et al. [61] achieved convergence for 1/4 of a unit cell using 93,174 degree of freedom. However, to ensure the stress state is represented correctly by the model, results for stress concentration position and damage progression needed to be confirmed independently. This has been done in this thesis by first comparing the positions and evolution behaviour of damage within the unit cell with experimental data found in the literature [116], [124], [25], [31] and secondly by comparing the stress distribution on

the surface of the full finite element model with the full stress-field found using a TSA analysis (Chapter 5).

The microscopic analysis showed significant variation in all geometric parameters (Chapter 4). Both Daggumati et al [116] and Ivanov et al [117] have demonstrated, that these variations effect the local strain distributions and therefore lead to differences in local damage initiation and progression. However, investigating the effects of parameter variation on the damage behaviour is beyond the scope of this thesis. Also, Hivet and Boisse [119] have suggested that simplified models using averaged geometrical parameters should be preferred to complex models detailing the effects of local variations on the behaviour of the macrostructure.

The overall height of the unit cell was calculated to achieve the same fibre volume fraction V_f measured after specimen manufacture (Chapter 3) using equation 7-2 and the values listed in Table 4 for the elliptical axis parameters a, b and the wavelength L, which is identical to the length and width of the full finite element unit cell model.

$$V_f = \frac{2LA}{L^2 t}; A = \pi ab \tag{7-1}$$

$$t = \frac{2\pi ab}{V_f L} = 0.07 \, mm \tag{7-2}$$

Stacking 30 plies with the thickness calculated by equation 7-2, would result in a laminate of 2.1 mm, which is slightly thinner than the test laminate, which was around 2.5 mm thick due to variability of tow path and cross-section parameters. Since the model was loaded in in-plane tension and shear only but not in bending, the difference in thickness between model and test specimens could be neglected when experimentally determined stress-strain data was compared to model predictions.

7.1.3 Boundary conditions

Periodic boundary conditions, derived by Whitcomb et al [62], [129], were assumed. Two different load cases were investigated, in-plane uniaxial tension and in-plane pure shear. Figure 77: shows faces, coordinate axes and significant nodes used to define boundary conditions.
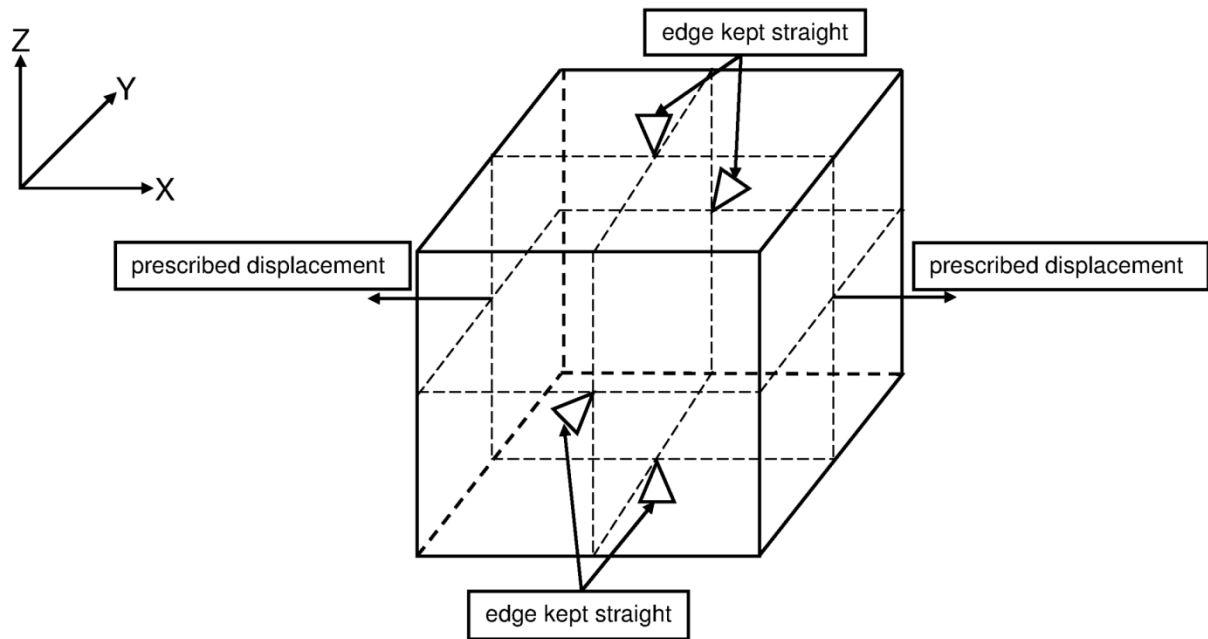
Figure 77: Unit Cell Boundary Conditions

For the uniaxial tension case a prescribed displacement was applied to all nodes on the y-z faces of the unit cell in the x-direction. The faces in the transverse directions of the unit cell, x-y and x-z faces, are kept straight, but not fixed to allow for Poisson's effect, to account for the effect of neighbouring cells in the weave. The *EQUATION keyword was used in ABAQUS so that the normal displacement was the same for all nodes on the same unit cell face. This also constrained all rotational rigid body motions. Since a displacement was prescribed in the x-direction translational rigid body motion only needed to be fixed in the y and z directions. This was achieved by fixing the centre node of the unit cell in those directions.

Boundary conditions for the pure shear case were more complex. The *EQUATION keyword can only be used in a predefined direction, the faces' normal however rotate with increasing shear strain (Figure 78). Other means of constraint had to be found to model the effect of neighbouring cells.
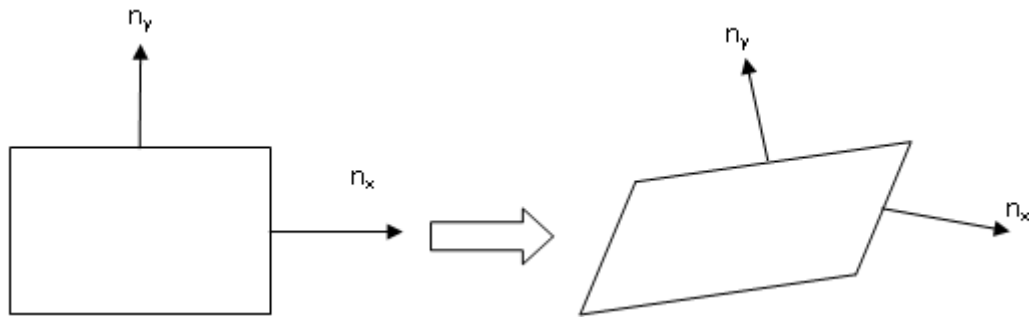
Figure 78: Rotating Normal under Pure Shear Conditions

Shear tests were conducted using ASTM D3518 [111], where a ±45° coupon was loaded in uniaxial tension (Chapter 5), which raises the question whether this actually results in a pure shear stress state or a combined shear and tensile stress state. Mohr's circle would suggest the latter and therefore it was felt that deriving boundary conditions using a submodelling technique would give a more accurate representation of the boundary conditions during the shear test. For this a binary model [84]-[86] of the critical cross-section of the shear test specimen (Figure 79) was used to model the ±45° coupon test (Figure 80). Boundary conditions, i.e. local nodal displacements, of the equivalent binary unit cell at the centre of the macrostructure binary model were written in a separate output file. This output file was then used to assign boundary conditions to a full finite element unit cell model using the procedure laid out in the ABAQUS/Standard User's Manual [130]. This procedure reads the displacements of the nodes of the binary unit cell model from the text file and assigns them to the nodes that are in the same geometrical position in the undeformed full finite element model. The displacements for the other nodes on the same face as the corner nodes are interpolated linearly depending on the position of the node relative to the corner nodes. Therefore, care had to be taken that the edges of the full finite element model were in the same position with the same orientation, in reference to the global coordinate frame, as the equivalent binary unit cell in the macrostructure binary model. The same procedure can also be used for structures with more complex loading conditions or macro-scale geometries when unit cell boundary conditions cannot be derived easily. A detailed description and test case for the submodelling technique can be found in Appendix B.
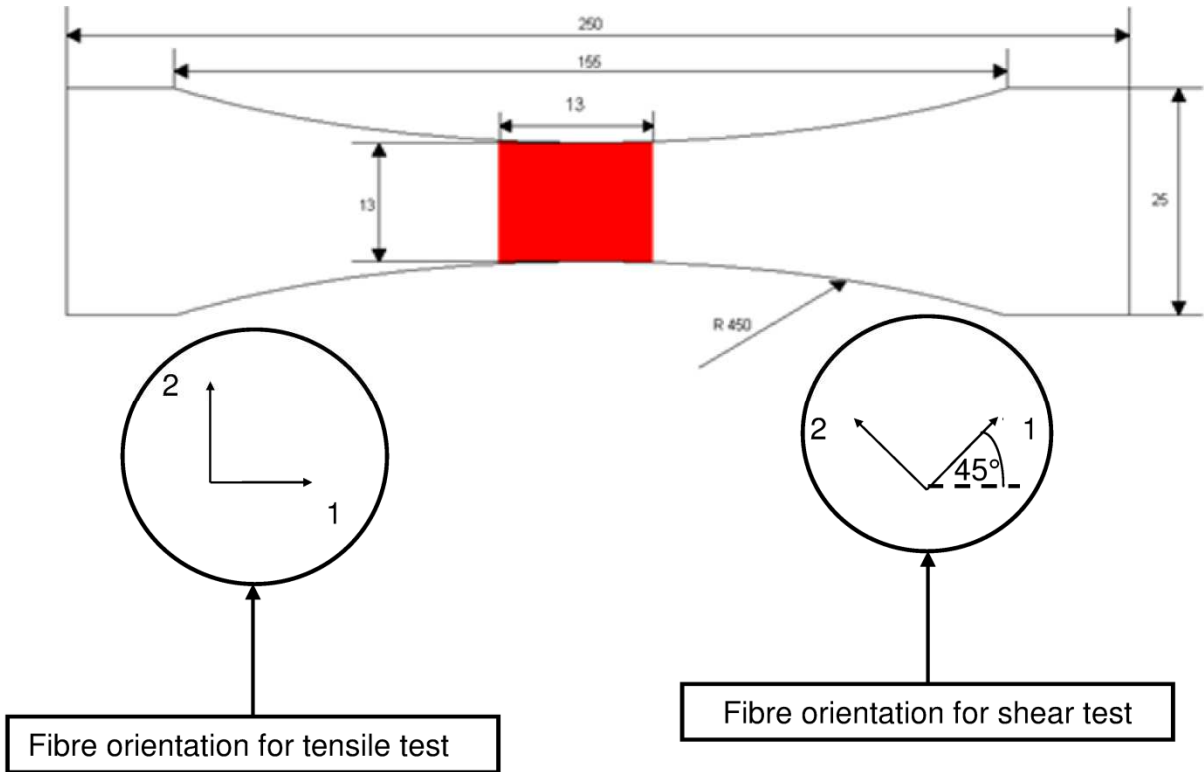
Figure 79: Test Specimen Geometry with Critical Cross Section Marked in Red
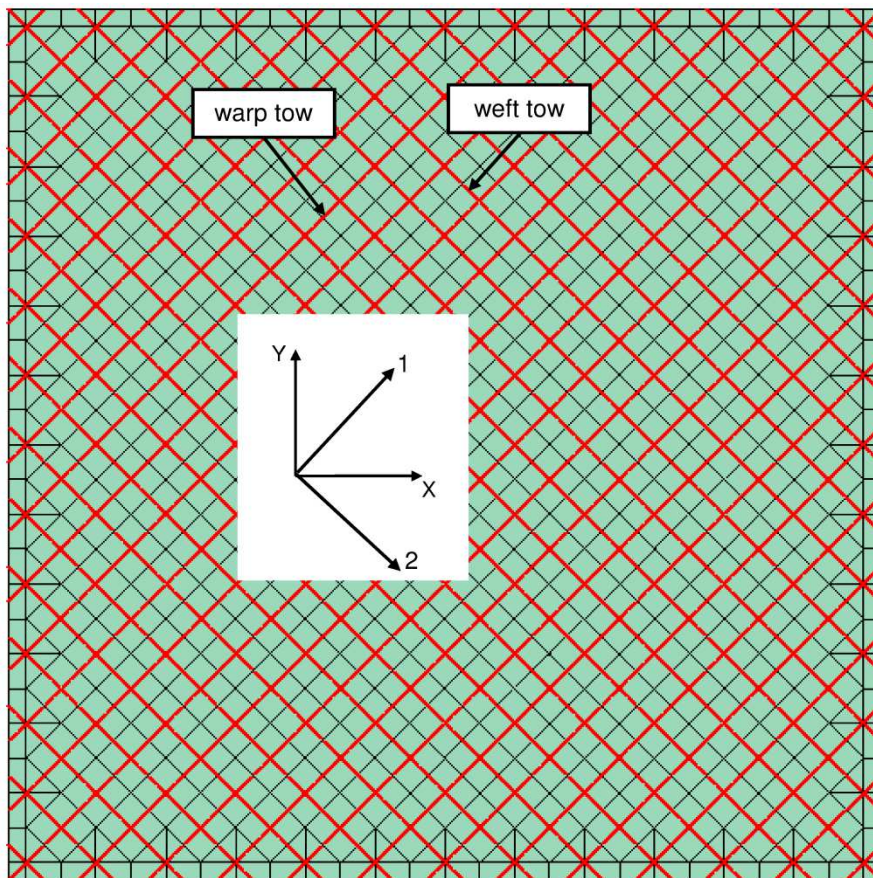
Figure 80: Binary Macroscale Model of Critical Cross-Section of Shear Test Specimen

7.1.4 Material Models

A number of material parameters were required for modelling constituent material behaviour. However, data on the constituents is very limited. Therefore a number of parameters had to be assumed with reference values found in the literature. Also isotropic linear elastic material behaviour was assumed for both the matrix and the glass fibre tows. However, it has been shown in the literature that both constituents exhibit non-linear behaviour [131]-[135], [128].

Epoxies like the one used as matrix material in the experimental analysis behave visco-elastically and/or plastically depending on their state of stress [131]-[134], [136], [137]. Yielding in polymers occurs due to molecular sliding caused by shear stresses. However, this motion requires free space to be available for siding into. Such available free space decreases with the amount of compression put on the material leading to a dependency of yielding on the hydrostatic state of stress.

The parameters required to model the matrix behaviour accurately were not available with reference values in the literature varying over a wide range. It was therefore not possible to make reasonable assumptions, which means linear elastic behaviour had to be assumed. Also for the PRIME LV20 resin used in the experimental analysis the manufacturer does not provide information on shear strength, fracture toughness and interface strength between the resin and glass fibre [113]. This information had to be assumed with reference values provided by the literature since an experimental characterisation of the resin used in the experimental part of this thesis was beyond the scope of this work. Material parameters used for the matrix in the numerical model are summarised in Table 11.

Parameter [unit]	value
Young's Modulus [GPa]	3.5
Shear Modulus [GPa]	1.3
Poisson's Ratio [-]	0.35
Tensile strength [MPa]	75
Shear strength [MPa]	137
Fracture toughness [MPa $(m)^{0.5}$]	3.69

Table 11: Matrix Material Properties

E-glass fibre behaves non-linearly elastic with the tangent modulus decreasing with increasing strain for small strain values and then increasing again with higher strain

values as has been shown experimentally by Bazhenov et al [128]. It has also been argued in the literature [128] that E-glass fibre shows visco-elastic behaviour. Again, the parameters required for a more realistic modelling of the glass fibre were not available in the literature and an experimental characterisation of the E-glass fibre used was beyond the scope of this thesis. Therefore, isotropic linear elastic behaviour of the glass fibre was assumed with the parameters used in the numerical analysis summarised in Table 12.

Parameter [unit]	value
Young's Modulus [GPa]	72.4
Shear Modulus [GPa]	30.0
Poisson's Ratio [-]	0.2

Table 12: Glass Fibre Tow Properties

7.1.5 Damage Model

Cohesive elements with a traction t –separation d formulation (Figure 81) were used to model both crack initiation and propagation within the unit cell and tow matrix debonding. For the traction-separation formulation stiffness parameters needed to be defined in the local normal and two transverse directions of the element. A maximum traction (t_{max}) criterion was used as damage initiation criterion. A damage parameter d was then defined, which increased linearly with increasing separation d(u) of the element faces. The linear increase of the damage parameter is governed by the traction separation work with the damage parameter assumed to be 1 when the integral of the traction separation curve is equal to the fracture toughness of the material.

$$d = \begin{cases} 0 & \left| \dfrac{t}{t_{max}} \leq 1 \right. \\ d(u) & \left| \dfrac{t}{t_{max}} > 1 \right. \end{cases} \quad (7\text{-}4)$$
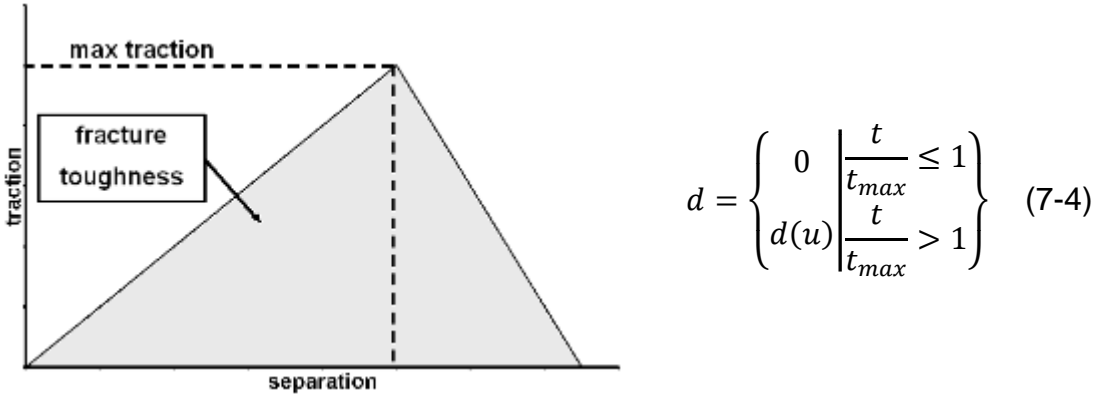
Figure 81: Traction – Separation Model

Since the traction and separation vectors are used to calculate this damage parameter it represents the overall damage in the unit cell rather than components in individual directions. The same parameter is therefore used to decrease all stiffnesses within the cell rather than the stiffness in individual orientations. Increasing the damage variable with increasing separation was governed by energy, meaning the damage variable reached a value of unity when the traction separation integral reached fracture toughness. This damage variable was used to reduce the element traction for a given strain as shown in equation 7-4.

The definition of the traction-separation damage formulation was tested using two simple models, a double lap joint (Figure 82 (b)) and a two part system, bonded together using layers of epoxy adhesive (Figure 82 (a)), under tensile loading. The models were generated using three dimensional solid elements. Metallic parts of the joint and tension system were assumed to be made of steel, the adhesive was modelled using cohesive elements with the same material properties as the matrix material in the composite used for the experimental analysis. Stresses and works for these simple test problems can be calculated using analytical approaches, the results of which were compared to the results of the numerical models to verify the traction-separation law used for the cohesive elements. Detailed calculations for the analytical solutions can be found in Appendix C.
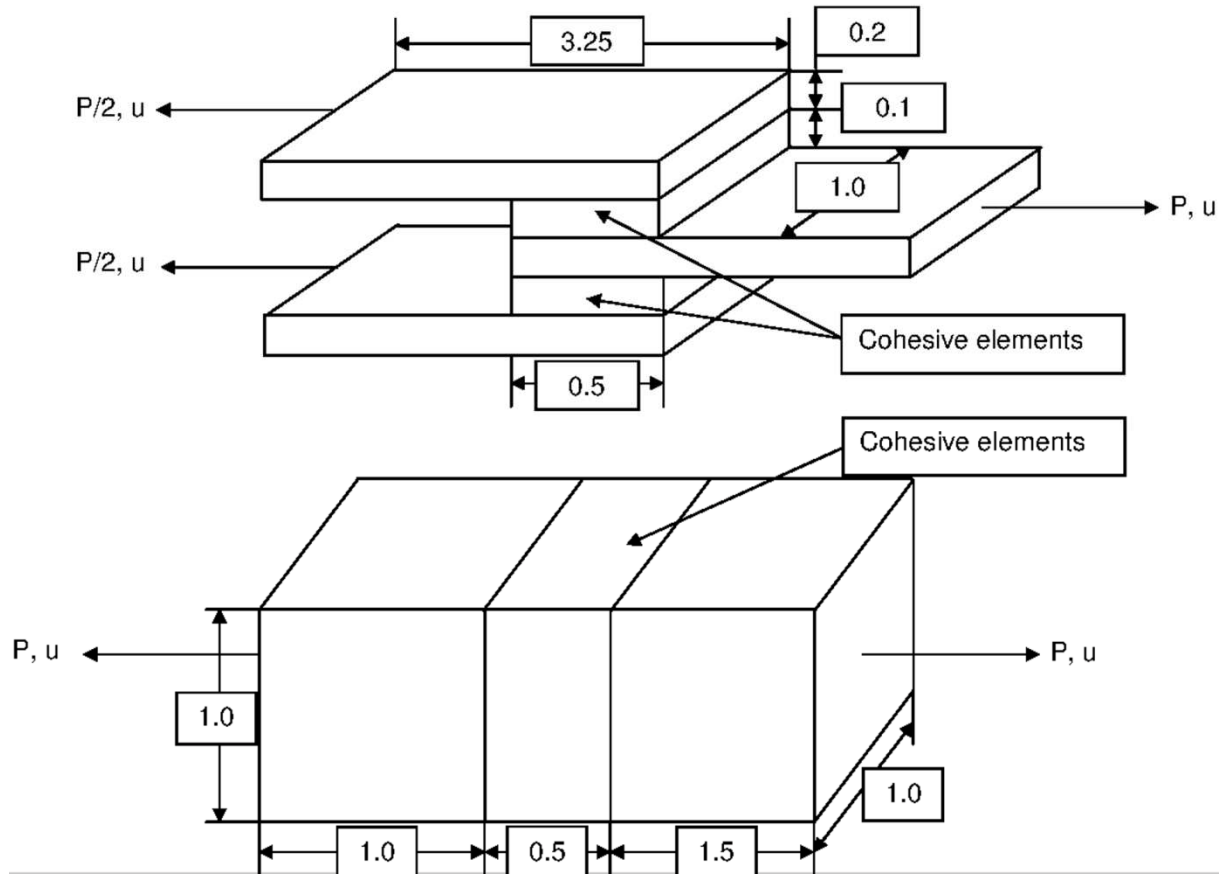
Figure 82: Cohesive Element Test Geometry

Numerical model results showed very good agreement with the analytical solutions. In the tensile load case the analytical solutions gives a force P of 1.30 kN for a given displacement u of 0.2 mm with an axial stress in the cohesive element of 1.30 GPa, whereas the FE model gives a load of 1.29 kN and an axial stress of 1.29 GPa. If damage is included, with a tensile strength of 75 MPa and a fracture toughness of 4 MPa $m^{0.5}$ for the epoxy adhesive the FE model gives a fracture toughness of 4.01 MPa $m^{0.5}$ at total failure (damage parameter d is equal to 1).

For the double lap joint the analytical solution gives a force P of 1.08 kN for a given displacement u of 0.2 mm and a shear stress of 1.08 GPa while the FE model gives a load P of 1.06 kN and a shear stress of 1.07 GPa. If a shear strength of 137 MPa and a fracture toughness of 4 MPa $m^{0.5}$ are included the FE model gives a fracture toughness of 4.22 MPa $m^{0.5}$ at total failure.

7.1.6 Postprocessing

During postprocessing global stresses and strains were calculated for the unit cell and later the macro-structure using the same procedure. Since all numerical analyses in this thesis were displacement controlled, calculating strains was straightforward. The prescribed displacements were divided by the axial length of the unit cell in the tensile load case. For the shear load case the displacement in the x direction at the x-z faces were divided by the width of the y-z faces and the displacement in the y direction at the y-z faces were divided by the width of the x-z faces. The sum of these divisions gives the shear strain.

In composite structures fibres carry a higher load than the surrounding matrix. However in the classical laminate theory [126] the load is averaged over a ply's width and thickness. The same was assumed for the global stresses in the unit cell model, therefore for the tensile load case the reaction forces on all nodes on the left y-z face were summed and the resulting total force divided by the cross section of the left y-z face, which gave axial stress. For the shear load case the force in x direction on the top x-z faces were divided by the cross sectional area of the same face, which gave the shear stress.

7.1.7 Numerical Modelling Results

7.1.7.1 Linear Analysis

As was discussed above in Subchapter 7.1.4, the matrix material behaviour is dependent on the hydrostatic state of stress. Figure 83, Figure 85 and Figure 86 show the hydrostatic stress distribution in the full finite element unit cell model under tension and shear loading. The figures suggest that the hydrostatic stress state is rather variable across the unit cell resulting in different matrix material behaviour across the unit cell, which is not captured by the material model used in this thesis. Whilst this is a source of error for the prediction of stress-strain behaviour for both load cases, the affect is expected to be more significant for the shear load case. This is due to the behaviour of composites under shear loading, unlike composites under tensile loading, being dominated by the matrix material rather than the tow material [126].

In the tensile load case a substantial area of the unit cell shows a positive hydrostatic stress, meaning the matrix material in those areas is being compressed (Figure 83). This is due to the warp tow straightening when a tensile load is applied in the X-direction resulting in the matrix material being pressed into the weft tow (Figure 84). Also, the difference in Poisson's ratio between the tow and the matrix material (see Table 11 and Table 12) results in a higher strain in the through thickness direction for the matrix material compared to the tow material. This would result in a larger contraction of the unit cell model in the area where no weft tow is present and a non-straight surface (Figure 84). However, since the boundary conditions applied to the unit cell keep the top and bottom edges of the unit cell straight (see Subchapter 7.1.3) to account for the supporting effect of neighbouring cells, a compressive through thickness stress component is introduced.
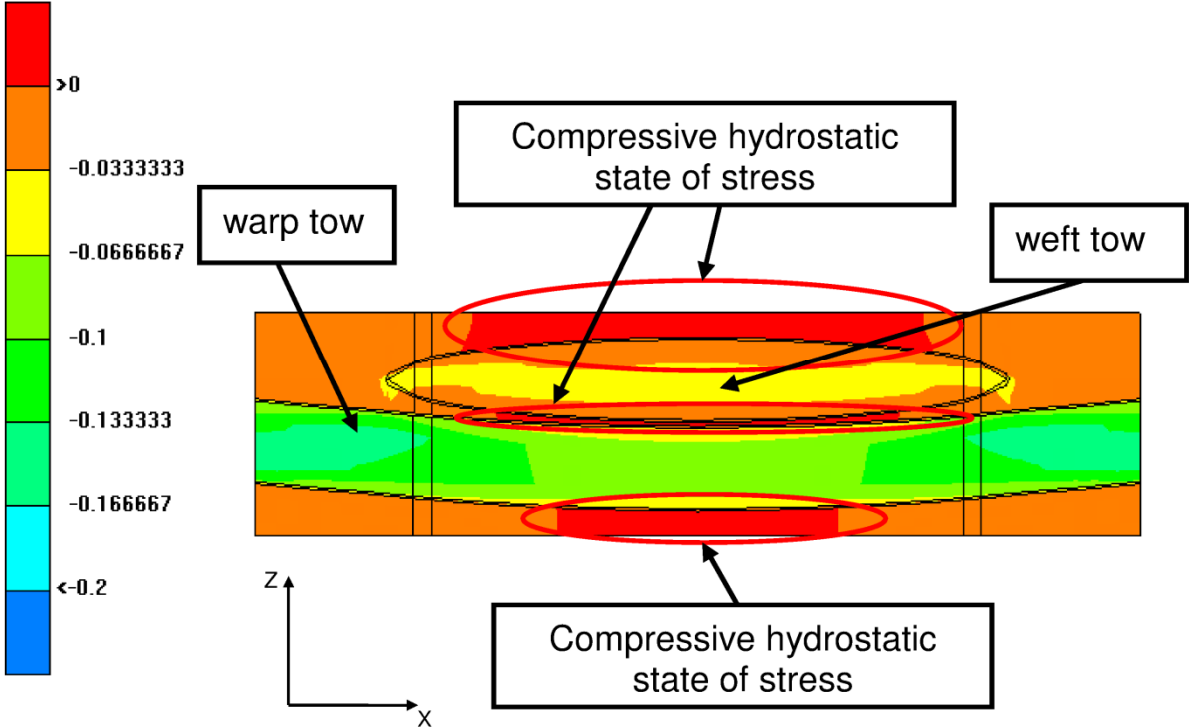
Figure 83: Hydrostatic State of Stress in Full Finite Element Unit Cell Model in Tension
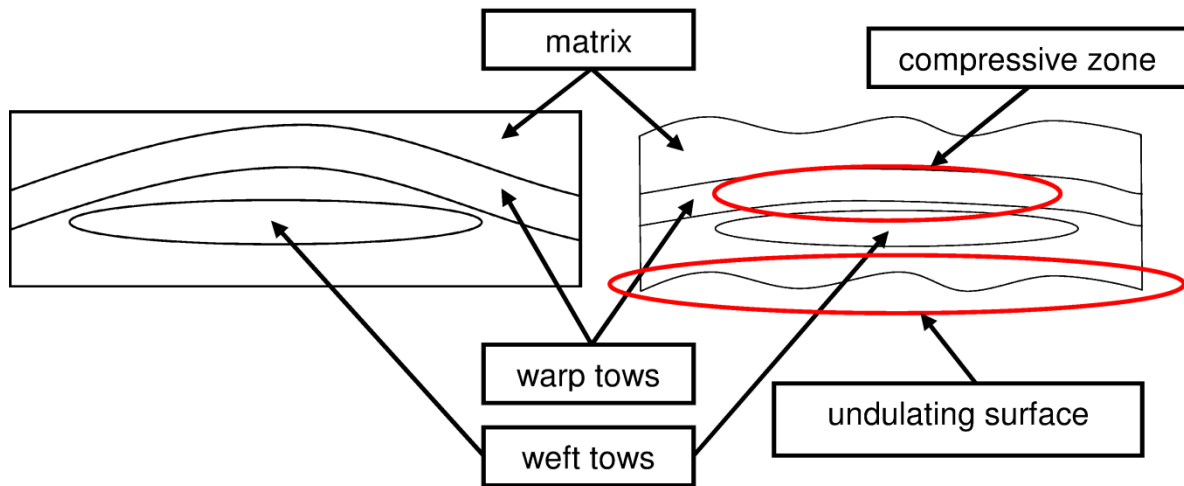
Figure 84: Effects of Tow Straightening and Difference in Poisson's Ratio of Tow and Matrix Materials

Compared to the hydrostatic state of stress in tension, the hydrostatic state in the matrix material for the shear load case is almost zero throughout the unit cell as can be seen in Figure 85. However, towards the edge of the unit cell the hydrostatic state of stress is significantly more complex, as can be seen in Figure 86, with the material being compressed on one edge whilst being in tension at the other.
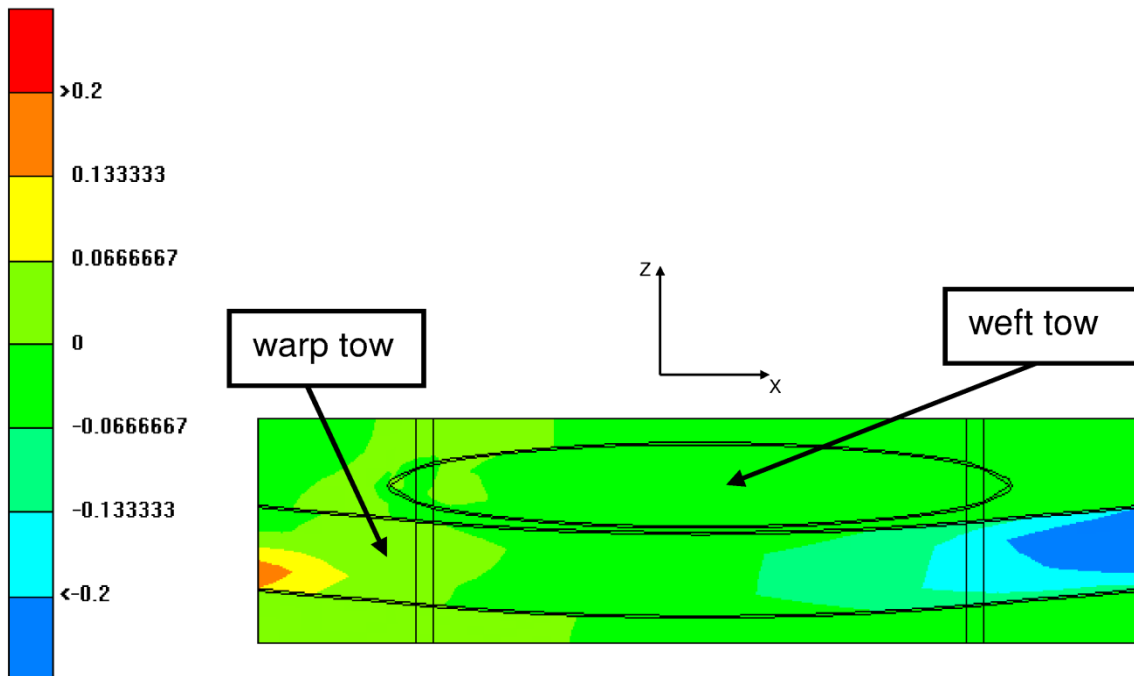
Figure 85: Hydrostatic State of Stress in Full Finite Element Unit Cell Model in Shear in the Unit Cell Centre
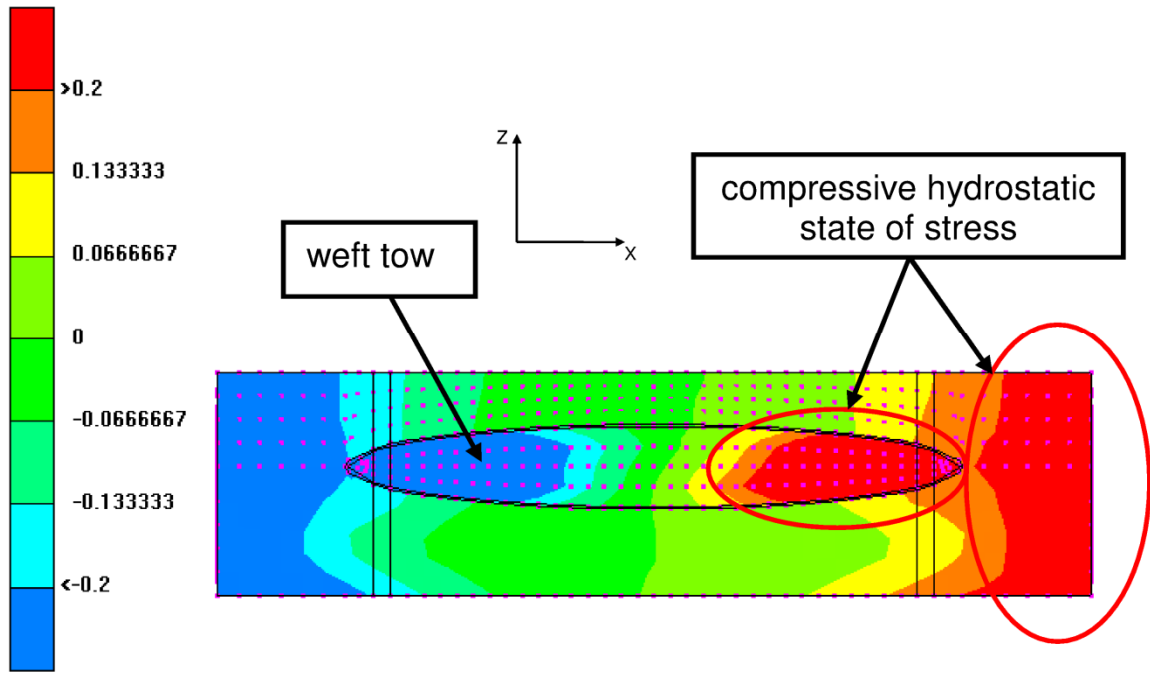
Figure 86: Hydrostatic State of Stress in Full Finite Element Unit Cell Model in Shear on the Unit Cell Edge

It was found that for the linear analysis the stress concentration points were in a similar position within the unit cell for both the tensile and the shear loading case as can be seen in Figure 87 and Figure 88, which show the first principal stress at the end of the linear analysis in the centre of the unit cell.
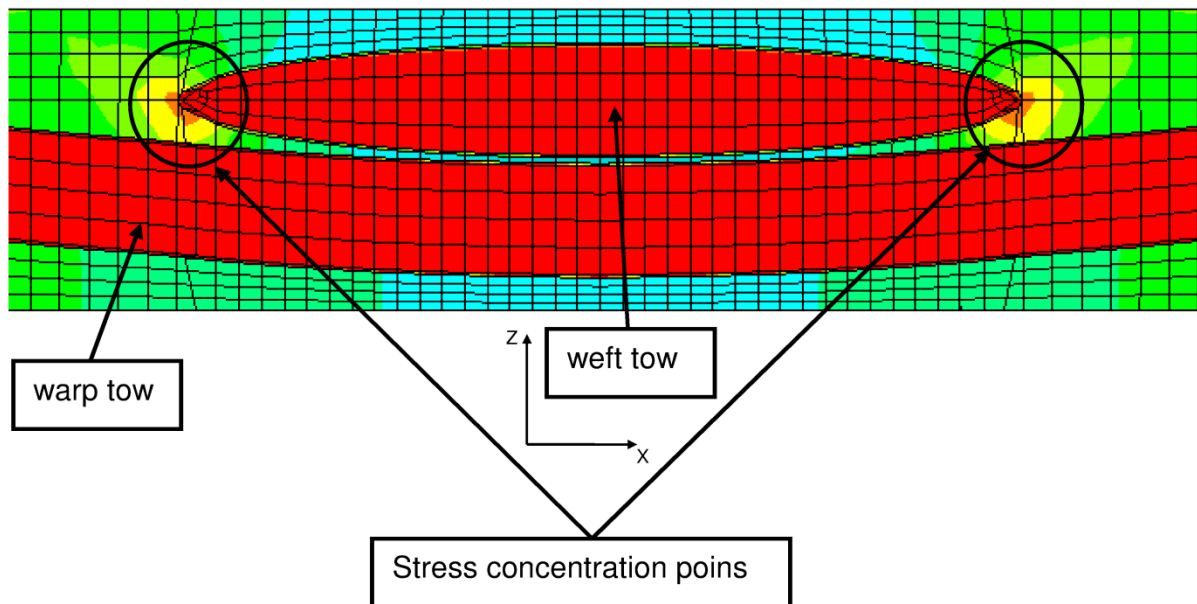
Figure 87: Stress Concentration in First Principal Stress for the Tension Loadcase
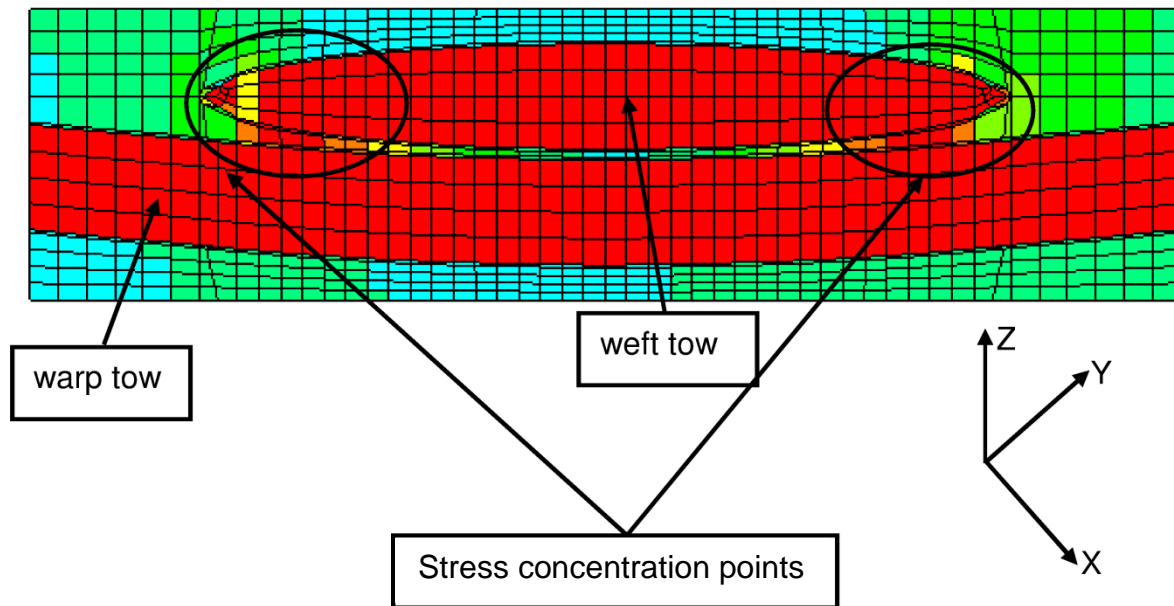
Figure 88: Stress Concentration in First Principal Stress for the Shear Loadcase

Stress concentration points in the model were where they were expected for the tensile load case. Experimental analyses by Daggumati et al [116], Callus et al [124], Gao et al [27] and Lomov et al [25] showed that damage initiates and propagates at the same position in woven laminates with similar architectures. No studies have looked at damage initiation and propagation at the microscopic scale for woven laminates under shear loading. Therefore, no microscopic test data was available for comparison of the results from the linear analysis and the full finite element results in pure shear. However, the specimens used for the tensile and shear tests described in chapter 6 show fracture occurring along the same direction through the unit cell as can be seen in Figure 61 and Figure 71. This would suggest that cracks initiate in similar areas and propagate along similar paths, which would agree with the stress concentration points being in similar positions within the unit cell.

To account for damage, the cohesive elements needed to be placed at the point of highest stress. The results from the linear analysis were used to place cohesive elements along the surface of highest stress within the matrix warp and weft tows as well as around the interface between tow and matrix to account for damage. The cohesive elements are shown in red in Figure 89. Data available in the literature suggested that tow failure happens rapidly across the entire tow cross-section, which in turn leads to complete composite failure [27], once failure stress is reached. Therefore, tow rupture was not included as a failure mode in the nonlinear full finite

element model and total failure was assumed to occur at a total unit cell strain of 0.025, which is close to the experimentally determined mean average failure strain of 0.224 in chapter 6.
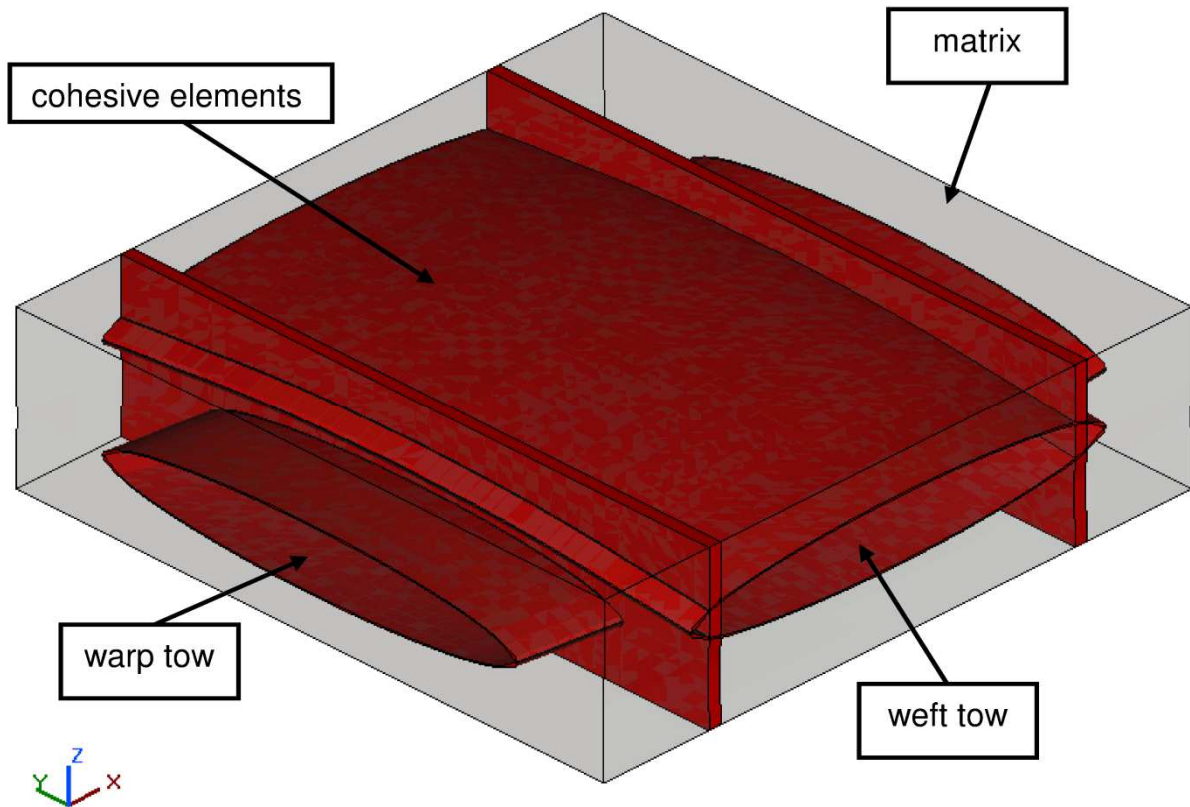
Figure 89: Cohesive Elements in Unit Cell Modell

7.1.7.2 Comparison of Linear Analysis Results with TSA Data

As has been discussed in Chapter 5, thermoelastic stress analysis (TSA) is a method of determining surface stresses by measuring the change in temperature of a composite specimen's surface under cyclic loading. For a composite material this change in temperature can be related to the sum of stresses in the fibre directions using equation 5-2. In order to compare the normalised thermoelastic signal with the stresses predicted by the full finite element unit cell model, the stresses in both warp and weft tow directions along two lines through the unit cell are determined. One of these lines runs in the warp direction, the other in the weft direction as shown in Figure 45 and Figure 90. The stresses at each point along the lines were then added and the mean average sum of the two stresses across each line was calculated.

However, as has been described by Dulieu-Barton et al [99] the low conductive properties of polymer resins result in the formation of "hot spots" either from local stress concentration or viscoelastic heating at damage sites. Frühmann et al [138] therefore called polymer resins strain witnesses. This effect of strain witnessing is not captured by the full finite element unit cell model as no heat transfer modelling is included. Therefore, stresses in the full finite element unit cell model should be measured at the tow matrix interface, where stress concentration points are located, rather than the unit cell model surface.
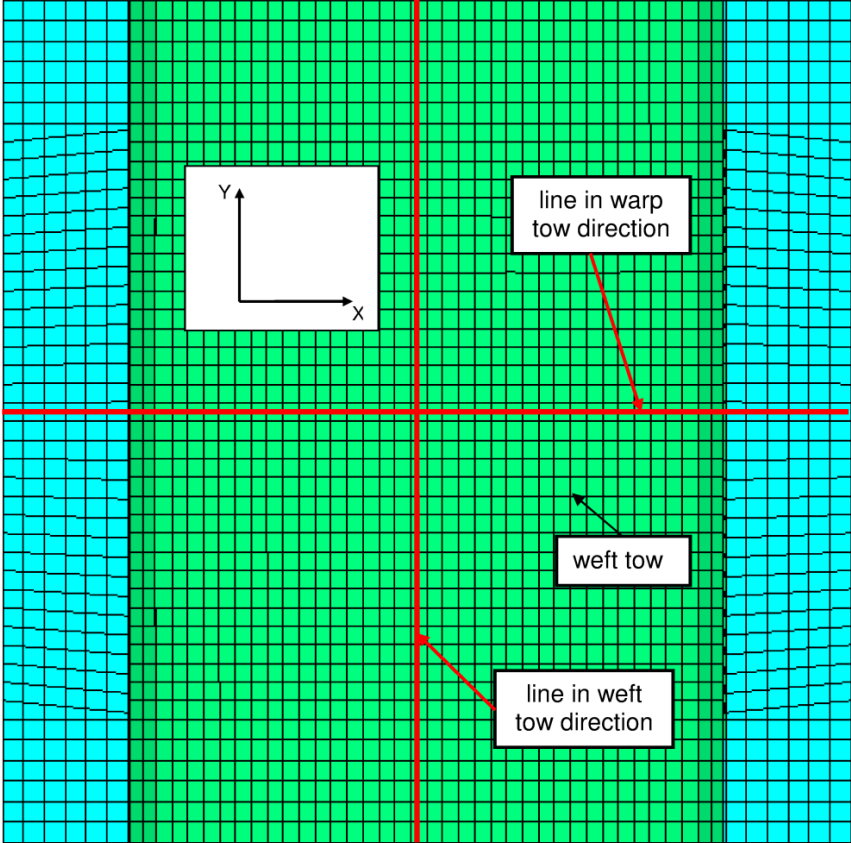
Figure 90: Postprocessing Lines for Comparison with TSA Data in Full Finite Element Unit Cell Model

The sum of stress values at each data point was the divided by the mean average of its corresponding line to calculate a normalised stress value sum, which could now be compared to the normalised thermoelastic signal since both are now unitless. Because the length unit of the lines along which the thermoelastic signal was measured in chapter 5 was pixels and the length unit of the line in the full finite element model was mm, both lengths also had to be normalised by dividing them by the total length of each line in its respective units.

Figure 91 and Figure 92 show the comparison of the measured thermoelastic signal with the sum of stress components in warp and weft direction for the full finite element unit cell model. In the warp direction both the TSA data and the full finite element unit cell model show the same trend with peak stresses at about 20% and 80% and a trough at about 50% of the unit cell length (Figure 91). However, the model predictions show two extra peaks at about 15% and 85% of the unit cell length. These extra two peaks are located at the edges of the weft tow where the tow matrix interface begins as can be seen in Figure 87. These extra two peaks in the predicted stress curve are due to the mesh quality in that area, which is less than ideal and has already been discussed earlier in this chapter.

In general the normalised thermoelastic signal curve is lower than the sum of stress components predicted by the full finite element model. This is due to the fact that the normalised thermoelastic signal curve is an averaged curve as has been discussed in chapter 5. Whilst this gives a good representation of the overall trend of the TSA data it also smoothes out high gradient changes. Also, though polymers are good isolators a small amount of local heat conduction leads to a loss of heat of a "hot spot" to the surrounding material, resulting in a smother gradient of the measured thermoelastic signal.
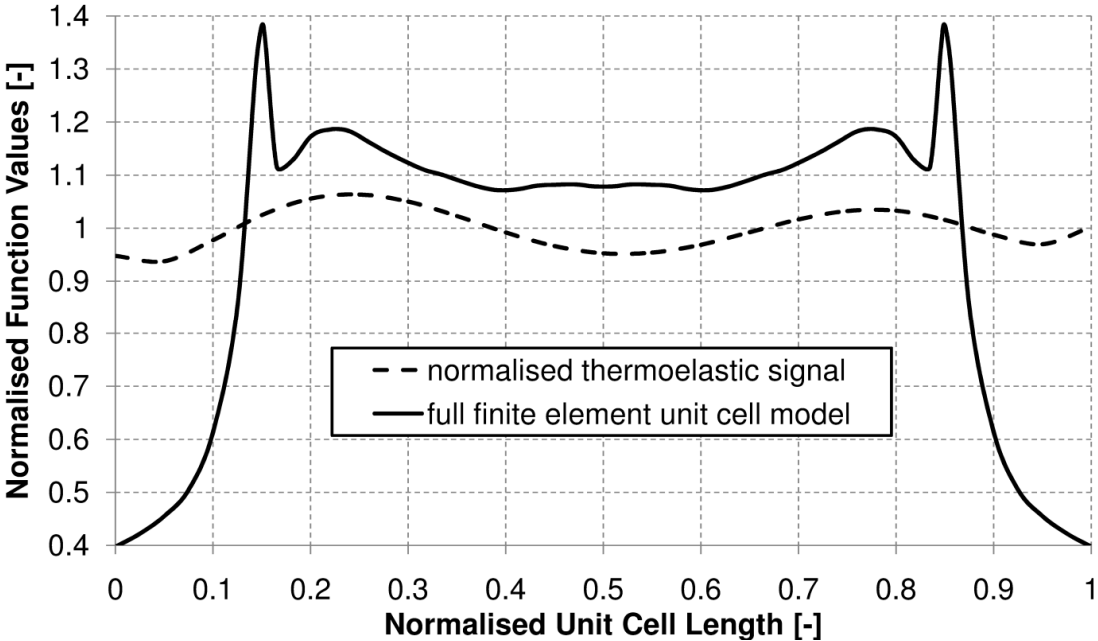
Figure 91: Comparison of Measured Thermoelastic Signal and Full Finite Element Unit Cell Model Prediction in Warp Direction

In the weft direction the TSA data and the predicted stress data do not show a similar trend. The TSA data shows a similar behaviour in warp and weft direction with two peaks at about 15% and 85% and a trough at about 50% of the unit cell width. The predicted stress distribution however shows a minimum of stresses at the outer edges of the unit cell and a maximum at about 50% of the unit cell width (Figure 92).
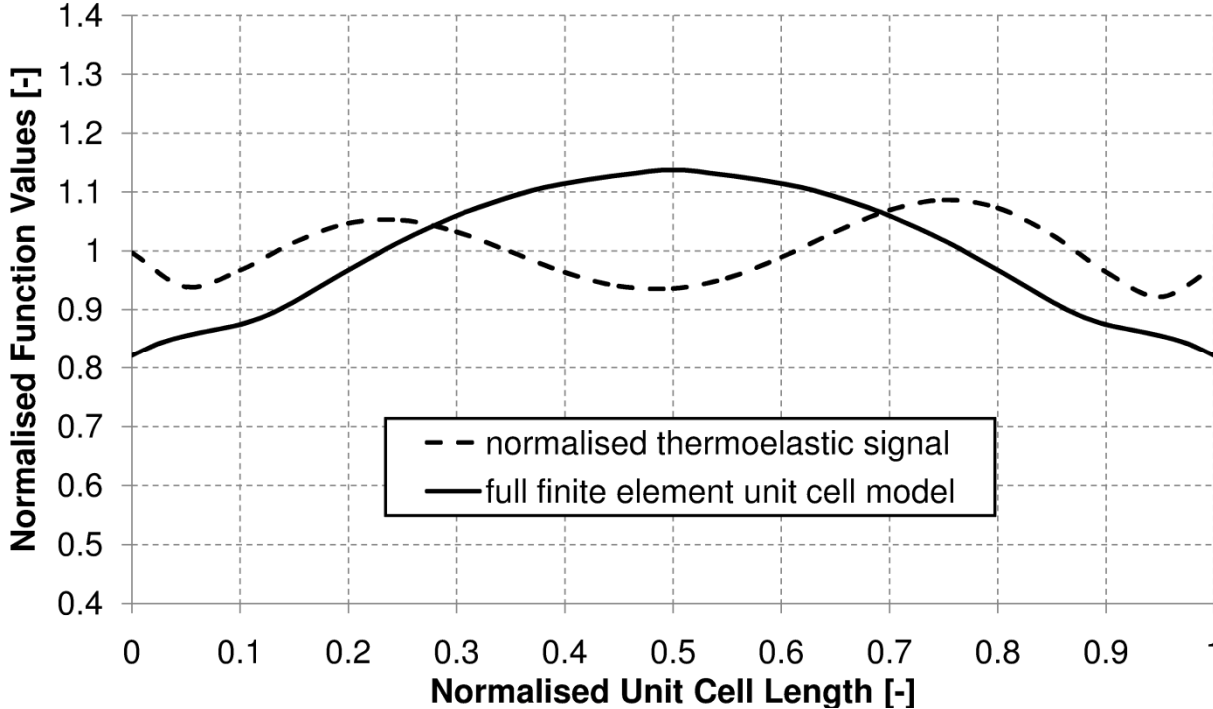
Figure 92: Comparison of Measured Thermoelastic Signal and Full Finite Element Unit Cell Model Prediction in Weft Direction

The comparison between the measured thermoelastic signal and the full finite element unit cell model suggests that the full finite element model does not capture a major stress concentration factor in the weft tow direction under tensile loading. This might be due to the use of 3D solid elements to model the tows. In reality a tow is a bundle of fibres running in parallel, which would allow relative sliding motions between individual fibres and therefore result in an inability of the tow to transfer shear stresses between fibres. Solid elements however do allow for the transfer of shear stresses resulting in a much stiffer response of the tow when loaded in compression and shear. This could affect the stress distribution for both the tensile and shear load case, because in the tensile load case the weft tow is loaded in compression (Figure 93) due to Poisson's effect and in the shear load case axial stresses for both warp and weft tow vary linearly across the tow cross-section (Figure 94) with one side loaded in tension and the other in compression. In order to offset

the effect and additional line of cohesive elements was introduced for the shear load case to reduce the amount of shear stresses being transferred within the weft and warp tow (Figure 95).
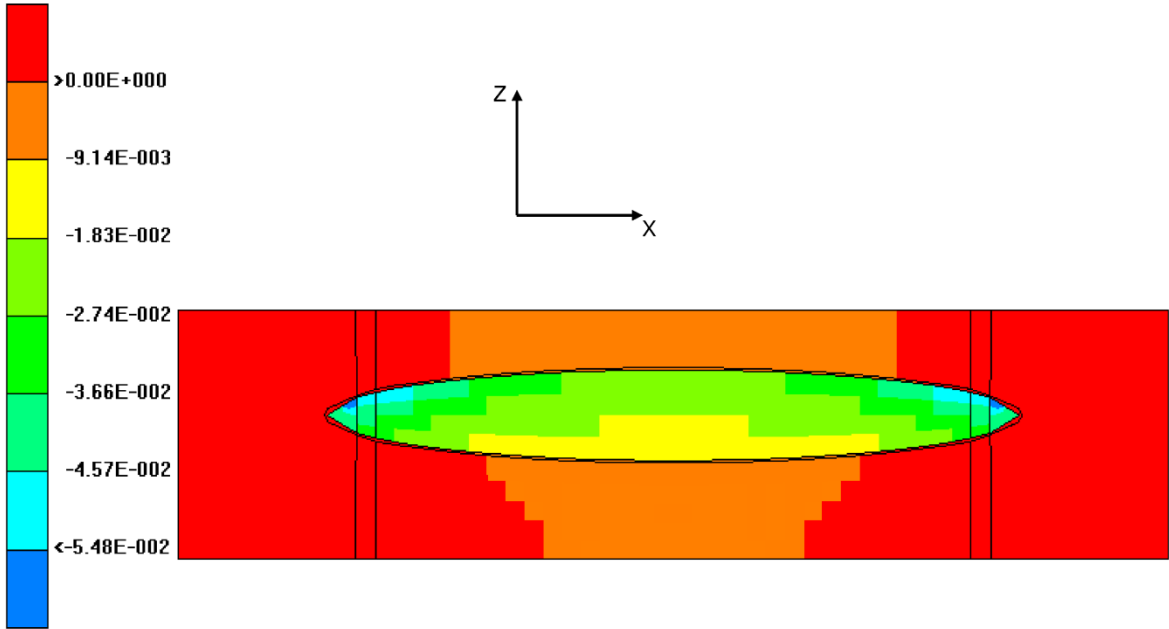
Figure 93: Stress in Weft Direction on the Unit Cell Boundary for the Tension Load Case
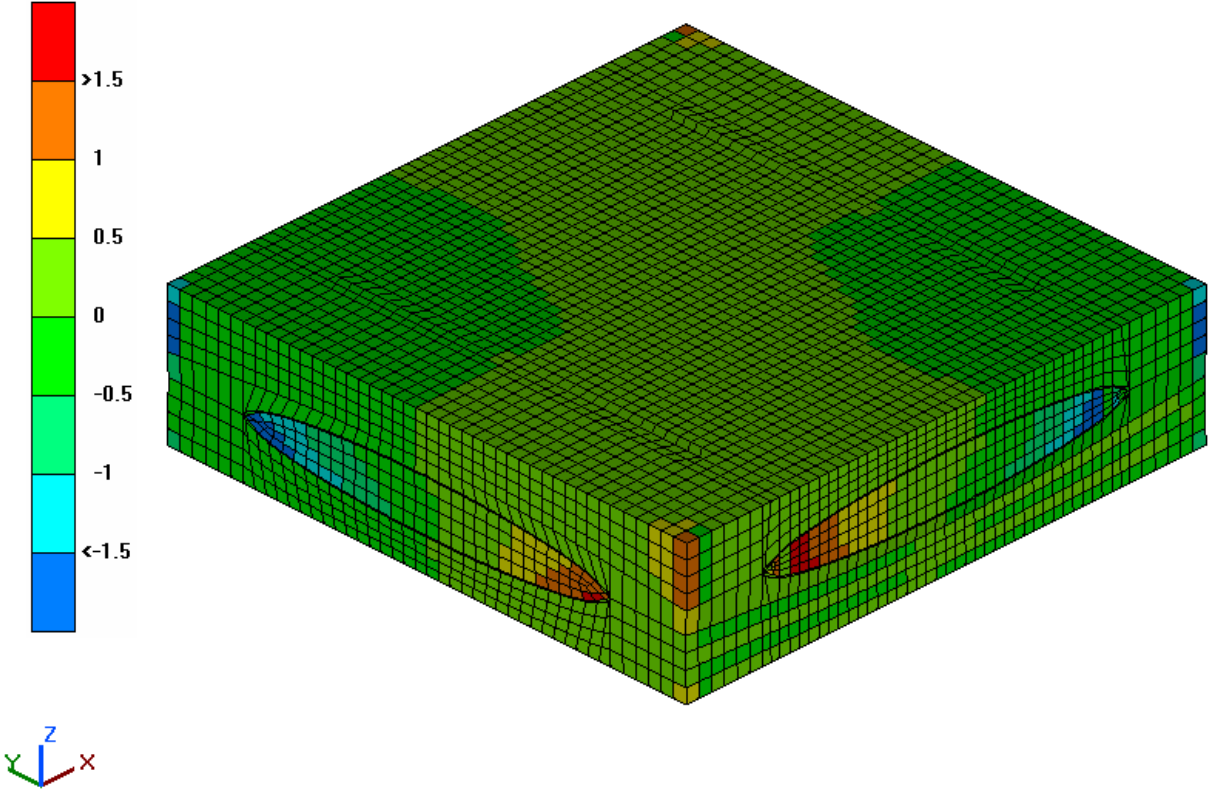
Figure 94: Stress in Weft Direction on the Unit Cell Boundary for the Shear Load Case
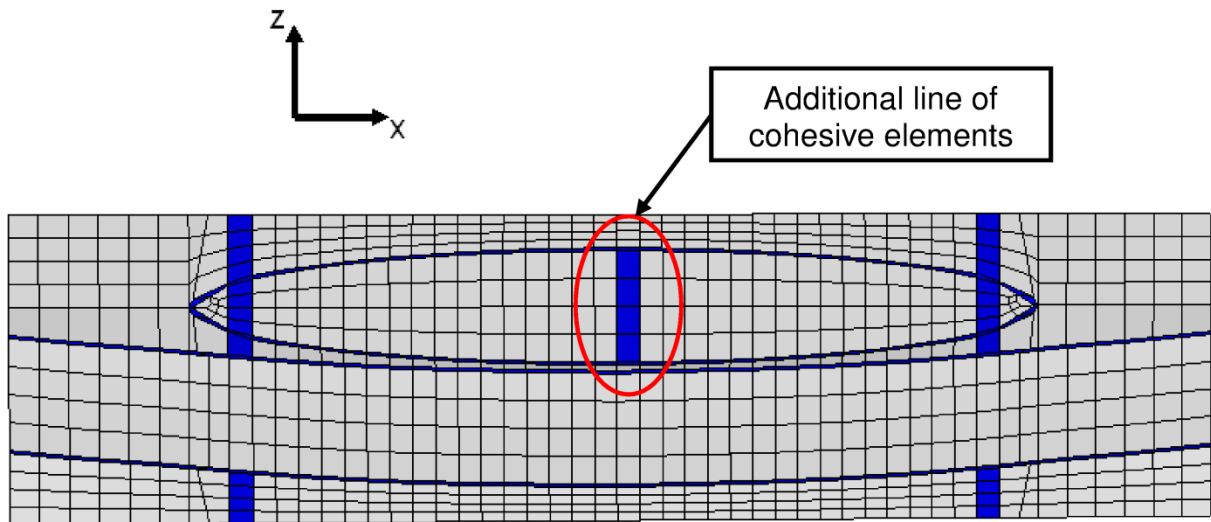
Figure 95: Additional Line of Cohesive Elements in Weft Tow for Shear Analysis

7.1.7.3 Nonlinear Analysis in Tension

For the tension load case damage initiates between the weft tow and the matrix at the point of highest stress concentration at the centre of the unit cell, Figure 96 a, at a global tensile strain of 0.0037. The damage level decreases towards the surface and the edge of the unit cell (Figure 96 b) where no damage is observed.

(a)

damage initiation

(b)

damage initiation
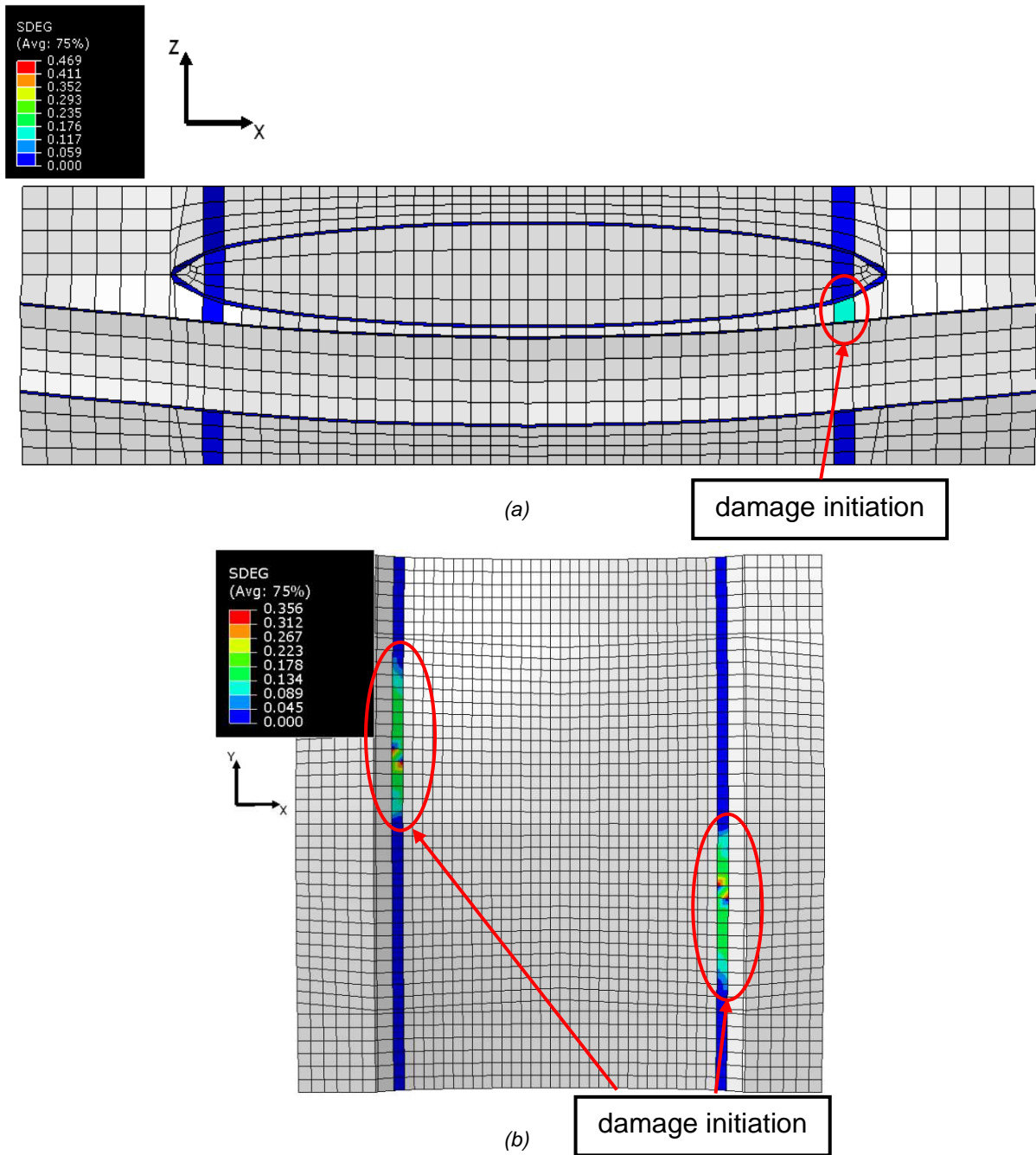
Figure 96: Damage in unit cell (a) centre and (b) middle at 0.0037 global axial strain

At a global tensile strain of 0.0075 damage propagates into the weft tow and the matrix both in the centre and on the edge of the unit cell (Figure 97 a, b and c). Damage propagates through the thickness of the cell and can be seen on the surface (Figure 97 d). Interface damage can also be seen in the centre but not on the edge (Figure 97 a). Damage levels are the highest, up to 80%, at the edge and lowest in the centre.
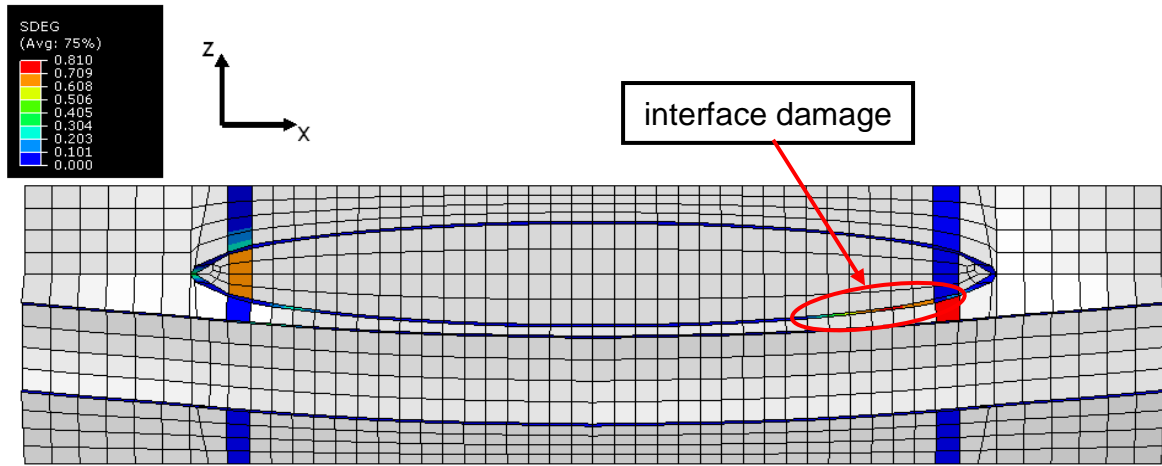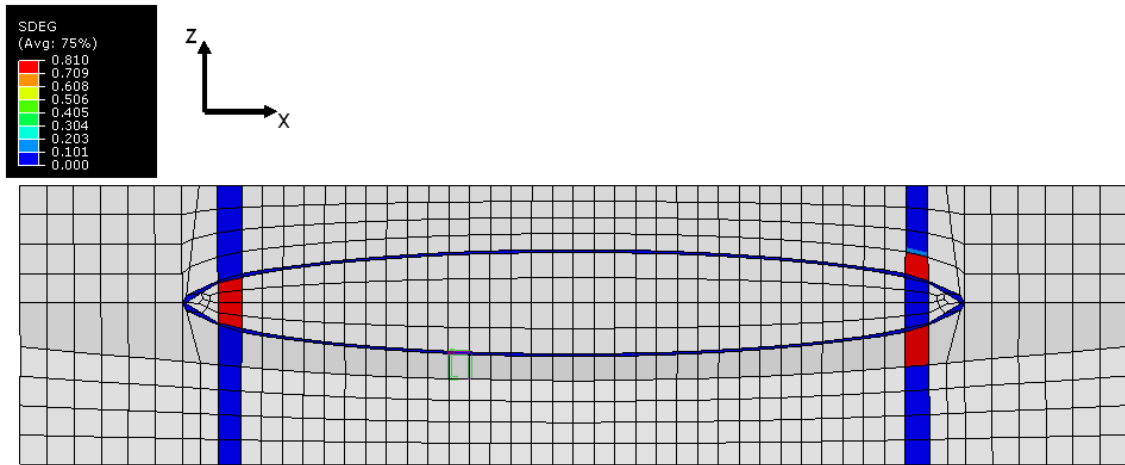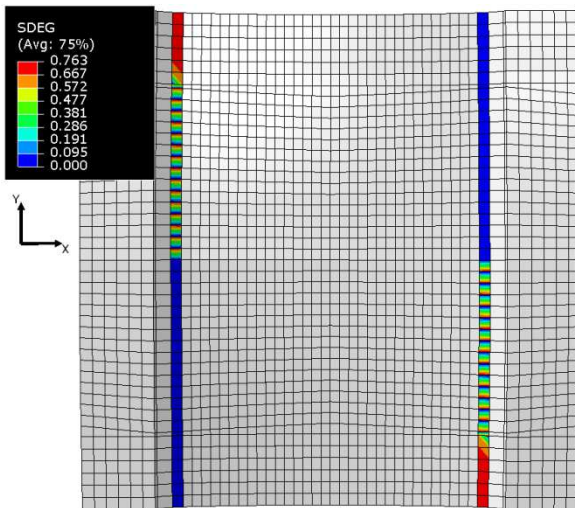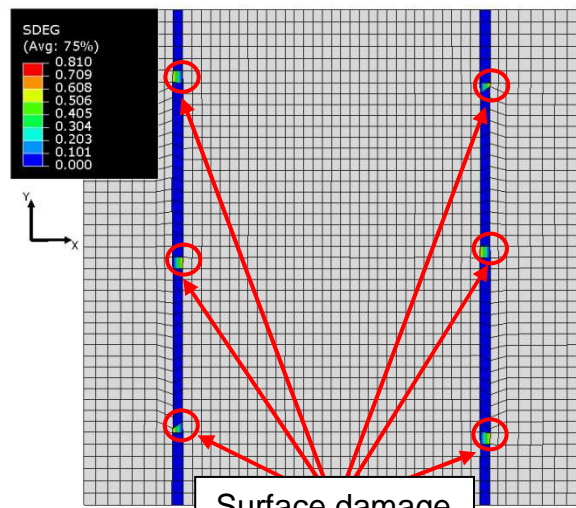
Figure 97: Damage in unit cell (a) centre plane (b) side wall (c) middle surface (d) top surface at 0.0075 global axial strain

Propagation of damage continues with the same pattern of distribution and increasing levels for higher strains (Figure 98 and Figure 99). Interface damage continues along all interfaces with the interfaces between warp and weft tows first and the interfaces towards the upper and lower surfaces of the unit cell respectively.
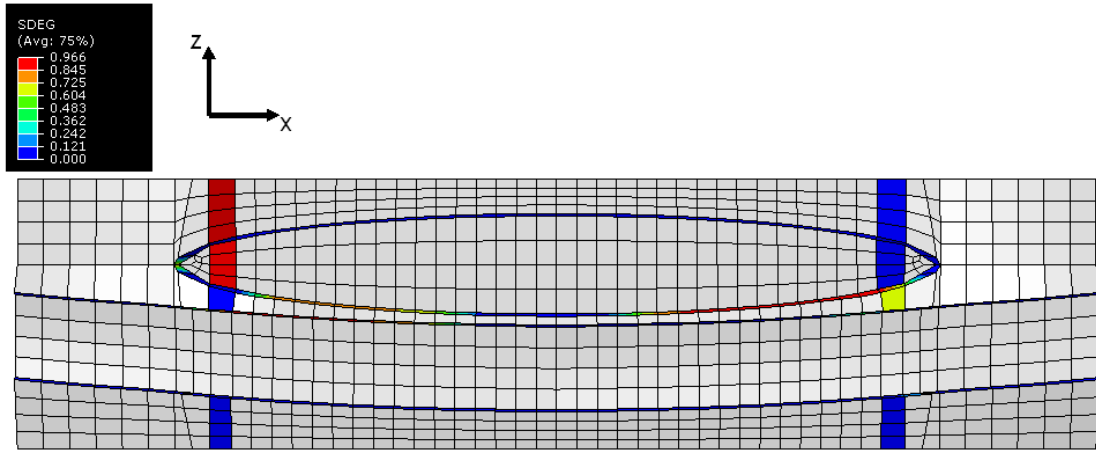
(a)
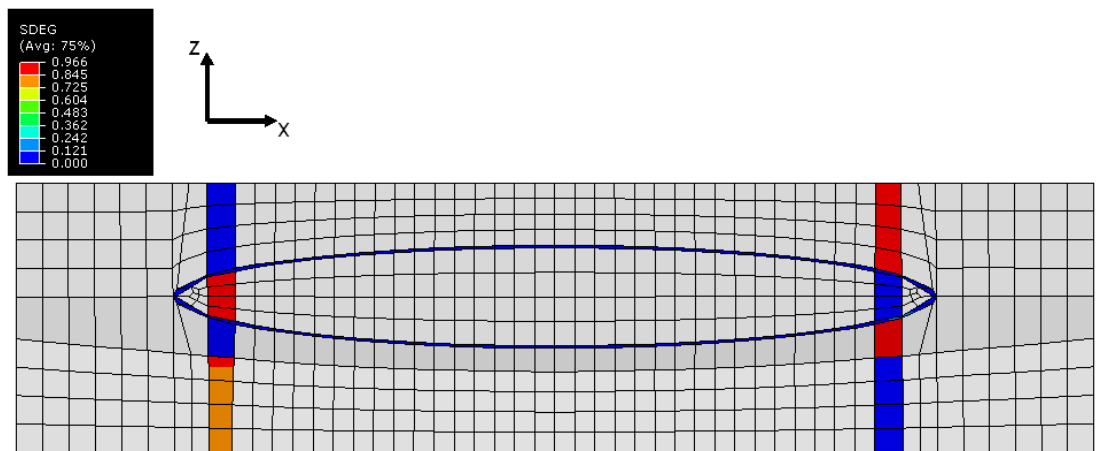
(b)
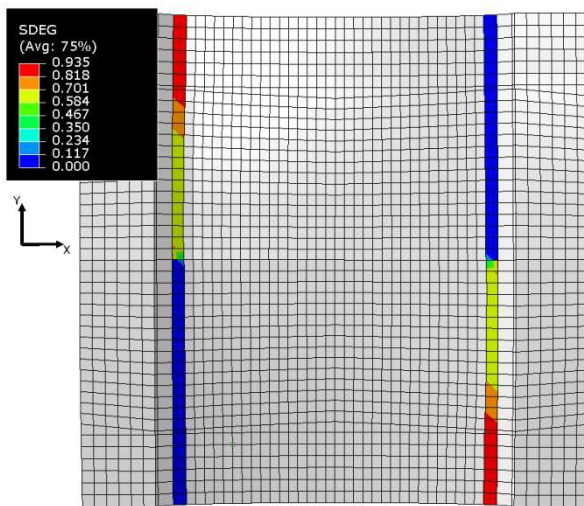
(c)
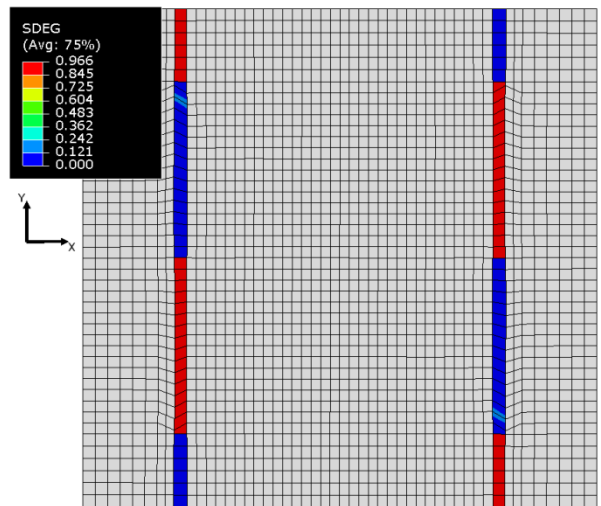
(d)

Figure 98: Damage in unit cell (a) centre surface (b) side wall (c) middle surface (d) top surface at 00116 global axial strain
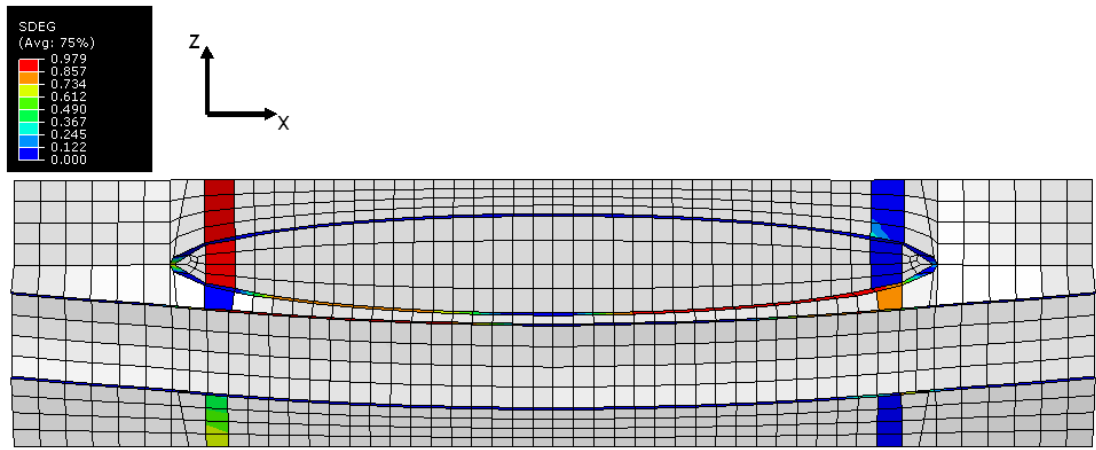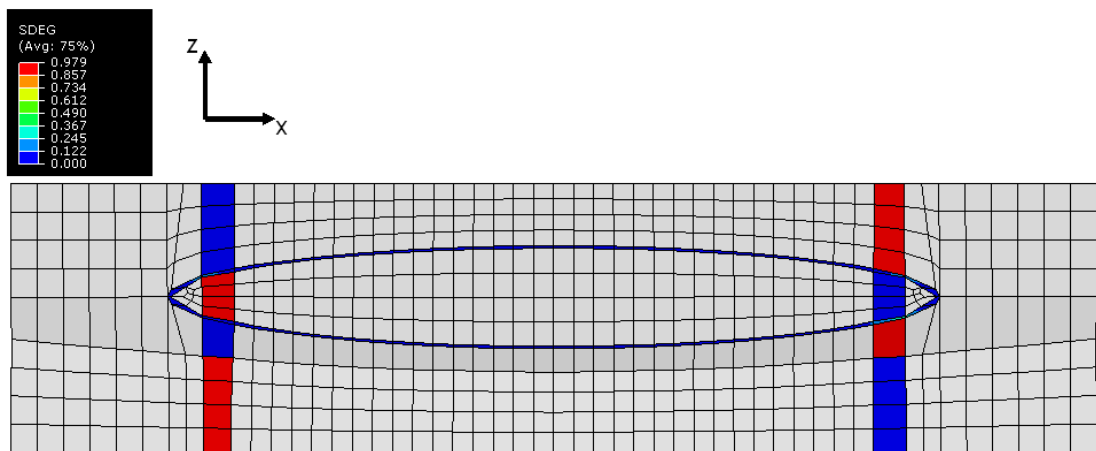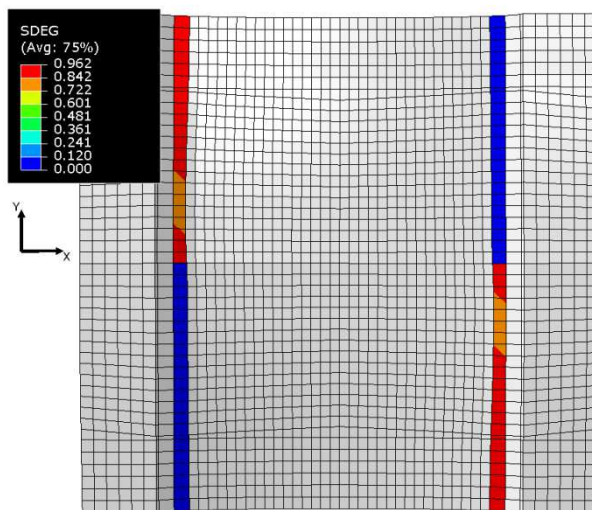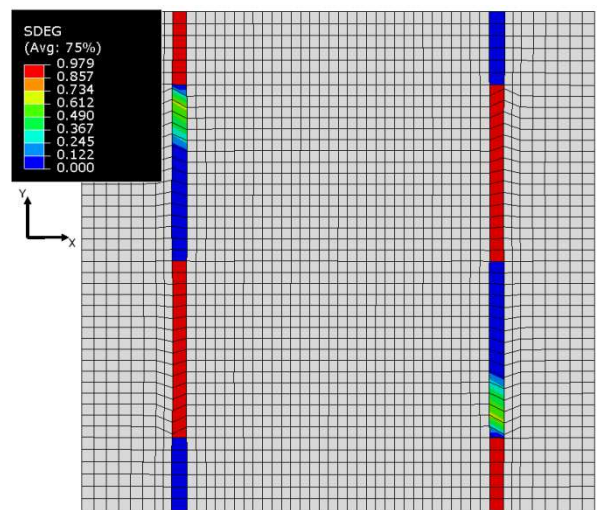
Figure 99: Damage in unit cell (a) centre surface (b) side wall (c) middle surface (d) top surface at 0.025 global axial strain

This distribution of damage, meaning the pattern of damage propagation, in the unit cell has also been observed in an experimental analysis by Gao et al [27] for a laminate of 8-harness satin weave plies. After damage initiation at the weft stress concentration and its propagation into the weft tow, the second mode of failure observed in the numerical model is tow – matrix debonding. This is also consistent with experimental findings in other works in the literature [25], [27], [116], [124].

The matrix between warp and weft is unloaded due to the crack propagating and tow matrix interface failure (Figure 99). Since it is assumed the warp tow behaves linear-elastic the overall stiffness of the unit cell model becomes linear, which is reflected in Figure 100 and Figure 101. Figure 100 shows the stress distribution in the unit cell at maximum global strain, with stress in the matrix at almost zero. The force distribution between the matrix and the warp tow against global strain are shown in Figure 101. After a strain level of about 0.01 the force taken by the matrix remains almost constant while the overall force as well as the force taken by the warp tow continue to rise at the same rate, which shows that increases in axial force are taken by the warp tow only and not by the matrix.
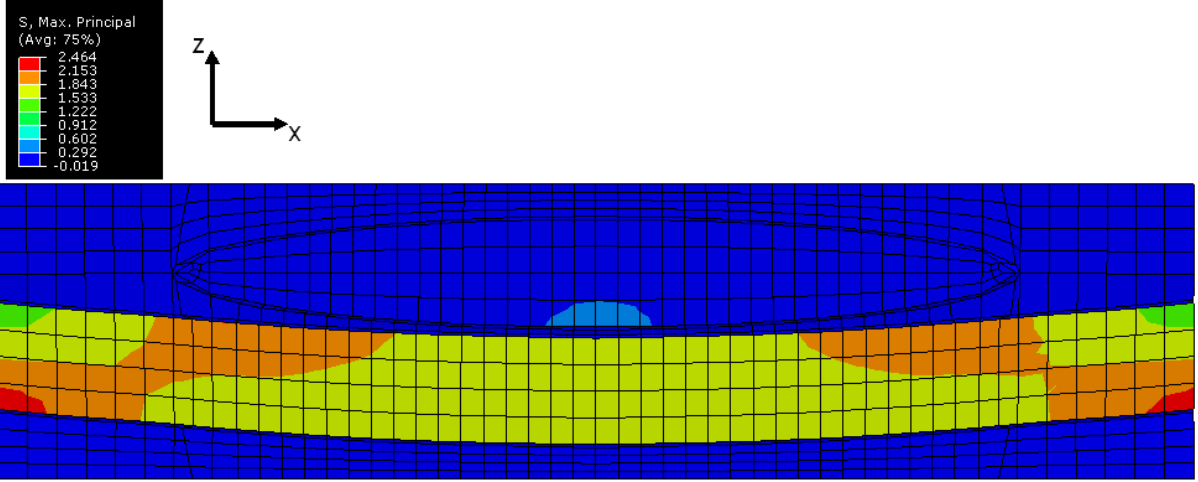
Figure 100: Stress distribution at the centre of the unit cell at 0.025 global axial strain
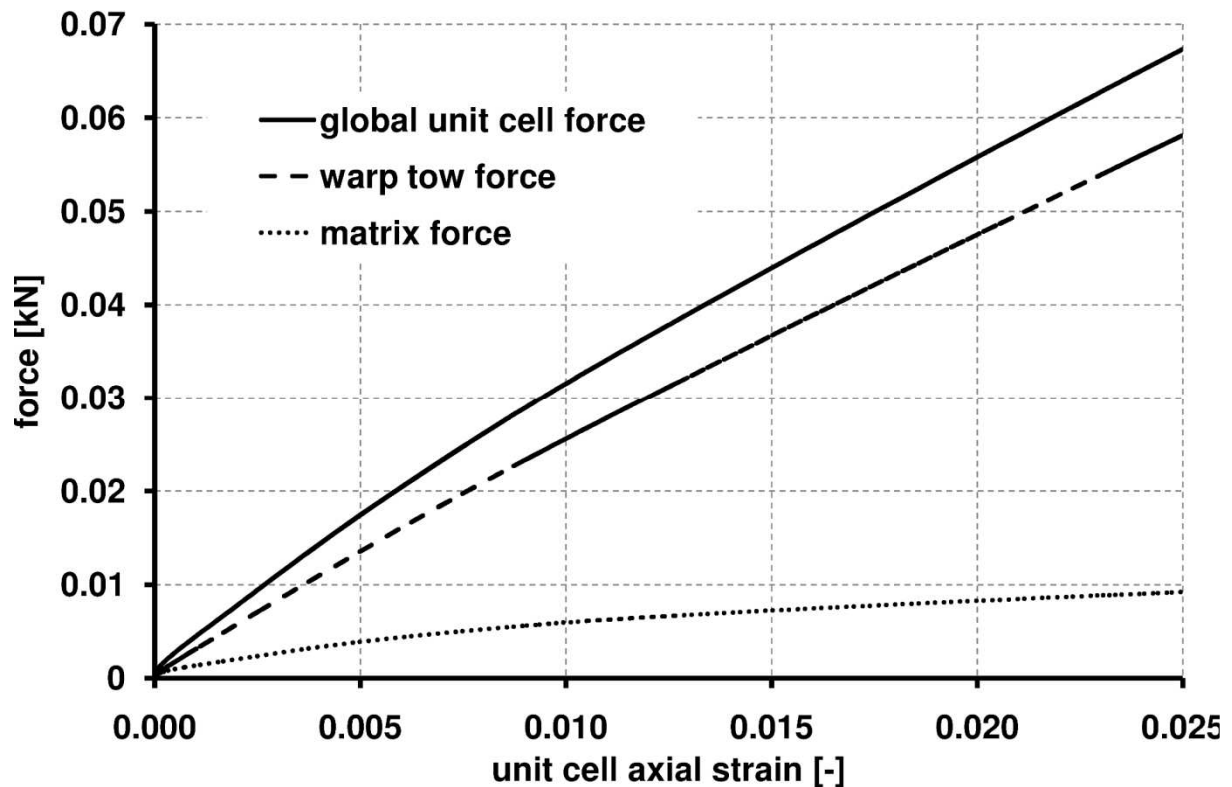
Figure 101: Force distribution between matrix and warp tow under axial tension

Figure 102 shows the predicted stress – strain curve for the tensile loadcase, which is almost linear up to the end of the analysis at 0.025 global axial strain, the failure value of the composites specimens loaded in tension. The stress – strain curve is nonlinear with the tangent modulus decreasing 36% from around 23 GPa to around 16 GPa for an axial strain of about 0.01, which is consistent with the findings on the force distribution within the unit cell over the entire strain range. For strains between 0.01 and the final strain of 0.025 the stress – strain curve stays linear with the tangent modulus remaining about 15%. This is because the matrix is almost completely unloaded, due to damage, for strains higher than 0.01 and any further increases in loading is carried by the tows only, for which are assumed to behave linear elastically.
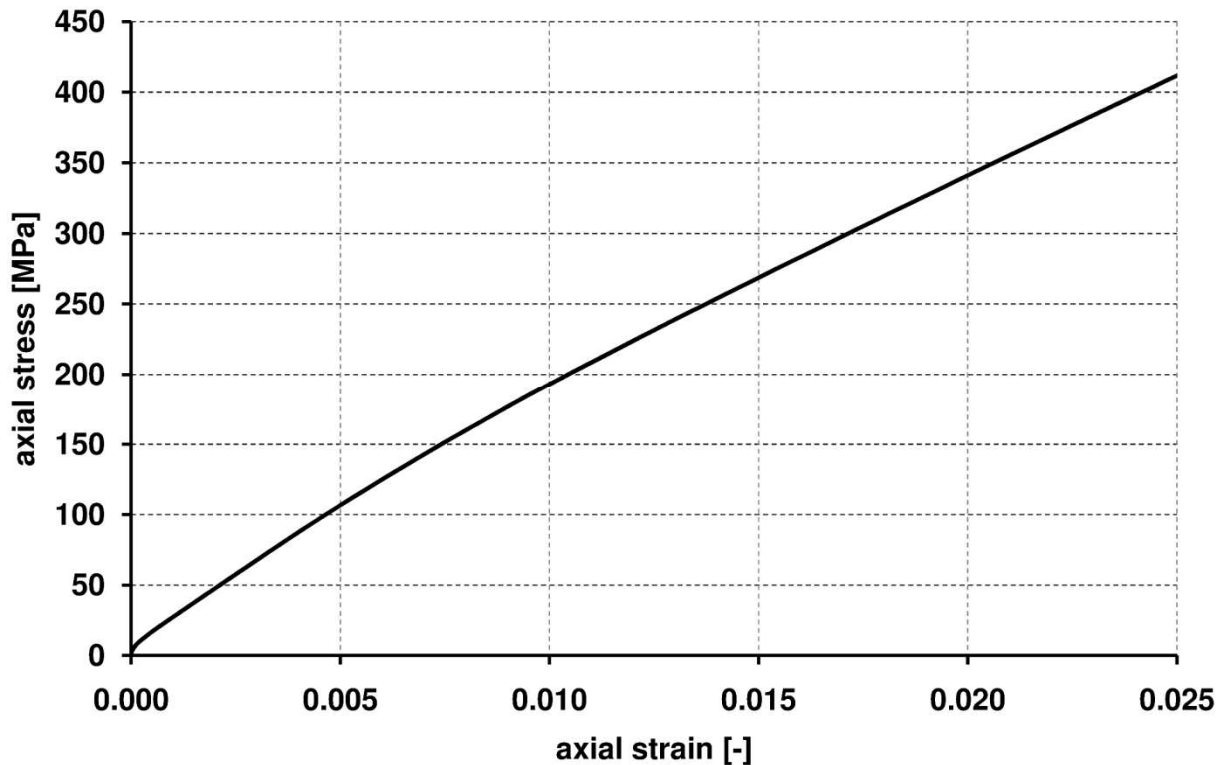
Figure 102: Predicted Stress-Strain Curve

7.1.7.4 Nonlinear Analysis in Shear

The linear analysis showed that the stress concentration points for both the tensile and shear load case are in a similar position. Damage initiation in a similar area and propagation along a similar path was therefore expected. This is supported by the fracture observed for the tensile and shear tests described in chapter 6, where the fracture surface is in a similar position for both types of tests (see Figure 61 and Figure 71).

For the nonlinear shear analysis initial damage in the unit cell occurred within the weft tow. Unlike for the tensile load case damage initiates in the centre of the weft tow (Figure 103) rather than in the matrix at the tow edges (Figure 96). Also, in the tensile analysis damage initiated at the centre of the unit cell first and then spread towards the edge. In the shear load case damage initiates in the weft tow at the edge of the unit cell at the same as time in the centre with damage occurring both in the centre and at the edge of the weft tow (Figure 103). Damage in the matrix does initiate in the centre of the unit cell and then spreads towards the edge of the cell (Figure 103 and Figure 104). Also, the matrix at the surface of the unit cell remains undamaged for longer compared to the matrix in the middle of the unit cell, where

damage initiates at a strain level of 0.0013, compared to a level of about 0.06 at the top/bottom surface (Figure 105). At the end of the analysis, damage has spread through the entire thickness of the unit cell, both in the centre and at the edge (Figure 106).

Interface damage is much more severe in the centre of the unit cell, where it initiates at a strain level of 0.0084 at both interfaces between weft and warp tow (Figure 104). From there it quickly spreads towards the front and back of the unit cell until almost all interfaces have failed at 0.605 strain (Figure 105). At the edge of the unit cell, interface damage is much less severe, with damage initiating at a strain level of 0.605 at the extreme edge of the weft tow where it stays localized until the end of the analysis (Figure 105 and Figure 106).

(a)

(b)

damage initiation
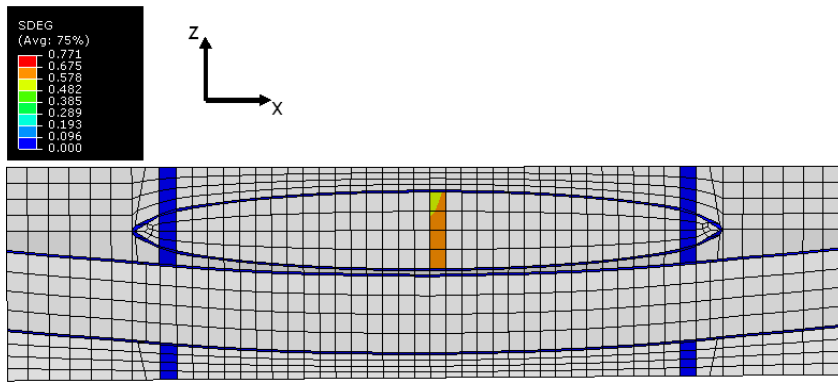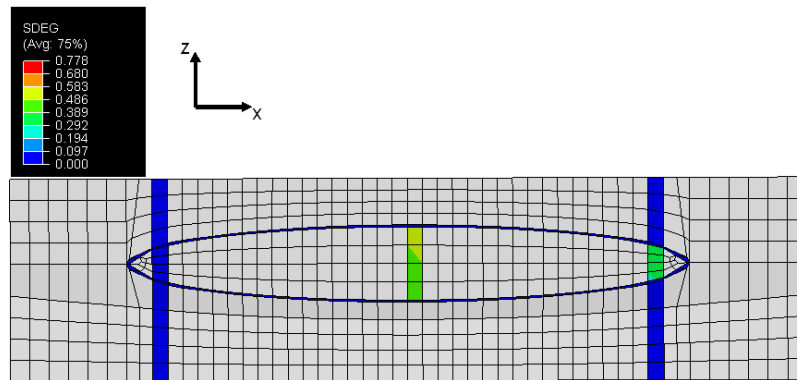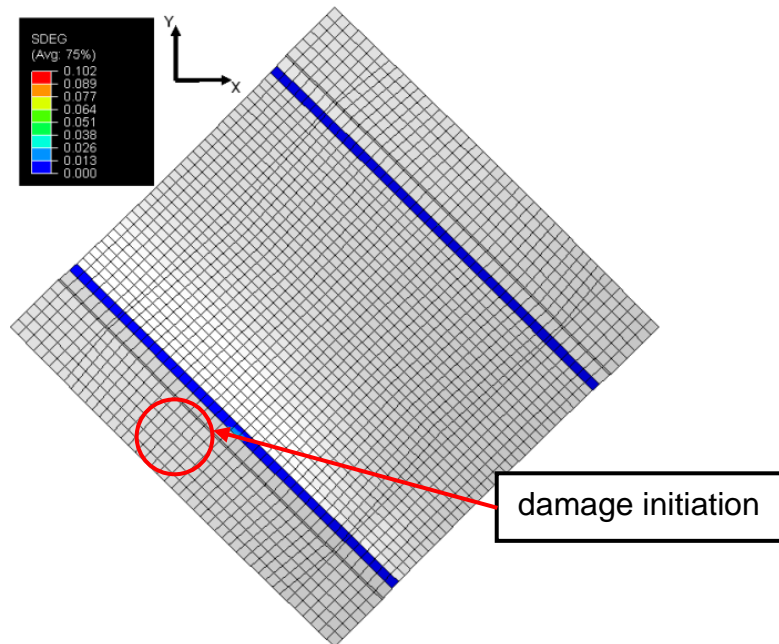
(c)

Figure 103: Damage in unit cell (a) centre surface (b) side wall and (c) middle surface at 0.0013 global shear strain
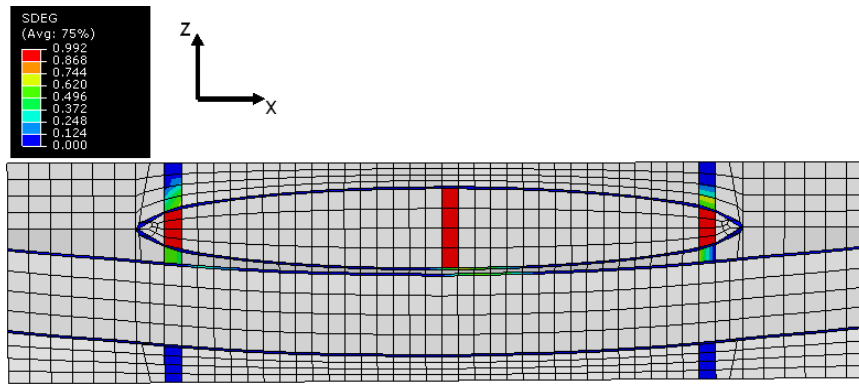
(a)
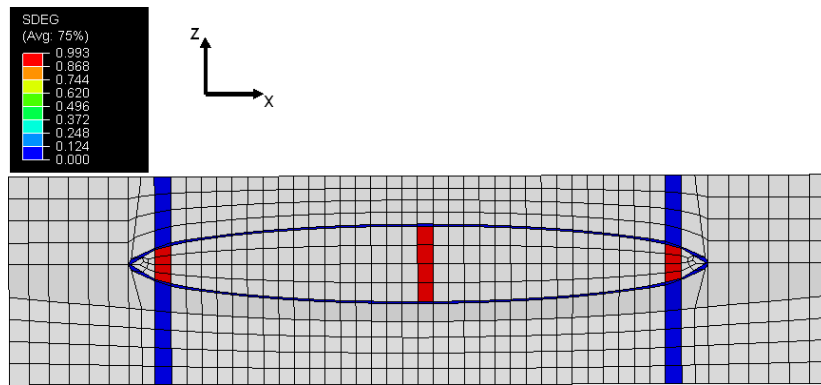
(b)
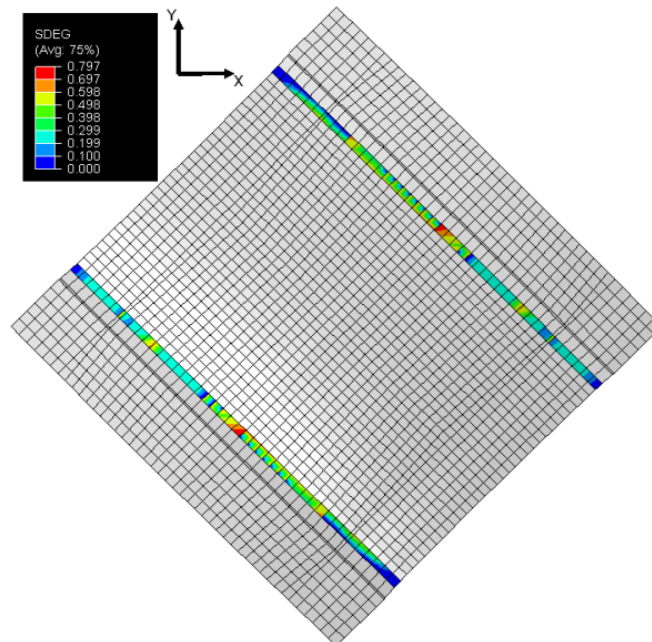
(c)

Figure 104: Damage in unit cell (a) centre surface (b) side wall and (c) middle surface at 0.0106 global shear strain
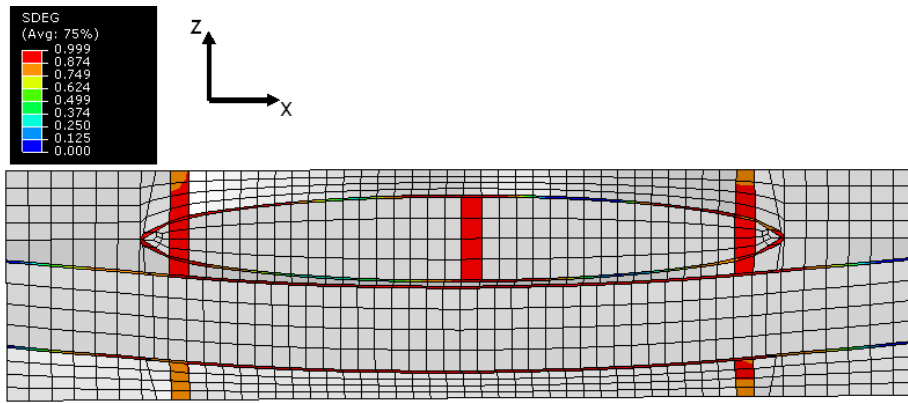
(a)
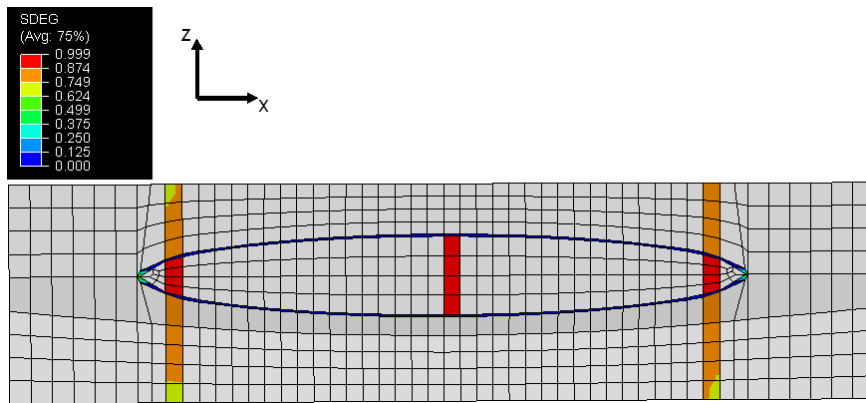
(b)
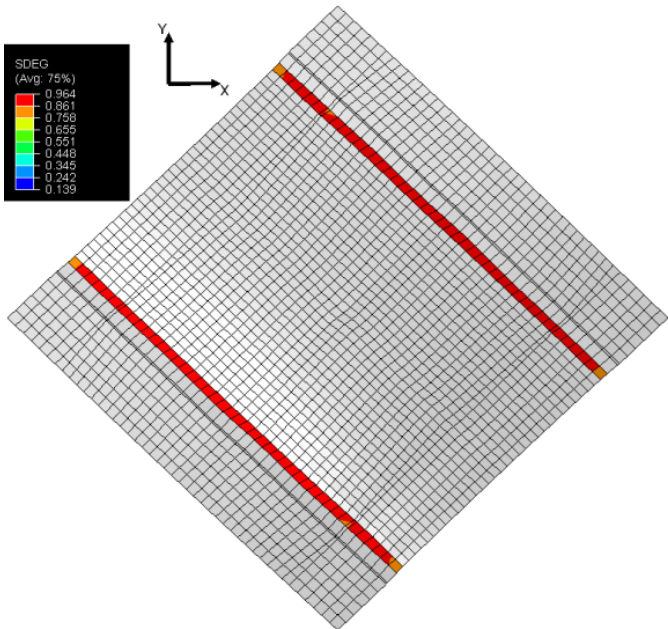
(c)
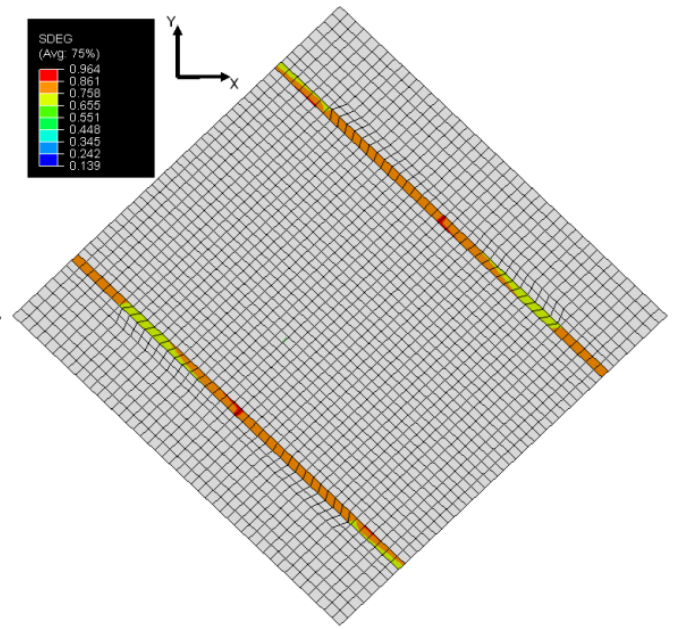
(d)

Figure 105: Damage in unit cell (a) centre surface (b) side wall (c) middle surface and (d) top surface at 0.0605 global shear strain
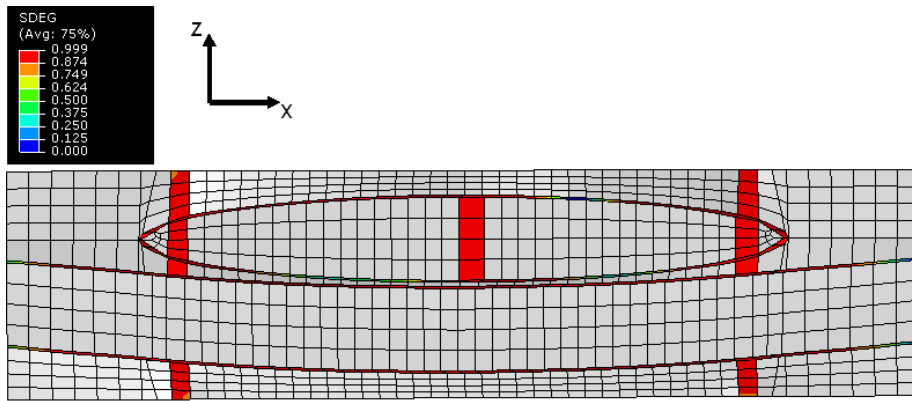
(a)
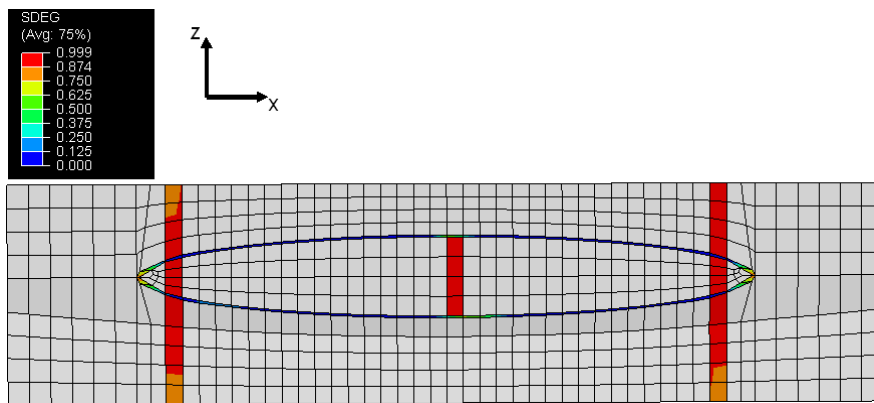
(b)
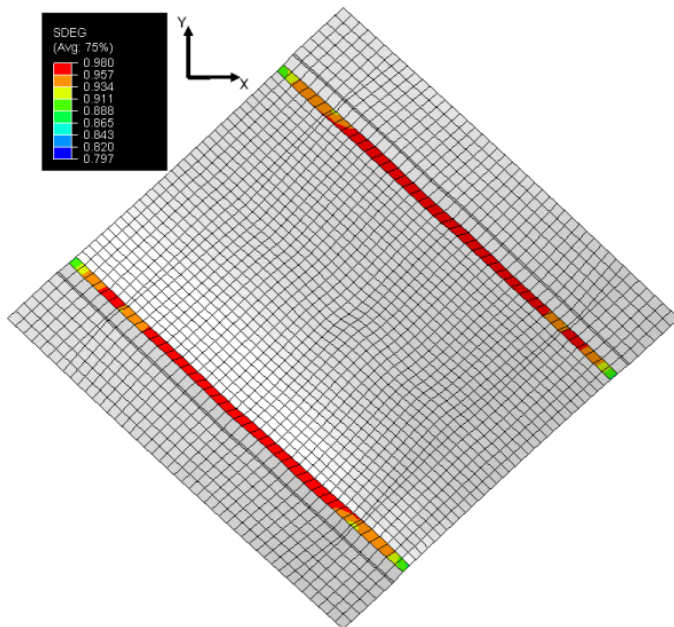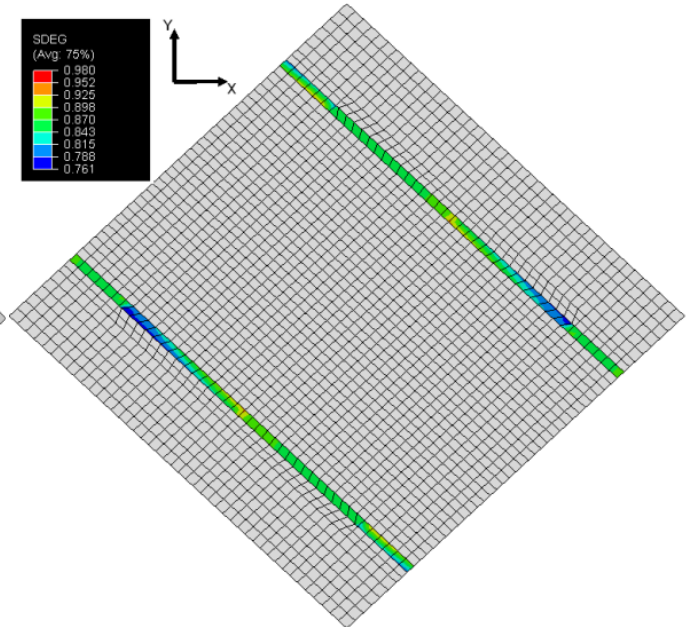
(c)   *(d)*

Figure 106: Damage unit cell (a) centre surface (b) side wall (c) middle surface and (d) top surface at 0.1 global shear strain

Figure 107 shows the max shear stress - principal shear strain curve predicted by the full finite element unit cell model under shear loading, which shows similar behaviour to the axial stress – axial strain curve predicted by the model under tension. The curve behaves nonlinear for small strains from 0 to 0.02 shear strain with the shear modulus decreasing by around 10% from about 2.3 GPa to about 2.1 GPa and then stays constant at about 2.1GPa until the final strain of 0.0775 shear strain. This is for the same reason as for the behaviour of the axial stress – strain curve. With increasing damage the stiffness of the matrix decreases and additional loads are only taken by the tows which are assumed to be behaving linear elastic. However, due to the shear loading of the unit cell the tows are partially loaded in compression, which should lead to a significant decline in tow stiffness due to local fibre buckling in the tow, which is not captured by the full finite element model as has been discussed in section 7.1.7.2 of this chapter. The predicted shear stress – strain curve should therefore be significantly stiffer than the experimentally measured shear stress – strain curve.
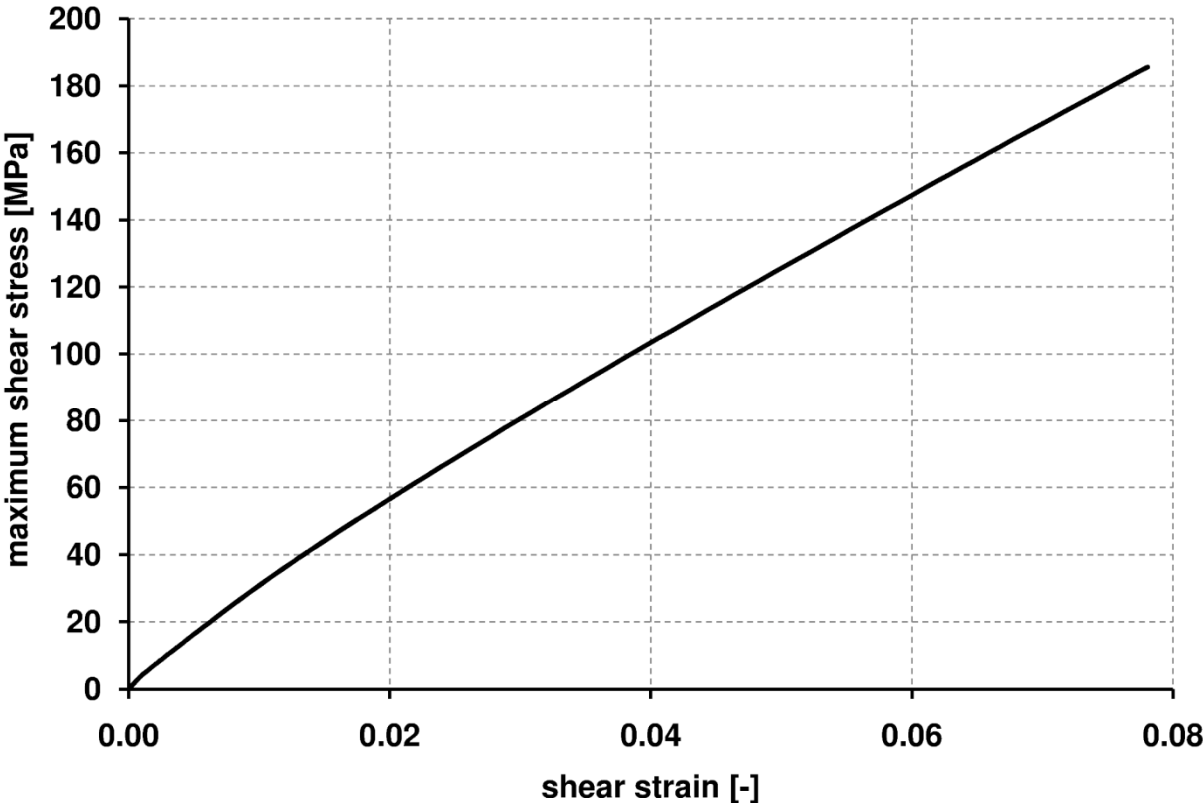
Figure 107: Predicted Shear Strain – Shear Stress Curve

7.1.8 Summary

Theoretical stress-strain curves have been generated and for the pure tension load case, which will be used as input parameters to formulate an equivalent binary unit cell model, meaning a model of the same unit cell using the binary model approach, with global mechanical properties that closely match the global mechanical properties of the full finite element unit cell model.

Generally, the full finite element model has shown that the state of stress in the unit cell is rather complex. This could severely affect the accuracy of the full finite element model since tow and matrix materials are assumed to behave linear elastic whilst in reality they can deform plastically under complex states of stress [136]. Also comparison of the predicted stress distribution within the unit cell with TSA data suggests that the full finite element model is not correctly predicting the stresses in weft direction with a major stress concentration not captured by the model. This is due to the use of 3D solid elements to model tows which allow for the transfer of shear stresses within the tow where this should not occur. The transfer of shear stresses within the tow results in a much stiffer response when loaded in compression or shear. This is the case for both the tensile load case, where the weft tow is loaded in compression due to Poisson's effect, and the shear load case, where both warp and weft tow are loaded in shear and compression.

7.2 Binary Model

7.2.1 Binary Unit Cell Model

Considering the computational costs of modelling a single unit cell using the full finite element approach discussed in the previous chapter, trying to model a macrostructure using the same approach is unreasonable. A way of modelling the behaviour of a single unit cell has to be found, which is less computationally expensive.

Substructuring, also called superelement, is sometimes used to define a cell which behaves equivalent to a more complex structure. For this the stiffness matrix of an entire area is calculated and only the dof on the cell boundary are retained. Some codes, e.g. ABAQUS/Standard, even allow for a repeated use of a substructure, e.g. a unit cell, within an analysis. This would be computationally efficient since the

stiffness matrix for the unit cell only has to be calculated once [130]. However, substructures can only be used for linear elastic parts of a structure [130] and are therefore not suitable for the use in this thesis.

The binary model [84]-[89] is another way of modelling a unit cell without a high demand for computational resources. It uses only nine elements in total (Figure 108), one three dimensional solid element and eight one dimensional spring elements, a total of 54 dof, compared to 39,032 three dimensional solid elements, a total of 117,096 dof, used in the full finite element approach. The nodes of the one dimensional spring elements are coupled to the nodes of the solid element using the ABAQUS "Embedded Element" keyword [130]. With this keyword the displacement of the spring elements are calculated from the displacement of the solid element nodes depending on their position within the solid element using interpolation functions. The disadvantage of the binary model is that the stress field within the unit cell is not predicted in great detailed but in an averaged manner, which is not suitable for estimating the initiation and propagation of damage.

In this chapter a unit cell is modelled using the Binary Model Approach [84]-[89]. Mechanical properties for that representative volume element or equivalent binary unit cell model are derived from stress and strain data predicted by the full finite element model for that unit cell in the previous chapter. Multiple equivalent unit cell models are then assembled to form a macrostructure model of the critical cross-section of the test specimens used in the mechanical tests in chapter 6. Models were reduced to the critical cross-section where failure occurred in the tests in order to save computational time. The stress – strain relationships, predicted by this macro-scale model are then compared to the tensile and shear test results for validation.
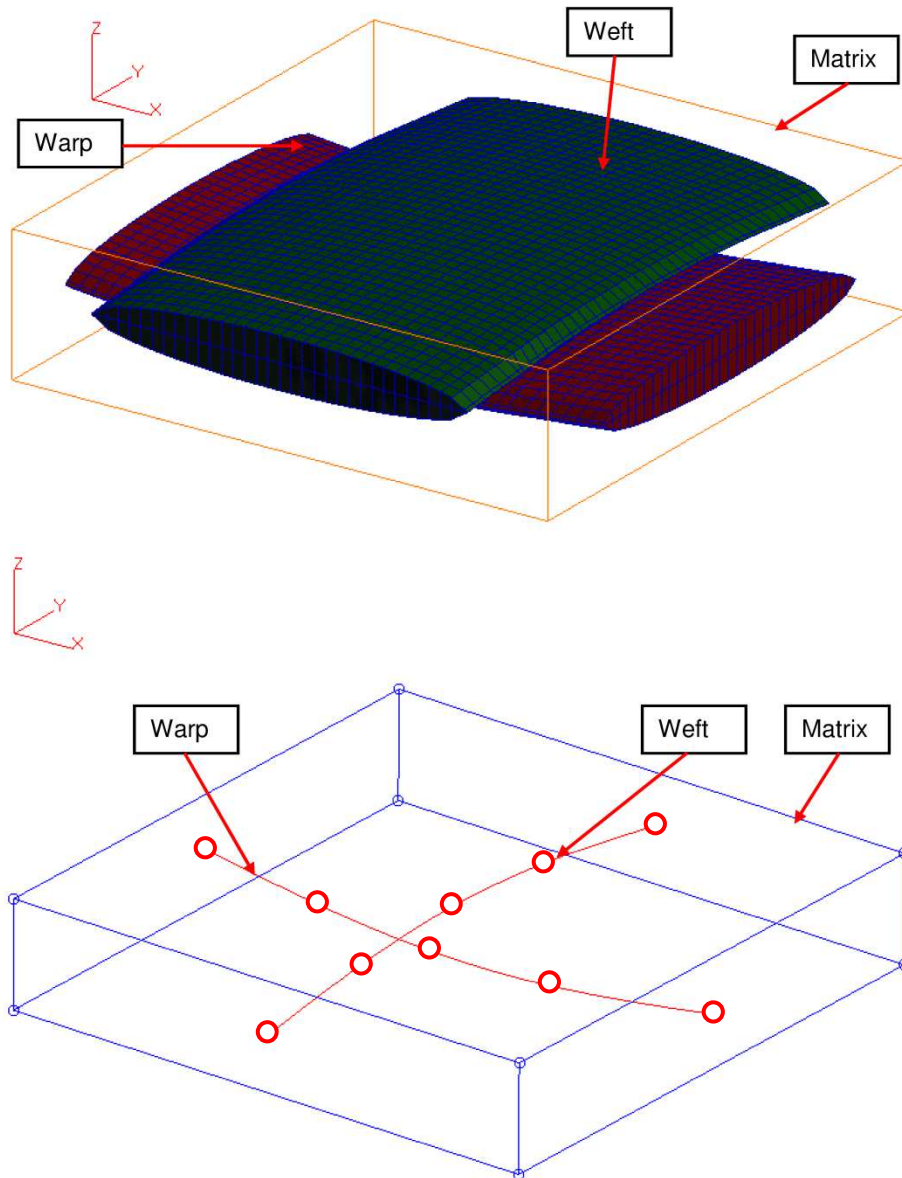
Figure 108: Full finite element model and binary model on the meso –scale

7.2.1.1 Boundary Conditions

Assigning the same boundary conditions as for the full finite element model to a single equivalent unit cell was not possible because only a single three dimensional solid element was used and therefore no centre node existed which could be constraint in all three translational degree of freedom. In theory it would be possible to use more than one solid within a single equivalent cell but this would significantly increase the number of dof and therefore the computational costs. If eight solids instead of one were to be used within one equivalent cell, the number of dof would increase from 54 to 87, an increase of about 61%, which would have a significant

effect on computational costs when a macro-structure is modelled using a large number of equivalent unit cells.

Therefore a block of eight equivalent binary unit cells was modelled so the same boundary conditions could be applied (Figure 109). This block of equivalent binary unit cells had a total of 72 elements (594 dof), eight three dimensional hexa element and 64 one dimensional spring elements.

Two analyses with different boundary conditions were conducted. In the first analysis the boundary conditions for the block of eight equivalent binary unit cells (Figure 109) are the same as for the full finite element model in tension, meaning a progressive displacement of 0.04 mm is applied to the block's yz faces in positive and negative x-direction, which equals a strain of 0.025 over the entire block. All other faces are kept straight using the *EQUATION keyword functionality in ABAQUS/Standard to account for the stiffness contributed by neighbouring unit cells in the composite specimens tested during the tensile and shear tests (chapter 6).

Since the submodelling technique was used to assign boundary conditions to the full finite element model (see chapter 7.1.3), the same technique was used to assign boundary conditions to the equivalent binary unit cell model. Displacements of nodes in the centre of a macrostructure binary model, estimated using Cox's initial binary unit cell model [84], are assigned to the boundaries of the eight unit cell block model (see Figure 109) using the same technique used to assign boundary conditions to the full finite element model.

For both the tensile and shear load case displacement were assigned in an incremental manner to allow for the update of element stiffness matrices with increasing strain. In both cases the automated increment size feature available in ABAQUS/Standard was used to determine a stable increment. However, increment size was limited between 1.0E-5 and 1.0E-2 times the total displacement with a starting increment of 1.0E-3 times the total displacement.
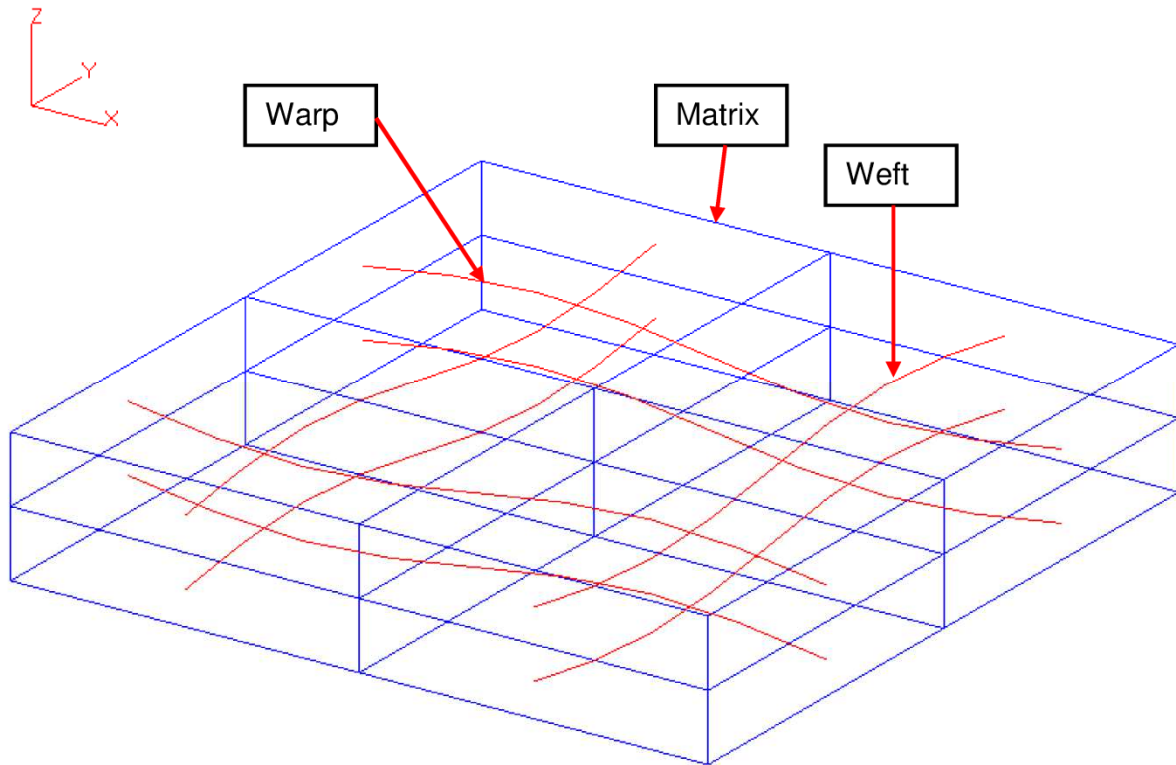
Figure 109: Model testing load – displacement relationship for one – dimensional tow elements

7.2.1.2 Binary Unit Cell Damage Model

Unlike the binary model initially proposed by Cox et al [84]-[89], a novel approach using nonlinear one dimensional elements to model the effect of decreasing stiffness in the unit cell due to damage propagation was used. This means all damage modes observed in the full finite element unit cell model were accounted for in the load–displacement relationship of the nonlinear one dimensional elements. The required stiffness of these one dimensional elements at different strain levels of the unit cell was estimated in an analytical approach, shown in Figure 110 and equations 7-5, using the tangent modulus E_t of the resultant full finite element model true stress – true strain curve, the cross-sectional area of a unit cell A_t and the length of a unit cell L. For this approach one dimensional elements and effective medium elements were assumed to behave like axial springs (Figure 110). Four elements were used to model the axial stiffness of the tow. These four elements (K_{1D}) were assumed to be in series with each other and in parallel with the three dimensional solid element (K_{3D}), which can be calculated using the solid element's Young's modulus E_{3D}. The local orientation of the one dimensional tow elements, which is different than the axial direction of the unit cell, had to be considered when calculating the required stiffness

element since the resultant stress-strain curve of the full finite element unit cell model was derived for the axial direction of the unit cell. This was done using the scalar product of the normalized local tow path tangent vector t with the global axial unit vector e_x.

$$K_t = E_t \frac{A_t}{L} = E_{3D} \frac{A_t}{L} + K_{spring} \qquad (7\text{-}5)$$

$$K_{spring} = (E_t - E_{3D}) \frac{A_t}{L} \qquad (7\text{-}6)$$

$$K_{1D} = K_{spring} \sum_{i=1}^{4} \frac{t_i}{|t_i|} \cdot e_x \qquad (7\text{-}7)$$
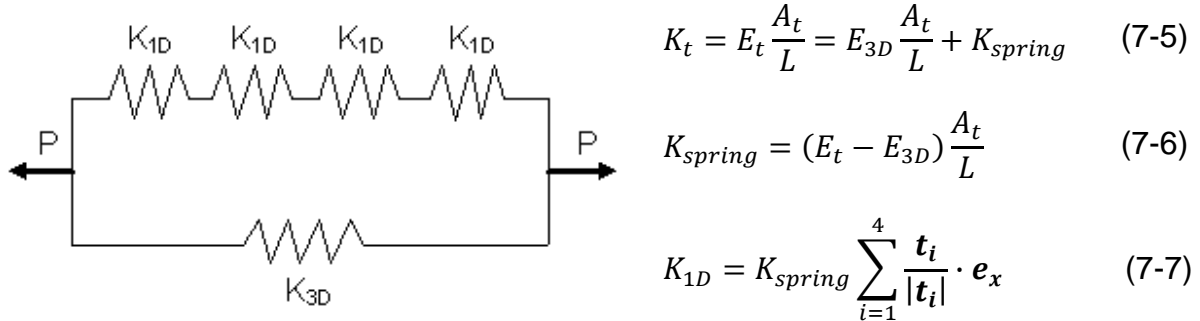
Figure 110: System of Springs Representing the Binary Model Unit Cell in Tension

A similar approach, shown in Figure 111 and equation 7-9, was used for the shear load case. The two lines of springs running in ±45° direction (Figure 80) were assumed to be in parallel to the solid element and each other while the elements in each line were assumed to be in series.

$$K_t = \frac{E_t A_t}{L} = \frac{E_{3D} A_t}{L} + 2 \frac{4}{K_{1D}} \cos\left(\frac{\pi}{4}\right) \qquad (7\text{-}8)$$

$$K_{1D} = \frac{4t}{\sqrt{2}} (E_t - E_{3D}) \sum_{i=1}^{4} \frac{t_i}{|t_i|} \cdot e_x \qquad (7\text{-}9)$$
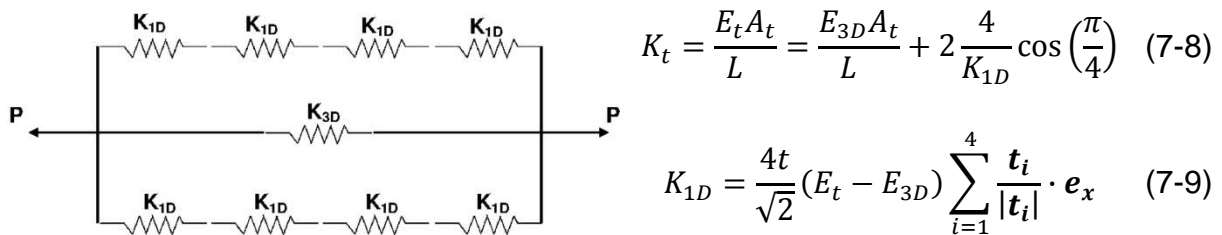
Figure 111: System of Springs Representing the Binary Model Unit Cell in Shear

Caution needs to be taken when using this analytical approach. The resulting force-displacement curve is mesh dependent, especially to the number of one dimensional line elements used to model tow path. Also, the thickness of the full finite element unit cell model, and therefore the thickness of the three-dimensional solid element, needs to be chosen to achieve the fibre volume fraction of the overall composite. Variation of geometrical unit cell parameters as well as nesting, the shift between individual plies, mean that the macro-scale composite is thinner than an equivalent stack of full finite element unit cell models. In order to achieve the same thickness for the same number of plies in the macrostructure binary model, the thickness of the equivalent binary unit cell model had to be reduced to the macro-scale composite thickness divided by the overall number of plies.

It should also be considered that this analytical approach assumes a one-dimensional stress-strain state. However, the stress-strain relationship in the equivalent binary unit cell model is more complex due to Poisson's effect in combination with periodic boundary conditions. For the global tensile load case shear strains in the equivalent binary unit cell model are zero due to the boundary conditions applied. Because of the unit cell model being double symmetric shear stresses at the boundary of the unit cell can be neglected. Therefore the assumption of a one-dimensional stress-strain state is reasonably accurate for small strains even thought the stress state in different positions in the unit cell, especially on the tow matrix interface and between the tows, is more complex. For higher strains however, the stresses in transverse directions due to Poisson's effect become significant and the analytical approach therefore less accurate.

For the shear load case the stress-strain relationship within the unit cell is more complex and the assumption of a one-dimensional stress-state affects the accuracy of the approach when calculating stiffnesses even for small strains.

7.2.1.3 Material Model

As mentioned above, non-linear line elements were used to model tows with an analytical approach used to generate the load-displacement curve. This load-displacement curve was assigned to elements in ABAQUS/Standard using a tabulated spring stiffness material model. The three dimensional effective medium solid element was assumed to be isotropic and linear elastic according to the initial formulation of the binary model by Cox et al [84]-[89] with Young's modulus E and Poisson's ratio v calculated using rule of mixture for a single ply unidirectional (UD) laminate as shown in equations 7-10 to 7-13 [126]. In these equations subscripts M and f denote the matrix and fibre materials respectively and variables G and K stand for shear and bulk modulus. The resulting properties for the effective medium are listed in Table 13, the load - displacement curves are shown in Figure 112 and Figure 114.

$$E_2 = E_M \frac{(1 + V_f)E_f + V_M E_M}{V_M E_f + (1 + V_f)E_M} \tag{7-10}$$

$$G_{23} = \frac{G_M \left[K_M \left(G_M + G_{23_f} \right) + 2G_{23_f} G_M + K_M \left(G_{23_f} - G_M \right) V_f \right]}{K_M \left(G_M + G_{23_f} \right) + 2G_{23_f} G_M + (K_M + 2G_M) \left(G_{23_f} - G_M \right) V_f} \tag{7-11}$$

$$K_M = \frac{E_M}{3(1 - 2v_M)} \tag{7-12}$$

$$v_{23} = \frac{E_2}{2G_{23}} - 1 \tag{7-13}$$

Parameter [unit]	
E [GPa]	7.34
v [-]	0.47

Table 13: Effective Medium Properties

7.2.1.4 Equivalent Binary Unit Cell Model in Tension

For the tensile load case the stress-strain curves derived from the full finite element unit cell model were used, with the analytical approach shown in Chapter 7, to generate nonlinear force-displacement curves for the one-dimensional tow elements. The resulting force – displacement curve is shown in Figure 112. In the figure the spring stiffness, the slope of the force-displacement curve, is degrading with increasing displacement as expected. However, for displacements greater than 0.004 mm, which equals a global tensile strain of 0.005, the increase in force required to increase displacements is linear at a higher value than for displacements less than 0.004 mm, which is due to a number of reasons.

In the full finite element model damage initiated at the weft tow matrix interface and progressed towards the top and bottom of the unit cell. As damage grew to the boundary of the unit cell, the increasing load was carried by the warp tow only (Figure 112). Since the tow was assumed to be linear elastic, the resulting stress-strain curve of the full finite element model became linear, requiring a linear increase in spring force. Also, damage could not progress beyond the unit cell boundary in the full finite element model, which effects the load distribution within the cell. Another assumption

made was that the matrix in the full finite element model only behaves nonlinear at the position of the cohesive elements. Outside these damage zones the matrix was assumed to behave linear elastic, meaning possible nonlinearities due plasticity effects in the matrix because of complex local stress states were not included in the full finite element model. Furthermore, the effects of differences in stress distribution due to local variations of geometric parameters and boundary conditions of individual unit cells have been neglected. Finally, the analytical approach used to calculate the nonlinear stiffness of the one-dimensional spring elements assumes a one-dimensional stress-strain state. The real stress-strain state in the equivalent binary unit cell model is more complex due to boundary conditions and unit cell architecture.
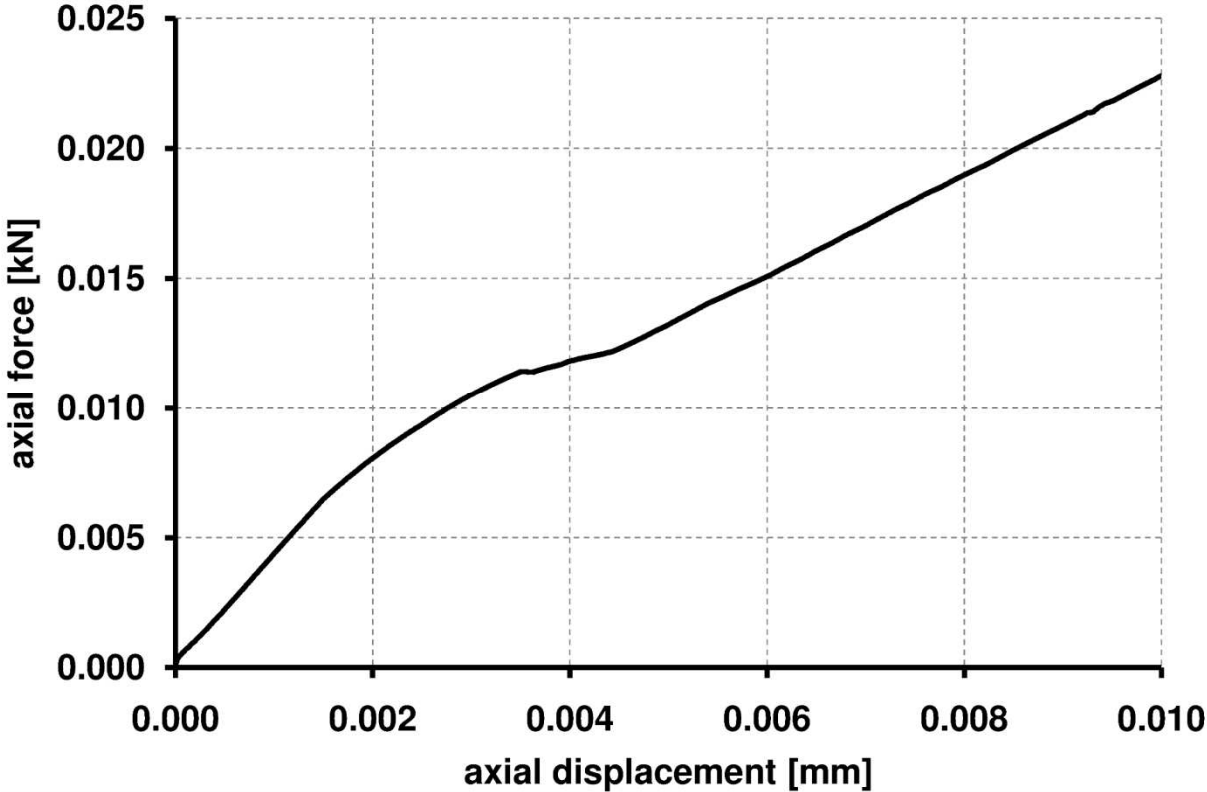
Figure 112: Force – displacement curve of spring elements in equivalent binary unit cell model in tension

Comparison of the response of the full finite element model to the response of the binary in the axial direction is shown in Figure 113. For the tension load case good correlation was achieved for the majority of the strain range with a deviation of less than 1% for strains up to about 0.015. However towards larger strains the correlation is less good with deviations of up to 4%. This can be explained by the unusual shape

of the load-displacement curve that was used as an input to calculate the one-dimensional tow element stiffness, which has been discussed earlier.
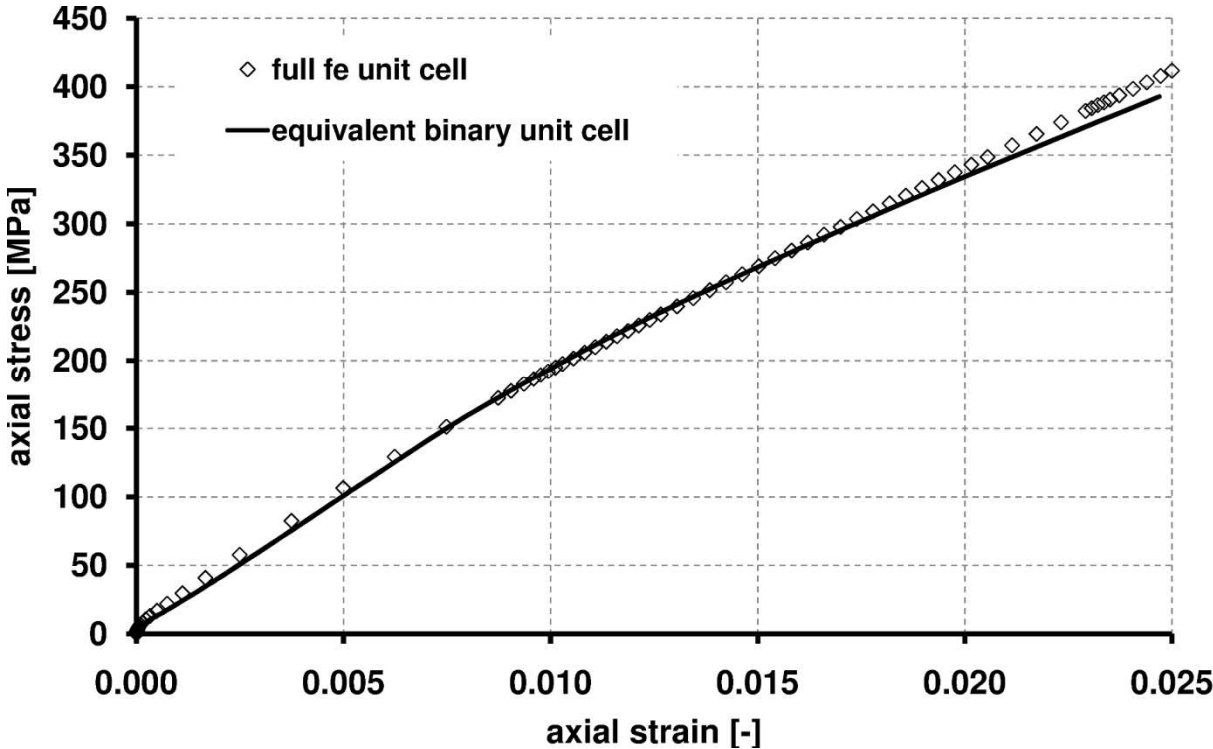
Figure 113: Stress – strain curve of equivalent binary and full finite element unit cell model for the tension load case

7.2.1.5 Equivalent Binary Unit Cell Model in Shear

The stress-strain curve resulting from the full finite element model in shear was used, with the analytical approach shown in equation 7-6 to calculate the spring force displacement curve shown in Figure 114. The slope of the curve, which is a measure for the spring stiffness, is initially decreasing up to a displacement of about 0.01 mm, which equals 0.028 of global shear strain and a force level of about 26 N, and then increasing again up to over 0.015 mm, a global shear strain of 0.078 and a force level of 45 N. The reasons for this behaviour are the same as for the resulting load – displacement curve of the tensile load case. Additionally, both weft and warp tow are partially in compression which is not represented correctly by the full finite element model as is discussed in 7.1.7.2.
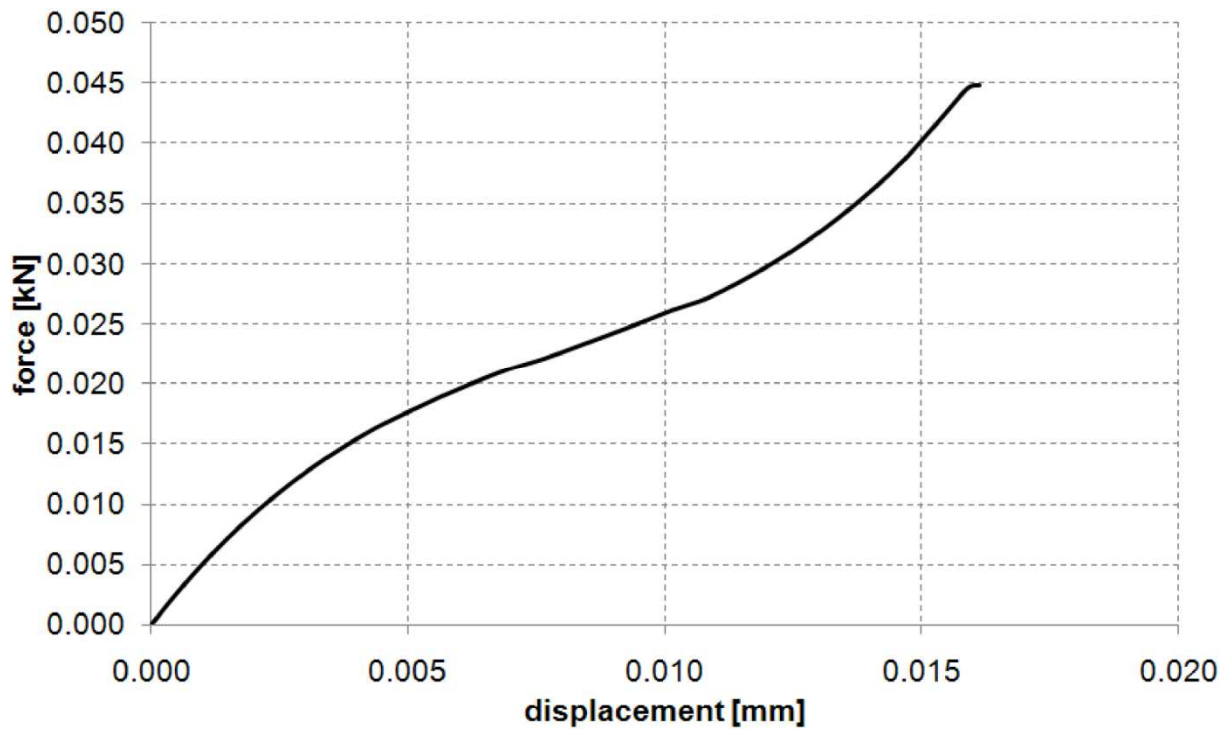
Figure 114: Force – displacement curve of spring elements in equivalent binary unit cell model in shear

The resulting force – displacement curves from both analytical approaches are almost coincident for small displacements (Figure 115). Since the test specimens failed at a lower tensile strain in tension, about 0.025, than shear strain in the shear load case, about 0.1, the force displacement curve of the shear load case goes up to higher displacement values. Up to a displacement of 1.8×10^{-3} mm the difference between these two curves is less than 10%. For displacements larger than 1.8×10^{-3} mm the curves start to divert more, at a displacement of 0.01 mm the difference between them is about 13%. However, after separating initially the two curves start to come closer together again for displacements larger than 0.005 mm. The largest difference between the curves, percent-wise, is at a displacement value of about 4.2×10^{-3} mm with a difference of about 27%.
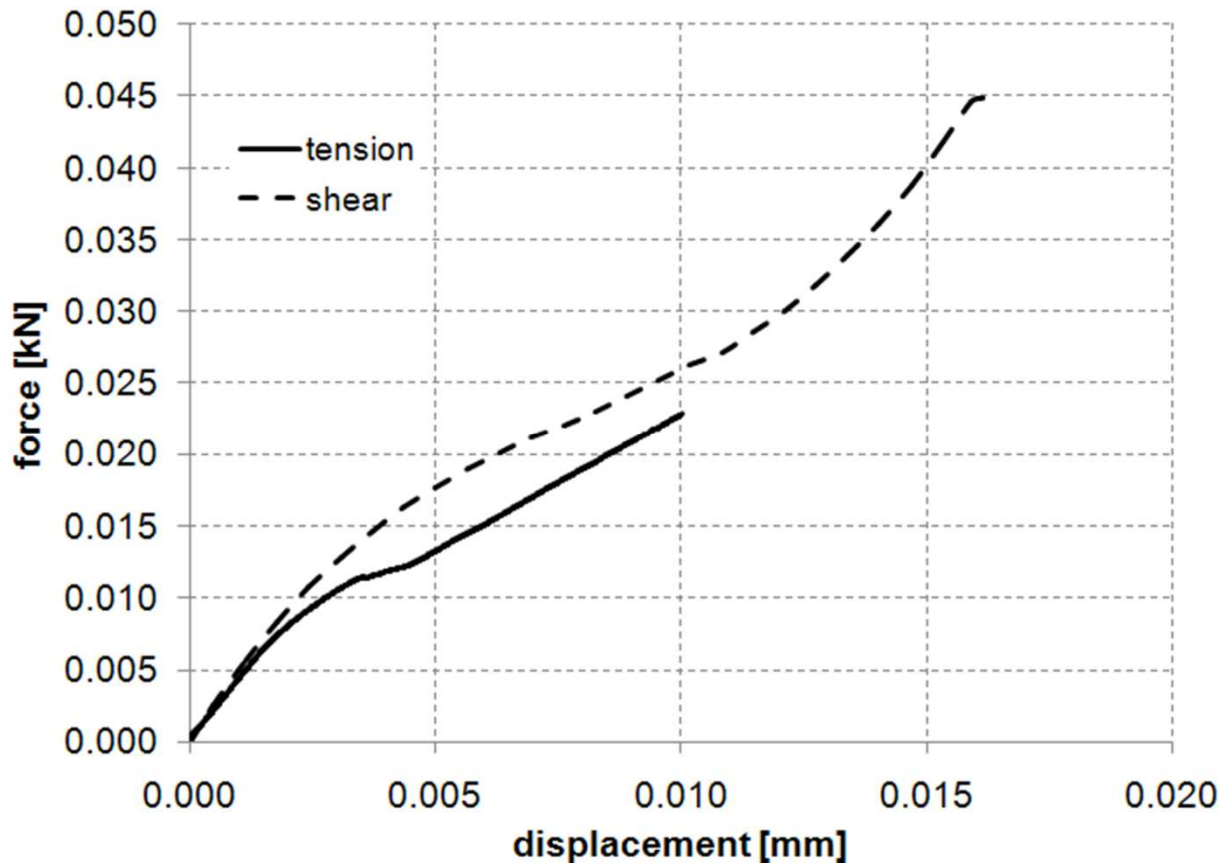
Figure 115: Comparison of Force – Displacement Curve for Tension and Shear

Unlike for the tensile load case, which deviated from the behaviour of the full finite element model by less than 5% even up to failure strain levels, the equivalent binary unit cell model does not match the behaviour of the full finite element model in shear (Figure 117). The difference between the two models is good for principal shear strains of about 0.02 with the deviation between the resulting stress-strain curves less than 7.5%. For principal shear strains larger than 0.02, the two results start diverging more significantly, over 16% for a principal shear strain of about 0.04, about 20% for a principal shear strain of about 0.06 and more than 22% at a principal strain of about 0.075. Comparing the two resultant shear stress – strain curves shows that the equivalent binary unit cell model gives a stiffer response than the full finite element model. In fact, the resulting stress – strain curve of the equivalent binary unit cell model is almost linear with only a small decrease in stiffness, about 22% compared to about 43% of the full finite element model, with increased loading. This difference is due to the nature of the binary model, where the three dimensional solid element dominates the shear behaviour of the entire cell under pure shear whereas

the one dimensional spring elements, due to their position in the solid element, do not experience much deformation (Figure 116).
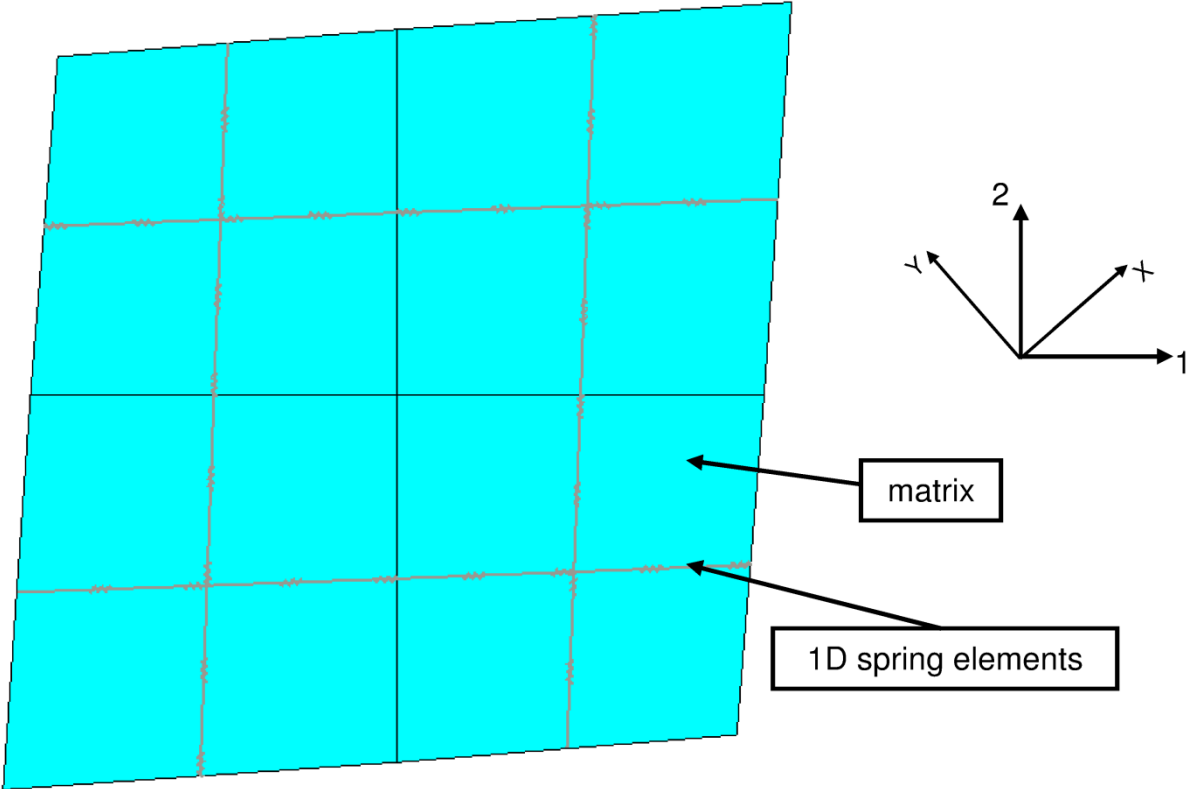
Figure 116: Deformation of Unit Cell Block under Shear Load

However, in the modelling approach presented in this thesis the entire loss of stiffness due to damage in the unit cell is controlled by the nonlinear spring elements while the solid element is assumed to behave linearly. Since the spring elements do not experience much deformation in shear, the linear solid dominates the behaviour of the equivalent binary unit cell model resulting in an almost linear response which is too stiff compared to the full finite element model. In order to mitigate this a nonlinear material model would have to be developed for the solid element, which incorporates the loss of stiffness of the matrix material and the tows due to shear loading.
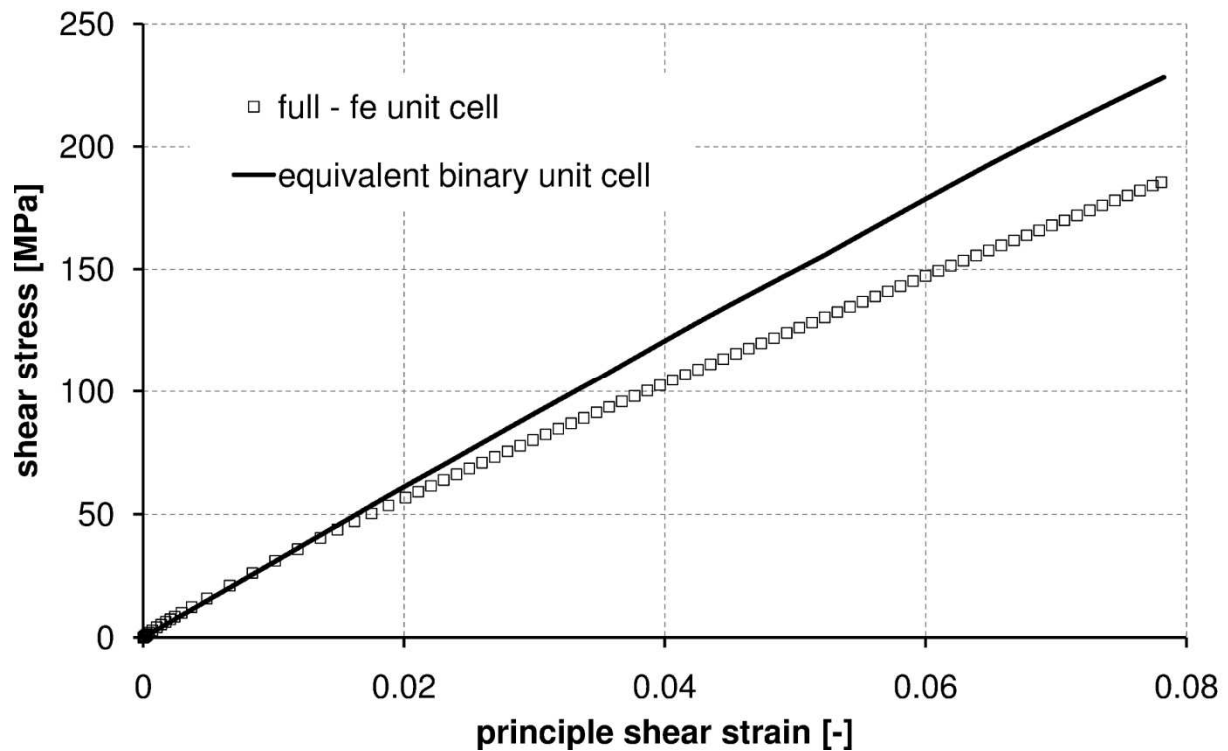
Figure 117: Comparison of Full Finite Element and Equivalent Binary Unit Cell Model for the Shear Load Case

7.2.2 Macrostructure Binary Model

In the final step of the multi-scale analysis the critical cross section of the test specimen (Figure 79) was modelled using the binary model. Nine equivalent binary unit cells were placed next to each other in the transverse and axial direction respectively, which equals a single ply in the thickness direction. Thirty of these plies were used, the same number of plies as in the tensile test specimen. The entire stack is shown in Figure 118. According to the two test setups used in the experimental analysis (Chapter 6), two models were generated with the equivalent binary unit cells oriented in the 0°/90° and ±45° directions.
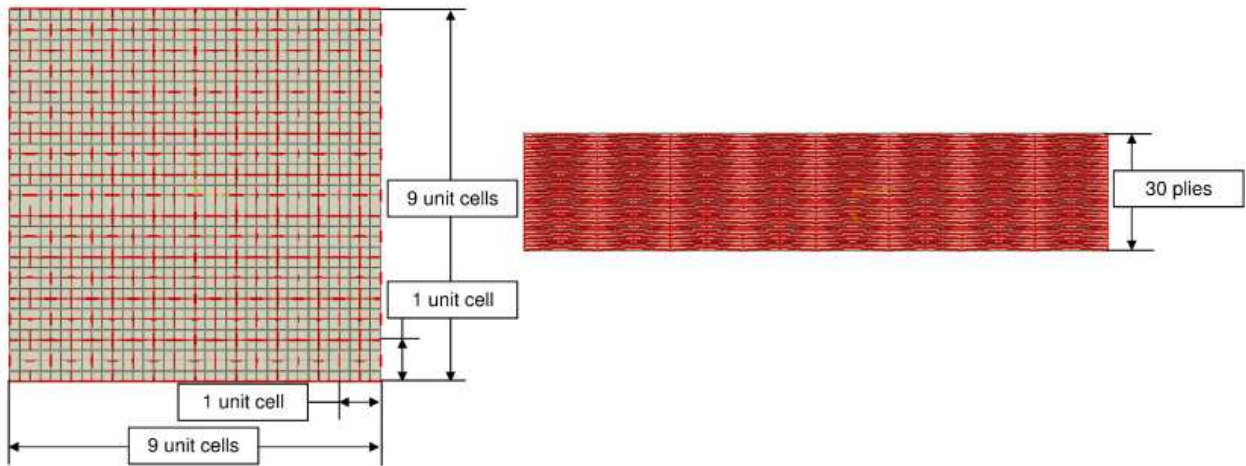
Figure 118: Critical Cross-Section modelled using Equivalent Binary Unit Cells

7.2.2.1 Boundary conditions

Boundary conditions were the same for both models since the global loading condition in both test setups was the same. The only difference between the tensile and the shear tests was the tow orientation in the specimen with the tows being oriented in the 0°/90° for the tensile tests and ±45° for the shear tests.

The applied boundary conditions on the critical cross-section are shown in Figure 119. A uniform displacement was applied to the y-z faces of the model. This condition not only constrained axial movement but also rotation around the z and y axes. The centre node of the model was fixed in both the y and z direction to constrain rigid body motion in both transverse directions. Finally, to constrain rotation around the x axis the two nodes in the centre of the x-z faces were constrained in the z direction.
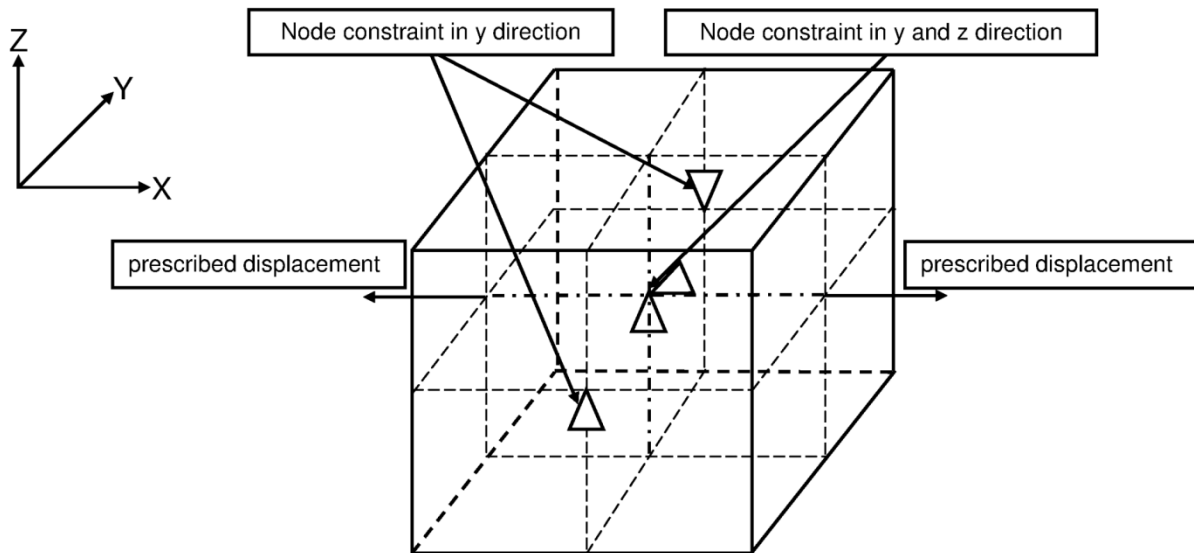
Figure 119: Boundary Conditions on the Critical Cross-Section of the Macro-Scale Binary Model

7.2.2.2 Macrostructure Binary Model Results in Tension

Figure 120 shows the comparison of the macro-scale model with the experimental results for the pure tension load case. Initially the stress-strain curve predicted by the macrostructure binary model follows the averaged experimental stress-strain curve up until to an axial strain of about 0.015. For higher strain levels the predicted stress-strain curve deviates from the mean average, 7% at the extreme, but stays within the experimental bounds.
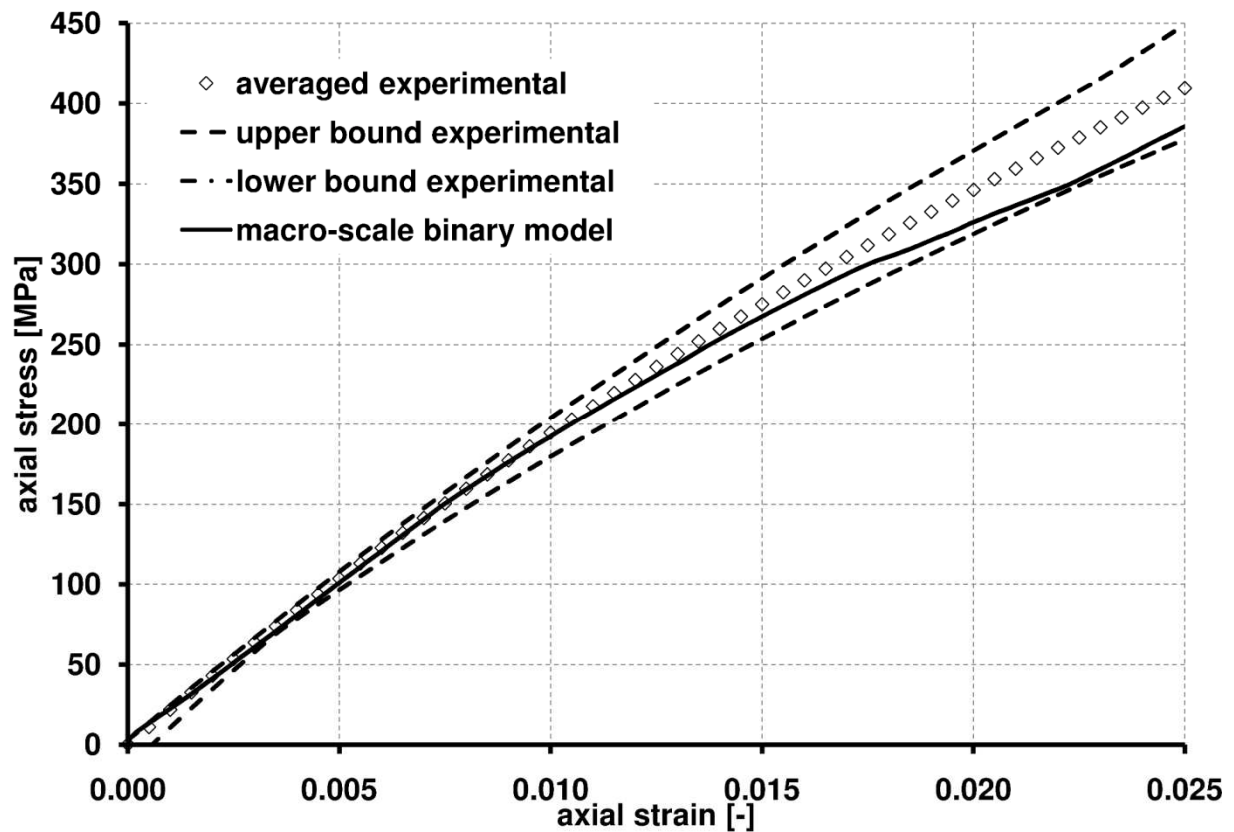
Figure 120: Macro-scale Model Stress – Strain Curve Compared to Experimental Results

This disagreement between numerical and experimental results is due to a number of reasons. In the numerical model cracks cannot grow across the unit cell boundary whereas in the experimental investigation cracks progress outside the boundary of the unit cell into neighbouring cells where they link up with cracks initiating in those cells [25], [27], [116]. Also, crack growth in the unit cells depends on the variation of geometrical parameters [116] and position of the crack within the laminate [64], resulting in different unit cell stiffnesses for a given strain value, which is not captured by the approach outlined in this thesis. Finally, the mechanical behaviour of both constituents in the numerical model is assumed to be linear with linear degradation of selected matrix elements while E-glass fibre tows not only show strain dependent material properties [128] but also plastic behaviour when straightening under tension [33]. Epoxies also show nonlinear behaviour due to plasticity and visco-elasticity for complex states of stress [128], [136].

Figure 121 shows the comparison between the experimentally determined axial strain – transverse strain curves and the predictions made by the macroscale binary unit cell model. The numerical model predictions do not match the experimentally

determined data, initially the predicted increase in transverse strain with increasing axial strain is too low near the origin but then rises above what was determined experimentally. Mean average experimental and numerically predicted curve cross over each other at a strain level of about 0.001 axial strain with the predicted curve becoming too soft meaning transverse strain increases much quicker than the experimental curve with increasing axial strain (Figure 121). The numerically predicted curve changes direction at an axial strain of about 0.013 and again at an axial strain of about 0.0175 to increase sharply towards the end of the curve (Figure 121).

The same factors that result in a deviation of the predicted stress – strain from the experimentally measured stress – strain curve are also contributing to the deviation of the predicted axial strain – transverse strain curve to the experimentally measured axial strain – transverse strain curve. However, these factors are significant enough to result in such a large deviation, meaning another factor has to contribute significantly. This factor is the use of 1D spring elements to model the axial stiffness of tows.
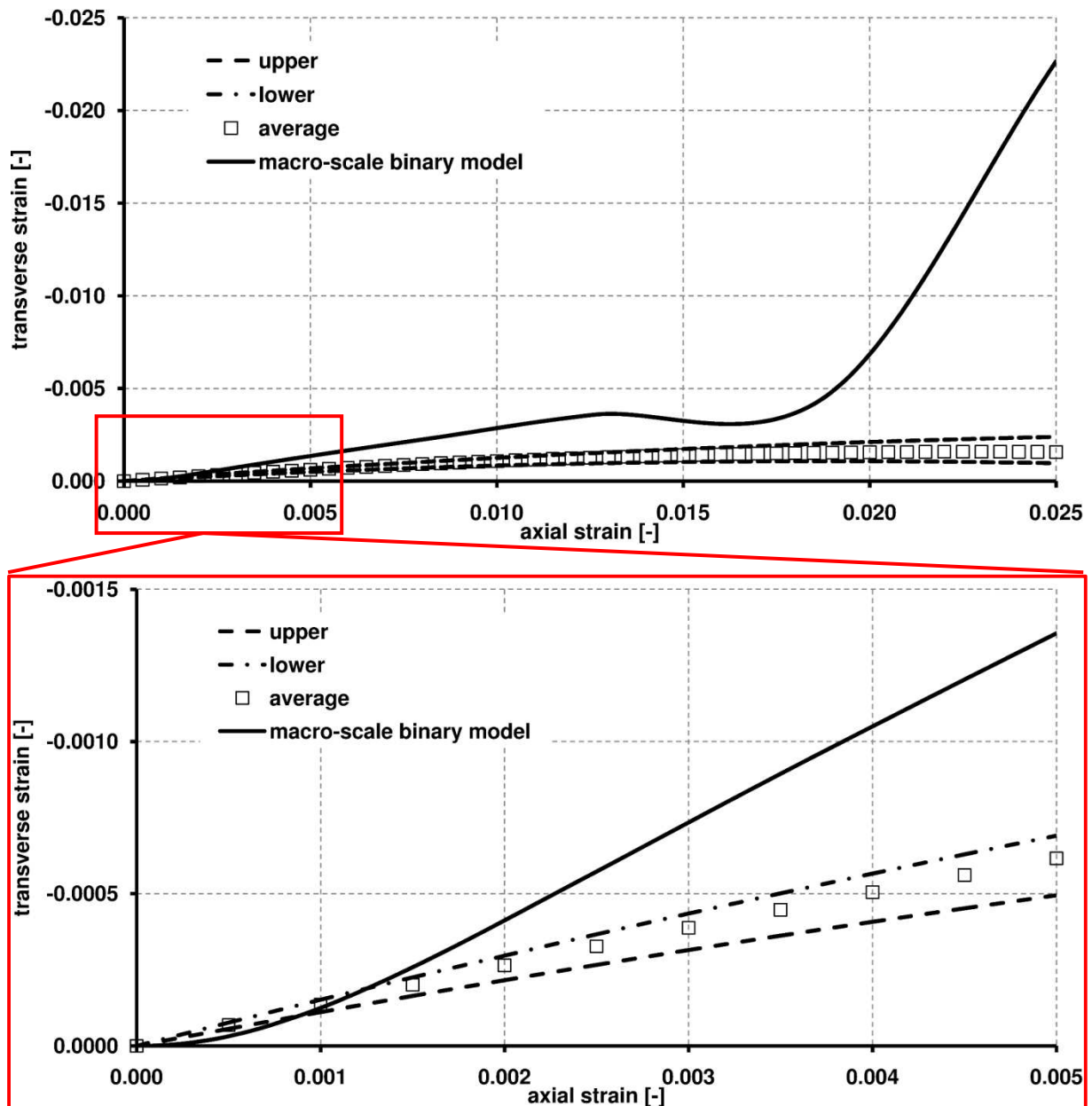
Figure 121: Comparison of Predicted and Measured Stress – Strain Curves in Tension

The node of the 1D spring elements are coupled to the nodes of the 3D solid element the springs using the ABAQUS "Embedded Element" keyword [130], meaning when the solid contracts in the transverse direction due to Poisson's effect the spring is put in compression as the nodes move closer to each other. However, since the tow is undulated the nodes of the 1D elements are not in the same plane as can be seen in Figure 122.
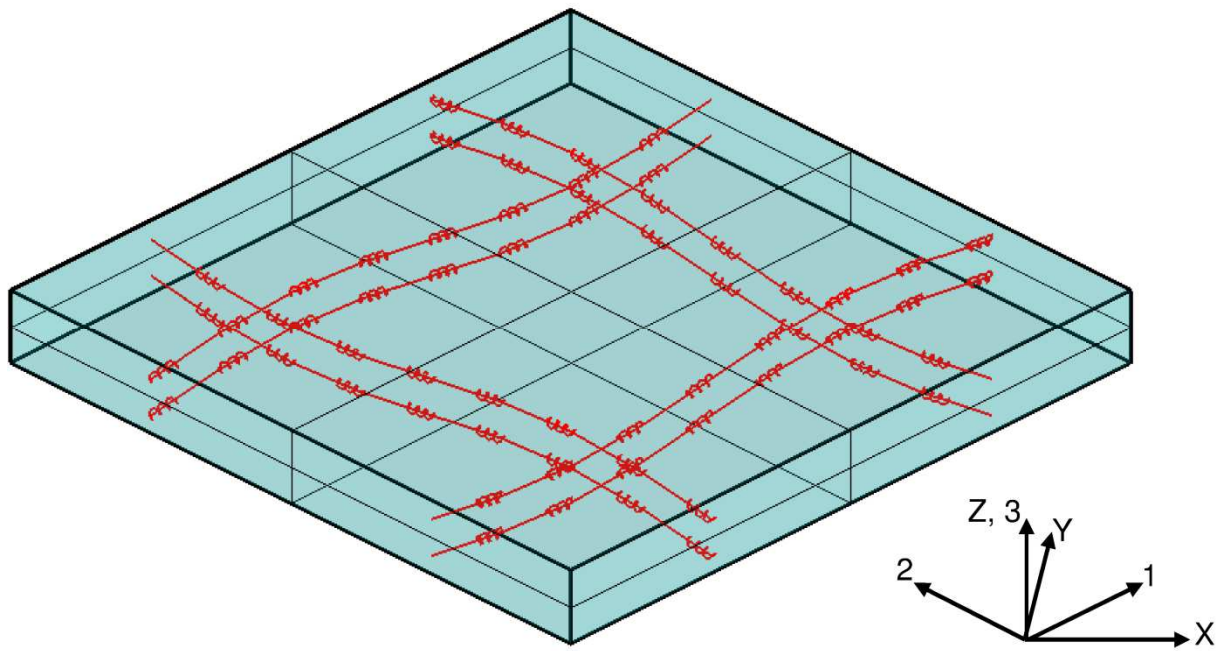
Figure 122: Out of Plane Nodes of Spring Elements in Unit Cell Model

Therefore, when the 3D solid elements contracts the angle between the 1D element nodes changes, rotating the spring axis around the x-axis and therefore. If the solid element contracts further, less of the deformation is in the axial direction of the 1D spring elements, which become less and less effective with increased solid contraction. This is shown schematically in Figure 123. This change in efficiency of the 1D spring element in compression combined with its non-linear behaviour results in the erratic behaviour of the axial strain – transverse strain curve shown in Figure 121.
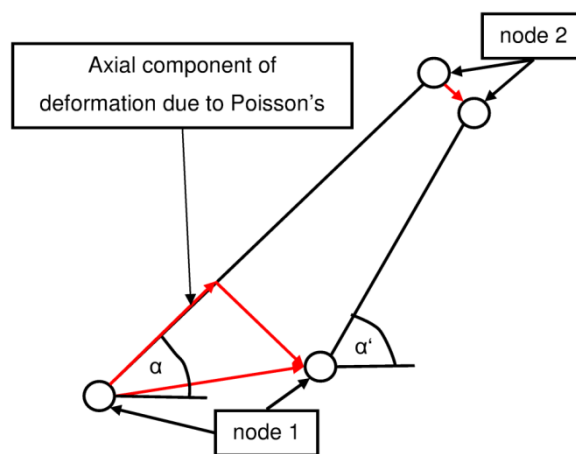
Figure 123: Deformation of Spring Element due to Poisson's Effect

In order for the behaviour described above to become significant, the deformation in transverse direction of the unit cell has to be higher than in the through-thickness direction. Therefore the transverse and through-thickness displacements of two nodes in the centre of the macro-scale binary model (Figure 124) are determined and plotted against the prescribed displacement of the model (Figure 125), where it can clearly be seen that the transverse distance between the two nodes indeed decreases much faster than the distance in the through-thickness direction.
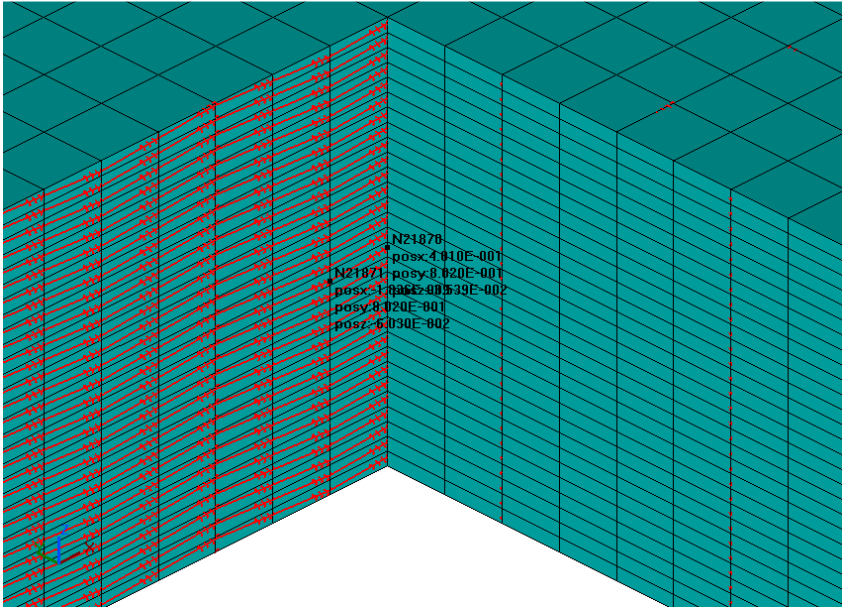
Figure 124: Nodes Selected for Deformation Processing
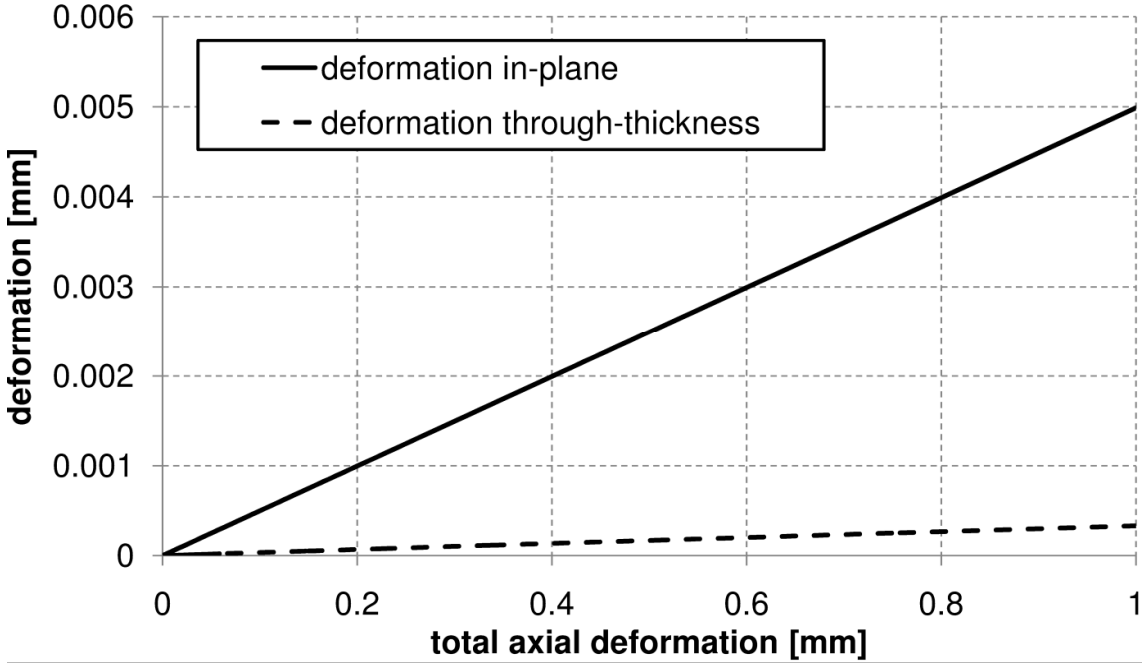
Figure 125: Deformation In-Plane and Through-Thickness

7.2.3 Macrostructure Binary Model Results in Shear
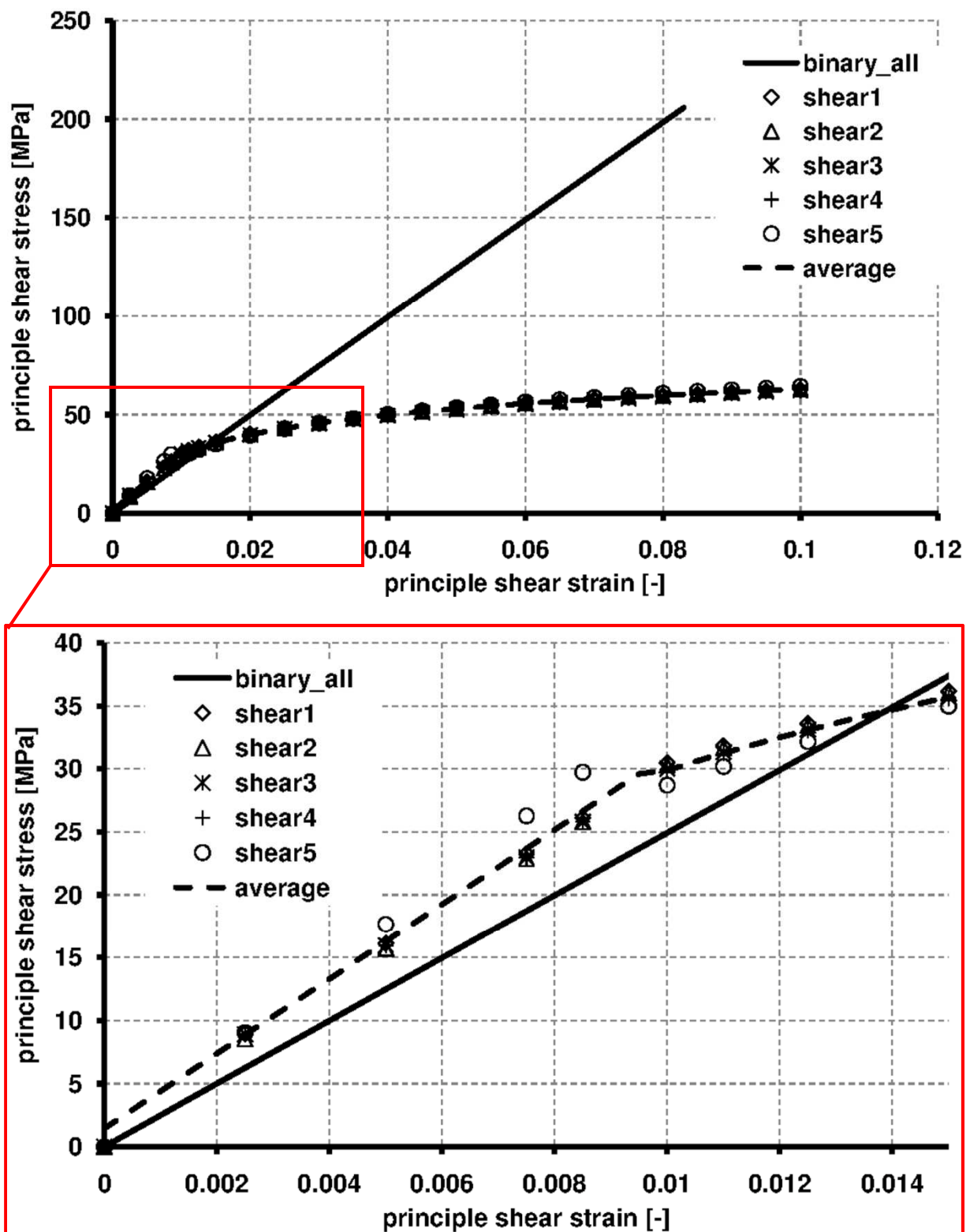
Figure 126: Comparison of Predicted and Measured Stress – Strain Curves in Shear

The resulting stress – strain curve for the shear load case doesn't match the mean average experimental stress-strain curve. Initially the numerical prediction is too soft,

with the shear modulus being 2.5 GPa compared to an experimental mean average of 3.1 GPa, a difference of about 24% (Figure 126). As was predicted in the previous chapter the numerical model predicts a stiffer stress – strain curve than the experimental mean average higher shear strains. The two curves cross at a shear strain of about 0.014. The macrostructure binary model prediction then rises at a higher slope compared to the experimental mean average to a shear stress level of over 200 MPa. While the experimental mean average starts to behave strongly non-linear from a shear strain of about 0.02 with an almost constant tangent shear modulus of 0.24 GPa, the numerical prediction's tangent modulus is about 2.46 GPa, more than 10% higher than the experimental mean average.

The differences between the numerical model and the experimental results in shear are due to the same reasons as for the tensile load case. However, in addition to the linearization of material properties, the inability to model crack growth beyond the unit cell boundary and the assumed simplification of the stress state for the analytical approach used, the full finite element model does not represent the behaviour of warp and weft tows correctly. In the shear load case, warp and weft tows are loaded unevenly with one side being in tension, the other in compression with a non-zero shear stress in the centre of the tow. Unlike for the real tow, which cannot transfer shear stresses between individual fibres in the tows, the 3D solid elements used in the full finite element model do transfer shear stresses across the tow, leading to a much stiffer response, which is included in the non-linear spring stiffness curve for the 1D spring elements in the representative binary unit cell model. This results in a predicted stress-strain curve which is too stiff compared to the experimentally measured stress-strain curve.

7.3 Summary

Stress – strain curves predicted by the modelling method described in this thesis correlate very well with measured data in axial direction for the pure tension load case. However, agreement of predicted behaviour for the transverse direction in tension and in axial direction for the pure shear load case is poor. In both cases this is due to the inability of the full finite element and equivalent binary unit cell models to correctly model tow behaviour under compressive and shear loading. Therefore, better material models and an appropriate micromechanics model are required to

correctly represent compressive and shear behaviour of the tows in the full finite element model. A non-linear material model is also required for the solid elements in the equivalent binary unit cell model to model the effects of shear stresses.

8 Conclusion and Further Work

8.1 Conclusion

In this thesis a multi-scale numerical approach has been developed to model damage initiation and progression for a macrostructure made of a multi-axial composite. In the approach local boundary conditions for a full finite element model of a single unit cell of the composite are derived running a linear analysis, i.e. not modelling damage, of the macrostructure under global loading conditions using the Binary Model as described by Cox et al [84]-[89]. These local boundary conditions are used for a linear analysis using a full finite element model of a unit cell to identify stress concentration points, the points of damage initiation, within the cell. Cohesive elements, which incorporate a damage model based on strain energy release rates, are placed at those stress concentration points within the full finite element model of the unit cell to model damage initiation and propagation within the cell. The resulting stress strain data are then used to define a representative Binary Unit Cell using nonlinear spring elements to account for stiffness degradations due to damage within the cell. The nonlinear force-displacement curve of these spring elements is calculated using an analytical approach. The resulting representative Binary Unit Cell is used then to model the macrostructure to predict the real stress-strain relationship, including damage, for that macrostructure.

Whilst in the past full finite element unit cell model approaches and unit cell based averaged approaches, like the binary model, have been developed, the approach presented in this thesis for the first time combines the two modelling techniques to predict macro-structure behaviour. This allows for the prediction of damage initiation and propagation within complex macrostructures at reasonable computational costs. A short but detailed description of the approach has been published by Römelt and Cunningham [139].

Loads can be redistributed within more complex structures after damage has initiated and starts propagating, which can result in local boundary conditions differing from those of the initial linear analysis of the macrostructure using the Binary Model as described by Cox et al [84]-[89]. The approach suggested in this thesis can be used iteratively, meaning the representative Binary Unit Cell model can be used to update

local boundary conditions for full finite element unit cell models of cells in positions of high loads, where damage is likely to occur, within the structure, with the resulting representative Binary Unit Cell used to update the macrostructure model.

The approach suggested in this thesis requires a number of input parameters, both geometrical and mechanical. Material properties for the constituent materials are required, including the nonlinear behaviour of those constituents for higher strains up until the point of failure. Data for the strength of the interface between the fibres and the matrix for different states of stress are also required. Information on the composite architecture, i.e. tow cross-section and tow path parameters, also needed to be obtained. For this a microscopic analysis was done using a high performance light dependent microscope. In this analysis images of composite samples were taken at two different levels of magnification. Points were placed along the centre of tow paths in images taken at 20 times magnification and along the periphery of tow cross-sections at 80 times magnification. Standard mathematical functions, a sin function in case of the tow path and an ellipse function in case of the tow cross-section, are fitted through the coordinates of these points and mean average values for tow path wavelength and amplitude and major and minor elliptical axis parameter are calculated, which are the used to build a full finite element model of a unit cell.

Model verification is done by comparing predicted stress-strain behaviour for two different loading conditions, pure tension and pure shear, with stress-strain data from coupon tests under the same loading conditions. Further verification was attempted by comparison of the stress distribution on the surface of the unit cell predicted by the full finite element model with the results from a TSA analysis, which measures the stress distribution on the surface of a test specimen using the thermoelastic effect.

Agreement of model predictions with experimentally measured data for transverse strain for the pure tension loadcase and stress-strain for the pure shear loadcase is poor with deviations between the data up to 27% and 22% respectively.

Results from the TSA analysis suggest that the stress concentration due to uniaxial tensile loading in the loading direction is correctly predicted by the full finite element model. However, the model seems to be unable to predict stress concentrations in the matrix transverse to the loading direction. This is most likely due to the use of 3D

solid elements to model the tows, since these solid elements allow for the transfer of shear stresses across the tow, which does not happen in the real-world tow.

The poor agreement with transverse strain and shear stress strain data suggests that both constituent material and tow behaviour in compression and shear are not modelled sufficiently accurate. Other modelling issues, like the behaviour of 1D spring elements in the equivalent binary unit cell model in compression also contribute to the inability to correctly predict transverse and shear behaviour of textile composites. However, comparing experimentally measured stress-strain data for the pure tension load case with the results predicted using the approach outlined in this thesis shows good agreement between the two data sets. For strains of up to 0.015 both data sets deviate less than 5% from each other. For strains larger than 0.015 both data sets start to deviate more with a maximum deviation of about 7% at the failure strain of 0.025. Therefore, the multi-scale modelling approach as it is presented in this thesis provides a solid base for the prediction of the behaviour of textile composites under mechanical loading. Suggestions and further research required to improving the predictive capabilities of the multi-scale approach are made in the next section of this chapter.

8.2 Further Work

8.2.1 Full Finite Element Unit Cell Model

Linear elastic behaviour had been assumed for the tow and matrix in the full finite element analysis due to the fact that no detailed mechanical properties of these materials were available and measurement of the required parameters was beyond the scope of this thesis. However, in order to correctly model the behaviour within the unit cell more detailed material properties of constituent materials and appropriate models are required. Meaning a full material characterization test program, looking at material characteristics and modes of failure, is required. The resulting characteristics then have to be used to generate representative material models that not only take strain level and viscoelastic effects on properties into account but also effects of the material's loading history for fatigue analysis purposes.

Damage in the warp and weft tows, especially for the shear load case, was not modelled. However, experimental work presented in the literature, eg by Cox et al

[32], [34], have suggested that microbuckling of fibres in tows under compressive loading play a significant role in the global behaviour of textile composites. Unfortunately this means that the tow cannot be modelled as a solid continuum. Either a more detailed model of fibres in the tows has to be developed or the instability of fibres in compression has to be incorporated in the material model used for the tow material.

Damage in the matrix material and of the tow matrix interface has been modelled by including cohesive elements at the points of highest stress in the unit cell. This assumes that damage grows along the path of cohesive elements and that no load redistribution takes place during loading. In order to achieve a more general predictive capability, the material models for the finite element code used have to be defined not only to represent the elastic and plastic behaviour of the materials but also have to include a damage model so that the damage path does not need to be pre-assigned by the analyst. This would also capture changes in damage paths due to load redistribution within the cell.

8.2.2 Equivalent Binary Unit Cell Model

Linear elastic behaviour is assumed for the representative medium of the 3D solid element in the representative binary unit cell model while all damage modes are included in the 1D spring elements' load displacement curves. However, this is not efficient since the 1D elements experience hardly any deformation in the shear load case. Improvements in the equivalent binary unit cell model can be achieved by using a non-linear material model for the 3D solid element, which also includes a damage model, so that for loading conditions which are dominated by shear the loss of stiffness is due to the degradation of the 3D solid elements rather than the 1D spring elements.

The analytical approach used to calculate the nonlinear spring stiffness for the spring elements used in the representative Binary Unit Cell Model does not account for Poisson's Effect and even more importantly, does not account for the complex local stress state within the unit cell. Therefore the resulting representative unit cell does not model the real unit cell behaviour for other global stress states than uniaxial tension. If, additionally, the 3D solid element is now assumed to behave nonlinear instead of linear, significant changes will have to be made to the analytical approach

presented here, making for a much more complicated set of equations, which might not necessarily have an analytical solution. Therefore, the analytical approach should be replaced by a numerical approach employing an optimization algorithm. Analyses for a range of different loading conditions should be performed using the full finite element model and the resulting stress-strain curves should then be used to optimize material parameters for both the 3D solid elements and the 1D spring elements of the representative binary unit cell model. For this the same loading conditions can be applied to an eight cell equivalent binary unit cell model and the material properties of the equivalent binary unit cell can be adjusted to closely fit the resulting stress strain curves to the stress – strain curves predicted by the full finite element unit cell model.

Kink band formation is a macroscale localized buckling phenomenon of a bundles of tows and the primary failure mode for textile composites loaded in compression [32]. Because it is a macroscale phenomenon, it cannot be modelled in the full finite element or the equivalent binary unit cell model but must be incorporated in the macroscale binary model. This posses quite a problem since kink band formation is triggered by large scale tow matrix debonding, a phenomenon that starts at the microlevel. Cox et al [87], [88] have suggested using a strain averaging technique coupled with an empirical criterion for kink band formation but this method is still in its infancy. However, this mode of failure has somehow to be included into a working modelling approach.

9 References

[1]   Kamiya R, Cheeseman BA, Popper P, Chou TW. Some recent advances in the fabrication and design of three-dimensional textile preforms: a review. Composites Science and Technology 2000:60;33-47

[2]   Dr. A. Brent Strong. Fundamentals of Composite Manufacturing: Materials, Methods, and Applications. Society of Manufacturing Engineers 1989

[3]   Bogdanovich AE. Multi-Scale Modeling, Stress and Failure Analyses of 3-D Woven Composites. Journal of Material Science 2006:41;6547-6590

[4]   El Hage Ch, Younes R, Aboura Z, Benzeggagh ML, Zoaeter M. Analytical and numerical modelling of mechanical properties of orthogonal 3D CFRP. Composites Science and Technology 2009:69;111-116

[5]   Leong KH, Ramakrishna S, Huang ZM, Bibo GA. The potential of knitting for engineering composites – a review. Composites Part A 2000:31;197-220

[6]   Mouritz AP. Review of z-pinned composites laminates. Composites Part A 2007:38;2383-2397

[7]   Greenhalgh E, Hiley M. The assessment of novel materials and processes for the impact tolerant design of stiffened composite aerospace structures. Composites Part A 2003:34;151-161

[8]   Rueckert C, Kolax M. New Design Approaches for Composite Fuselage Structures – Requirements for Advanced Materials, Processes and Manufacturing Technologies 14-18 July 2003:14th International Conference on Composite Materials, San Diego, California, USA

[9]   Kobayashi Y, Ito M. Development of 3-D Woven Composites to Aircraft Structures. 16th International Conference on Composite Materials 2007, Kyoto, Japan

[10]   Bogdanovich AE. Advancements in Manufacturing and Applications of 3-D Woven Preforms and Composites. 16th International Conference on Composite Materials 2007, Kyoto, Japan

[11]   Mouritz AP, Bannister MK, Falzon PJ, Leong KH. Review of applications for advanced three-dimensional fibre textile composites: Composites Part A 1999:30;1445-1461

[12] Finckh H. Numerische Simulation der mechanischen Eigenschaften textiler Flächengebilde – Gewebeherstellung. 3rd LS-Dyna User Conference, 2003 Bamberg, Germany

[13] George A. Optimization of Resin Infusion Processing for Composites Materials: Simulation and Characterization Strategies. PhD Thesis, University of Stuttgart 2011.

[14] Pastore CM. Illustrated Glossary of Textile Terms for Composites. NASA Contractor Report 191539 1993, last access: 18. July 2012http://ntrs.nasa.gov/archive/nasa/casi.ntrs.nasa.gov/19940011011_1994011011.pdf

[15] Bader MG. Selection of composite materials and manufacturing routes for cost-effective performance. Composites Part A 2002:33;913-934

[16] Han NL, Suh SS, Yang JM, Hahn HT. Resin film infusion of stitched stiffened composite panels. Composites Part A 2003:34;227-236

[17] Somashekar AA, Bickerton S, Bhattacharyya D. Compression deformation of a biaxial stitched glass fibre reinforcement: Visualisation and image analysis using X-ray micro-CT. Composites Part A 2011:42;140-150

[18] Summerscales J, Searle TJ. Low-pressure (vacuum infusion) techniques for moulding large composite structures. ProcIMechE L JDMA 2005:219;45-58

[19] Sevostianov IB, Verijenko VE, von Klemperer CJ, Chevallereau B. Mathematical model of stress formation during vacuum resin infusion process. Composites Part B 1999:30;513-521

[20] Hou TH, Jensen BJ. Evaluation of Double-Bag Process for Composite Fabrication. NASA Langley Research Center, Hampton, Virginia 23681

[21] Lang EJ, Chou TW. The Effect of Strain Gage Size on Measurement Errors in Textile Composite Materials. Composites Science and Technology 1998:58;539-548

[22] Cox BN, Dadkhah MS. The Macroscopic Elasticity of 3D Woven Composites. Journal of Composite Materials 1995:29;785-819

[23] Cox BN, Dadkhah MS, Morris WL. On the tensile failure of 3D woven composites. Composites Part A 1996:27A;447-458

[24]   Naceri A, Vautrin A. Analysis of the Mechanical Behaviour in Shear of Woven Fabric Reinforced Composite under Uniaxial Tension. Key Engineering Materials 2004:274-276;643-648

[25]   Lomov SV, Ivanov DS, Truong TC, Verpoest I, Baudry F, Vanden Bosche K, Xie H. Experimental methodology of study of damage initiation and development in textile composites in uniaxial tensile test. Composites Science and Technologies 2008:68;2340-2349

[26]   Daggumati S, De Baere I, Van Paepegem W, Degrieck J, Xu J, Lomov SV, Verpoest I. Local damage in a 5-harness satin weave composites under static tension: part i – experimental analysis. Composites Science and Technology 2010:70;1926-1933

[27]   Gao F, Boniface L, Ogin SL, Smith PA, Greaves RP. Damage accumulation in woven-fabric CFRP laminates under tensile loading: Part 1. Observations of damage accumulation. Composites Science and Technology 1999:59;123-136

[28]   Ivanov DS, Baudry F, Van Den Broucke B, Lomov SV, Xie H, Verpoest I. Failure analysis of triaxial braided composite. Composites Science and Technology 2009:69;1372-1380

[29]   Quinn JP, McIlhagger AT, McIlhagger R. Examination of the failure of 3D woven composites. Composites Part A 2008:39;273-283

[30]   Stig F, Hallström S. Assessment of the mechanical properties of a new 3D woven fibre composite material. Composites Science and Technology 2009:62;1686-1692

[31]   Pochiraju K. Three-Dimensionally Woven and Braided Composites. II: Experimental Characterization. Polymer Composites 1999:20;733-747

[32]   Cox BN, Dadkhah MS, Inman RV, Morris WL, Zupon J. Mechanisms of Compressive Failure in 3D Composites. Acta metall. Mater. 1992:40;3285-3298

[33]   Callus PJ, Mouritz AP, Bannister MK, Leong KH. Tensile properties and failure mechanisms of 3D woven GRP composites. Composites Part A 1999:30;1277-1287

[34] Cox BN, Dadkhah MS, Morris WL, Flinthoff JG. Failure Mechanisms of 3D Woven Composites in Tension, Compression and Bending. Acta metall. Mater. 1994:42;3967-3984

[35] Leong KH, Lee B, Herszberg I, Bannister MK. The effect of binder path on the tensile properties and failure of multilayer woven CFRP composites. Composites Science and Technologies 2000:60;149-156

[36] Kuo W-S, Ko T-H, Lo T-S. Failure behavior of three-axis woven carbon/carbon composites under compressive and transverse shear loads. Composites Science and Technology 2002:62;989-999

[37] Kuo WS, Fang J, Lin HW. Failure behavior of 3D woven composites under transverse shear. Composites Part A 2003:34;561-575

[38] Mouritz AP, Baini C, Herszberg I. Mode I interlaminar fracture toughness properties of advanced textile fibreglass composites. Composites Part A 1999:30;859-870

[39] Rudov-Clark S, Mouritz AP. Tensile fatigue properties of a 3D orthogonal woven composite. Composites Part A 2008:39;1018-1024

[40] Mouritz AP. Tensile fatigue properties of 3D composites with through-thickness reinforcement. Composites Science and Technology 2008:68;2503-2510

[41] Dadkhah MS, Cox BN, Morris WL. Compression-Compression Fatigue of 3D Woven Composites. Acta metall. Mater. 1995:43;4235-4245

[42] Lomov SV, Ivanov DS, Verpoest I, Zako M, Kurashiki T, Nakai H, Hirosawa S. Meso-FE modelling of textile composites: Road map, data flow and algorithms. Composites Science and Technology 2007:67;1870-1891

[43] Crookston JJ, Long AC, Jones IA. A summary review of mechanical properties prediction methods for textile reinforced polymer composites. Proc. IMechE Part L: J. Materials: Design and Applications 2005:219;91-109

[44] McBride TM, Chen J. Unit-cell geometry in plain-weave fabrics during shear deformations. Composites Science and Technology 1997:57;345-351

[45] Verpoest I, Lomov SV. Virtual Textile Composites Software WiseTex: Integration with micro-mechanical, permeability and structural analysis. Composites Science and Technology 2005:65;2563-2574

[46] Long AC, Robitaille F, Rudd CD, Jones IA. Modelling Strategies for Textile Composites. Proc. ICCM-14, July 2003, San Diego, CA, USA

[47] Ansar M, Wang X, Chouwei Z. Modeling Strategies of 3D Woven Composites: A Review. Composites Structures 2011:93;1947-1963

[48] Sherburn M. Geometric and Mechanical Modelling of Textiles. University of Nottingham, PhD Thesis, 2007

[49] Blacklock M, Bale H, Begley M, Cox BN. Generating virtual textile composite specimens using statistical data from micro-computed tomography: 1D tow representations for the Binary Model. Journal of the Mechanics and Physics of Solids 2012:60;451-470

[50] Rinaldi RG, Blacklock M, Bale H, Begley M, Cox BN. Generating virtual textile composite specimens using statistical data from micro-computed tomography: II. 3D tow representations. Journal of the Mechanics and Physics of Solids 2012 DOI:10.1016/j.jmps.2012.02.008

[51] Daggumati S, Van Paepegem W, Degrieck J, Xu J, Lomov SV, Verpoest I. Local damage in a 5-harness satin weave composite under static tension: part ii – meso – FE modelling. Composites Science and Technology 2010:70;1934-1941

[52] Bogdanovich AE. Multi-scale modelling, stress and failure analyses of 3D woven composites. J. Mater. Sci. 2006:41;6547-6590

[53] Naik NK, Ganesh VK. Prediction of on-axes elastic properties of plain weave fabric composites. Composites Science and Technology 1992:45;135-152

[54] Tan P, Tong L, Steven GP. Micromechanics models for the elastic constants and failure strengths of plain weave composites. Composites Structures 1999:47;797-804

[55] Glaessgen EH, Pastore CM, Griffin HO, Birger A. Geometrical and finite element modelling of textile composites. Composites Part B 1996:27B;43-50

[56] Lin H, Sherburn M, Crookston J, Long AC, Clifford MJ, Jones IA. Finite element modelling of fabric compression. Modelling Simul. Mater. Sci. Eng. 2008:16;1-16

[57] Blassiau S, Thionnet A, Bunsell AR. Three-dimensional analysis of load transfer micromechanisms in fibre/matrix composites. Composites Science and Technology 2009:69;33-39

[58] Mayes JS, Hansen AC. Composite laminate failure analysis using multicontinuum theory. Composites Science and Technology 2004:64;379-394

[59] Dasgupta A, Agarwal RK, Bhandarkar SM. Three-Dimensional Modeling of Woven-Fabric Composites for Effective Thermo-Mechanical and Thermal Properties. Composites Science and Technology 1996:56;209-223

[60] Whitcomb J, Srirengan K. Effect of various approximations on predicted progressive failure in plain weave composites. Composite Structures 1996:34;13-20

[61] Owens BC, Whitcomb JD, Varghese J. Effect of Finite Thickness and Free Edges on Stresses in Plain Weave Composites. Journal of Composite Materials 2010:44;675-692

[62] Whitcomb JD, Chapman CD, Tang X. Derivation of Boundary Conditions for Micromechanics Analyses of Plain and Satin Weave Composites. Journal of Composites Materials 2000:34;724-747

[63] Guagliano M, Riva E. Mechanical behaviour prediction in plain weave composites. Journal of Strain Analysis 2001:36;153-162

[64] Ivanov DS, Lomov SV, Ivanov SG, Verpoest I. Stress distribution in outer and inner plies of textile laminates and novel boundary conditions for unit cell analysis. Composites Part A 2010:41;571-580

[65] Rupnowski P, Kumosa M. Meso- and micro-stress analyses in an 8HS graphite/polyimide woven composite subjected to biaxial in-plane loads at room temperature. Composite Science and Technology 2003:63;785-799

[66] Lomov SV, Verpoest I, Peeters T, Roose D, Zako M. Nesting in Textile Laminates: Geometrical Modelling on the laminate. Composites Science and Technology 2003:63;993-1007

[67] Le Page BH, Manger CIC, Guild FJ, Ogin SL, Smith PA. Modelling the effect of layer shift on properties of woven fabric composites. Plastics, Rubber and Composites 2002:31;385-391

[68] Le Page BH, Guild FJ, Ogin SL, Smith PA. Finite element simulation of woven fabric composites. Composites Part A 2004:35;861-872

[69] Blackketter DM, Walrath DE, Hansen AC. Modeling Damage in a Plain Weave Fabric-Reinforced Composite Material. Journal of Composites Technology & Research 1993:15;136-142

[70] Heß H, Himmel N. Structurally Stitched NCF CFRP Laminates. Part 2: Finite Element Unit Cell Based Prediction of In-Plane Strength. Composites Science and Technology 2011:71;569-585

[71] Tserpes KI, Labeas GN. Mesomechanical analysis of non-crimp fabric composite structural parts. Composite Structures 2009:87;358-369

[72] Ivanov DS, Lomov SV, Vallons K, Troung Chi T, Verpoest I. Analysis of Failure in Textile Composites Via Meso-Damage Mechanics. 27 – 29 Jul 2009:17th International Conference on Composite Materials, Edinburgh, UK

[73] Iannucci L, Willows ML. An energy based damage mechanics approach to modelling impact onto woven composite materials – Part I: Numerical models. Composites Part A 2006:37;2041-2056

[74] Iannucci L, Willows ML. An energy based damage mechanics approach to modelling impact onto woven composite materials – Part II: Experimental and numerical results. Composites Part A 2007:38;540-554

[75] Key CT, Six RW, Hansen AC. A three-constituent multicontinuum theory for woven fabric composite materials. Composites Science and Technology 2003:63;1857-1864

[76] Key CT, Schumacher SC, Hansen AC. Progressive failure modeling of woven fabric composite materials using multicontinuum theory. Composites Part B 2007:38;247-257

[77] Šmilauer V, Hoover CG, Bažant ZP, Caner FC, Waas AM, Shahwan KW. Multiscale Simulation of Fracture of Braided Composites via Repetitive Unit Cells. Engineering Fracture Mechanics 2010:78;901-918

[78] Venkat Rao M, Mahajan P, Mittal RK. Effect of architecture on mechanical properties of carbon/carbon composites. Composite Structures 2008:83;131-142

[79] Ruijter W, Crookston JJ, Long AC, Jones IA. Computational meso-scale analysis of textile composites using adaptive finite element analysis.

Proceedings of the 47th AIAA/ASME/ASCE/AHS/ASC Structures, Structural Dynamics and Materials (SDM 47) Conference, 1-5th June 2006, Newport, RI, USA

[80] Crookston JJ, Ruijter W, Long AC, Jones IA. Modelling Mechanical Performance including Damage Development for Textile Composites using a Grid-Based Finite Element Method with Adaptive Mesh Refinement. 8th International Conference on Textile Composites (TEXCOMP-8), 16-18 Oct 2006, Nottingham, UK

[81] Blackketter DM, Walrath DE, Hansen AC. Modeling Damage in a Plain Weave Fabric-Reinforced Composite Material. Journal of Composites Technology & Research JCTRER 1993:15;136-142

[82] Bauwens JC. Yield condition and propagation of Lüders' lines in tension-torsion experiments on poly(vinyl chloride). Journal of Polymer Science Part A-2: Polymer Physics 1970:8;893-901

[83] Tserpes KI, Labeas G, Pantelakis Sp. Multi-scale modeling of the mechanical response of plain weave composites and cellular solids. Theoretical and Applied Fracture Mechanics 2010:54;172-179

[84] Cox BN, Carter WC, Fleck NA. A Binary Model of Textile Composites – I. Formulation. Acta metall. mater. 1994:42;3463-3479

[85] Xu J, Cox BN, McGlockton MA, Carter WC. A Binary Model of Textile Composites – II. The Elastic Regime. Acta metall. mater. 1995:43;3511-3524

[86] McGlockton MA, Cox BN, McMeeking RM. A Binary Model of Textile Composites – III. High Failure Strain and Work of Fracture in 3D Weaves. Journal of the Mechanics and Physics of Solids 2003:51;1573-1600

[87] Yang Q, Cox BN. Predicting Local Strains in Textile Composites using the Binary Model Formulation. Proceedings of the ICCM 2003, San Diego, CA, USA

[88] Cox BN, Yang Q. Predicting failure in textile composites using the Binary Model with gauge averaging. Engineering Fracture Mechanics 2010:77;3174-3189

[89] Cox BN, McMeeking RM, McGlockton MA. The Binary Model – A Computational Approach to Textile Composites. Proceedings of the ICCM 2000, Paris, France

[90] Ivanov D, Ivanov S, Lomov S, Verpoest I. Strain mapping analysis of textile composites. Optics and Lasers in Engineering 2009:47;360-370

[91] Lomov SV, Ivanov DS, Verpoest I, Zako M, Kurashiki T, Nakai H, Molimard J, Vautrin A. Full-field strain measurements for validation of meso-FE analysis of textile composites. Composites Part A 2008:39;1218-1231

[92] Pitarresi G, Patterson EA. A review of the general theory of thermoelastic stress analysis. J. Strain Analysis 2003:38;405-417

[93] Emery T, Dulieu-Barton JM, Cunningham PR. Identification of Damage in Composite Structures using Thermoelastic Stress Analysis. Key Engineering Materials 2005:293-294;583-590

[94] Wong AK, Jones R, Sparrow JG. Thermoelastic Constant or Thermoelastic Parameter. J. Phys. Chem. Solids 1987:48;749-753

[95] Wong AK, Sparrow JG, Dunn SA. On the revised theory of the thermoelastic effect. J. Phys. Chem. Solids 1988:49;395-400

[96] Van Hemelrijck D, Schillemans L, Cardon AH. The Effects of Motion on Thermoelastic Stress Analysis. Composite Structures 1991:18;221-238

[97] Stanley P, Chan WK. The Application of Thermoelastic Stress Analysis Techniques to Composite Materials. Journal of Strain Analysis 1988:23;137-143

[98] Wong AK. A Non-Adiabatic Thermoelastic Theory for Composite Laminates. J. Phys. Chem. Solids 1991:52;483-494

[99] Dulieu-Barton JM, Emery TR, Quinn S, Cunningham PR. A temperature correction methodology for quantitative thermoelastic stress analysis and damage assessment. Meas. Sci. Technol. 2006:17;1627-1637

[100] Frühmann RK, Dulieu-Barton JM, Quinn S. On the thermoelastic response of woven composite materials. J. Strain Analysis 2007:43;435-450

[101] Schapery RA. Thermal Expansion Coefficients of Composite Materials Based on Energy Principals. J. Compos. Mater 1968:2;380-404

[102] Khan KA, Muliana AH. Effective thermal properties of viscoelastic composites having field-dependent constituent properties. Acta Mech 2010:209;153-178

[103] Frühmann RK. Stress and Damage Assessment in Woven Composite Materials by Means of Thermoelastic Stress Analysis. University of Southampton, Faculty of Engineering, Science and Mathematics, School of Engineering Sciences. PhD Thesis

[104] Frühmann RK, Dulieu-Barton JM, Quinn S. Material Heterogeneity or Stress Concentration: The Thermoelastic Response from Woven Composite Materials Subjected to Cyclic Fatigue. 27 – 29 Jul 2009:17th International Conference on Composite Materials, Edinburgh, UK

[105] Fruehmann RK, Dulieu-Barton JM, Quinn S. Assessment of fatigue damage evolution in woven composites materials using infra-red techniques. Composites Science and Technology 2010:70;937-946

[106] Frühmann RK, Dulieu-Barton JM, Quinn S. Thermoelastic Stress and Damage Analysis using Transient Loading. Experimental Mechanics 2010:50;1075-1086

[107] Kinney JH, Stock SR, Nichols MC, Bonse U, Breunig TM, Saroyan RA, Nusshardt R, Johnson QC, Busch F, Antolovich SD. Nondestructive investigation of damage in composites using x-ray tomographic microscopy (XTM). J. Mater. Res. 1990:5;1123-1129

[108] Badel P, Vidal-Sallé E, Maire E, Boisse P. Simulation and tomography analysis of textile composite reinforcement deformation at the mesoscopic scale. Composites Science and Technology 2008:68;2433-2440

[109] Hufenbach W, Richter H, Langkamp A, Böhm R. Application of acoustic emission analysis for damage investigations in fibre and textile reinforced composites. E-Journal of Nondestructive Testing 2006:11;1-10

[110] ASTM Standard D3039/D 3039M - 08 2008 "Standard Test Method for Tensile Properties of Polymer Matrix Composite Materials" West Conshohocken, PA, 2008 DOI: 10.1520/D3039_D3039M-08

[111] ASTM Standard D3518/D3518M - 94 2007 "Standard Test Method for In-Plane Shear Response of Polymer Matrix Composite Materials by Tensile

Test of a ±45° Laminate" West Conshohocken, PA, 2007 DOI: 10.1520/D3518_D3518M-94R07

[112] http://www.nevamarine.com/images/ katalog/RE86P%281%29.pdf;15th of May 2012

[113] http://www.gurit.com/files/documents/prime-20lvv9pdf.pdf, 15th of May 2012

[114] http://www.swiss-composite.ch/pdf/i-Werkstoffdaten.pdf 16th of May 2012

[115] Rinaldi RG, Blacklock M, Bale H, Begley MR and Cox BN. Generating virtual textile composite specimens using statistical data from micro-computed tomography: II. 3D tow representations, Journal of the Mechanics and Physics of Solids, doi:10.1016/j.jmps.2012.02.008

[116] Daggumati S, De Baere I, Van Paepegem W, Degrieck J, Xu J, Lomov SV, Verpoest I. Local damage in a 5 – harness satin weave composite under static tension: part i – experimental analysis. Composites Science and Technology 2010;doi:10.1016/j.compscitech.2010.07.003.

[117] Ivanov DS, Lomov SV, Ivanov SG, Verpoest I. Stress distribution in outer and inner plies of textile laminates and novel boundary conditions for unit cell analysis. Composites Part A 2010;41:571-580

[118] Le Page BH, Guild FJ, Ogin SL, Smith PA. Finite element simulation of woven fabric composites. Composites Part A 2004;35:861-872

[119] Hivet G, Boisse P. Consistent 3D geometrical model of fabric elementary cell. Application to a meshing pre-processor for 3D finite element analysis. Finite Elements in Analysis and Design 2005;42:25-49

[120] Emery TR, Dulieu-Barton JM, Earl JS, Cunningham PR. A Generalised Approach to the Calibration of Orthotropic Materials for Thermoelastic Stress Analysis. Composites Science and Technology 2009;68:743-752

[121] British Standard Institution (1983) "BS 2782-10: Method of testing Plastics – Part 10: Glass Reinforced Plastics – Method 1003: Determination of Tensile Properties" British Standards Online. (Acessed: 17 May 2012) https://bsol.bsigroup.com/en/Bsol-Item-Detail Page/?pid=00000000000038392

[122] Lang EJ, Chou T-W. The effect of strain gage size on measurement errors in textile composite materials. Composites Science and Technology 1998;58:539-548

[123] ASTM Standard "E1237 - 93 (2009) Standard Guide for Installing Bonded Resistance Strain Gages" West Conshohocken, PA, 2009 DOI: 10.1520/E1237-93R09

[124] Callus PJ, Mouritz AP, Bannister MK, Leong KH. Tensile properties and failure mechanisms of 3D woven GRP composites. Composites Part A 1999;30:1277-1287

[125] ASTM Standard E111-04 (2010) "Standard Test Method for Young's Modulus, Tangent Modulus and Chord Modulus" West Conshohocken, PA, 2010 DOI: 10.1520/E111-04R10

[126] Danial IM, Ishai O. Engineering Mechanics of Composite Materials 2nd Edition 2006, Oxford University Press ISBN-13: 978-0195075069

[127] Hu Y, Xia Z, Ellyin F. Deformation Behaviour of an Epoxy Resin Subject to Multiaxial Loadings. Part I: Experimental Investigations. Polymer Engineering and Science 2003;43:721-733

[128] Bazhenov SL, Rogozinskii AK, Evstiforov SS, Berlin AA. Abnormal Effect of Tensile Strain on Young's Modulus of Inorganic E-Glass Fibres. Doklady Physical Chemistry 2010;433:118-120

[129] Tang X, Whitcomb JD. General Techniques for Exploiting Periodicity and Symmetries in Micromechanics Analysis of Textile Composites. Journal of Composite Materials 2003;37:1167-188

[130] ABAQUS/Standard User's Manual 2008, Hibbit, Karlsson and Sorensen, Inc., Pawtucket, Rhode Island

[131] Ellyin F, Zihui X. Nonlinear Viscoelastic Constitutive Model for Thermoset Polymers. Journal of Engineering Materials and Technology. 2006;128:579-585

[132] Hu Y, Xia Z, Ellyin F. Deformation Behavior of an Epoxy Resin Subject to Multiaxial Loadings Part I: Experimental Investigations. Polymer Engineering & Science 2003;43:721-733

[133] Dean G. Modelling non-linear creep behaviour of an epoxy adhesive. International Journal of Adhesion and Adhesives 2007;27:636-646

[134] Bardella L. A phenomenological constitutive law for the nonlinear viscoelastic behaviour of epoxy resins in the glassy state. European Journal of Mechanics – A/Solids 2001;20:907-924

[135] Mondragon I, Remiro PM, Martin MD, Valea A, Franco M, Bellenguer V. Viscoelastic Behaviour of Epoxy Resins Modified with Poly(methyl methacrylate. Polymer International 1998;47:152-158

[136] Jeong HY. A new yield function and a hydrostatic stress-controlled void nucleation model for porous solids with pressure-sensitive matrices. International Journal of Solids and Structures 2002;39:1385-1403

[137] Roylance D. Yield and Plastic Flow. Course Material Mechanics of Materials (October 15 2001), Department of Materials Science and Engineering, Massachusetts Institute of Technology (Accessed 03.Sept.2012). http://ocw.mit.edu/courses/materials-science-and-engineering/3-11-mechanics-of-materials-fall-1999/modules/yield.pdf

[138] Frühmann RK, Sambasivam S, Dulieu-Barton JM, Quinn S. Material Properties in Quantitative Thermoelastic Stress Analysis of Composite Structures. Applied Mechanics and Materials 2008;13-14:99-104

[139] Römelt P, Cunningham PR. A multi-scale finite element approach for modelling damage progression in woven composite structures. Composite Structures 2012;94:977-986

Appendix A – Iterative Code Test

Tow Path Parameters

The following code was used to iteratively find the tow path amplitude and phase using a least-square fit algorithm with a regular falsi iterative procedure.

```python
import math
import string


i = 0
lineA = ['0']
lineB = ['0','0']
lineC = [0.0,0.0]
data = [0.0]


#READ DATA POINTS
f = file('path_test.txt','r')
while 1:
    lineA = f.readline()
    if len(lineA) == 0:
        break
    lineB = lineA.split()
    m = float(lineB[0])
    n = float(lineB[1])
    data.append([m,n])
    i=i+1
del data[0]
```

```
f.close()


X_MIN = X_MAX = data[0][0]

Y_MIN = Y_MAX = data[0][1]


#FIND CENTRE POINT

for g in range(0,len(data),1):

    if data[g][0] < X_MIN:

        X_MIN = data[g][0]

    if data[g][0] > X_MAX:

        X_MAX = data[g][0]

    if data[g][1] < Y_MIN:

        Y_MIN = data[g][1]

    if data[g][1] > Y_MAX:

        Y_MAX = data[g][1]


YM = (Y_MAX - Y_MIN)/2. + Y_MIN

#MOVE CENTRE POINT TO (0,0)

for g in range(0,len(data),1):

    data[g][1] = data[g][1] - YM


#INITIAL VALUES

sum1 = sum2 = sum3 = sum4 = sum5 = 0.0

L = 2.


A_old = B_old = A_new = B_new = (abs(Y_MIN) + abs(Y_MAX))/2.
```

```python
for g in range(0,len(data),1):

    sum1 = sum1 + data[g][1]*math.sin(2*3.142*data[g][0]/L)

    sum2 = sum2 + math.sin(4*3.142*data[g][0]/L)

    sum3 = sum3 + (1-math.cos(4*3.142*data[g][0]/L))

    sum4 = sum4 + data[g][1]*math.cos(2*3.142*data[g][0]/L)

    sum5 = sum5 + (1+math.cos(4*3.142*data[g][0]/L))


#ITERATION
for g in range(0,100000,1):

    A_old = A_new

    A_new = (2.*sum1 - B_new*sum2)/sum3

    if abs(A_new) > 1.0E100:

        print 'failed'

        break

    for h in range(0,100000,1):

        B_old = B_new

        B_new = (2.*sum4 - A_new*sum2)/sum5

        if abs(B_new - B_old) < 0.0001:

            print 'B_new'

            break

        elif abs(B_new) > 1.0E100:

            print 'failed'

            break

    if abs(A_old - A_new) < 0.0001:

        print 'A_new'
```

```
        break
```

print A_new, B_new, YM

A simple test case has been defined using a standard sin function $y(x) = A \sin\left(\frac{2\pi x}{L}\right) + B \cos\left(\frac{2\pi x}{L}\right)$ with parameters A = 3, B = 5 and L = 2 and an offset $Y_M = 3$ on the y-axis. The code found a value of 3.003 for parameter A and a value of 4.997 for parameter B, which is an error of less than 0.1% for both parameters.

Tow Cross Section Parameters

The following code was used to iteratively find the tow cross section parameters meaning major and minor axis parameters of a standard ellipse.

```
import math

import string

i = 0

lineA = ['0']

lineB = ['0','0']

lineC = [0.0,0.0]

data = [0.0]

#READ DATA POINTS

f = file('test_case_ellipse2.txt','r')

while 1:

   lineA = f.readline()

   if len(lineA) == 0:
```

```python
        break

    lineB = lineA.split()

    m = float(lineB[0])

    n = float(lineB[1])

    data.append([m,n])

    i=i+1

del data[0]

f.close()

X_MIN = X_MAX = data[0][0]

Y_MIN = Y_MAX = data[0][1]

#FIND CENTRE POINT

for g in range(0,len(data),1):

    if data[g][0] < X_MIN:

        X_MIN = data[g][0]

    if data[g][0] > X_MAX:

        X_MAX = data[g][0]

    if data[g][1] < Y_MIN:

        Y_MIN = data[g][1]

    if data[g][1] > Y_MAX:

        Y_MAX = data[g][1]

XM = (X_MAX - X_MIN)/2. + X_MIN
```

YM = (Y_MAX - Y_MIN)/2. + Y_MIN

#MOVE CENTRE POINT TO (0,0)

for g in range(0,len(data),1):

   data[g][0] = data[g][0] - XM

   data[g][1] = data[g][1] - YM

#INITIAL VALUES

sum1 = sum2 = sum3 = sum4 = sum5 = 0.0

theta = 0.0

lowest = 0

result = [['','','',1.0E100]]

a_new = (X_MAX - X_MIN)/2.

b_new = (Y_MAX - Y_MIN)/2.

#ITERATION

for g in range(0,20,1):

   alpha = (theta + g)*3.142/180.

   k = 0.

   for e in range(0,len(data),1):

     x = data[e][0]*math.cos(alpha)+data[e][1]*math.sin(alpha)

     y = data[e][0]*math.sin(alpha)+data[e][1]*math.cos(alpha)

     sum1 = sum1 + math.pow(x,4)

     sum2 = sum2 + math.pow(y,4)

```
        sum3 = sum3 + math.pow(x,2)

        sum4 = sum4 + math.pow(y,2)

        sum5 = sum5 + math.pow(x,2)*math.pow(y,2)

    for e in range(0,10000,1):

        a_old = a_new

        b_old = b_new

        a_new = sum1/(sum3-sum5/b_new)

        b_new = sum2/(sum4-sum5/a_new)

        if (abs(a_new)-abs(a_old)) < 0.0001 AND (abs(b_new)-abs(b_old)) < 0.0001

            break

    for e in range(0,len(data),1):

        k = k + abs(math.pow(y,2) - math.pow(b_new,2)*(1-math.pow((x/a_new),2)))
/a_new+math.pow(data[e][0]*math.sin(alpha)+data[e][1]*math.cos(alpha),2)/b_new-1

    list1 = [a_new, b_new, alpha*180/3.142, k]

    result.append(list1)

del result[0]

for g in range(0,len(result),1):

    if result[g][3] < result[lowest][3]:

        lowest = g

print result[lowest], XM, YM
```

Similar to the test case defined for the tow path amplitude and phase, a test case was defined for this code using a standard ellipse function with a major axis

parameter of 5 mm and a minor axis parameter of 3. An offset of 1 mm and -2 mm were also defined for the x- and y-axis respectively. Finally, the ellipse was rotated by 24° around the z-axis. The error resulting from the code is less than 0.01% for both parameters.

Appendix B – Submodelling Technique

In this Appendix a simple model is investigated to verify the submodelling technique used to assign displacement values on the boundary of the full finite element model under shear loading conditions. For this a block of four solid elements, each side of a solid being 1 mm in size, is defined with tensile a displacement of 0.1 mm assigned to the yz-faces in global x direction (Figure 127). This model is the larger scale or global model used in this submodel analysis.
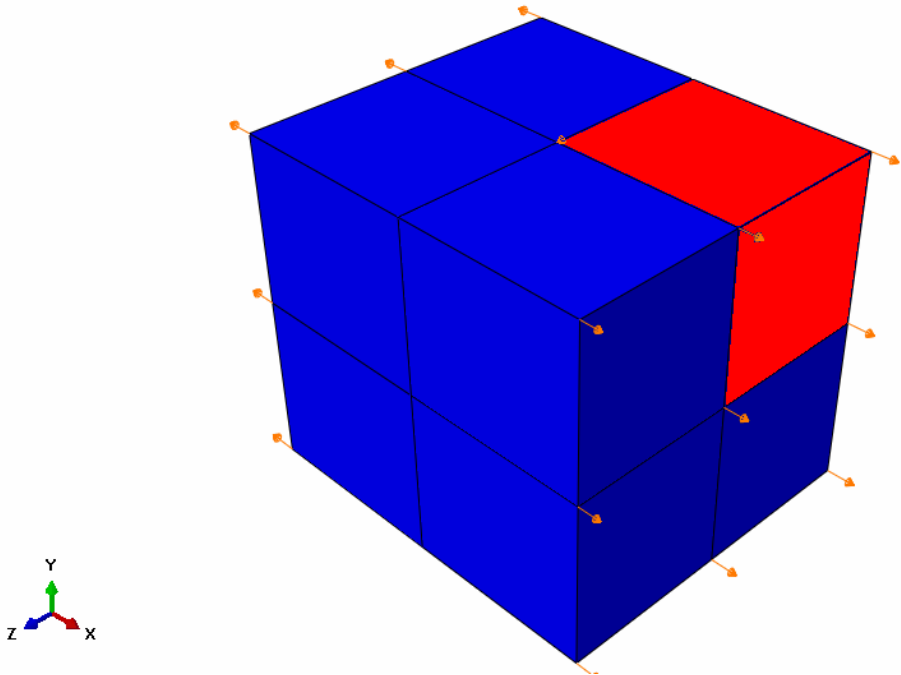
Figure 127: Submodelling Technique

The resulting displacement on the nodes of the solid marked in red in Figure 127 are assigned as boundary conditions to a block of 4 solids, each side being 0.5 mm, which are located in the same position as the solid marked in red. For this the *BOUNDARY, SUBMODEL option available in ABAQUS/Standard is used. This model is called the local or submodel. Figure 128 shows the displacement in x direction of the resulting submodel run. The nodes on the yz face in positive x direction are displaced by 0.1 mm like they are in the global model. Nodes on the yz face in negative x direction are the centre nodes in the global model. They remain in their initial positions in the global model since the same displacement is assigned in opposite directions on opposite faces in global x direction. In the submodel these nodes are also not displaced as can be seen in Figure 128. The pattern of

displacements shown in the submodel showed the set-up of the submodelling technique was correct, which verifies the technique.
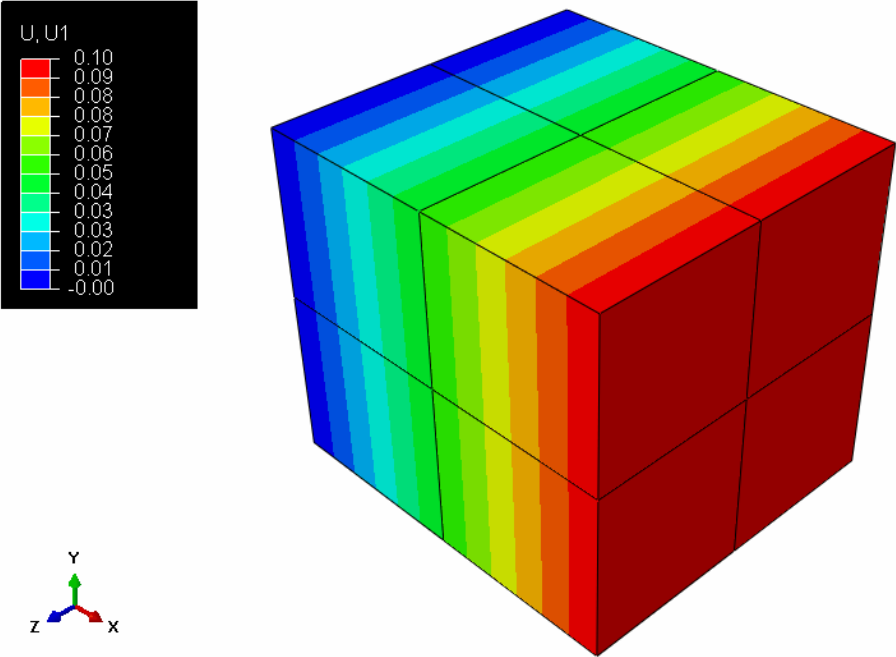

Figure 128: Submodel Displacement

Appendix C – Cohesive element formulation test
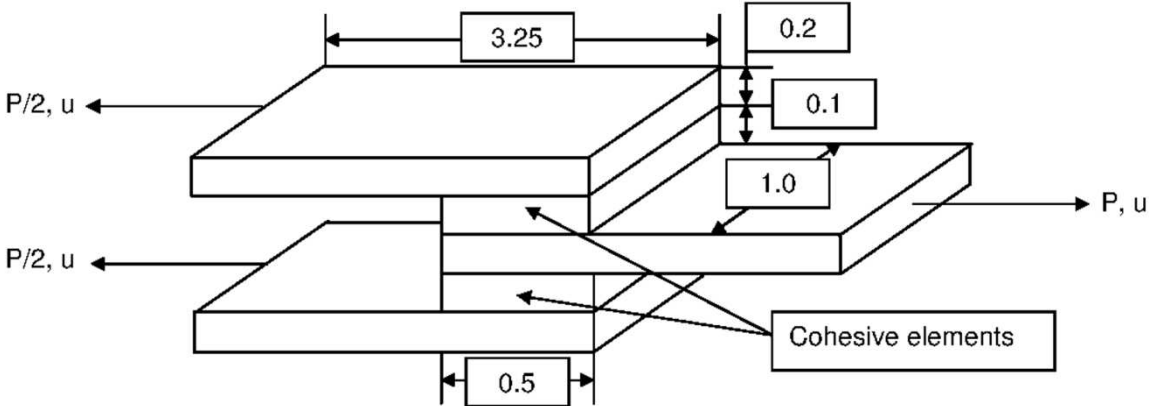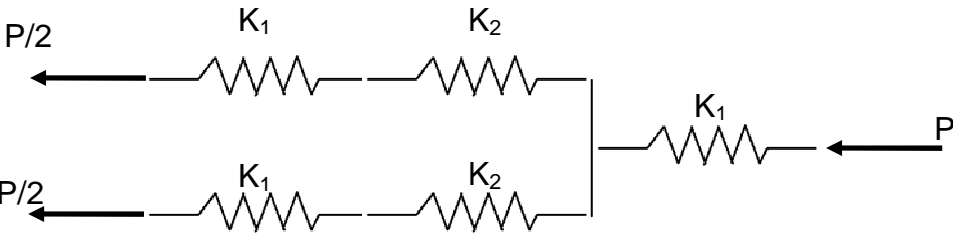

Figure 129: Double Lap Joint for Cohesive Element Tests

A substitute system using springs for the structure above would look as follows:

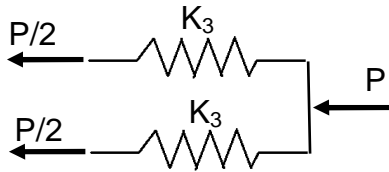The spring stiffnesses for the individual parts of the structure are:

$$K_1 = \frac{E_{steel} A_{steel}}{L_{steel}} = \frac{210 \times 0.2 \times 1}{3.25} = 12.9 \frac{kN}{mm}$$

$$K_2 = \frac{G_{epoxy} A_{epoxy}}{t_{epoxy}} = \frac{1.3 \times 0.5 \times 1}{0.1} = 7.5 \frac{kN}{mm}$$
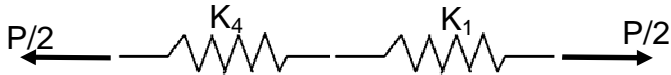
Using the laws of springs in series and parallel the overall stiffness of the system is calculated.

$$K_3 = \frac{K_1 K_2}{K_1 + K_2} = \frac{12.9 \times 7.5}{12.9 + 7.5} = 4.7 \frac{kN}{mm}$$

$$K_4 = 2K_3 = 2 \times 4.7 = 9.4\frac{kN}{mm}$$

$$K_{total} = \frac{K_1 K_4}{K_1 + K_4} = \frac{12.9 \times 9.4}{12.9 + 9.4} = 5.4\frac{kN}{mm}$$

With a prescribed displacement u of 0.2 mm results a force and a shear stress of

$$P = K_{total} \times u = 5.4 \times 0.2 = 1.08\ kN$$

$$\tau = \frac{P}{2A} = \frac{1.08}{2 \times 1 \times 0.5} = 1.08\ GPa$$
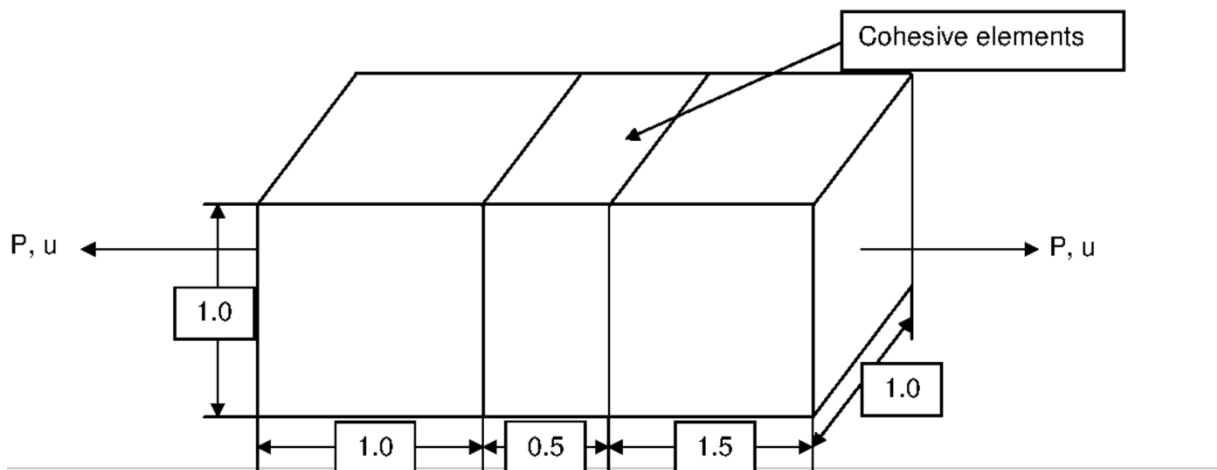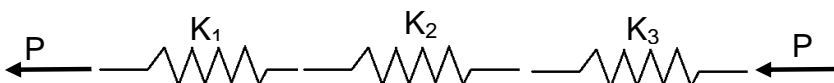
Tensile Test

Figure 130: Tension Test for Cohesive Element Formulation

The substitute system using springs for the structure above looks as follows:

The spring stiffnesses for the individual parts of the structure are:

$$K_1 = \frac{E_{steel}A_{steel}}{L_{steel}} = \frac{210 \times 1 \times 1}{1} = 210 \; \frac{kN}{mm}$$

$$K_2 = \frac{E_{epoxy}A_{epoxy}}{L_{epoxy}} = \frac{3.5 \times 1 \times 1}{0.5} = 7 \; \frac{kN}{mm}$$

$$K_3 = \frac{E_{steel}A_{steel}}{L_{steel}} = \frac{210 \times 1 \times 1}{1.5} = 140 \; \frac{kN}{mm}$$

$$\frac{1}{K_{total}} = \frac{1}{K_1} + \frac{1}{K_2} + \frac{1}{K_3} = \frac{1}{210} + \frac{1}{7} + \frac{1}{140} = 0.155 \; \rightarrow \; K_{total} = 6.5 \frac{kN}{mm}$$

With a prescribed displacement of 0.2 mm results a force and tensile stress of

$$P = K_{total} \times u = 6.5 \times 0.2 = 1.3 \; kN$$

$$\sigma = \frac{P}{A} = \frac{1.3}{1 \times 1} = 1.3 \; GPa$$